Martin Nuss, BSc

A cluster many-body approach to quantum impurity models

MASTER THESIS

for obtaining the academic degree
Diplom-Ingenieur

Master's Programme of
Technical Physics

Graz University of Technology

Supervisor:
Univ.-Prof. Dipl.-Phys. Dr.rer.nat. Wolfgang von der Linden
Institute of Theoretical and Computational Physics, TU Graz

Graz, January 4, 2012

Contents

Abstract

Strongly correlated quantum impurity problems have been an important field of condensed matter physics for almost eighty years. Models have been designed to explore the manifold of quantum behavior observed in impurity doped materials. In recent years they served as a cornerstone in the theoretical understanding of novel nano-scale devices like quantum-dots or molecular electronics. These devices have attracted a vast amount of research interest and gave remarkable, key-insights into the behavior of matter at the atomic scale, which is so important for tomorrow's technology. In this thesis, the physics of quantum impurity models is probed by means of the variational cluster approach (VCA) and cluster perturbation theory. Making use of these methods, static and dynamic quantities of the single impurity Anderson model are studied. An expression for the VCA grand potential for a system in a non-interacting infinite bath is presented. Results for dynamic correlation functions in different parameter regimes are shown to be in good agreement with renormalization group results. We address the question of whether the elusive low energy properties of the model are properly reproduced within the framework of VCA. These are furthermore compared to continuous time quantum Monte Carlo calculations. We also discuss results obtained by an alternative, i. e. self-consistent formulation of VCA, which was introduced recently in the context of non-equilibrium systems. A non-equilibrium extension of the variational cluster approach is applied to the problem of a strongly correlated quantum dot under bias. Thereby the question of how to model systems out of equilibrium is addressed. We calculate the steady-state current as well as the non-equilibrium density of states for such a device. Furthermore the properties of Graphene with randomly positioned magnetic vacancies is studied. This problem has aroused a lot of interest in recent experiments with proton irradiated Graphene. Such a setup poses a challenge to any theoretical method because it is not only strongly correlated but highly disordered as well. It is shown that in the variational cluster approach it is possible to treat such a system and harvest results for the density of states.

Kurzfassung

Stark-korrelierte Quanten-Vielteilchensysteme sind seit fast achtzig Jahren ein wichtiges Arbeitsgebiet im Bereich der Physik kondensierter Materie. Zur Beschreibung der vielfältigen, quantenmechanischen Vorgänge, welche zum Beispiel in Materialien mit Störstellen beobachtbar sind, wurden theoretische Modelle entwickelt. In den letzten Jahren wurden diese Modelle auch zur Beschreibung von nano-skaligen Bauteilen, wie Quantenpunkten oder molekularer Elektronik angewendet. Bauteile dieser Art haben ein riesiges Forschungsinteresse generiert und liefern erstaunliche Einsichten in das Verhalten von Materie auf atomaren Längenskalen. Diese Erkenntnisse sind unabdingbar für die Technologie von morgen. In dieser Arbeit wird die Physik von Quanten-Störstellenmodellen mit Hilfe des Variationellen Cluster Zugangs (VCA) und der Cluster Störungsrechnung untersucht. Diese Methoden werden benutzt um statische und dynamische Größen des Ein-Störstellen-Anderson Modells zu studieren. Hierfür wird ein Ausdruck für das VCA Großkanonische Potential, für Systeme in nicht wechselwirkenden, unendlich großen Bädern präsentiert. Es wird gezeigt, dass die erzielten Resultate für dynamische Korrelationsfunktionen in verschiedenen Parameterbereichen mit Renormierungsgruppen-Rechnungen gut übereinstimmen. Weiterhin wird untersucht, ob die schwer berechenbaren Niederenergieeigenschaften des Modells von VCA wiedergegeben werden können. Diese werden außerdem mit kontinuierlichen Zeit - Quanten Monte Carlo Rechnungen verglichen. Zudem werden Ergebnisse, welche mittels einer alternativen, selbstkonsistenten Formulierung von VCA erzielt wurden, diskutiert. Eine Nichtgleichgewichts Erweiterung des Variationellen Cluster Zugangs wird auf das Problem eines stark-korrelierten Quantenpunktes unter Spannung angewendet. Es wird beschrieben wie ein solches Modellsystem im Nichtgleichgewicht modelliert und simuliert werden kann. Dabei wird der Strom im stationären Zustand und die Nichtgleichgewichts- Zustandsdichte berechnet. Weiters studieren wir die Eigenschaften von Graphen mit zufällig verteilten, magnetischen Leerstellen. Dieses Material hat in der letzten Zeit viel Interesse in Experimenten mit protonenbestrahltem Graphen generiert. Solch ein System stellt allerdings eine Herausforderung für theoretische Methoden dar, da es nicht nur stark-korreliert sondern auch hoch ungeordnet ist. Es wird gezeigt, wie solche Systeme mit Hilfe des Variationellen Cluster Zugangs untersucht werden können. Ergebnisse für, unter anderem, die Zustandsdichte werden präsentiert.

Deutsche Fassung:
Beschluss der Curricula-Kommission für Bachelor-, Master- und Diplomstudien vom 10.11.2008
Genehmigung des Senates am 1.12.2008

EIDESSTATTLICHE ERKLÄRUNG

Ich erkläre an Eides statt, dass ich die vorliegende Arbeit selbstständig verfasst, andere als die angegebenen Quellen/Hilfsmittel nicht benutzt, und die den benutzten Quellen wörtlich und inhaltlich entnommene Stellen als solche kenntlich gemacht habe.

Graz, am …… ……..
(Unterschrift)

Englische Fassung:

STATUTORY DECLARATION

I declare that I have authored this thesis independently, that I have not used other than the declared sources / resources, and that I have explicitly marked all material which has been quoted either literally or by content from the used sources.

…… ……..
date (signature)

1. Introduction/Motivation

The rich physics of complex impurities immersed in various materials is dominated by quantum effects. Solving the full interacting many-body problem including electron-electron interactions is impossible even in the Born-Oppenheimer approximation [1], which leads to a purely electronic problem on a background lattice potential. Physical details like electron-phonon interaction or the random component of disorder complicate the problem even more. A starting point to gain insight into the underlying mechanisms is provided by quantum impurity models. These models typically try to focus on the essential, renormalized, degrees of freedom, resorting to caricatures of the physical interactions. However, the inherent many body problem of these very simplistic models has proven to reveal its fascinating aspects only reluctantly over time. In general, models for the quantum mechanical description of condensed matter systems are unsolvable again. Powerful methods have been created during the last century to solve those models in the one approximate way or the other limit. One of the prime models for a quantum impurity problem is the single impurity Anderson model [2]. It consists of a single magnetic impurity (like an electron in a narrow f-orbital) in an otherwise perfect metal (s-electrons). This may be for example the case for iron atoms immersed in gold. Amazing physical phenomena like the resistance minimum in doped metals as well as an unexpected behavior of the entropy and specific heat have been qualitatively explained for the first time by Kondo in 1964 [3]. He showed that below a certain crossover temperature T_K, named after him, the Kondo temperature, the physics drastically changes. Increased scattering is observed which leads to an unexpected increase in resistivity [4]. The key mechanism here is a third order effect, namely spin-flip scattering. In a physical picture the local magnetic moments [5] of the impurities get screened below a temperature T_K by the conduction electrons. This leads to a singlet formation, losing all the magnetism, which is observed in specific heat measurements. Kondo's perturbative calculation still suffered from a low energy logarithmic divergence. His calculation was further refined by various authors in self consistent perturbative approaches as well as renormalization group based approaches, amongst others. Ten years later Wilson introduced a renormalization group method to obtain accurately the low energy properties of this problem [6]. One of the main reasons why the Kondo problem is so difficult to solve is that the interactions get non-perturbatively strong at low energies, a phenomenon termed asymptotic freedom in high energy physics. In 1981 an analytic Bethe Ansatz calculation became available for static thermodynamic quantities [7]. Today a variety of different methods are available for treating the single impurity Anderson model in an approximate way. It took about fifty years from the first experimental observations around 1930 to a sound theoretical understanding of the physics of magnetic impurities in metals. Even today some issues still remain unsolved, like for example the size and structure of the screening cloud [8]. The extension to many-impurity models (like the periodic Anderson model), and the interplay between impurities bares an even more elusive problem. This becomes important in the branch of heavy fermion physics, Kondo insulators, spin liquids or when studying the competition with RKKY interaction in a Doniach phase diagram [9].

A renewed interest in methods to solve such models originated in the 1990's for the description of quantum dots and other mesoscopic devices [10]. In these artificial elements quantum effects, resembling closely those of magnetic impurities in metals, become important. A great advantage over bulk systems lies in the tunability of all system parameters, which enables a better comparison to theoretical models. A wide range of technological applications like nano or molecular electronics depend on the understanding of effects like the giant magneto resistance, coulomb blockade or quantized conduction. These models are also important in the field of quantum information processing [11]. The advent of dynamical mean field theory [12, 13, 14, 15] fueled the interest in computational methods to obtain dynamic quantities of the single impurity Anderson model, which acts as an auxiliary problem in that powerful method.

The aim of this thesis is three-fold: The first step is to extend and apply cluster perturbation theory and the variational cluster approach to the single impurity Anderson model. The goal is to obtain dynamic correlation functions and static expectation values. The model is studied in great detail by means of these methods to establish a solid base upon which further applications and models of this class may be constructed. Parts of the results presented in this chapter have recently been published by the author in collaboration with Wolfgang von der Linden, Enrico Arrigoni and Markus Aichhorn in ref. [16]. All calculations done in this theses are for zero temperature, although the methods may be extended to the finite temperature case.

Once the methods are shown to yield good results for a single impurity in an equilibrium situation, the

methods are extended to the non-equilibrium case and the transport properties through a strongly correlated quantum dot are studied. The non-equilibrium properties of mesoscopic devices, exhibiting strong correlation phenomena are still not understood in detail today, but crucial for future technology [17].
As a third part, magnetic vacancies in Graphene are studied as an application to disordered quantum impurity problems. This part is motivated by recent studies [18], which showed that vacancies induced into the Graphene lattice behave like magnetic defects. Here the applicability of the method to strongly disordered problems will be outlined.
This work is structured as follows: The methods to tackle quantum impurity problems, used in this thesis, cluster perturbation theory and the variational cluster approach, will be discussed in detail in ch. 2. The rest of the thesis, which contains the results of the work which I carried out within my Master thesis work, is structured into three main parts. The first one presenting results for the single impurity Anderson model in equilibrium (see ch. 3). These results have been already published in ref. [16] by the author in collaboration with Wolfgang von der Linden, Enrico Arrigoni and Markus Aichhorn. The second, on providing data obtained for a strongly correlated quantum dot out of equilibrium (see ch. 4). Finally the third part presents results obtained for the disordered problem of magnetic vacancies in Graphene (see ch. 5).

2. Numerical Methods

In general the interacting quantum many-body problem is unsolvable (except for some limiting cases), although the governing equations are known exactly. Conducting severe simplifications and devising a suitable model/effective Hamiltonian or action for a given many-body system usually leads to an unsolvable problem again. To gain insights into these models one has to resort to sophisticated, often very computationally demanding, numerical methods. These methods may involve brute force calculations, further approximations and/or finite size scaling. Today a large variety of numerical methods exist to find (approximate) solutions of interacting quantum many-body models. Amongst the most famous are

- mean field approaches (MF),
- (diagrammatic) perturbation theory (PT),
- exact diagonalization (ED),
- Quantum Monte Carlo (QMC) methods, which is a very diverse field of its own,
- Numerical- and Functional-Renormalization Group (NRG/FRG),
- methods based on variational wavefunctions,
- the density matrix renormalization group (DMRG) or more generally matrix product state (MPS) methods,
- dynamical mean field theory (DMFT) and
- many-body cluster methods.

Today's most accurate method to treat the single impurity problem may be the NRG [6] which was specifically designed for this model. The extension to the case of several impurities proofs troublesome for this approach. Continuous time QMC [19] is a statistically exact method yielding spectra in imaginary frequency, which need to be continued to the real energy axis in an ill-defined inversion process, using for example the maximum-entropy method [20, 21]. This work is mainly concerned with cluster perturbation theory (CPT) [22, 23] and the variational cluster approach (VCA) [24] which are many-body cluster methods. An advantage of these methods is the flexible extensibility from a single- to the many- impurity problem. It is adaptable to any geometries and dimensions. In addition dynamic quantities, such as the Green's function, may be obtained as a function of a complex variable z , which may especially be taken to be the real energy axis ω. Two well known methods which belong to the same family but are not further explored in this work are cluster/cellular dynamical mean field theory (CDMFT) and its momentum space analogon the dynamical cluster approximation (DCA).
This chapter is organized as follows: First cluster perturbation theory is introduced and a review on the method of Green's function in context with CPT is presented in sec. 2.1. Then the variational extension of CPT, the variational cluster approach is introduced in sec. 2.3. An extension of VCA for infinite reference systems is presented in sec. 2.3.2. An alternative formulation of VCA previously introduced in the context of non-equilibrium systems is described in sec. 2.3.4. A short review of exact diagonalization algorithms is given in sec. 2.2 as in this work we use it as the backbone for CPT/VCA. VCA furthermore relies on methods for finding stationary points in many dimensions or in an alternative formulation roots of multivariate functions, both will be reviewed shortly in sec. 2.3.3 and sec. 2.3.5. The recently introduced non-equilibrium VCA [25] is reviewed in sec. 2.4.2. This method is based on the Keldysh Green's function technique, which is introduced in sec. 2.4.1.

2.1. Cluster Perturbation Theory

In this section the main concepts of CPT will be reviewed. This section serves also the purpose of setting the notation for this document. It is widely based on the excellent review article by Sénéchal [26]. In the following we consider a general model Hamiltonian on any given (large/infinite) lattice. The idea of CPT [22, 23] is to use the results of a small system and extrapolate them to the thermodynamic limit as

discussed in the following. The rigorous derivation of CPT which is possible within functional integral formalism (see for example ref. [27]) and may be found for example in ref. [28] will not be given here. Instead the focus lies on the technical implementation. As a compromise a heuristic argument for the CPT equation is given. A good overview of the topic is also presented in ref. [29].
CPT yields the single-particle Green's function $\mathrm{G}_{ij}^{\sigma\sigma'}(z)$, which is a matrix in site/spin space and in general a function of a complex variable z. This argument z may be chosen to be $z = i\omega + i0^+$ (where ω is a real energy) to yield the retarded Green's function, $z = i\omega - i0^+$ to yield the advanced Green's function or $z = i\omega$ to yield the Green's function on the Matsubara axis [30, 31]. Here $i0^+$ is short for

$$f(i0^+) \equiv \lim_{\eta \to 0^+} f(\eta) \,,$$

where the limit has to be taken at the end of all operations (i.e. integrals, ...). The single-particle Green's function is one of the most important quantities in theoretical condensed matter physics since it allows the calculation of the single-particle spectral function

$$A(\mathbf{k}, \omega) = -\frac{1}{\pi} \Im\mathrm{m}\mathrm{G}(\mathbf{k}, \omega + i0^+) \,. \tag{2.1}$$

This quantity may be measured in experiments by photo emission spectroscopy (PES), inverse photo emission spectroscopy (IPES) or angle resolved photo emission spectroscopy (ARPES), depending if one is interested in the momentum dependence or not.
Using exact methods, like exact diagonalization, it is possible to find the exact ground-state and the single-particle Green's function for small lattices. Exact diagonalization is limited to system sizes of a few (up to ≈ 20) sites/orbitals which is clearly far from the large/infinite systems we are interested in here. For CPT the lattice under consideration is first broken apart into smaller, exactly solvable tiles. The cluster Green's function G' is obtained for the tiles by an exact method (for example exact diagonalization). In the end the cluster Green's functions are sewed back together to yield the total Green's function G. Next the process of breaking apart a lattice will be outlined. How a Green's function may be obtained for a cluster is discussed in sec. 2.2. Because this constitutes a major part of CPT and is a powerful technique of its own, it is presented in its own section in detail, not to interrupt the introduction to CPT. The process of constructing the total Green's function within the CPT approximation is discussed in sec. 2.1.2.

2.1.1. Cluster tiling

Consider a large lattice γ of L^γ sites and its tiling into clusters C of L^C sites each. This creates a superlattice Γ of L^Γ sites. The original lattice γ is recovered upon attaching one cluster C at each site of the superlattice Γ. The coordinates of the lattice may be expressed as

$$\mathbf{r}_i^\gamma = \mathbf{r}_I^\Gamma + \mathbf{r}_\alpha^C \,, \qquad i \to (I, \alpha) \,.$$

The L^γ reciprocal space vectors $\mathbf{k}^\gamma$ in the first Brillouin zone (BZ) of the original lattice BZ^γ may be expressed as

$$\mathbf{k}^\gamma = \mathbf{K} + \mathbf{k}^\Gamma \,,$$

where $\mathbf{K}$ belongs to both the reciprocal superlattice Γ^{-1} and to BZ^γ while $\mathbf{k}^\Gamma$ belongs to the Brillouin zone of the superlattice BZ^Γ. The process of constructing a cluster tiling is illustrated for simple cubic lattices in one-, two- and three- dimensions in fig. 2.1. How the exact solution for one cluster may be obtained by exact diagonalization is described in sec. 2.2. Next we assume to have the ground-state properties and the single-particle Greens's function G' of the cluster obtained by some means and proceed by constructing the Green's function of the total system G.

2.1.2. Obtaining the total Green's function

CPT is a cluster extension of strong coupling perturbation theory [32, 33], valid to first order in the inter-cluster hopping. It can be shown that the first order result for the lattice Green's function G is

$$\mathrm{G}^{-1}(z, \mathbf{k}) = \mathrm{G}'(z) - \mathrm{T}(\mathbf{k}) \,, \tag{2.2}$$

where G' is the cluster Green's function and T contains only the single-particle inter-cluster terms. This means usually the hoppings, which connect the clusters. This equation may be motivated heuristically

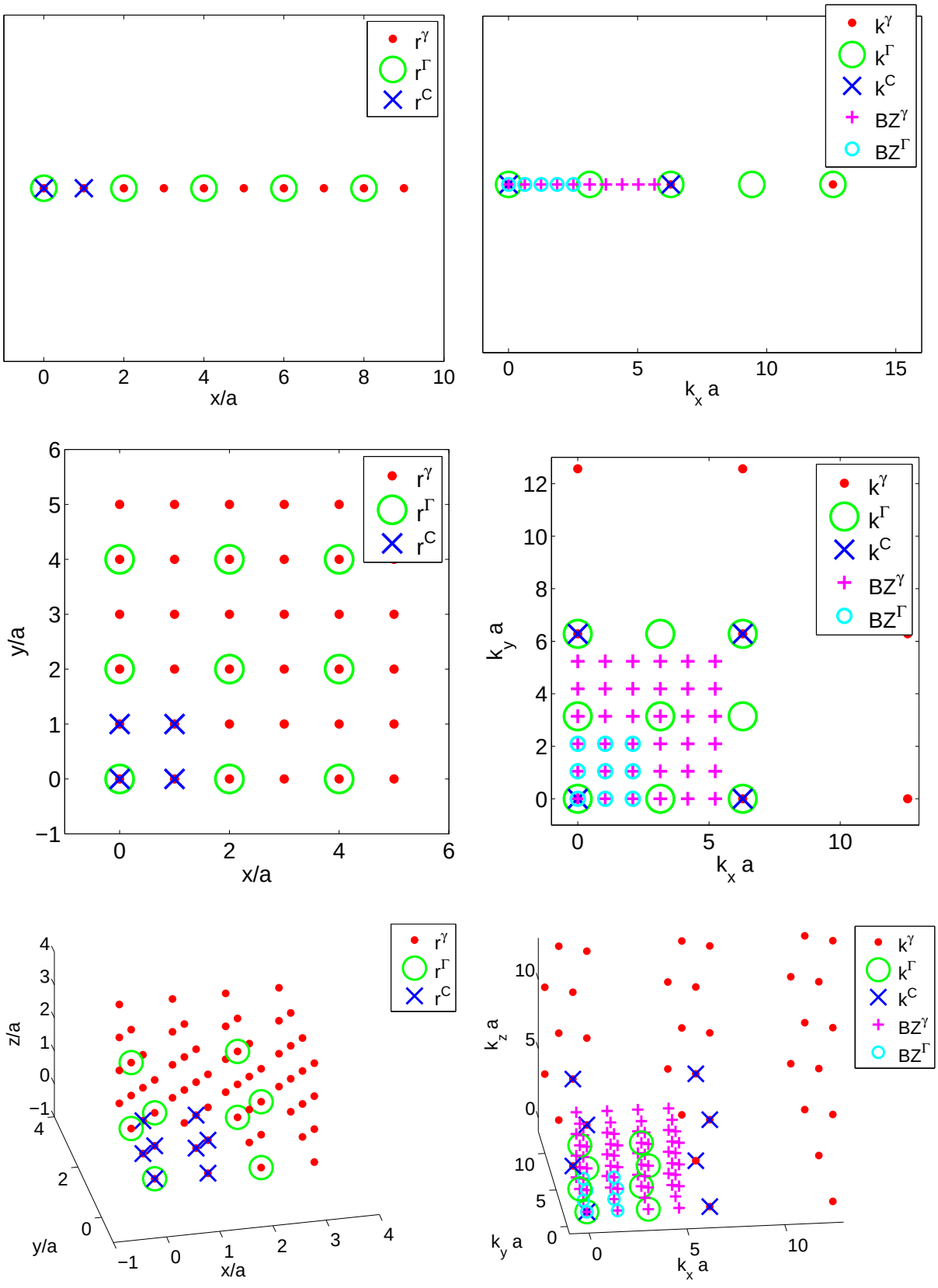

Figure 2.1.: Visualization of cluster tilings for simple cubic lattices in one- (top row), two- (middle row) and three-(bottom row) dimensions. The plot axis are scaled with the lattice parameter a. The one-dimensional lattice is a $N^\gamma = 10$ site lattice with $N^c = 2$ site clusters. In the two-dimensional case a $N^\gamma = 6 \times 6$ site lattice with $N^c = 2 \times 2$ site clusters is shown. For the three-dimensional case a $N^\gamma = 4 \times 4 \times 4$ site lattice with $N^c = 2 \times 2 \times 2$ site clusters was chosen. The left column shows the real space lattice r^γ, super-lattice r^Γ and cluster r^C. The right column shows the respective k-space picture where $\mathbf{k}^\gamma = \mathbf{K} + \mathbf{k}^\Gamma$.

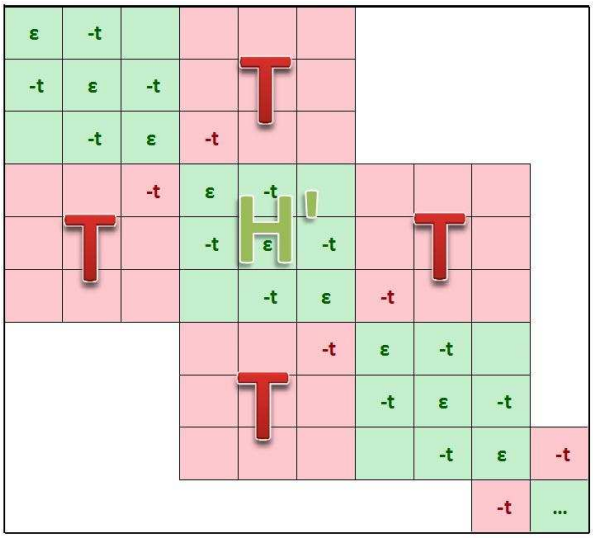

Figure 2.2.: Cluster tiling of a one-dimensional tight-binding model with on-site energy ϵ and nearest-neighbor hopping t. The chain is split into three-site clusters $\hat{\mathcal{H}}'$ (green). The matrix elements of T, which are the inter-cluster hoppings are indicated in red.

by considering Dyson's equation for the total system, as well as for the cluster

$$\begin{aligned} \mathrm{G}^{-1} &= \mathrm{G}_0^{-1} - \Sigma \\ \mathrm{G}'^{-1} &= \mathrm{G}_0'^{-1} - \Sigma' \,, \end{aligned}$$

where the subscript $_0$ denotes free Green's functions and Σ/Σ' the self-energy of the total system/cluster. Approximating the self-energy of the total system by the self-energy of the cluster $\Sigma = \Sigma'$ it follows that

$$\begin{aligned} \mathrm{G}^{-1} &= \mathrm{G}_0^{-1} - \Sigma' \\ &= \mathrm{G}_0^{-1} - \left(\mathrm{G}_0'^{-1} - \mathrm{G}'^{-1}\right) \\ &= \mathrm{G}'^{-1} - \left(\mathrm{G}_0'^{-1} - \mathrm{G}_0^{-1}\right) \\ &= \mathrm{G}'^{-1} - \left((z - H') - (z - H)\right) \\ &= \mathrm{G}'^{-1} - (H - H') \\ &= \mathrm{G}'^{-1} - \mathrm{T} \,, \end{aligned}$$

where H/H' are the one-particle terms of the total Hamiltonian $\hat{\mathcal{H}}$ / cluster Hamiltonian $\hat{\mathcal{H}}'$. One sees that all that is left in T are those single-particle terms of the Hamiltonian not present in the cluster Hamiltonian $\hat{\mathcal{H}}'$, which are the inter-cluster hoppings. This is illustrated in fig. 2.2 for a one-dimensional tight-binding system with on-site energy ϵ and nearest-neighbor hopping t. The chain is split into three-site clusters which have to be solved individually. The matrix elements of T, which are the inter-cluster hoppings are indicated in red. The process of performing a CPT calculation is visualized in a flow diagram in fig. 2.5. Next some important, exact relations for CPT will be discussed.

2.1.3. Exact relations for CPT

CPT becomes exact in three limiting cases:

- CPT yields the exact solution for interaction-strength $U \to 0$. This means that for non-interacting systems, where the self-energy Σ vanishes, CPT is exact.
- It is exact in the limit hopping $t \to 0$, where one recovers the atomic problem.
- CPT converges to the exact total Green's function when the cluster size L^C approaches the system size L^γ: $L^C \to L^\gamma$. Usually one considers systems of infinite size, then CPT is exact in the limit $L^C \to \infty$.

Better approximations within CPT are usually not constructed by considering higher orders in perturbation theory but by increasing the cluster size L^C.

In the next section an outline of how to handle Green's functions within CPT and derive important quantities like the ground-state energy, the momentum distribution and the density of states is presented. The case of a Green's function consisting of a set of isolated poles as it is the case for translationally invariant interacting model Hamiltonians is considered in sec. 2.1.4. This will be needed for the study of defects in Graphene. Then an overview of the analogous procedure for the case of a not translationally invariant system coupled to a continuous bath is given in sec. 2.1.5, which requires a radically different treatment. This will later be applied to the study of the single impurity Anderson model.

2.1.4. CPT Green's functions for discrete spectra of translationally invariant models

In this section the calculation of CPT Green's functions for discrete spectra is outlined. For the basics of the Q-matrix formalism the reader is referred to sec. 2.2.2. The CPT Green's function is determined by the Green's function of the cluster G' and the inter-cluster hopping matrix T by eq. (2.2). Inserting eq. (2.14) into eq. (2.2) one obtains in Q-matrix notation

$$\begin{aligned}
\mathrm{G}(\omega,\mathbf{k}) &= \left(\mathbb{1} - \mathrm{G}'(\omega)\mathrm{T}(\mathbf{k})\right)^{-1} \mathrm{G}' \\
&= \left(\mathbb{1} - \mathrm{Q}'g'(\omega)\mathrm{Q}'^{\dagger}\mathrm{T}(\mathbf{k})\right)^{-1} \mathrm{Q}'g(\omega)\mathrm{Q}'^{\dagger} \\
&= \left(\mathbb{1} + \mathrm{Q}'g'(\omega)\mathrm{Q}'^{\dagger}\mathrm{T}(\mathbf{k}) + \ldots\right) \mathrm{Q}'g'(\omega)\mathrm{Q}'^{\dagger} \\
&= \left(\mathrm{Q}'g'(\omega) + \mathrm{Q}'g'(\omega)\mathrm{Q}'^{\dagger}\mathrm{T}(\mathbf{k})\mathrm{Q}'g'(\omega) + \ldots\right) \mathrm{Q}'^{\dagger} \\
&= \mathrm{Q}'g'(\omega)\left(\mathbb{1} + \mathrm{Q}'^{\dagger}\mathrm{T}(\mathbf{k})\mathrm{Q}'g'(\omega) + \ldots\right) \mathrm{Q}'^{\dagger} \\
&= \mathrm{Q}'g'(\omega)\left(\mathbb{1} - \mathrm{Q}'^{\dagger}\mathrm{T}(\mathbf{k})\mathrm{Q}'g'(\omega)\right)^{-1} \mathrm{Q}'^{\dagger} \\
&= \mathrm{Q}'\frac{1}{g'(\omega)^{-1} - \mathrm{Q}'^{\dagger}\mathrm{T}(\mathbf{k})\mathrm{Q}'}\mathrm{Q}'^{\dagger} .
\end{aligned}$$

In the second line the fraction has been Taylor expanded and in the fifth line the terms have been recollected. The resulting expression is exact. Introducing a diagonal matrix for the excitation energies λ' of the cluster

$$\Lambda'_{\gamma\gamma'} := \lambda'_{\gamma}\delta_{\gamma\gamma'} , \tag{2.3}$$

one can further rewrite the expression for the Green's function

$$\mathrm{G}(\omega,\mathbf{k}) = \mathrm{Q}'\frac{1}{\omega - \left(\Lambda' + \mathrm{Q}'^{\dagger}\mathrm{T}(\mathbf{k})\mathrm{Q}'\right)}\mathrm{Q}'^{\dagger} .$$

Note that the energy ω-dependence is nicely separated from the wavevector $\mathbf{k}$-dependence in this expression. The dependence on $\mathbf{k}$ only appears in $\mathrm{T}(\mathbf{k})$.
To put this into an even more handy form we introduce the matrix

$$\mathrm{M}_{\mathbf{k}} := \Lambda' + \mathrm{Q}'^{\dagger}\mathrm{T}(\mathbf{k})\mathrm{Q}' ,$$

so that the CPT Green's function is then given by

$$\mathrm{G}(\omega,\mathbf{k}) = \mathrm{Q}'\frac{1}{\omega - \mathrm{M}(\mathbf{k})}\mathrm{Q}'^{\dagger} . \tag{2.4}$$

Upon solving the (ω-independent) eigenvalue problem

$$\mathrm{M}_{\mathbf{k}} X_{\mathbf{k}} = X_{\mathbf{k}} \Lambda_{\mathbf{k}}, \tag{2.5}$$

it is possible to rewrite the fraction appearing in eq. (2.4) as

$$\frac{1}{\omega - \mathrm{M}_{\mathbf{k}}} = X_{\mathbf{k}} \left(\omega - \Lambda_{\mathbf{k}}\right)^{-1} X_{\mathbf{k}}^{-1} .$$

The $\Lambda_{\mathbf{k}}$ are diagonal matrices holding the excitation energies of the full system on the diagonal. They are the $\mathbf{k}$-dependent equivalent to the Λ' defined in eq. (2.3) for the cluster solution. Inserting this result

into eq. (2.4) one obtains the $\mathbf{k}$-dependent weights $\mathrm{Q}_{\mathbf{k}}$ for the CPT Green's function

$$\mathrm{G}(\omega,\mathbf{k}) = \underbrace{\mathrm{Q}' X_{\mathbf{k}}}_{\mathrm{Q}_{\mathbf{k}}} \left(\omega - \Lambda_{\mathbf{k}}\right)^{-1} \underbrace{X_{\mathbf{k}}^{-1}\mathrm{Q}'^{\dagger}}_{\mathrm{Q}_{\mathbf{k}}^{\dagger}} , \tag{2.6}$$

$$[L \times L] = [L \times N_\gamma][N_\gamma \times N_\gamma][N_\gamma \times L] .$$

The last line indicates the matrix dimensions of the quantities above. Here N_γ is the number of excitations in Q and L the cluster size. A slight complication arises here because the cluster tiling breaks the translational symmetry of the model.

Green's function periodization

The factorization of the total lattice into clusters breaks the translational symmetry of the lattice. Therefore the total Green's function G depends on two wave vectors $\mathbf{k}$ and $\mathbf{k}'$, which is certainly not correct for a periodic lattice. This may be circumvented by a periodization prescription that provides a total Green's function $\mathrm{G}(\omega,\mathbf{k})$, depending only on the indices of the physical unit cell and one wave vector $\mathbf{k}$. As outlined for example in ref. [26] one may impose a periodization upon the self-energy Σ or the Green's function G. Here the Green's-function periodization is pursued due to good results obtained by that method. The periodization prescription proposed for systems with a single orbital unit cell in ref. [34] reads:

$$\begin{aligned}\mathrm{G}(\omega,\mathbf{k}) &= \frac{1}{L}\sum_{\mathbf{r}^C,\mathbf{r}^{C'}}^{L} e^{-i\mathbf{k}\cdot\left(\mathbf{r}^C-\mathbf{r}^{C'}\right)}\,\mathrm{G}_{\mathbf{r}^C\mathbf{r}^{C'}}(\omega,\mathbf{k}) \\ &= \frac{1}{L}\sum_{i,j}^{L} e^{-i\mathbf{k}\cdot(\mathbf{c}_i-\mathbf{c}_j)}\,\mathrm{G}_{ij}(\omega,\mathbf{k}) .\end{aligned}$$

The $\mathbf{c}_i$ are the cluster basis vectors. This expression may be generalized for physical unit cells consisting of more than one atom:

$$\mathrm{G}_{\alpha\beta}(\omega,\mathbf{k}) = \frac{L_{\text{phys.}}}{L}\sum_{i\in\alpha}\sum_{j\in\beta} e^{-i\mathbf{k}\cdot(\mathbf{c}_i-\mathbf{c}_j)}\,\mathrm{G}_{ij}(\omega,\mathbf{k}) ,$$

where α,β denote the translationally inequivalent lattice sites of the model under consideration and $L_{\text{phys.}}$ the size of the physical unit cell. Consider for example the case of a six-site ring cluster in Graphene which has a two-site physical unit cell:

$$\mathrm{G}_{\alpha\beta}(\mathbf{k},\omega) = \frac{2}{6}\sum_{i\in\{1,3,5\}}\sum_{j\in\{2,4,6\}} e^{-i\mathbf{k}\cdot\left(\mathbf{c}_i^{C_6}-\mathbf{c}_j^{C_6}\right)}\,\mathrm{G}_{ij}(\omega,\mathbf{k}) .$$

There is an elegant way to impose this periodization prescription upon the total Greens' function eq. (2.6). Introducing the matrix $\mathcal{F}_k^{\dagger}$ of dimension $[L_{\text{phys.}} \times L]$

$$\mathcal{F}_k^{\dagger} = \sqrt{\frac{L_{\text{phys.}}}{L}}\begin{pmatrix} e^{-i\,\mathbf{k}\cdot\mathbf{u}_i} & e^{-i\,\mathbf{k}\cdot\mathbf{u}_j} & \dots \\ e^{-i\,\mathbf{k}\cdot\mathbf{u}_i} & e^{-i\,\mathbf{k}\cdot\mathbf{u}_j} & \dots \\ \dots & \dots & \dots \end{pmatrix} . \times\, \zeta_{\alpha,i} , \tag{2.7}$$

where .× denotes an element wise product and the matrix $\zeta_{\alpha,i}$ is one for cluster sites i which are translationally equivalent to the site α of the physical unit cell (i.e. belongs to the same Bravais-sub-lattice), and zero otherwise:

$$\zeta_{\alpha,i} = \begin{cases} 1 \text{ if cluster site } i \text{ is translationally equivalent to site } \alpha \text{ of physical unit cell} \\ 0 \text{ otherwise} \end{cases} .$$

The periodized Green's function G_{per} is obtained by applying the transformation eq. (2.7) to eq. (2.6)

$$\mathrm{G}_{\text{per}}(\omega,\mathbf{k}) = \underbrace{\mathcal{F}_k^{\dagger}\mathrm{Q}_{\mathbf{k}}}_{\mathrm{Q}_{\text{per},\mathbf{k}}} \left(\omega - \Lambda_{\mathbf{k}}\right)^{-1} \underbrace{\mathrm{Q}_{\mathbf{k}}^{\dagger}\mathcal{F}_k}_{\mathrm{Q}_{\text{per},\mathbf{k}}^{\dagger}} \tag{2.8}$$

$$[L_{\text{phys.}} \times L_{\text{phys.}}] = [L_{\text{phys.}} \times N_\gamma][N_\gamma \times N_\gamma][N_\gamma \times L_{\text{phys.}}] .$$

It follows that the periodized weights $\mathrm{Q}^{\dagger}_{\mathrm{per},\mathbf{k}}$ are given by

$$\begin{aligned}\mathrm{Q}_{\mathrm{per},\mathbf{k}} &= \mathcal{F}_k^{\dagger}\mathrm{Q}' X_{\mathbf{k}} \\ \mathrm{Q}^{\dagger}_{\mathrm{per},\mathbf{k}} &= X_{\mathbf{k}}^{-1}\mathrm{Q}'^{\dagger}\mathcal{F}_k \,.\end{aligned}$$

Eq. (2.8) concludes the derivation of the expression for the single-particle Green's function. Next we derive some useful quantities from this function. Note that within CPT only the single-particle Green's function is available. Because CPT builds upon an interacting ground-state, Wick's theorem [35] does not hold. This prevents the calculation of higher correlation functions by standard means.

Quantities derived from the Green's function

The (retarded) Green's function enables the calculation of the single-particle spectral function $A(\omega,\mathbf{k})$ eq. (2.1). In this section all quantities are matrices in the space of orbitals of the unit cell i and spin σ (and of energy ω and wavevector $\mathbf{k}$). For spin symmetric Hamiltonians one usually obtains the Green's function G for one spin direction only, so all calculated quantities have to be multiplied by a factor of two. The single-particle spectral function $A(\omega,\mathbf{k})$ provides information about the density of states $\rho(\omega)$

$$\rho(\omega) = \int_{1.\mathrm{BZ.}} d\mathbf{k}\, A(\omega,\mathbf{k}) = \frac{1}{N}\sum_{\mathbf{k}} A(\omega,\mathbf{k}) \,,$$

where N is the number of $\mathbf{k}$-points in the first BZ. The momentum distribution $n(\mathbf{k})$ is given by

$$n(\mathbf{k}) = \int_{-\infty}^{\epsilon_F} d\omega\, A(\omega,\mathbf{k}) \,.$$

A quantity of particular interest is the average occupancy $< n >_{ij}$ (matrix in space of physical unit cell)

$$\begin{aligned}< n >_{ij} &= \int_{1.\mathrm{BZ.}} d\mathbf{k}\, n(\mathbf{k}) = \frac{1}{N}\sum_{\mathbf{k}} n(\mathbf{k}) \\ &= \frac{1}{N}\sum_{\mathbf{k}}\int_{-\infty}^{\epsilon_F} d\omega\, A(\omega,\mathbf{k}) \\ &= \frac{1}{N}\sum_{\mathbf{k}}\int_{-\infty}^{0} d\omega\, \delta(\omega-\omega_\gamma) W_\gamma \\ &= \frac{1}{N}\sum_{\mathbf{k}}\sum_{\lambda:\omega_\lambda<0} \mathrm{Q}_{\mathrm{per},\mathbf{k}}\,\mathrm{Q}^{\dagger}_{\mathrm{per},\mathbf{k}} \,.\end{aligned}$$

Here W_γ denotes the weight of excitation γ. The average occupancy per site is given by $< n >$

$$< n > = \frac{1}{N}\sum_{\mathbf{k}}\sum_{\lambda_k<0}\frac{1}{L_{\mathrm{phys.}}}\mathrm{tr}\left(\mathrm{Q}_{\mathrm{per},\mathbf{k}}\,\mathrm{Q}^{\dagger}_{\mathrm{per},\mathbf{k}}\right) \,.$$

Note that the spin index is absorbed into the index of the site in this notation. The ground-state energy per site is given by

$$\begin{aligned}\omega_o &= \int_{-\infty}^{\epsilon_F} d\omega\, \omega\, \rho(\omega) \\ &= \frac{1}{N}\sum_{\mathbf{k}}\sum_{\lambda_k<0}\frac{1}{L_{\mathrm{phys.}}}\mathrm{tr}\left(\mathrm{Q}_{\mathrm{per},\mathbf{k}}\,\Lambda_{\mathbf{k}}\,\mathrm{Q}^{\dagger}_{\mathrm{per},\mathbf{k}}\right) \,.\end{aligned}$$

The single-particle gap Δ_{sp} is simply given by the sum of the magnitude of the lowest positive and highest negative eigenvalue of M eq. (2.5)

$$\Delta_{sp} = \min_{\lambda_\gamma>0}\lambda_\gamma + \max_{\lambda_\gamma<0}\lambda_\gamma \,.$$

Next the case of clusters with mixed discrete/continuous spectra is discussed.

2.1.5. CPT Green's functions for mixed discrete/continuous spectra of models without translational symmetry

Up to now we have dealt with translationally invariant models. These were broken apart into tiles - which were all equal. One such representative tile could be solved exactly for the single-particle Green's function G' which was made up of a set of discrete poles. Dealing with non-translationally invariant models, or models where the translational period is too large to be represented by one, exactly-solvable, cluster, one can imagine breaking such models into different tiles. Consider for example the case of the single impurity Anderson model outlined in sec. 3.1. Such tiles may involve clusters (for example infinite non-interacting baths) which yield continuous spectra/branch cuts of the Green's function on the real axis ω. These can not be represented conveniently by a finite number of poles, which makes the Q-matrix formalism not a good choice. Some interacting parts of the system however may be most conveniently expressed in this formalism. In the end we are left with clusters which are only partly representable in the form of Q-matrices. The way to proceed here is to evaluate G'_Q, the part of the Green's function which was represented in Q-matrix form, and G'_C, the part which was represented by other means, separately. From there on one has to work with those functions evaluated at discrete points z_i. One therefore loses the favorable representation of all quantities which follows from the single-particle Green's function, in terms of eigenvalue problems, and has to resort to numerical integration of $G'(z_i)$.
Explicitly the (numerically stable) calculation of single-particle expectation values from the Green's function $G(z_i)$ will be outlined in the following. Note that here G stands for any Green's function, not just the one of the total system. This discussion is of course also applicable to systems discussed in the last section, but it is absolutely necessary here. A zero temperature expectation value of a single-particle operator in terms of the fermionic Green's function is given by

$$\begin{aligned} < c_i c_j^\dagger > &= \frac{1}{\beta} \sum_{\omega_n} \mathrm{G}_{ij}(\omega_n) e^{i\omega_n 0^+} \\ &= -\int_C \frac{dz}{2\pi i} \mathrm{G}_{ij}(z)\, e^{z0^+} \\ &= -\int_{C_A} \frac{dz}{2\pi i} \mathrm{G}_{ij}(z) - \frac{\mathrm{Q}^\dagger \mathrm{Q}}{z-\rho} \\ &= \frac{\delta_{ij}}{2} + \frac{1}{\pi} \int_0^\infty d\omega\, \mathfrak{Re}\mathrm{G}_{ij}(i\omega)\,. \end{aligned}$$

Here β denotes the inverse temperature. The integration of the Green's function along the real axis is very troublesome due to the numerically necessary convergence factor 0^+. To achieve a stable integration, the integral is deformed to the complex plane (for contour C_A see fig. D.2) and re-expressed as an integral over the Matsubara axis. The integral is regularized by the large constant δ (see app. D). The details of this calculation are analogous to those for the integral for the grand potential, outlined in detail in app. D. In the next section a review of exact diagonalization is given, which is used to obtain the ground-state properties of Green's functions of clusters, in this work.

2.2. Solving clusters - Exact Diagonalization

To gain insight into the physics governed by a particular Hamiltonian operator one may want to calculate various ground- and excited state properties. In order to evaluate any observables or correlation functions the stationary many body Schrödinger equation

$$\hat{\mathcal{H}} \left|\Psi\right\rangle_n = E_n \left|\Psi\right\rangle_n \ ,$$

has to be solved. This represents an algebraic eigenvalue problem of large dimension. The Hamiltonian $\hat{\mathcal{H}}$ has to be expressed in a suitable basis resulting in a hermitian / symmetric matrix in the complex / real case. There is a great variety of methods available to solve such problems numerically. Even greater as the variety of methods itself are the means by which one may categorize them. Maybe the most relevant criterion for our application is the separation of methods which are sometimes termed full solvers and methods which are often referred to as sparse solvers. A full solver is one which usually needs to store the full matrix representation of the Hamiltonian in memory and will yield the entire eigenvalue spectrum and all corresponding eigenvectors. Sparse solvers on the contrary may be used with a matrix stored in a sparse format (i.e. omitting the storage of zeros) and will in general yield one or some eigenvalues only. The very different nature of these two classes of eigensolvers makes them favorable for different applications. The big issue in quantum many-body problems is that the size of the Hilbert space grows

exponentially with system size [36]. Therefore the dimension of the Hamiltonian matrix and the state vectors $|\Psi\rangle$ may exceed a critical size exponentially fast. Consider for example the size of the Hilbert space M for the Hubbard model [37]

$$M = \sum_{N_\uparrow}^{L} \sum_{N_\downarrow}^{L} \frac{L!}{N_\uparrow!\,(L-N_\uparrow)!} \frac{L!}{N_\downarrow!\,(L-N_\downarrow)!} = 4^L \ ,$$

where L is the number of lattice sites and $N_\uparrow$ and$N_\downarrow$ are the number of electrons with spin up and down respectively. Depending on the hard- and software a double precision floating point number takes 64 bits (which makes it accurate to about 16 decimal digits). Taking into account that in general one has to deal with complex numbers it will take 16 byte to store one matrix element or one coefficient for a basis vector. So for a system consisting of $L = 4$ sites the amount of memory needed to store the full hamiltonian matrix will be roughly one megabyte, which is of course nothing on modern machines. Examining a model made up of six sites the same matrix will already take about 300 megabytes. To see the dilemma one is facing consider eight sites: In this case the matrix needs more or less 79 gigabytes of memory. Finally the matrix representation of a twenty site system would need the extraordinary number of $\approx 10^{16}$ gigabytes. As an amusing side remark it may be mentioned that a system of only seventy sites would need 10^{80} bits to be stored which is about the estimated number of atoms in the whole known universe. It should be noted at this point that in general it is possible to take into account symmetries of the Hamiltonian to reduce the size of the Hilbert space considerably making calculation of slightly enlarged systems feasible. The exponential growth of the size however cannot be circumvented. Another dramatic aspect is runtime. Full eigenvalue solvers in general scale like N^3, where N is the dimension of the problem. To conclude this short discussion about feasibility it is to be mentioned that solving the full eigenvalue problem is numerically exact and yields access to all physical quantities. The application of full eigenvalue solvers is however only possible for systems not exceeding matrix sizes of $N \approx 2000 \times 2000$ (which translates to eight sites for typical many body models) due to runtime reasons. The only way to expand in system size is to use sparse eigenvalue solvers. One of such methods, the Lanczos algorithm, is used extensively in this work to calculate the groundstate of system for up to sixteen sites. The Band Lanczos algorithm can be used to obtain information about excited states, like the single-particle Green function, in a very good approximation. In the sections to follow, a method for full diagonalization the QR methods is briefly mentioned in sec. 2.2.3 as it is used in this work to deal with small systems (system size $L < 7$). The main focus here will lie on sparse solver for hermitian matrices. The Lanczos algorithm will be discussed in some detail in sec. 2.2.1 as it is an essential part of this work. Sec. 2.2.2 reviews the Band Lanczos method which is used to obtain the single-particle Green function and degenerate groundstates vectors.

2.2.1. Groundstate properties - The Lanczos algorithm

The method commonly known as Lanczos algorithm [38] is an iterative projection method suitable to solve large hermitian eigenvalue problems. In this work the Lanczos algorithm is used to obtain the groundstate properties of clusters for CPT/VCA. Here a short overview of the method should be provided. This paragraph is loosely based on the good and practical overview of eigenvalue solvers by Bai *et al.* [39] and the short but very good review in ref. [29].
The Lanczos algorithm is applicable to the standard hermitian eigenvalue problem

$$H\,|v\rangle = E\,|v\rangle \ .$$

This method yields a few extremal eigenvalues and eigenvectors of H with high precision. The matrix H is the matrix-representation of the Hamiltonian $\hat{\mathcal{H}}$ in the Fock-basis $H = \langle n_1, n_2, ..., n_M|\,\hat{\mathcal{H}}\,|n'_1, n'_2, ..., n'_M\rangle$. This method may be considered a standard tool of many-body physics because it has comparatively low memory requirements. In the most primitive version only three state vectors $|v_i\rangle$ and the sparse Hamiltonian need to be stored in memory.
The algorithm starts out with a (random) initial vector $|v_0\rangle$ upon which the orthonormal basis V of the Krylov subspace K is constructed by sequential application of the matrix H. The Krylov subspace after n-iterations is given by

$$K^n(H, |v_0\rangle) = \mathrm{span}\left\{|v_0\rangle, H\,|v_0\rangle, H^2\,|v_0\rangle, H^3\,|v_0\rangle, \ldots, H^n\,|v_0\rangle\right\} \ .$$

An approximation for H is obtained after n iterations by projecting H onto the Krylov subspace

$$\widetilde{H} \approx V^T H V \ , \tag{2.9}$$

where V contains the n vectors $|v_i\rangle$ as columns. The matrix V is of dimensions $[M \times n]$ where M is the dimension of H. Therefore the approximation to H, $\widetilde{H}$ is a small matrix of dimensions $[n \times n] = [n \times M][M \times M][M \times n]$. Diagonalization of $\widetilde{H}$ yields

$$U^T \widetilde{H} U = D \,, \tag{2.10}$$

where the eigenvectors of $\widetilde{H}$ are the columns of U and the diagonal matrix D contains the corresponding eigenvalues of $\widetilde{H}$. Plugging eq. (2.10) back into eq. (2.9) one finds that D contains the approximative eigenvalues (Ritz values) of H

$$\underbrace{U^T V^T}_{X^T} H \underbrace{V U}_{X} \approx D \,,$$

from which one can also see that the columns of $X \approx V U$ are the approximate eigenvectors of H.
Next the individual steps of the algorithm will be discussed. The starting point is a random vector $|v_0\rangle$ of dimension M. The successive Krylov vectors are constructed by application of H and consecutive orthogonalization (and normalization):

$$\begin{aligned}
\widetilde{|v_{n+1}\rangle} &= H|v_n\rangle - \epsilon_n |v_n\rangle - \beta_n |v_{n-1}\rangle \\
\epsilon_n &= \langle v_n | H | v_n \rangle \\
\beta_n &= \sqrt{\widetilde{\langle v_n|}\widetilde{|v_n\rangle}} = \widetilde{\langle v_n|}\, v_n\rangle \\
|v_{n+1}\rangle &= \frac{\widetilde{|v_{n+1}\rangle}}{\sqrt{\widetilde{\langle v_{n+1}|}\widetilde{|v_{n+1}\rangle}}} \,,
\end{aligned} \tag{2.11}$$

Here tilded quantities $\widetilde{|v\rangle}$ denote non-orthonormal vectors, while $|v_n\rangle$ denote the orthonormal ones. The projection $\widetilde{H}$ of H onto the Krylov subspace may be read off from eq. (2.11)

$$\langle v_m | H | v_n \rangle = \underbrace{\langle v_m | \widetilde{v_{n+1}\rangle}}_{\beta_{n+1}\delta_{m,n+1}} + \epsilon_n \underbrace{\langle v_m | v_n \rangle}_{\delta_{m,n}} + \beta_n \underbrace{\langle v_m | v_{n-1}\rangle}_{\delta_{m,n-1}} \,,$$

which leads to a tridiagonal form of the Hamiltonian

$$\widetilde{H} = \begin{pmatrix}
\epsilon_0 & \beta_1 & 0 & 0 & \cdots \\
\beta_1 & \epsilon_1 & \beta_2 & 0 & \cdots \\
0 & \beta_2 & \epsilon_2 & \beta_3 & \cdots \\
0 & 0 & \beta_3 & \epsilon_3 & \cdots \\
\vdots & \vdots & \vdots & \vdots & \ddots
\end{pmatrix} ,$$

which has to be diagonalized by some other standard method. Convergence is reached when the change in the ground state energy between two successive iterations is smaller than a given limit

$$|\omega_0^n - \omega_0^{n-1}| \leq \mathrm{lim} \,.$$

Additionally the iteration has to stop when the Krylov subspace is exhausted for a given starting vector $|v_0\rangle$

$$\beta_n = \sqrt{\widetilde{\langle v_n|}\widetilde{|v_n\rangle}} \leq \mathrm{lim} \,.$$

Especially for small systems the results should be checked by running the algorithm twice with different starting vectors. A saver convergence-criterion is to monitor the ≈ 5 lowest lying energies individually to notice crossings after some iterations. This algorithm is used in this work to obtain the ground-state of $\hat{\mathcal{H}}$. Its extended version, the Band Lanczos algorithm, is introduced in the next section to deal with single-particle Green's functions.

2.2.2. Single-particle Green's functions - The Band Lanczos algorithm

The Band Lanczos algorithm is used in this work to compute the single-particle Green's functions. The description of the mechanics of the algorithm, given here, follows ref. [39] closely. The spectral (Lehmann) representation of the single particle Green's function for the zero temperature case in the energy domain

is given by

$$G_{ij}^{\sigma\sigma'}(z) = \sum_{\alpha}\left(\sum_{n}\frac{{}^{\alpha}\langle\Psi_0|\,c_i^{\sigma}\;|n\rangle^{\alpha}\;{}^{\alpha}\langle n|\,c_j^{\sigma'\dagger}\,|\Psi_0\rangle^{\alpha}}{z-(\omega_n^{\alpha}-\omega_0^{\alpha})}-\eta\sum_{m}\frac{{}^{\alpha}\langle\Psi_0|\,c_j^{\sigma'\dagger}\,|m\rangle^{\alpha}\;{}^{\alpha}\langle m|\,c_i^{\sigma}\;|\Psi_0\rangle^{\alpha}}{z+(\omega_m^{\alpha}-\omega_0^{\alpha})}\right). \tag{2.12}$$

The sum over α denotes a sum over a possibly d-fold degenerate set of groundstates. For groundstates of fixed particle number, the sums over n and m denote the subspaces with N_0+1 (particle part) and N_0-1 (hole part) particles respectively (all other matrix elements vanish identically). The index η is -1 for Fermions and $+1$ for Bosons.
This may be recast in a convenient matrix form the so-called Q-matrices [40]

$$G_{ij}^{\sigma\sigma'}(z) = \sum_{\alpha}\left(\sum_{\gamma}Q_{i\gamma}^{\sigma}\frac{1}{z-\lambda_\gamma}Q_{j\gamma}^{\sigma'\dagger}\right)_{\alpha} \tag{2.13}$$

$$Q_{i\gamma}^{\sigma\dagger} = \begin{cases}\frac{1}{\sqrt{d}} < \gamma|\hat{c}_i^{\sigma\dagger}|\Psi_0 > & \text{particle part}\\ \frac{1}{\sqrt{d}} < \Psi_0|\hat{c}_i^{\sigma\dagger}|\gamma > & \text{hole part}\end{cases}$$

$$\lambda_\gamma = \begin{cases}\omega_\gamma-\omega_0 & \text{particle part}\\ \omega_0-\omega_\gamma & \text{hole part}\end{cases}.$$

To ease the notation the degeneracy index α is suppressed on the individual quantities. Furthermore the sum over γ is over a set of orthonormal basis-states having one more particle than the groundstate (particle part) and one less particle than the groundstate (hole part). The excited state energies are denoted by ω_γ
Introducing the diagonal matrix

$$g_{\gamma\gamma'}(\omega) := \frac{\delta_{\gamma\gamma'}}{\omega-\lambda_\gamma},$$

the Green's function may be rewritten in matrix form

$$\begin{aligned}G(\omega) &= Q\,g(\omega)Q^{\dagger}\\ [L\times L] &= [L\times N_\gamma][N_\gamma\times N_\gamma][N_\gamma\times L]\,.\end{aligned} \tag{2.14}$$

Here N_γ is the size of the excited state space and L the size of the physical system. It should be noted that the dimension of the Green's function is of system size (in general of system-size times spin multiplicity). The matrices Q, containing the weights of the excitations, are of dimension $L\times N_\gamma$. The matrix g is the only dynamic quantity and is diagonal of size $N_\gamma\times N_\gamma$.
The Band Lanczos method uses a block of L starting vectors, which are, in our case, constructed from the application of the respective creation $c_i^{\sigma\dagger}$ and annihilation c_i^{σ} operators on the ground state $|\Psi_0\rangle$ of an L-site system

$$\begin{aligned}&\left\{|v_1\rangle = c_1^{\sigma\dagger}\,|\Psi_0\rangle, |v_2\rangle = c_2^{\sigma\dagger}\,|\Psi_0\rangle, \ldots, |v_L\rangle = c_L^{\sigma\dagger}\,|\Psi_0\rangle\right\},\\ &\left\{|v_1\rangle = c_1^{\sigma}\;|\Psi_0\rangle, |v_2\rangle = c_2^{\sigma}\;|\Psi_0\rangle, \ldots, |v_L\rangle = c_L^{\sigma}\;|\Psi_0\rangle\right\}.\end{aligned}$$

As the previous lines indicate this procedure has to be done for the N_0+1 particle sector and for the N_0-1 particle sector individually. If the model is spin symmetric it suffices to consider one spin direction σ - otherwise one has to take care of different spin directions too. In this work the groundstate $|\Psi_0\rangle$ is determined beforehand by the Lanczos algorithm. The Band Lanczos algorithm proceeds similarly to the original Lanczos algorithm by constructing the block Krylov subspace, this time starting from L vectors

$$K^n(H,|v\rangle_i) = \text{span}\left\{|v\rangle_1, |v\rangle_2, \ldots, |v\rangle_L; H\,|v\rangle_1, H\,|v\rangle_2, \ldots, H\,|v\rangle_L; \ldots; H^n\,|v\rangle_1, H^n\,|v\rangle_2, \ldots, H^n\,|v\rangle_L\right\}.$$

Again an orthonormal basis of n vectors is constructed to project H onto this subspace. While in the case of the Lanczos algorithm the first occurrence of a linearly dependent vector in the Krylov subspace indicates that the subspace is exhausted, for the Band Lanczos procedure this point is more subtle. Starting with a set of L vectors the first occurrence of a linearly dependent vector does not mean that the block Krylov subspace is exhausted. It simply indicates that the linearly dependent vector and all vectors constructed from consecutive application of H onto this vector do not contain any new information. Therefore this vector is removed from the sequence in a process termed deflation. The condition for linear

dependency is

$$\beta_n = \sqrt{\widetilde{\langle v_n | v_n \rangle}} \leq \mathrm{lim}\,.$$

After L deflations the algorithm has to be stopped because the block Krylov subspace is exhausted. After n iterations the algorithm has generated n orthonormal basis vectors and $L-D$ candidates for the next possible vectors. Here D denotes the number of deflations undergone in the first n iterations. The Band Lanczos algorithm will generate a banded matrix $\widetilde{H}$ whose eigenvalues are the approximate eigenvalues of H. Orthogonality only has to be explicitly enforced among $2(L-D)+1$ consecutive Lanczos vectors and once deflation has occurred, against D earlier vectors. Therefore the resulting matrix $\widetilde{H}$ is banded with bandwidth $2(L-D)+1$, where the bandwidth is reduced by 2 every time a deflation occurs. Additionally each deflation causes $\widetilde{H}$ to have nonzero elements p in a row/column outside of the banded part at row/column index $n-L+D(k)$ where n is the number of the iteration at which the deflation has occurred and $D(k)$ is the number of deflations already occurred at iteration n. As an example, consider the case of $L=4$ starting vectors and assume that during the first $n=10$ iterations, deflations have occurred at steps $n_1=7$ and $n_2=9$. These two deflations correspond to deleting the vectors $H^2|v\rangle_3$ and $H^3|v\rangle_1$ as well as all vectors which would be constructed from them by application of H. The structure of the generated matrix $\tilde{H}$ would then be

$$\tilde{H} = \begin{pmatrix}
x & x & x & x & x & & & & & \\
x & x & x & x & x & x & & & & \\
x & x & x & x & x & x & p & p & p & p \\
x & x & x & x & x & x & x & & & \\
x & x & x & x & x & x & x & x & & \\
 & x & x & x & x & x & x & x & p & p \\
 & & p^* & x & x & x & x & x & x & \\
 & & p^* & & x & x & x & x & x & x \\
 & & p^* & & & p^* & x & x & x & x \\
 & & p^* & & & p^* & & x & x & x
\end{pmatrix}.$$

Here x denotes potentially nonzero entries within the banded part and p denotes potentially nonzero entries due to deflations. Note that the two deflations have reduced the initial bandwidth $2L+1=9$ to $2(L-D)+1=5$.

To obtain the Q matrix representation eq. (2.13) of the Green's function we need both the excitation energies ω_γ for the position of the excitations and the excited state-vectors $|\gamma\rangle$ for the respective weights. The excitation energies are obtained as the eigenvalues of the matrix $\widetilde{H}$. The weights follow from the j^{th} iteration vector

$$|v_j\rangle = \frac{1}{N_j}\left(\widetilde{|v_j\rangle} - \sum_{i=1}^{j-1} |v_i\rangle \langle v_i | \widetilde{v_j}\rangle\right), \tag{2.15}$$

where $N_j = \sqrt{\widetilde{\langle v_j | v_j \rangle}}$ is the norm of the vector. To evaluate the weight of for example the N_0+1 particle sector $\mathrm{Q}^\dagger_{\gamma i} = \langle\gamma| c_i^{\sigma\dagger} |\Psi_0\rangle$, eq. (2.15) has to be rearranged

$$\widetilde{|v_j\rangle} = N_j |v_j\rangle + \sum_{i=1}^{j-1} |v_i\rangle \langle v_i | \widetilde{v_j}\rangle\,.$$

Multiplying this equation by $\langle\gamma|$, one obtains

$$\mathrm{Q}^\dagger_{\gamma i} = \langle\gamma| \widetilde{v_j}\rangle = N_j \langle\gamma| v_j\rangle + \sum_{i=1}^{j-1} \langle\gamma| v_i\rangle \langle v_i | \widetilde{v_j}\rangle\,.$$

All quantities occurring in this equation are accessible within the Band Lanczos procedure. The norm N_j and $\langle v_i | \widetilde{v_j}\rangle$ are calculated at the orthogonalization step and $\langle\gamma|$ is the complex conjugate of the eigenvector of the matrix $\widetilde{H}$ which is an approximate eigenvector of H.

One can understand the success of this method since the Lanczos method converges to the extremal eigenvalues in a given subspace. One can target the correct subspace for single-particle excitations by the explicit choice $|v_i\rangle = c_i^\dagger/c_i\,|\Psi_0\rangle$ as the starting vectors for Band Lanczos. Then the algorithm will yield those excitations having the largest weight very accurately. In the calculations 300 excitations in the N_0+1- and $N_\gamma = 300$ in the N_0-1 sector are evaluated, although it turns out that for most Hamiltonians,

at system sizes suitable for ED, $N_\gamma \approx 100$ excitations in total are more than sufficient to exhaust the sum rule

$$-\frac{1}{\pi}\sum_{\mathbf{k}}\int_{-\infty}^{\infty} d\omega\, \Im\mathrm{m}\mathrm{G}(\omega,\mathbf{k}) = 1\,, \tag{2.16}$$

and therefore obtain an accurate Green's function within numerical precision. This means although the Band Lanczos method is an iterative algorithm yielding not all eigenvalues and eigenvectors in principle needed for the determination of the Green's function, it turns out to be a more or less exact method for this application.
For small systems it is possible to obtain all eigenvalues and eigenvectors by full diagonalization. This yields all the required information about the system.

2.2.3. Full diagonalization

Although the focus of this work is clearly on large scale sparse eigenvalue problems for which iterative algorithms like the Lanczos- (or Arnoldi- in the non-hermitian case) algorithm are appropriate, it is often convenient to have a full eigenvalue solver at hand. A full solver yields all eigenvalues and eigenvectors. Such solvers are efficiently implemented in standard numerical packages like LAPACK [41]. In this work the QR method [42, 43] is used to fully diagonalize small systems ($L \leq 6$). A summary of this method is unfortunately beyond the scope of the present work. For a recent review see for example Watkins [44].
Having all eigenvalues and eigenvectors of a given matrix at hand, it is straight forward to compute the Green's function by using the spectral representation eq. (2.12). The excited state vectors $|\gamma\rangle$ are the eigenvectors of the corresponding subspace of the Hamiltonian which are all obtained within numerical accuracy by full diagonalization. The excitation energies ω_γ are the respective eigenvalues. Using QR for system-sizes between two and six sites and Band Lanczos between seven and sixteen sites, the question arises if one can go to larger systems. The limiting factor for Band Lanczos besides runtime is mainly memory consumption. It turns out that a method is currently under development, which enables access to larger systems, as will be discussed in the next section.

2.2.4. A possibility to reach larger systems - Matrix Product State Lanczos

Recently an iterative Lanczos based eigensolver using matrix product states has been developed [45]. The advantage of this method is the minimal memory consumption at the cost of a truncation of the Hamiltonian which induces a new source of error each time the Hamiltonian is applied to a state-vector. For computing Green's functions this algorithm currently works very well for the ≈ 10 poles with largest weight. Enabling access to system sizes which are easily double the size reachable with a 'classic' Band-Lanczos method. However the Band Lanczos method is able to really reproduce enough poles with corresponding weights accurately to exhaust the sum rule eq. (2.16). It turns out that the ≈ 10 accurate poles obtained by MPS-Lanczos lack approximately 1% of the sum rule for system sizes not reachable with Band Lanczos. For Hubbard systems up to ≈ 14 sites, the results of the two methods are the same. The interface to CPT is provided again by the Q-matrix formalism. As preliminary calculations for the SIAM show (see sec. 3.3.7) the missing spectral weight, in the MPS method, manifests itself in a spurious behavior of the single-particle spectral function $A(\omega)$ in the vicinity of $\omega = 0$ after CPT/VCA. This means that CPT/VCA are extremely sensitive to an accurate cluster solution for the Green's function. This algorithm is still under development and gives hope to double the CPT/VCA cluster/reference system L sizes in the near future. After discussing some options for solving clusters we turn to a method which is able to improve dramatically on CPT results.

2.3. Variational Cluster Approach

In this section the variational cluster approach will be reviewed. An alternative self-consistent formulation of the VCA suitable for equilibrium as well as non-equilibrium problems will be discussed. An expression for the grand potential for infinite-size reference systems will be presented. VCA is in general capable of dealing with fermionic- [46, 47, 48, 49, 50, 51] as well as bosonic- [52] systems. In contrast to CPT it may be applied in broken symmetry phases [53, 54, 55]. Disordered systems [56, 57] may be treated using VCA. Recently an extension of VCA to non-equilibrium problems was introduced [25]. The models which have been investigated by VCA are numerous. VCA was inter alia applied to the fermionic Hubbard model [58], the Bose-Hubbard model [59], the Falicoff-Kimball model [60], the Periodic Anderson model [61] and the Jaynes-Cummings-Lattice model [62]. Recently VCA was combined with ab-initio band-structure

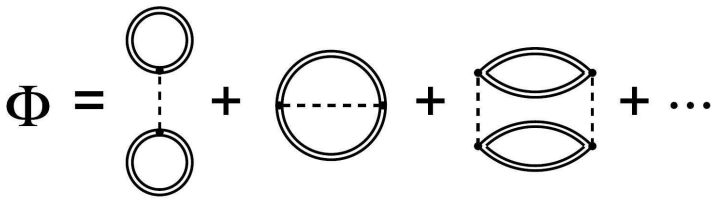

Figure 2.3.: Diagrammatic definition of the Luttinger-Ward functional $\Phi[G]$. The double lines denote the fully interacting propagator G, the dashed lines the interaction.

calculations [63]. Applications to spin systems [64] however have failed up to now.
In the following a short introduction to this method shall be presented.

2.3.1. Variational Cluster Approach - Theory

The variational cluster approach may be seen as a variational extension of CPT based on the self-energy functional approach (SFA) [65, 66]. This section is widely based on the review article by Potthoff [67] as well as ref. [52].
We are interested in the interacting single-particle Green's function G of a given Hamiltonian

$$\hat{\mathcal{H}}(\mathsf{x}, U) = \hat{\mathcal{H}}_I(\mathsf{x}) + \hat{\mathcal{H}}_{II}(U) \,, \tag{2.17}$$

consisting of a one-particle part $\hat{\mathcal{H}}_I$ and a two-particle interaction part $\hat{\mathcal{H}}_{II}$. In the SFA the Luttinger-Ward functional $\Phi[G]$ [68] is used as a starting point to construct the generalized grand potential functional $\Omega[G, G_0]$

$$\Omega[G, G_0] = \Phi[G] - \mathrm{Tr}\left\{\left(G_0^{-1} - G^{-1}\right) G\right\} + \mathrm{Tr}\left\{\ln\left(-G\right)\right\} \,, \tag{2.18}$$

where the subscript $_0$ denotes the non-interacting Green's function. The trace Tr is short for $\mathrm{Tr} \equiv \frac{1}{\beta} \sum_{\omega_n} \mathrm{tr}$, where β is the inverse temperature, the sum is over fermionic Matsubara frequencies and the small form trace tr denotes a sum over lattice sites and spin. The Luttinger-Ward functional $\Phi[G]$ is defined as the sum over all two-particle irreducible diagrams. The functional derivative of $\Phi[G]$ with respect to the interacting Green's function yields the self-energy Σ

$$\frac{\delta \Phi[G]}{\delta G} = \Sigma \,, \tag{2.19}$$

as may be inferred from its diagrammatic definition (see fig. 2.3). Taking a derivative corresponds in the diagrammatic language roughly to taking out an interacting propagator. At this point it should be mentioned, that VCA may be constructed completely non-perturbatively [69, 67]. It can be shown that expression eq. (2.19) is locally invertible. Legendre transforming the Luttinger-Ward functional $\Phi[\Sigma]$

$$F[\Sigma] = \Phi[\Sigma] - \mathrm{Tr}\left\{\Sigma G\right\} \,,$$

allows for expressing $\Sigma[G]$

$$\beta \frac{\delta F[\Sigma]}{\delta \Sigma} = -G[\Sigma] \,.$$

one may rewrite eq. (2.18)

$$\Omega[\Sigma, G_0] = F[\Sigma] - \mathrm{Tr} \ln\left(-G_0^{-1} + \Sigma\right) \,. \tag{2.20}$$

The functional derivative of the self-energy functional $\Omega[\Sigma, G_0]$ with respect to Σ yields Dyson's equation at the stationary point

$$\frac{\delta \Omega[\Sigma, G_0]}{\delta \Sigma} = -G + \left(G_0^{-1} - \Sigma\right)^{-1} \stackrel{!}{=} 0 \,. \tag{2.21}$$

This is an equation for the physical self-energy Σ given the Luttinger-Ward functional $F[\Sigma]$ and the free Green's function G_0. Eq. (2.19) and eq. (2.21) comprise a set of two equations for the two unknown

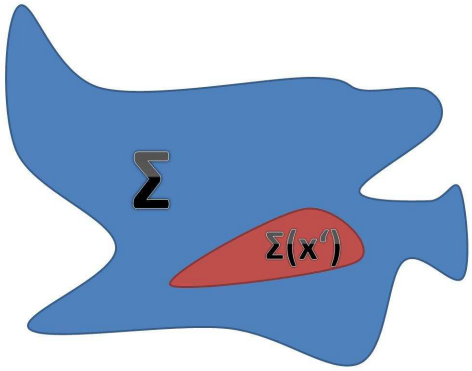

Figure 2.4.: The space of self-energies Σ is restricted by those which may be generated by the single-particle parametrization of an exactly solvable reference-system Σ'.

functions G and Σ.
The Luttinger-Ward functional is a universal functional in the sense, that only depends on the interaction and is not a functional of G_0. This means systems sharing the same interaction part in their Hamiltonian have the same Luttinger-Ward functional. This fact is exploited in introducing a so called "reference system"

$$\hat{\mathcal{H}}'(x', U) = \hat{\mathcal{H}}'_I(x') + \hat{\mathcal{H}}_{II}(U) \,,$$

defined on the same lattice and having the same two-particle term $\hat{\mathcal{H}}_{II}$ as the original Hamiltonian eq. (2.17), but may differ in the one-particle terms x'. Here primed quantities denote quantities belonging to the reference system. This means it differs from the the original system in G_0. The point of erecting this auxiliary system is to choose it to be an exactly solvable one. To be definite one usually chooses it to be a cluster decomposition of the original system. The Luttinger-Ward functional is eliminated from the equations by comparing eq. (2.20) for the original and the reference system

$$\begin{aligned}
\Omega[\Sigma, G_0] &= F[\Sigma] - \mathrm{Tr}\left\{\ln\left(-G_0^{-1} + \Sigma\right)\right\} \\
- \quad \Omega'[\Sigma, G'_0] &= -\left(F[\Sigma] - \mathrm{Tr}\ln\left(-G_0'^{-1} + \Sigma\right)\right) \\
\Rightarrow \Omega[\Sigma, G_0] &= \Omega'[\Sigma, G'_0] - \mathrm{Tr}\ln\left(-G_0'^{-1} + \Sigma\right) + \mathrm{Tr}\ln\left(-G_0^{-1} + \Sigma\right) \\
&= \Omega'[\Sigma, G'_0] - \mathrm{Tr}\ln\left(-G'[\Sigma]\right) + \mathrm{Tr}\ln\left(-G[\Sigma]\right) \,.
\end{aligned} \tag{2.22}$$

Note that for bosonic systems the $\pm$-signs of the second and third term are interchanged. Also note that in VCA the self-energy Σ is taken to be the self energy of the reference system Σ', which is usually not explicit in the notation. Eq. (2.22) is still exact if the reference system is able to provide the exact self-energy of the full system. In practice the single-particle parameters x' of the reference system are free to be varied since this does not change the interacting part and eq. (2.18) still holds. This means that the functional $\Omega[\Sigma, G_0]$ eq. (2.22) becomes a function of those parameters

$$\Omega(x') = \Omega'(x') + \mathrm{Tr}\,\ln\left(-G(x, x')\right) - \mathrm{Tr}\,\ln\left(-G'(x')\right) \,, \tag{2.23}$$

The VCA approximation consists therefore in restricting the space of available self-energies to those produce-able by the reference system and its single-particle parametrization (see fig. 2.4). The stationarity condition determining the physical parameters eq. (2.21) is then given by

$$\nabla_{x'}\Omega(x') \stackrel{!}{=} 0 \,. \tag{2.24}$$

Note that this is a dynamic variational principle since it involves $G(\omega)$ and therefore excited states. The Green's function G of the physical system $\hat{\mathcal{H}}$ is obtained by the CPT equation (eq. (2.2)). This time in contrast to CPT the matrix $T = G_0'^{-1} - G_0^{-1}$ contains all single particle terms not included in the reference system as well as the deviation, introduced by VCA, $\Delta x \equiv x' - x$ of the single-particle parameters of the reference system x' with respect to the ones of the original system x. Some remarks about the definition of signs in G' and T are appropriate. The signs of the variational parameters are fixed by the Dyson

equation eq. (2.21)

$$\begin{aligned} G^{-1} &= G'^{-1} - T \\ &= (\omega - \mathcal{H}) - T \\ &= \omega - (\mathcal{H} + T) \ . \end{aligned}$$

This means that if a variationally introduced parameter $\delta\alpha$ for a one particle quantity is defined in $\mathcal{H}$ (and therefore G) as: $(\alpha + \delta\alpha)\hat{O}$, it, of course, is negative in T: $-\delta\alpha$. For parameters which are intrinsically negatively defined in $\mathcal{H}$ (i.e. usually the hopping t) it is like follows: in $\mathcal{H}$ (and therefore G): $-(\alpha+\delta\alpha)\hat{O}$ and in T: $+\delta\alpha$. For the evaluation of Dyson's equation eq. (2.21) several forms may be used

$$\begin{aligned} G^{-1} &= G'^{-1} - T \\ G &= G' + G'TG = G' + GTG' \\ G &= \left(\mathbb{1} - G'T\right)^{-1} G' \ . \end{aligned}$$

The last one is particularly useful for numerical calculations because only one inversion is needed. The process of performing a CPT/VCA calculation is summarized in a flow diagram in fig. 2.5. Next we turn to the question of how the self-energy functional eq. (2.23) may be evaluated numerically.

2.3.2. Evaluation of the self-energy functional

The grand potential in the form of eq. (2.23) has to be evaluated numerically in order to find its stationary point and thus the optimal single-particle parameters x'_{stat}. In ref. [26] two methods to evaluate eq. (2.23) have been proposed. One is based on an exact (analytic) frequency integration, which yields an expression involving sums over excitation energies. Therefore it is especially suited for problems, where the full Q-matrix representation of the cluster as well as the total system is available (see sec. 2.1.4). The second option would be a numeric frequency integration. This is the way to go in dealing systems, whose excitations can not be put into Q-matrix form entirely (see sec. 2.1.5). As we shall see the real integrals have to be transformed to complex contour integrals in order to achieve a stable numerical routine. In the following both cases will be discussed. The first one is needed for the calculations for Graphene, although here the numerical integration would be applicable too, however with slightly less accuracy. The second method is used for the single impurity Anderson model, where the spectrum is not explicitly representable by a finite number of poles.
The evaluation of the first term of eq. (2.23): $\Omega'(x')$, which is the grand potential of the cluster, is the same in both cases. It may be calculated from the partition functional

$$Z = e^{-\beta\,\Omega'(x')} = \sum_n e^{-\beta\,\omega'_n} \ ,$$

which reduces in the limit of zero temperature ($\beta \to +\infty$) to the contribution of the ground state energy of the cluster ω'_0 only

$$\lim_{\beta\to+\infty} \sum_n e^{-\beta\,\omega'_n} = e^{-\beta\,\omega'_0} \ .$$

Therefore, in the zero temperature case, the grand potential of the cluster $\Omega'(x')$ is given by its ground-state energy ω'_0

$$\Omega'(x') = \omega'_0 \ .$$

Next we turn to the two different approaches of evaluating the additional terms in eq. (2.23).

Exact frequency integration

This method of evaluating the grand potential eq. (2.23) is used for systems, where the full Q-matrix representation of the cluster as well as the total system is available. In this work this is the case in the study of defects in Graphene (see ch. 5). The results (for example obtained in ref. [26]) will be stated here without derivation, since the calculation is rather lengthy and was not part of this work. It may for

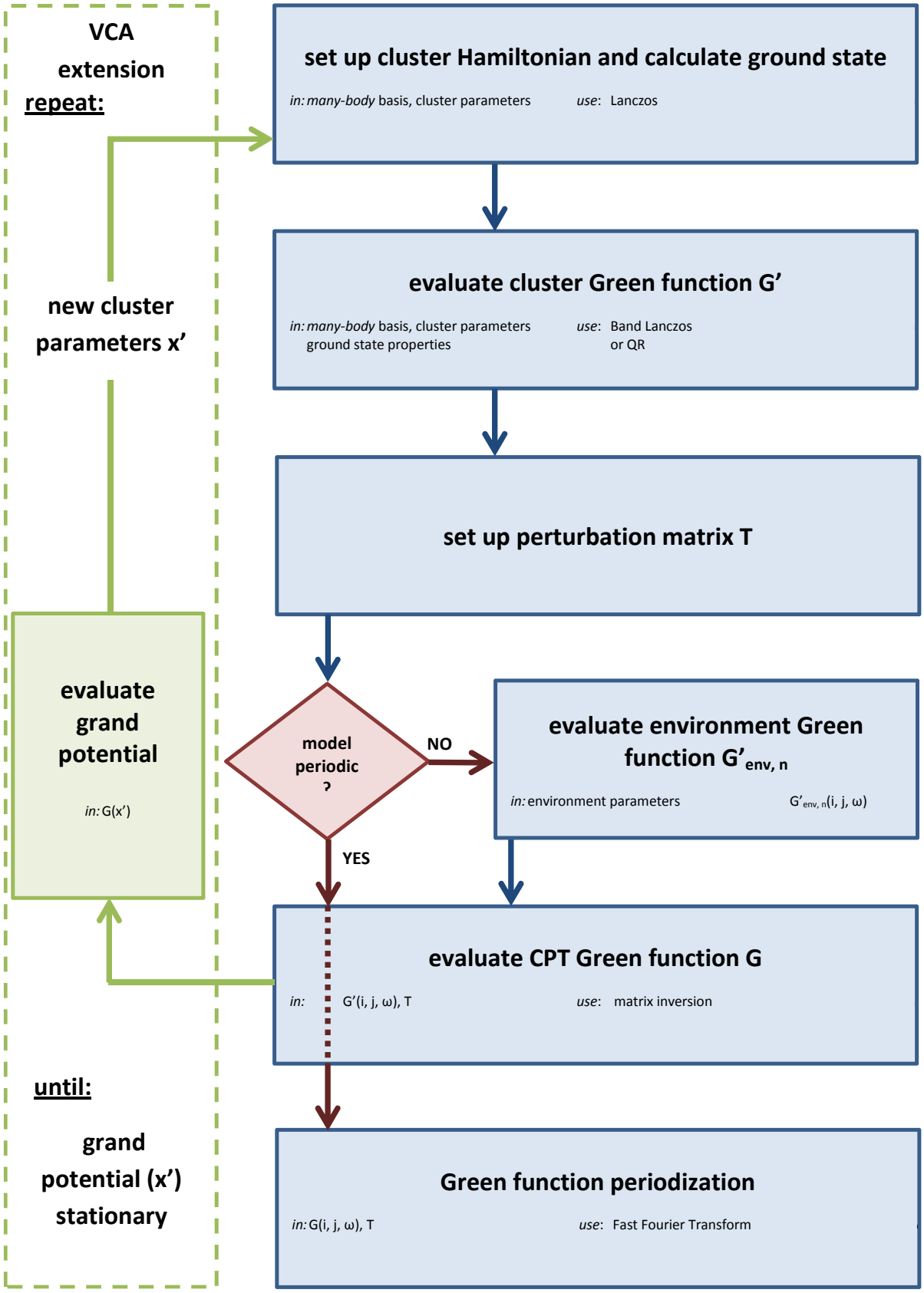

Figure 2.5.: Flow chart diagram for a CPT/VCA calculation.

example be found in ref. [29]. The analytic frequency integration of eq. (2.23) (for fermions) leads to

$$\Omega(\mathsf{x}) = \Omega'(\mathsf{x}') + \frac{1}{\beta}\sum_{\gamma}\ln\left|1-e^{-\beta\lambda'_\gamma}\right| - \frac{1}{\beta}\frac{1}{N^\Gamma}\sum_{\mathbf{k}^\Gamma}\sum_{\gamma}\ln\left|1-e^{-\beta\lambda_\gamma(\mathbf{k}^\Gamma)}\right|,$$

which reduces in the case of zero temperature ($\beta\to+\infty$) to

$$\Omega(\mathsf{x}) = \Omega'(\mathsf{x}') - \sum_{\mathfrak{Re}\lambda'_\gamma<0}\lambda'_\gamma + \frac{1}{N^\Gamma}\sum_{\mathfrak{Re}\lambda_\gamma(\mathbf{k}^\Gamma)<0}\lambda_\gamma(\mathbf{k}^\Gamma).$$

Note that in the bosonic case the ±-signs in front of term two and three are exchanged. The excitation energies of the cluster λ'_γ are obtained in eq. (2.3), while the excitation energies of the total system for a given superlattice wavevector $\mathbf{k}^\Gamma$ are available from the diagonalization of eq. (2.5). Note that the last sum goes over the 1st BZ of the superlattice Γ. N^Γ is the number of points on the superlattice Γ, i.e. the number of clusters in the total system. All quantities in this expression are readily available. Next we turn to the case where those quantities are not easily accessible in Q-matrix form and a numeric frequency integration has to be used.

Numerical frequency integration for infinite reference systems

In this section we have in mind a special kind of reference system, which is not expressible in Q-matrix form and of infinite extent. This is the case for the single impurity Anderson model, although the expressions derived in this section are applicable to any system of that kind. We consider a reference system consisting of two parts, one being a finite interacting system, the cluster, and one a non-interacting system of infinite size, the environment. The grand potential $\Omega'(\mathsf{x}')$ is given by the sum of the grand-potentials of the cluster part of the reference system (Ω'_{cluster}) and of the environment part of the reference system (Ω'_{env}). The last part being infinite but constant and we consider from now on the shifted grand potential $\Omega(\mathsf{x})-\Omega'_{\text{env}}$.
We start out by discussing the Green's function G for an infinite reference system. This system is represented by the Green's function of the reference system and G' and T

$$\mathrm{G}' = \begin{pmatrix}\mathrm{G}'_{cc} & \mathrm{G}'_{ce}\\ \mathrm{G}'_{ec} & \mathrm{G}'_{ee}\end{pmatrix}, \qquad \mathrm{T} = \begin{pmatrix}\mathrm{T}_{cc} & \mathrm{T}_{ce}\\ \mathrm{T}_{ec} & 0\end{pmatrix},$$

where the subscript c denotes the sites of the cluster part of the reference system, while the collective index e denotes the sites of the environment part of the reference system. Up to this point all matrices involving environment indices have infinite size. As far as the Green's function itself is concerned this is no problem as we are primarily interested in the cluster part of the reference system given by G_{cc} for which the Dyson equation reduces to

$$\begin{aligned}
\mathrm{G}_{cc} &= \mathrm{G}'_{cc} + \mathrm{G}'_{cc}\mathrm{T}_{cc}\mathrm{G}_{cc} + \mathrm{G}'_{cc}\mathrm{T}_{ce}\mathrm{G}_{ec}\\
\mathrm{G}_{ec} &= \mathrm{G}'_{ee}\mathrm{T}_{ec}\mathrm{G}_{cc}\\
\mathrm{G}_{cc} &= \mathrm{G}'_{cc} + \mathrm{G}'_{cc}\tilde{\Sigma}_{cc}\mathrm{G}_{cc}\\
\tilde{\Sigma}_{cc} &\coloneqq \mathrm{T}_{cc} + \mathrm{T}_{ce}\mathrm{G}'_{ee}\mathrm{T}_{ec}
\end{aligned}$$

As far as the grand potential is concerned, the calculation to eliminate the infinite environmental degrees of freedom is rather lengthy and presented in app. C. Based on this result the numerical frequency integration of eq. (2.23) is possible. Again this results in tedious work following ref. [26], which is done in detail in app. D. Starting out from

$$\Omega(\mathsf{x}') = \Omega'(\mathsf{x}') - \mathrm{Tr}\,\ln\left(\mathbb{1} - \mathrm{T}\mathrm{G}'(\mathsf{x}')\right),$$

and performing a transformation to a complex contour integral as well as an integral regularization, one ends up with

$$\begin{aligned}
\Omega(\mathsf{x}') - \Omega'_{\text{env}} = {}& \omega'_{0,\text{cluster}}(\mathsf{x}') + \mathrm{tr}\,(\mathrm{T})\\
& - \frac{1}{\pi}\sum_{\sigma}\int_0^\infty d\omega\,\ln\left|\det\left(\mathbb{1}_{cc} - \tilde{\Sigma}_{cc}(i\omega)\mathrm{G}'_{cc}(i\omega)\right)\right|.
\end{aligned}$$

This integral may be evaluated as suggested in ref. [26] by integrating from 0 to Λ_1, from Λ_1 to Λ_2 and from Λ_2 to ∞. Λ_1 and Λ_2 represent two characteristic scales in the problem (for example the smallest/largest

eigenvalue of the Hamiltonian matrix). For the last part of the integral a substitution $\tilde{\omega} = \frac{1}{\omega}$ is performed. In this work an adaptive Gauss Legendre integrator (see for example ref. [70]) for the evaluation of the integrals is used. Having discussed how the grand potential is evaluated for a given set of single-particle parameters x' we proceed by discussing methods to find its stationary point.

2.3.3. Finding stationary points of the grand potential

In VCA the stationary point of the grand potential functional has to be determined. The stationary point of the grand potential $\Omega(\mathsf{x}')$ which is in general a multivariate function may be a maximum, a minimum or a saddle-point. Generally enormously large deviations from the physical parameters x do not make sense. Therefore it is difficult to apply a standard numerical algorithm. In fact I am not aware of an algorithm which finds arbitrary stationary points of a (often quite complicated) multivariate function with boundary constraints. Literature exists for the so called Nudged elastic band [71] and dimer methods [72] which are not suitable for the problem at hand. The approach taken here is to separate calculations involving low dimensional (one to two variational parameters) parameter spaces, where the nature of the stationary point is often known from the general higher dimensional case, where it is impossible to predict the nature of the stationary point. For example it is known that varying the chemical potential (or on-site energy), the stationary point is always a maximum. We furthermore found that varying the hopping, there exist in most parameter regions three stationary points, one which is an unphysical maximum and two equivalent minima. For further discussion see sec. 3.3.1.
In this work a Brent method [70], which combines a parabolic interpolation with the golden section algorithm is used for one variational parameter if the stationary point is known to be a minimum or a maximum. For higher dimensional cases, where the stationary point is known to be either a minimum or a maximum, a derivative free Nelder-Mead simplex algorithm [73] is used. Both these algorithms are available from standard numerical libraries like GSL [74]. For the mechanics of these methods the reader is referred to the literature since a description of these algorithms would go beyond the scope of this work. In the general case where the nature of the stationary point is not known a self-made algorithm is used which is based on parabolic interpolation. The idea is that the function $\Omega(\mathsf{x}')$ is fitted by a high dimensional paraboloid, whereby the consecutive points, by which the paraboloid is fit, contract to the stationary point. Since this method was developed specifically for this application it is presented in the following. A similar method may exist in literature, but no perfectly suitable standard-algorithm could be found. During the finalisation of this thesis E. Arrigoni pointed out to me a similar method presented in ref. [53] sec. III.D, which includes a suggestion for improvement.

Finding stationary points in many dimensions

Our goal here is to find the stationary point of the N_{x} dimensional function $\Omega(\mathsf{x})$. Therefore we approximate this function by a quadratic form

$$(\mathbf{x}^i)^T C \mathbf{x}^i ,$$

where C is a symmetric matrix with

$$N_C = \frac{N_{\mathsf{x}}^2 + 3N_{\mathsf{x}} + 2}{2} ,$$

independent unknown coefficients. To identify the coefficients of C, N_C trial vectors $\mathbf{x}^i$, $i = [1, \dots N_C]$ are needed

$$\mathbf{x}^i = \begin{pmatrix} x_1^i \\ x_2^i \\ \vdots \\ x_{N_x}^i \\ 1 \end{pmatrix} .$$

This leads to a system of equations for the coefficients of C

$$(\mathbf{x}^i)^T C \mathbf{x}^i = \Omega(\mathbf{x}^i), \quad i = [1, \dots N_C] . \tag{2.25}$$

Consider as an example the two-dimensional case: $N_{\mathsf{x}} = 2$, which leads to $N_C = 6$. We need six, three-dimensional trial points $\mathbf{x}^i$ to obtain the system

$$
\begin{aligned}
(\mathbf{x}^i)^T\, C\, \mathbf{x}^i &= \Omega(\mathbf{x}^i) \\
\begin{pmatrix} x_1^i & x_2^i & 1 \end{pmatrix} \begin{pmatrix} C_{11} & C_{12} & C_{13} \\ C_{12} & C_{22} & C_{13} \\ C_{13} & C_{13} & C_{33} \end{pmatrix} \begin{pmatrix} x_1^i \\ x_2^i \\ 1 \end{pmatrix} &= \Omega(x_1^i, x_2^i)
\end{aligned}
$$

$$
\begin{array}{ll}
C_{11}(x_1^1)^2 + C_{22}(x_2^1)^2 + 2C_{12}x_1^1x_2^1 + C_{33} + 2C_{12}x_1^1 + 2C_{13}x_2^1 & \Omega(x_1^1, x_2^1) \\
C_{11}(x_1^2)^2 + C_{22}(x_2^2)^2 + 2C_{12}x_1^2x_2^2 + C_{33} + 2C_{12}x_1^2 + 2C_{13}x_2^2 & \Omega(x_1^2, x_2^2) \\
C_{11}(x_1^3)^2 + C_{22}(x_2^3)^2 + 2C_{12}x_1^3x_2^3 + C_{33} + 2C_{12}x_1^3 + 2C_{13}x_2^3 & \Omega(x_1^3, x_2^3) \\
C_{11}(x_1^4)^2 + C_{22}(x_2^4)^2 + 2C_{12}x_1^4x_2^4 + C_{33} + 2C_{12}x_1^4 + 2C_{13}x_2^4 & \Omega(x_1^4, x_2^4) \\
C_{11}(x_1^5)^2 + C_{22}(x_2^5)^2 + 2C_{12}x_1^5x_2^5 + C_{33} + 2C_{12}x_1^5 + 2C_{13}x_2^5 & \Omega(x_1^5, x_2^5) \\
C_{11}(x_1^6)^2 + C_{22}(x_2^6)^2 + 2C_{12}x_1^6x_2^6 + C_{33} + 2C_{12}x_1^6 + 2C_{13}x_2^6 & \Omega(x_1^6, x_2^6)
\end{array}
$$

The N_C trial vectors are chosen in the vicinity of an initial guess for the stationary point $\mathbf{x^S}_0$

$$
\mathbf{x}^i = \mathbf{x^S}_0 + \sum_j g_j^i \beta_j \mathbf{e}_j \,, \tag{2.26}
$$

where the function g_j^i may be chosen to take integer values $\in [0, \pm 1, \pm 2, \ldots]$ to encage $\mathbf{x^S}_0$. A guess for the stationary point of $\Omega(\mathsf{x})$ is given by the stationary point of its local quadratic approximation by

$$
\nabla\Omega(\mathsf{x}) \approx \nabla\left((\mathbf{x^S})^T\, C\, \mathbf{x^S}\right) \stackrel{!}{=} 0 \,,
$$

where the coefficients of C are known from eq. (2.25). This leads to another system of equations for the approximation of the stationary point $\mathbf{x^S}$

$$
\begin{aligned}
\nabla(\mathbf{x^S})^T\, C\, \mathbf{x^S} + (\mathbf{x^S})^T\, \nabla C\, \mathbf{x^S} &\stackrel{!}{=} 0 \\
2C\, \mathbf{x^S} &\stackrel{!}{=} 0 \,,
\end{aligned}
$$

which may be solved by bringing the constant terms to the right. Again for the two-dimensional example this takes the form

$$
\begin{array}{ll}
C_{11}x_1^S + C_{12}x_2^S & -C_{13} \\
C_{12}x_1^S + C_{22}x_2^S & -C_{23}
\end{array} \,.
$$

The newly obtained approximation for the stationary point $\mathbf{x^S}$ is then taken to be a new guess $\mathbf{x^S}_0$ and the procedure is repeated until the point stabilizes from one iteration to the next. One important point to note here is that the convergence is strongly dependent on the function β_j which is used to quantify the size of the cage around $\mathbf{x^S}_0$ in eq. (2.26). This function has to contract to a point, the closer one comes to the true stationary point to avoid instabilities. This concludes the discussion of VCA based on the grand potential Ω. Next we turn to a different, self-consistent formulation of VCA.

2.3.4. Self consistent VCA

In this work we compare results obtained by the conventional VCA which we from now on term VCA_Ω to an alternative formulation $\mathrm{VCA}_{\mathrm{SC}}$. The need for an alternative formulation is motivated by the extension of VCA to non-equilibrium systems which will be discussed in sec. 2.4. The conventional VCA_Ω may not be straight forwardly used in the non-equilibrium situation since it relies on the grand potential which is not well defined in this case. The self-consistent reformulation of VCA: $\mathrm{VCA}_{\mathrm{SC}}$ was recently developed in ref. [25] to treat systems out of equilibrium, although it can equally be adopted in equilibrium. Up to now this formulation lacks a rigorous fundamental mathematical justification although it may be related to CDMFT in some limits [25].

In $\mathrm{VCA}_{\mathrm{SC}}$ the variational parameters x' are determined by comparing static expectation values of the reference system and the total system. The idea of this self-consistent approach is to use a reference system which resembles the full system best. The strategy is to find those values x' for the set of parameters of the reference system which let the expectation values of their corresponding single-particle operators $< \hat{O} >_{\mathrm{cluster},\mathsf{x}'}$ coincide with those of the full system $< \hat{O} >_{\mathrm{CPT},\mathsf{x},\mathsf{x}'}$. Here, the angle brackets denote expectation values in the reference and the full system coupled by CPT or VCA respectively. Consider the on-site energies ϵ_f' and ϵ_s' as variational parameters. One then has to look for those cluster

parameters ϵ'_f and ϵ'_s which fulfill the relations

$$\begin{aligned} \left\langle \hat{n}^f_\sigma \right\rangle_{\text{cluster},\epsilon'_f,\epsilon'_s} &\stackrel{!}{=} \left\langle \hat{n}^f_\sigma \right\rangle_{\text{CPT},\epsilon_f,\epsilon_s,\epsilon'_f,\epsilon'_s} \\ \sum_i^{L-1} \left\langle \hat{n}^i_\sigma \right\rangle_{\text{cluster},\epsilon'_f,\epsilon'_s} &\stackrel{!}{=} \sum_i^{L-1} \left\langle \hat{n}^i_\sigma \right\rangle_{\text{CPT},\epsilon_f,\epsilon_s,\epsilon'_f,\epsilon'_s} . \end{aligned} \tag{2.27}$$

The sum is over all non-interacting sites included in the cluster. Eq. (2.27) amounts to solving a system of non-linear equations in each step of the self consistency cycle. In general it is possible to vary each single particle parameter separately. For reasons of keeping the numerics tractable in this work we restrict ourselves to one ϵ'_s only, which we take to be the same for each site. Extension to a larger number of ϵ'_s is straightforward. To fix this parameter we require the average particle density on the noninteracting sites to fulfill the condition eq. (2.27). In some situations, the hybridization matrix element V' and the intra-cluster hopping t' will alternatively be considered as variational parameters. Then the particle number expectation values in eq. (2.27) are replaced by hopping expectation values. Again for t we use a single variational parameter for hopping between all uncorrelated sites and fix it by requiring the mean value of hopping in the cluster and the full system to coincidence. An improved multidimensional Newton-Rhapson algorithm is used to find the roots of the system eq. (2.27). In some parameter regions no solution may be found.

2.3.5. Finding the roots of multi-variate functions

In contrast to the standard formulation where one has to find stationary points of the grand potential Ω, the self-consistent formulation requires finding the roots of a non-linear system of equations. In this work a modified Newton-Rhapson method [70] is used to solve a non-linear system like eq. (2.27). The Newton-Rhapson procedure converges to a root by an iterative process. A starting point $\mathbf{x}_0$ for the roots, is updated by the prescription

$$\mathbf{x}_{n+1} = \mathbf{x}_n - \left[J_f(\mathbf{x}_n)\right]^{-1} f(\mathbf{x}_n) ,$$

where J_f is the Jacobian defined as

$$J_f(\mathbf{x}) = \begin{pmatrix} \frac{\partial f_1}{\partial x_1} & \frac{\partial f_1}{\partial x_2} & \cdots & \frac{\partial f_1}{\partial x_N} \\ \frac{\partial f_2}{\partial x_1} & \frac{\partial f_2}{\partial x_2} & \cdots & \frac{\partial f_2}{\partial x_N} \\ \vdots & \vdots & \ddots & \vdots \\ \frac{\partial f_N}{\partial x_1} & \frac{\partial f_N}{\partial x_2} & \cdots & \frac{\partial f_N}{\partial x_N} \end{pmatrix} ,$$

which is calculated by a finite-difference approximation to the partial-derivative.
The self-consistent VCA_{SC} introduced in the last two sections provides the basis for the non-equilibrium formulation of VCA, which will be discussed in the next section.

2.4. Non-equilibrium Variational Cluster Approach

The extension of CPT/VCA to the non-equilibrium case was started by Balzer *et al.* [75] who studied short-time behavior using CPT. Knap *et al.* [25] were investigating the long-time, steady-state of two-dimensional Hubbard systems using a self-consistent VCA_{SC}. In this work the long-time, steady-state behavior of a strongly correlated quantum dot, modeled by the SIAM, is investigated by VCA_{SC}. In this section the non-equilibrium extension of VCA will be presented. First a short introduction to the Keldysh-Green's function technique, on which the non-equilibrium VCA is based, is presented in sec. 2.4.1. Then the self-consistent VCA_{SC} introduced in sec. 2.3.4, will be extended to the non-equilibrium case in sec. 2.4.2.

2.4.1. The Keldysh-Green's function technique

Here the basics of the Keldysh-Green's function technique are outlined. This section is based on the very nice review article by Jauho [76]. Further information on the topic is available at the more comprehensive reviews ref. [77] or ref. [78]. Introductory lecture notes are available in ref. [79] and ref. [80]. A good overview is presented in the book by Haug and Jauho [81]. The contour ordered (Keldysh-) Green's function technique was named after the pioneering work by Keldysh [82], although earlier closely related

approaches exist, for example by Schwinger [83] and Feynman and Vernon [84].
One great advantage of non-equilibrium Keldysh Green's function theory is that it is formally similar to the equilibrium theory. Consider a system described by a general Hamiltonian

$$\hat{\mathcal{H}} = \hat{\mathcal{H}}_0 + \hat{\mathcal{H}}_1(t) \,,$$

where the time dependent part is assumed to vanish in the distant past $t \to -\infty$, so

$$\hat{\mathcal{H}}_1(t) \equiv 0 \quad \text{for} \;\; t < 0 \,,$$

Adiabatically switching on the interaction $\hat{\mathcal{H}}_1(t) = e^{-0^+|t|}\,\hat{V}(t)$, the interaction attains its full strength at time $t = 0$. Note that this implies that at time $t \to -\infty$ all operators in the Heisenberg-picture O^H equal operators in the interaction representation with respect to $\hat{\mathcal{H}}_0$, $O^{I,\hat{\mathcal{H}}_0}(-\infty)$. Zero-temperature equilibrium many-body theory may be formulated in terms of the time-ordered Green's function [85, 86]

$$\mathrm{G}^T_{\hat{A}\hat{B}}(x_1,t_1;x_2,t_2) = -i\frac{\langle\Psi_0|\,\hat{\hat{T}}\left(\hat{A}^H(x_1,t_1)\hat{B}^H(x_2,t_2)\right)|\Psi_0\rangle}{\langle-\infty|-\infty\rangle} \,. \tag{2.28}$$

The index x, representing space, spin, ... will be suppressed from now on to focus on the important index in this chapter which is time t. The time-ordering operator is defined as

$$\hat{\hat{T}}\left(\hat{A}(t)\hat{B}(t')\right) = \begin{cases} \hat{A}(t)\hat{B}(t') & \text{if } t > t' \\ \hat{B}(t')\hat{A}(t) & \text{if } t' > t \end{cases} \tag{2.29}$$

$$= \theta(t-t')\,\hat{A}(t)\hat{B}(t') + \eta\,\theta(t'-t)\,\hat{B}(t')\hat{A}(t) \,, \tag{2.30}$$

where $\eta = +1$ for bosons and $\eta = -1$ for fermions. Note that averages over thermal ensembles in the finite temperature formalism are not considered in this work, and therefore no reference to them is made in this section. An extension of the concepts presented here however is easily possible. A troublesome thing with expression eq. (2.28) is that it involves the unknown ground-state $|\Psi_0\rangle$ of an interacting Hamiltonian $\hat{\mathcal{H}}$. We assume that the ground-state at time $t \to -\infty$ is given by the solvable ground-state $|-\infty\rangle$ of $\hat{\mathcal{H}}_0$. Thus the interacting ground-state $|\Psi_0\rangle$ is given by time evolution

$$|\Psi_0\rangle = S(0,-\infty)\,|\Phi_0\rangle \;.$$

It is convenient to transform to the interaction representation with respect to $\hat{\mathcal{H}}_0$

$$\begin{aligned} |\Psi^{I,\hat{\mathcal{H}}_0}(t)\rangle &= S(t,-\infty)\,|\Psi^H\rangle = S(t,-\infty)\,|-\infty\rangle \\ O^{\hat{H}}(t) &= S(-\infty,t)\hat{O}^{I,\hat{\mathcal{H}}_0}(t)S(t,-\infty) \\ S(t_2,t_1) &= \hat{\hat{T}}\left(e^{-i\int_{t_1}^{t_2}\,dt'\,\hat{\mathcal{H}}_1(t')}\right) \,. \end{aligned}$$

This yields an expression for the time-ordered Green's function eq. (2.28) for $t_1 > t_2$

$$\mathrm{G}^T_{\hat{A}\hat{B}}(t_1,t_2) = -i\frac{\langle-\infty|\,S(-\infty,t_1)\hat{A}^{I,\hat{\mathcal{H}}_0}(t_1)S(t_1,-\infty)S(-\infty,t_2)\hat{B}^{I,\hat{\mathcal{H}}_0}(t_2)S(t_2,-\infty)\,|-\infty\rangle}{\langle-\infty|-\infty\rangle} \,.$$

Using $S(t_1,-\infty)S(-\infty,t_2) = S(t_1,t_2)$ and re-introducing the time-ordering which permits us to exchange operators at different times within it, one obtains

$$\mathrm{G}^T_{\hat{A}\hat{B}}(t_1,t_2) = -i\frac{\langle-\infty|\,S(-\infty,t_1)\hat{\hat{T}}\left(S(t_1,-\infty)\hat{A}^{I,\hat{\mathcal{H}}_0}(t_1)\hat{B}^{I,\hat{\mathcal{H}}_0}(t_2)\right)|-\infty\rangle}{\langle-\infty|-\infty\rangle} \,,$$

where $S(-\infty,t_1)$ can not be pulled inside $\hat{\hat{T}}$ since it is itself not time-ordered, remember $-\infty < t_2 < t_1 < \infty$ by construction. Expressing $\langle-\infty| = \langle\infty|\,S(+\infty,-\infty)$ and combining $S(\infty,-\infty)S(-\infty,t_1)S(t_1,-\infty) = S(\infty,-\infty)$ yields an operator which is time-ordered by itself and may be pulled inside the time-ordered

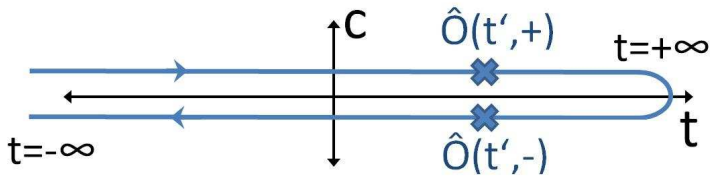

Figure 2.6.: The Keldysh contour (closed-time-contour) for systems without initial correlations. Operators are defined at a time t and on a branch c on the complex contour.

product at the cost of introducing the state in the distant future $|+\infty\rangle$

$$G^T_{\hat{A}\hat{B}}(t_1,t_2) = -i\frac{\langle+\infty|\hat{\hat{T}}\left(S(+\infty,-\infty)\hat{A}^{I,\hat{\mathcal{H}}_1}(t_1)\hat{B}^{I,\hat{\mathcal{H}}_1}(t_2)\right)|-\infty\rangle}{\langle+\infty|S(+\infty,-\infty)|-\infty\rangle}\,. \tag{2.31}$$

The way the time-dependent part of the Hamiltonian $\hat{\mathcal{H}}_1(t)$ was introduced it is adiabatically switched on and off again. We therefore assume that the system finds its way back to the ground-state of $\hat{\mathcal{H}}_0$ at times $t \to +\infty$ and we have $|+\infty\rangle = e^{i\phi}|-\infty\rangle$. This relation is made rigorous in the Gell-Mann and Low theorem [87], which is satisfied in this case ($\hat{\mathcal{H}}(t\to+\infty) = \hat{\mathcal{H}}(t\to-\infty) = \hat{\mathcal{H}}_0$, plus adiabatic time-dependence in-between). Therefore one ends up with

$$G^T_{\hat{A}\hat{B}}(t_1,t_2) = -i\frac{\langle-\infty|\hat{\hat{T}}\left(S(+\infty,-\infty)\hat{A}^{I,\hat{\mathcal{H}}_1}(t_1)\hat{B}^{I,\hat{\mathcal{H}}_1}(t_2)\right)|-\infty\rangle}{\langle-\infty|S(+\infty,-\infty)|-\infty\rangle}\,, \tag{2.32}$$

which serves as a starting point for perturbation theory.
At this point the non-equilibrium case starts to deviate. In the non-equilibrium situation it is not reasonable that by adiabatically switching off the interaction, the system will return to its non-interacting ground-state. This means $|+\infty\rangle = e^{i\phi}|-\infty\rangle$ does not hold any longer and we are left without knowledge of the final state. This forces us to take the unknown $|+\infty\rangle$ out of eq. (2.31) to obtain

$$G^T_{\hat{A}\hat{B}}(t_1,t_2) = -i\frac{\langle-\infty|S(-\infty,+\infty)\hat{\hat{T}}\left(S(+\infty,-\infty)\hat{A}^{I,\hat{\mathcal{H}}_1}(t_1)\hat{B}^{I,\hat{\mathcal{H}}_1}(t_2)\right)|-\infty\rangle}{\langle-\infty|S(-\infty,+\infty)S(+\infty,-\infty)|-\infty\rangle}\,,$$

where again $S(-\infty,+\infty)$ can not be pulled inside the time-ordering. The 'trick' here is to introduce the so-called closed-path or Keldysh- contour (see fig. 2.6) and define each object not only at a certain time t but also on a certain branch of the contour $c = \{+,-\}$. Note that this contour is valid for systems without initial correlations, where t_0 may be taken to $-\infty$. Extending the time-ordering operator $\hat{\hat{T}}$ eq. (2.30) to the contour-ordering operator $\hat{\hat{T}}_c$

$$\hat{\hat{T}}_c\left(\hat{A}(t,c)\hat{B}(t',c')\right) = \begin{cases}\hat{A}(t,c)\hat{B}(t',c') & \text{if } \{t,c\} > \{t',c'\}\\ \hat{B}(t',c')\hat{A}(t,c) & \text{if } \{t',c'\} > t,c\}\end{cases}\,,$$

which orders operators along the contour, it is possible again to pull everything inside the ordering

$$G^{T_c}_{\hat{A}\hat{B}}(t_1,c_1;t_2,c_2) = -i\frac{\langle-\infty|\hat{\hat{T}}_c\left(S(-\infty,-;+\infty)S(+\infty;-\infty,+)\hat{A}^{I,\hat{\mathcal{H}}_1}(t_1,+)\hat{B}^{I,\hat{\mathcal{H}}_1}(t_2,+)\right)|-\infty\rangle}{\langle-\infty|S(-\infty,-;+\infty)S(+\infty;-\infty,+)|-\infty\rangle}\,, \tag{2.33}$$

This means one lets the system evolve in the forward time direction from $-|\infty\rangle$ to $|+\infty\rangle$ and then back from $|+\infty\rangle$ to $|-\infty\rangle$ in the backwards time direction. Thereby all interactions are unwind. This essentially comes along with a doubling of degrees of freedom since every operator acting at time t now acts at time t on contour c. Eq. (2.33) defines the four-component single-particle Green's function in Keldysh space

$$\mathrm{G}^{++}(t_1,t_2) = \mathrm{G}^{T_c}_{cc^\dagger}(t_1,+;t_2,+) = \mathrm{G}^{T}(t_1,t_2) = -i < \hat{\hat{T}}\left(c(t_1)c^\dagger(t_2)\right) > \quad \text{time-ordered Green's function,}$$

$$\mathrm{G}^{+-}(t_1,t_2) = \mathrm{G}^{T_c}_{cc^\dagger}(t_1,+;t_2,-) = \mathrm{G}^{<}(t_1,t_2) = -\eta\, i < c^\dagger(t_1)c(t_2) > \quad \text{lesser Green's function,} \tag{2.34}$$

$$\mathrm{G}^{-+}(t_1,t_2) = \mathrm{G}^{T_c}_{cc^\dagger}(t_1,-;t_2,+) = \mathrm{G}^{>}(t_1,t_2) = -i < c(t_1)c^\dagger(t_2) > \quad \text{greater Green's function,} \tag{2.35}$$

$$\mathrm{G}^{--}(t_1,t_2) = \mathrm{G}^{T_c}_{cc^\dagger}(t_1,-;t_2,-) = \mathrm{G}^{\bar{T}}(t_1,t_2) = -i < \hat{\hat{\bar{T}}}\left(c(t_1)c^\dagger(t_2)\right) > \quad \text{anti-time-ordered Green's function .}$$

These four Green's functions are not linearly independent, since

$$\mathrm{G}^{T} + \mathrm{G}^{\bar{T}} = \mathrm{G}^{>} + \mathrm{G}^{<} = \mathrm{G}^{K} .$$

This allows performing a rotation in Keldysh-space

$$\begin{pmatrix} \mathrm{G}^{T} & \mathrm{G}^{<} \\ \mathrm{G}^{>} & \mathrm{G}^{\bar{T}} \end{pmatrix} \mapsto \begin{pmatrix} \mathrm{G}^{R} & \mathrm{G}^{K} \\ 0 & \mathrm{G}^{A} \end{pmatrix} = \widetilde{\mathrm{G}} , \tag{2.36}$$

where the rotated form is denoted $\widetilde{\mathrm{G}}$ and will be used in this work. The individual Green's functions contained in $\widetilde{\mathrm{G}}$ are

$$\begin{aligned}
\mathrm{G}^{R}_{cc^\dagger}(t_1,t_2) &= \frac{1}{2}\left(\mathrm{G}^{T} - \mathrm{G}^{\bar{T}} - \mathrm{G}^{<} - \mathrm{G}^{>}\right) = \theta(t_1-t_2)\left(\mathrm{G}^{>} - \mathrm{G}^{<}\right) \quad \text{retarded Green's function,} \\
\mathrm{G}^{A}_{cc^\dagger}(t_1,t_2) &= \frac{1}{2}\left(\mathrm{G}^{T} - \mathrm{G}^{\bar{T}} + \mathrm{G}^{<} - \mathrm{G}^{>}\right) = \theta(t_2-t_1)\left(\mathrm{G}^{<} - \mathrm{G}^{>}\right) \quad \text{advanced function,} \\
\mathrm{G}^{K}_{cc^\dagger}(t_1,t_2) &= \frac{1}{2}\left(\mathrm{G}^{T} + \mathrm{G}^{\bar{T}} + \mathrm{G}^{<} + \mathrm{G}^{>}\right) = \mathrm{G}^{<} + \mathrm{G}^{>} \quad \text{Keldysh Green's function .}
\end{aligned} \tag{2.37}$$

Since the greater- and the lesser- Green's function $\mathrm{G}^{>}$/ $\mathrm{G}^{<}$ are by definition anti-hermitian (see eq. (2.35) and eq. (2.34)), two handy relations follow

$$\begin{aligned}
\mathrm{G}^{A} &= (\mathrm{G}^{R})^\dagger \\
\mathrm{G}^{K} &= -(\mathrm{G}^{K})^\dagger .
\end{aligned} \tag{2.38}$$

In the next section the marriage of VCA with the concepts presented here will be described.

2.4.2. Non-equilibrium VCA$_{\mathrm{SC}}$

In non-equilibrium VCA [25] the single-particle Green's function is calculated in Keldysh-space $\widetilde{\mathrm{G}}$ eq. (2.36). This means that it is in general a matrix in Keldysh, site, spin, ... indices and a function of energy ω and wavevector $\mathbf{k}$. Since the original formulation of VCA based on the grand potential is not well defined in the non-equilibrium situation, here the alternative- self-consistent formulation presented in sec. 2.3.4 will be used.
One may rewrite eq. (2.27) in a more formal way in the non-equilibrium case

$$\int_{-\infty}^{\infty} \frac{d\omega}{2\pi} \mathrm{tr}\, \hat{\tau}_1 \frac{\partial\left(\widetilde{\mathrm{G}}_0'\right)^{-1}}{\partial \mathsf{x}'}\left(\widetilde{\mathrm{G}}' - \widetilde{\mathrm{G}}\right) = 0 ,$$

Where $\hat{\tau}_1$ is the first Pauli matrix in Keldysh space. Having the variational criterion and the foundations of Keldysh-Green's functions at hand it is straight forward to apply non-equilibrium VCA. Consider a system consisting of an interacting region and a non-interacting environment of infinite size. At time $t \to -\infty$ these two components are decoupled until at a certain time the coupling is switched on. We are interested in the long-time, steady-state behavior of the coupled system. As in the non-equilibrium case, the reference-systems (i.e. interacting cluster and non-interacting environment) have to be exactly solvable. The retarded Green's function is then calculated as in the equilibrium case, from which the advanced Green's function may be obtained by taking the hermitian-conjugate. The Keldysh part of the Green's function for fermions, before coupling to the environment is given by

$$\mathrm{G}^{\mathrm{K}}(\omega,\mu) = \left(\mathrm{G}^{\mathrm{R}}(\omega) - \mathrm{G}^{\mathrm{A}}(\omega)\right)\left(1 - 2p_{\mathrm{FD}}(\omega,\mu,\beta)\right) , \tag{2.39}$$

where $p_{\mathrm{FD}}(\omega,\mu,\beta)$ is the Fermi-Dirac distribution eq. (D.1). The last part of this equation may be rewritten in the zero temperature case as $(1 - 2p_{\mathrm{FD}}(\omega,\mu,\beta)) = \mathrm{sign}(\omega-\mu)$. Note that this is the only quantity in which the chemical potential μ enters. This procedure will be illustrated by the particular example of a quantum dot in ch. 5. It is interesting to mention here, that the authors of ref. [75] found that

the short-time dynamics of a non-equilibrium system are remarkably well captured within CPT. However the long-time behavior cannot be expected to come out reasonable within CPT, since the system does not know that it is subjected to a non-equilibrium situation. The self-consistency within $\mathrm{VCA_{SC}}$ introduces this crucial and necessary feedback. In the following the calculation of several important quantities like single-particle expectation values, the steady-state current-density and the effective-distribution function shall be outlined.

Static single-particle expectation values

In this paragraph an expression for single-particle expectation values is presented to be used in the self-consistency condition sec. 2.3.4. The expectation value is expressed in terms of the Keldysh Green's function as follows

$$\begin{aligned}
< c_i^\dagger c_j > &= \frac{1}{2}\left(< c_i^\dagger c_j > + < c_i^\dagger c_j > \right) \\
&= \frac{1}{2} < c_i^\dagger c_j - c_j c_i^\dagger + \delta_{ij} > \\
&= \frac{\delta_{ij}}{2} - \frac{i}{2}\left(i < c_i^\dagger c_j > -i < c_j c_i^\dagger > \right) \\
&= \frac{\delta_{ij}}{2} - \frac{i}{2}\left(\mathrm{G}^<_{ji} + \mathrm{G}^>_{ji} \right) \\
&= \frac{\delta_{ij}}{2} - \frac{i}{2}\mathrm{G}^K_{ji}(t,t) \\
&= \frac{\delta_{ij}}{2} + \frac{1}{2}\int_{-\infty}^{\infty} \frac{d\omega}{2\pi}\, \Im\mathrm{m}\mathrm{G}^K_{ij}(\omega)\,.
\end{aligned}$$

Here the correlator was first symmetrized and re-expressed in terms of lesser- and greater- Green's function (eq. (2.34) and eq. (2.35)) in line four. Then those were combined to yield the equal-time Keldysh Green's function eq. (2.37) in line five. Finally an equal-time Fourier-transformation was applied to express the Keldysh Green's function in the energy domain. Note that upon numerically evaluating this integral a convergence study in 0^+ is absolutely necessary. Too small values of 0^+ will yield zero for the correlator while too large values will yield arbitrarily wrong numbers. The problem is that G^K does not possess the analytic properties of a Green's function (like G^R) and behaves rather like a spectral function. Therefore rewriting this integral as a complex contour integral as in app. D is not possible.
Next an expression for the steady-state current density will be presented.

Steady-state current density

Here a representation for the steady-state current density in terms of Keldysh-Green's functions in site space is given. For a detailed derivation see ref. [81] or ref. [76]. We consider a general Hubbard-like interacting model system. The Hamiltonian is given by

$$\hat{\mathcal{H}} = \sum_i \epsilon_i \hat{n}_i + \sum_i U_i \hat{n}_i^\uparrow \hat{n}_i^\downarrow - \sum_{<ij>\setminus\{l,r\}} t_{ij} c_i^\dagger c_j - t_{lr}\left(c_l^\dagger c_r + c_r^\dagger c_l \right)\,,$$

where l and r are the two sites between which we intend to measure the current. The notation of other quantum numbers is suppressed here. The current-density from site l to site r is given by the time evolution of the expectation value of the total particle-number to the left of site l

$$\begin{aligned}
j &= -e < \dot{\hat{N}}_L(t) > \\
&= - < i\,[\hat{\mathcal{H}}, \sum_{i\le l} \hat{n}_i] > \\
&= -i \sum_{i\le l} \sum_m < \left[t_{m+1m}\, c_{m+1}^\dagger c_m + t_{mm+1}\, c_m^\dagger c_{m+1}, \hat{n}_i \right] > \\
&= -i \sum_{i\le l} < t_{i-1i}\, c_i^\dagger c_{i-1} - t_{ii+1}\, c_{i+1}^\dagger c_i + t_{ii+1}\, c_i^\dagger c_{i+1} - t_{i-1i}\, c_{i-1}^\dagger c_i > \\
&= -i\left(\sum_{i=1}^{l} t_{ii+1} < c_i^\dagger c_{i+1} - c_{i+1}^\dagger c_i > - \sum_{i=1}^{l-1} t_{ii+1} < c_i^\dagger c_{i+1} - c_{i+1}^\dagger c_i > \right)\,,
\end{aligned} \tag{2.40}$$

where in the first line the occurrence of the electronic charge e was indicated, which is then set to one in the spirit of this document. Note that also the explicit dependence on time t, indicated in the first line

is dropped in favor of a convenient notation. It is important to keep in mind that all operators c and $c^\dagger$ act at the same time t here. The last line may be obtained since $\hat{n}_l$ commutes with the rest of the Hamiltonian and we are interested in the current to the right! This can be seen from the commutators

$$\begin{aligned}
[\hat{n}_i, c_j^\dagger] &= c_i^\dagger c_i c_j^\dagger - c_j^\dagger c_i^\dagger c_i = c_i^\dagger c_i c_j^\dagger + c_i^\dagger c_j^\dagger c_i \\
&= c_i^\dagger c_i c_j^\dagger + c_i^\dagger \left(\delta_{ij} - c_i c_j^\dagger\right) = c_i^\dagger \delta_{ij} \qquad (2.41) \\
[\hat{n}_i, c_j] &= c_i^\dagger c_i c_j - c_j c_i^\dagger c_i = c_i^\dagger c_i c_j - \left(\delta_{ij} - c_i^\dagger c_j\right) c_i \\
&= c_i^\dagger c_i c_j - \delta_{ij} c_i - c_i^\dagger c_i c_j = -c_i \delta_{ij} \qquad (2.42) \\
[\hat{n}_i, \hat{n}_j] &= [\hat{n}_i, c_j^\dagger] c_j + c_j^\dagger [\hat{n}_i, c_j] = c_i^\dagger \delta_{ij} c_j - c_j^\dagger c_i \delta_{ij} = 0 \,, \qquad (2.43)
\end{aligned}$$

which follow from the elementary fermionic commutators

$$\{c_i, c_j^\dagger\} = \delta_{ij} \;, \quad \{c_i, c_j\} \;, \; = 0 \quad \{c_i^\dagger, c_j^\dagger\} = 0 \,, \qquad (2.44)$$

and the relations

$$[\hat{a}, \hat{b}\hat{c}] = [\hat{a}, \hat{b}]\hat{c} + \hat{b}[\hat{a}, \hat{c}] = \{\hat{a}, \hat{b}\}\hat{c} - \hat{b}\{\hat{a}, \hat{c}\} \,. \qquad (2.45)$$

Here $[\hat{a}, \hat{b}] = \hat{a}\hat{b} - \hat{b}\hat{a}$ denotes the commutator and $\{\hat{a}, \hat{b}\} = \hat{a}\hat{b} + \hat{b}\hat{a}$ the anti-commutator. Proceeding with the evaluation of the sums left in eq. (2.40) (, which partially cancel,) we end up with an expression for the current

$$\begin{aligned}
j &= -i\, t_{lr} < c_l^\dagger c_r - c_r^\dagger c_l > \\
&= -i\, \frac{t_{lr}}{2} < c_l^\dagger c_r - c_r c_l^\dagger + \delta_{lr} - c_r^\dagger c_l + c_l c_r^\dagger - \delta_{rl} > \\
&= -\frac{t_{lr}}{2} \left(i < c_l^\dagger c_r > -i < c_r c_l^\dagger > -i < c_r^\dagger c_l > +i < c_l c_r^\dagger >\right) \\
&= -\frac{t_{lr}}{2} \left(\mathrm{G}^<_{rl} + \mathrm{G}^>_{rl} - \mathrm{G}^<_{lr} - \mathrm{G}^>_{lr}\right) \\
&= -\frac{t_{lr}}{2} \left(\mathrm{G}^K_{rl} - \mathrm{G}^K_{lr}\right) \\
&= -\frac{t_{lr}}{2} \left(\mathfrak{Re}\mathrm{G}^K_{rl} + i\mathfrak{Im}\mathrm{G}^K_{rl} - \mathfrak{Re}\mathrm{G}^K_{lr} - i\mathfrak{Im}\mathrm{G}^K_{lr}\right) \\
&= -\frac{t_{lr}}{2} \left(-\mathfrak{Re}\mathrm{G}^K_{lr} + i\mathfrak{Im}\mathrm{G}^K_{lr} - \mathfrak{Re}\mathrm{G}^K_{lr} - i\mathfrak{Im}\mathrm{G}^K_{lr}\right) \\
&= t_{lr} \mathfrak{Re}\mathrm{G}^K_{lr}(t,t) \\
&= t_{lr} \sum_\sigma \int_{-\infty}^{\infty} \frac{d\omega}{2\pi}\, \mathfrak{Re}\mathrm{G}^{K\sigma}_{lr}(\omega) \,. \qquad (2.46)
\end{aligned}$$

Here the operators were symmetrized in the second line to obtain an expression for the current in terms of the Keldysh Green's function instead of lesser Green's functions. In the third line the definition of the lesser- and greater- Green's functions (eq. (2.34) and eq. (2.35)), and in the fourth line the definition of the Keldysh Green's function eq. (2.37) were used. In the sixth line eq. (2.38) was used to exchange the r, l labels of the Keldysh Green's function. From the second-last to the last line a Fourier transformation of the equal-time Keldysh Green's function to energy space was done. In the last line the trace over spin components was added, which has to be executed to calculate the total current of all spin flavors. In VCA eq. (2.46) may be evaluated because G^K_{lr} can be directly obtained. One may also use the symmetrized form

$$j_{ij} = \frac{t_{ij}}{2} \sum_\sigma \int_{-\infty}^{+\infty} \frac{d\omega}{2\pi} \mathfrak{Re}\left(\mathrm{G}^{K\sigma}_{ij}(w) - \mathrm{G}^{K\sigma}_{ji}(w)\right) . \qquad (2.47)$$

The continuity equation is fulfilled for that relation, but numerical simulations show that it will be violated if the current is calculated with a finite numerical broadening 0^+. Therefore it is very important to set $0^+ \equiv 0$ when obtaining Green's functions for current calculations.
To round up the discussion about non-equilibrium properties, the effective distribution function is defined in the next paragraph.

Effective distribution function

In equilibrium the Keldysh component of the Green's function is given by eq. (2.39). One may define an effective distribution function in non-equilibrium

$$p_{\text{eff}}(\omega,\mu) = \frac{1}{2} - \frac{\mathrm{G}^K(\omega,\mu)}{2\left(\mathrm{G}^R(\omega) - \mathrm{G}^A(\omega)\right)} \,. \tag{2.48}$$

Note that $\mathrm{G}^{R,A,K}$ are still matrices in site, spin, ... space and the above relation is not well defined. In general the effective distribution function can not be expected to be the same for each element after the coupling to the environment has been switched on. In this work three particular definitions are explored

$$\begin{aligned}
p^{(1)}_{\text{eff}}(\omega,\mu) &= \frac{1}{2} - \frac{\mathrm{G}^K_{ff}(\omega,\mu)}{2\left(\mathrm{G}^R_{ff}(\omega) - \mathrm{G}^A_{ff}(\omega)\right)} \\
p^{(2)}_{\text{eff}}(\omega,\mu) &= \frac{1}{2} - \frac{\mathrm{tr}\left(\mathrm{G}^K_{ij}(\omega,\mu)\right)}{2\mathrm{tr}\left(\mathrm{G}^R_{ij}(\omega) - \mathrm{G}^A_{ij}(\omega)\right)} \\
p^{(3)}_{\text{eff}}(\omega,\mu) &= \frac{1}{2} - \frac{\sum\limits_{ij}\left(\mathrm{G}^K_{ij}(\omega,\mu)\right)}{2\sum\limits_{ij}\left(\mathrm{G}^R_{ij}(\omega) - \mathrm{G}^A_{ij}(\omega)\right)} \,.
\end{aligned}$$

The first option is taking a particular site (i.e. the correlated site when dealing with quantum-dot systems), the second option may be to trace over the Green's function matrices in site/spin space and a third to average over all matrix elements. They all show qualitatively the same picture, although the first version gives the best result. Remarkably the imaginary part of the effective distribution function stays almost zero as it should be, but can not be expected from the definition. Results for the effective distribution function are obtained in sec. 4.2.
This concludes the chapter on the methods used throughout this thesis. In the next chapter, results obtained for the SIAM will be presented.

3. The single impurity Anderson model in equilibrium

The single impurity Anderson model (SIAM) is one of the most widely studied models in condensed matter physics. It was introduced to describe the effects of magnetic transition metal impurities immersed in metallic hosts [2, 88]. Originally it was derived to capture remarkable physical properties like the resistance minimum [5, 3] at a specific temperature scale T_K [89] or the anomalous magnetic susceptibility and specific heat of such materials. Quantum impurity models have further been applied to understand the adsorption of atoms onto surfaces [90, 91, 92]. In addition, they are of theoretical interest as solvable models of quantum field theories [6, 93]. A renewed interest in understanding and calculating dynamic quantities of these models was created with the advent of dynamical mean-field theory (DMFT) [15, 12, 13]. In the foundations of this theory quantum impurity models have to be solved as an auxiliary problem. The behavior of various magnetic phenomena and the remarkable branch of heavy fermion physics is described by strongly correlated quantum impurity models [94, 95], like the periodic Anderson impurity model.
As one can imagine, because of the enormously large area of application, a wide range of methods and approximations have been suggested for the solution of the SIAM. They however prove to be a very delicate subject because standard perturbative approaches diverge [89]. Prominent techniques include a self consistent perturbative expansion [96] and Bethe Ansatz techniques [97] for one dimensional problems. The low energy physics are very well described by numerical renormalization group (NRG) [98], functional renormalization group (FRG) [99, 100, 101] and density matrix renormalization group (DMRG) [102, 103, 104]. There is a range of slave particle methods [105, 106] available as well as methods based on Hubbard's X-operator technique [37, 107] and calculations using variational wavefunctions [90]. Valuable physical insight has been gained by using equation of motion techniques applying different approximation schemes [81]. Quantum Monte Carlo (QMC) methods in general suffer from the sign problem for this class of models [19]. Early results were nevertheless achieved for example in ref. [108]. For moderate system sizes the Hirsch-Fye QMC [109] algorithm has proven to achieve good results. In the past years different approaches to continuous time QMC [19] have been applied very successfully to solve quantum impurity models especially in application with DMFT. In this context exact diagonalization methods have been used to solve small systems [110].
As of today some limits of quantum impurity models are understood with great precision but there appear several gaps to be bridged. The low energy properties of these models are reproduced very well by renormalization group based approaches. These approaches in general have trouble to capture the high energy parts of the spectrum. The same may be said about QMC methods which if applicable yield dynamic quantities in imaginary time. The analytic continuation to the real energy axis is ill conditioned. Spectra obtained by for example the maximum-entropy method [20, 21] have a large uncertainty for higher energies. Exact diagonalization methods, in principle, grant access to low as well as high energy parts of the spectrum at the same time. Due to the prohibitively large Hilbert space however only small systems (about ten to twenty sites) may be treated with this method, whose low-energy behavior is expected to deviate from the one of the infinite lattice. Nevertheless, the advantage consists in the fact that the spectral properties may be determined directly on the real energy axis. Besides the issue of the low energy scale, also the flexibility to adapt to various impurity configurations and geometries is limited in most methods.
Here, cluster perturbation theory (CPT) [22, 23] and the variational cluster approach (VCA) [24, 65, 66] are applied to the single impurity Anderson model. These cluster methods attempt at bridging the gap between diagrammatic approaches and exact diagonalization. In contrast to QMC based methods, dynamic quantities may be evaluated directly on the real energy axis. The computational cost of performing a CPT/VCA calculation is moderate, i.e. of the order of standard exact diagonalization. We will show that these methods reproduce important features of the low energy part as well as of the high energy part of the spectrum. The great flexibility and versatility of the method allows for treatment of all sorts of impurity configurations in any dimension. The CPT/VCA results for the SIAM presented in this chapter have already been published by us in a slightly less exhaustive manner in ref. [16].
We start out by defining the SIAM.

3.1. The single impurity Anderson model

In real space the SIAM is defined by the model Hamiltonian

$$\hat{\mathcal{H}}_{\mathrm{SIAM}} = \hat{\mathcal{H}}_{\mathrm{conduction}} + \hat{\mathcal{H}}_{\mathrm{impurity}} + \hat{\mathcal{H}}_{\mathrm{hybridization}} \,. \tag{3.1}$$

A tight binding band of non-interacting electrons with nearest neighbor hopping $\langle i, j\rangle$ is described by

$$\hat{\mathcal{H}}^{L}_{\mathrm{conduction}} = \epsilon_s \sum_{i}^{L} \sum_{\sigma} c^{\dagger}_{i\sigma}\, c_{i\sigma} - t \sum_{\langle i,j\rangle\,\sigma} c^{\dagger}_{i\sigma}\, c_{j\sigma} \,, \tag{3.2}$$

where ϵ_s is the on-site energy of the particles and t is the overlap integral between neighboring sites. The operators $c^{\dagger}_{i\sigma}$ and $c_{i\sigma}$, respectively, create and annihilate electrons on site i with spin σ. The parameter L is taken to be infinity and is introduced here for convenient notation in later chapters where this Hamiltonian will be decomposed in real space. The impurity Hamiltonian consists of a single site with local Coulomb repulsion U,

$$\hat{\mathcal{H}}_{\mathrm{impurity}} = \epsilon_f \sum_{\sigma} f^{\dagger}_{\sigma}\, f_{\sigma} + U\, \hat{n}^{f}_{\uparrow}\, \hat{n}^{f}_{\downarrow} \,, \tag{3.3}$$

with $f^{\dagger}_{\sigma}$ creating an electron with spin σ and on-site energy ϵ_f located at the impurity. The particle number operator is defined as $\hat{n}^{f}_{\sigma} = f^{\dagger}_{\sigma}\, f_{\sigma}$. Finally the coupling between the non-interacting bath orbitals and the impurity is given by

$$\hat{\mathcal{H}}_{\mathrm{hybridization}} = -V \sum_{\sigma} \left(c^{\dagger}_{I\sigma}\, f_{\sigma} + f^{\dagger}_{\sigma}\, c_{I\sigma} \right) \,, \tag{3.4}$$

where V is the hybridization matrix element between the free electronic site $I \in [1, L]$ and the impurity (see fig. 3.2 for illustration).
The Anderson width Δ is defined as

$$\Delta \equiv \pi\, V^2\, \rho_s(\epsilon_F = 0) = \frac{V^2}{t} \,, \tag{3.5}$$

where, for simplicity, we have taken Δ at the center of the bath density of states. The local density of states of the conduction electrons $\rho_s(0)$ is given for the model defined in eq. (3.2) by $\rho_s(0) = \frac{1}{\pi\, t}$ (see eq. (3.23)). In the forthcoming discussion we refer to the particle-hole symmetric case when we set $\epsilon_f = -\frac{U}{2}$.
A first impression of the behavior of this model may be obtained by considering the conduction electrons and the impurity in isolation ($V = 0$). This atomic limit then consists of an s-electron Fermi sea with Fermi energy ϵ_F and a single state of the f-electrons. For $\epsilon_f < \epsilon_f + U$ and $\epsilon_f < \epsilon_F$, the impurity is doubly occupied and for $\epsilon_F < \epsilon_f + U$ and $\epsilon_F < \epsilon_f$, the impurity is unoccupied. The interesting local moment region arises in a parameter regime where the impurity is singly occupied.
In discussing the physics of an impurity one often resorts to an effective Hamiltonian which focuses on the essential spin fluctuations (the Kondo Hamiltonian) and then applies renormalization group ideas to harvest its physics. A discussion of those important ideas is beyond the scope of this work and may be found for example in ref. [111, 89].
The detailed discussion of this model will be started by a mean field analysis in sec. 3.2, to get a first impression of the physics of this model. Then the two-site problem, the Anderson molecule, will be presented in sec. 3.3.3. It provides different kinds of insights into the behavior of the SIAM. The basic results of this calculation will be carried over to be used as a cluster perturbation theory (CPT) / variational cluster approach (VCA) reference system in a semi-analytical way. Finally we will turn to the discussion of the CPT/VCA results.

3.2. Mean field analysis of the Single Impurity Anderson Model

It is instructive to attempt a mean field analysis of the SIAM. This analysis was first undertaken by Anderson [2]. The calculation, ornated with some helpful explanations and figures, is also available in the overview article by Coleman [112].
To proceed analytically with the SIAM, a Hartree-type mean field decoupling is undertaken. Note that in Hubbard-type models, with local interactions only, the exchange part is always zero. The four fermion

part of the Hamiltonian eq. (3.1) is split by the prescription

$$\begin{aligned}\left(\Delta\hat{n}^f_\sigma\right)\left(\Delta\hat{n}^f_{-\sigma}\right) &= \left(\hat{n}^f_\sigma - < n^f_\sigma >\right)\left(\hat{n}^f_{-\sigma} - < n_{f,-\sigma} >\right) \\ &= \hat{n}^f_\sigma\hat{n}^f_{-\sigma} - \hat{n}^f_\sigma < n^f_{-\sigma} > - \hat{n}^f_{-\sigma} < n_{f,\sigma} > + < n^f_\sigma >< n^f_{-\sigma} > \\ &\stackrel{!}{=} 0 \,.\end{aligned}$$

Introducing the order parameters $\phi_\sigma :=< n^f_\sigma >$ the interaction part of $\hat{\mathcal{H}}_{\text{impurity}}$ may be recast in a quadratic form

$$\hat{\mathcal{H}}^{MF}_{\text{impurity}} = \epsilon_f \sum_\sigma f^\dagger_\sigma f_\sigma + U\left(\hat{n}^f_\sigma\phi_{-\sigma} + \hat{n}^f_{-\sigma}\phi_\sigma - \phi_\sigma\phi_{-\sigma}\right) \,.$$

In a higher order equation of motion treatment of this model, it may be seen explicitly that this type of mean field treatment neglects fluctuations in the f occupancy altogether. As we will see later this is a terrible approximation for this model, since the main physics at low temperatures comes exactly from these fluctuations.
The structure of the following calculation is as follows. At first the bare f-electron propagator $g^\sigma_{ff}(\omega)$ will be determined by the equation of motion technique and so will the s-electron propagator $g^\sigma_{ss}(\omega)$. The self-energies arising due to the hybridization $\Sigma_{\text{hybridization}}$ and the Coulomb interaction Σ_{U} are determined. Note that $\Sigma_{\text{hybridization}}$, strictly speaking, is not a true self-energy because it arises from one-particle terms. These four ingredients will be put together, using Dyson's equation, to generate the mean field result for the f-electron propagator.
The bare f-electron Green's function is given by

$$\begin{aligned}\omega\, g^\sigma_{ff}(\omega) = \omega << f_\sigma; f^\dagger_\sigma >>_\omega &=< \{f_\sigma, f^\dagger_\sigma\} > + << [f_\sigma, \hat{\mathcal{H}}f]; f^\dagger_\sigma >>_\omega \\ &= 1 + << [f_\sigma, \epsilon_f \sum_\sigma f^\dagger_\sigma f_\sigma]; f^\dagger_\sigma >>_\omega \\ &= 1 + \epsilon_f << [f_\sigma, \hat{n}^f_\sigma]; f^\dagger_\sigma >>_\omega \\ &= 1 + \epsilon_f << f_\sigma; f^\dagger_\sigma >>_\omega \\ g_{ff}(\omega) &= \frac{1}{\omega - \epsilon_f} \,. \end{aligned} \tag{3.6}$$

In the third line relation eq. (2.42) was applied. A similar calculation yields the bare s-electron Green's function

$$g_{ss}(\omega) = \frac{1}{\omega - \epsilon_{\mathbf{k}}} \,. \tag{3.7}$$

The Coulomb self-energy Σ_{U} is given by

$$\Sigma^\sigma_{\text{U}} = U\phi_{-\sigma} \,. \tag{3.8}$$

The hybridization self-energy $\Sigma_{\text{hybridization}}$ is given by

$$\begin{aligned}\Sigma_{\text{hybridization}} &= \sum_{\mathbf{k}} \frac{|V_{\mathbf{k}}|^2}{\omega - \epsilon_{\mathbf{k}}} \\ &= \int_{-\infty}^{\infty} \frac{d\epsilon}{\pi} \frac{\pi \sum_{\mathbf{k}} |V_{\mathbf{k}}|^2 \delta(\epsilon - \epsilon_{\mathbf{k}})}{\omega - \epsilon} \,.\end{aligned}$$

Assuming that V is local in real space, it is a constant in $\mathbf{k}$ space and can be taken out of the sum. Usually this expression is further simplified by approximating the conduction electron density of states

$\sum_{\mathbf{k}} \delta(\epsilon - \epsilon_{\mathbf{k}})$ by its value at the Fermi energy. Then the approximate self-energy reads

$$\begin{aligned}
\Sigma_{\text{hybridization}}(\omega + i0^+) &\approx \int_{-D}^{D} \frac{d\epsilon}{\pi} \frac{|V|^2 \pi \rho(\epsilon)}{\omega + i0^+ - \epsilon} \\
&= \frac{\Delta}{\pi} \int_{-D}^{D} d\epsilon \frac{1}{\omega + i0^+ - \epsilon} \\
&= \frac{\Delta}{\pi} \left(i\pi\delta(\omega - \epsilon)\,\text{sign}\,(0^+) + \mathfrak{Re} \mathcal{P} \int_{-D}^{D} d\epsilon \frac{1}{\omega - \epsilon} \right) \\
&= \frac{\Delta}{\pi} \left(i\pi + \mathfrak{Re} \ln\left(\frac{\omega + D}{\omega - D} \right) \right) \\
&\approx \frac{\Delta}{\pi} \left(i\pi + 2\frac{\omega}{D} + \mathrm{O}\left(\frac{\omega}{D} \right)^3 \right) .
\end{aligned} \tag{3.9}$$

D denotes the half bandwidth $2t$. For the evaluation of the integral in the third line in the sense of a distribution the well known result of Sokhozky-Plemelj was used. In the last line the logarithm was expanded for small $\frac{\omega}{D}$. The final approximate expression for the self-energy valid at low energies/wide-bands therefore is

$$\Sigma_{\text{hybridization}}(\omega + i0^+) \approx \frac{\Delta}{\pi t}\omega + i\Delta \approx i\Delta\,. \tag{3.10}$$

The real part is small and may be ignored or put into a small renormalization of ϵ_f. Approximation eq. (3.10) is good in the Kondo regime, where the spectrum is peaked at the Fermi energy only. This approximation breaks down, when the interaction strength exceeds a critical value U_c and the spectrum splits into two peaks. Having all necessary quantities at hand we proceed by finding an expression for the full Green's function $G^\sigma_{ff}(\omega)$ of the f-electrons. Using Dyson's equation, Einstein's convention for summation, and auxiliary indices i and j which run over s and f each, we find

$$\begin{aligned}
G^\sigma_{ff}(\omega) &= g_{ff}(\omega) + g_{fi}(\omega) T_{ij}(\omega) G_{jf}(\omega) \\
&= g_{ff}(\omega) + g_{fs}(\omega) T_{ss}(\omega) G_{sf}(\omega) \\
&\quad + g_{fs}(\omega) T_{sf}(\omega) G_{ff}(\omega) \\
&\quad + g_{ff}(\omega) T_{fs}(\omega) G_{sf}(\omega) \\
&\quad + g_{ff}(\omega) T_{ff}(\omega) G_{ff}(\omega)\,.
\end{aligned}$$

The off-diagonal free Green's functions $g_{fs}(\omega)$ are zero as well as the element $T_{ss}(\omega)$. So we have

$$G^\sigma_{ff}(\omega) = g_{ff}(\omega) + g_{ff}(\omega) T_{fs}(\omega) G_{sf}(\omega) + g_{ff}(\omega) T_{ff}(\omega) G_{ff}(\omega)\,. \tag{3.11}$$

To proceed we need the off diagonal Green's function $G_{sf}(\omega)$ which is obtained in an analogous way

$$\begin{aligned}
G^\sigma_{sf}(\omega) &= g_{sf}(\omega) + g_{si}(\omega) T_{ij}(\omega) G_{jf}(\omega) \\
&= g_{ss}(\omega) T_{sf}(\omega) G_{ff}(\omega)\,.
\end{aligned} \tag{3.12}$$

Inserting eq. (3.12) into eq. (3.14) we obtain the full f Green's function

$$\begin{aligned}
G^\sigma_{ff}(\omega) &= g_{ff}(\omega) + g_{ff}(\omega) T_{fs}(\omega) g_{ss}(\omega) T_{sf}(\omega) G_{ff}(\omega) + g_{ff}(\omega) T_{ff}(\omega) G_{ff}(\omega) \\
&= \left(1 - g_{ff}(\omega) \underbrace{T_{fs}(\omega) g_{ss}(\omega) T_{sf}(\omega)}_{\Sigma_{\text{hybridization}}} - g_{ff}(\omega) \underbrace{T_{ff}(\omega)}_{\Sigma_{\text{U}}} \right)^{-1} g_{ff}(\omega)\,.
\end{aligned} \tag{3.13}$$

Inserting the expressions for the free Green's functions eq. (3.6) and eq. (3.7) and for the self-energies eq. (3.10) and eq. (3.8) into eq. (3.13) we can write

$$\begin{aligned}
G^\sigma_{ff}(\omega) &= \frac{1}{\omega - \epsilon_f - \Sigma_{\text{hybridization}} - \Sigma_{\text{U}}} \\
&= \frac{1}{\omega - (\epsilon_f + U\phi_{-\sigma}) + i\Delta}\,.
\end{aligned} \tag{3.14}$$

From the result eq. (3.14) one can now proceed and evaluate a quantity of interest, the density of states of the f-electrons

$$\begin{aligned}\rho_f^\sigma(\omega) &= -\frac{1}{\pi}\Im\mathrm{m}G_{ff}^{\sigma,\mathrm{ret}}(\omega)\\ &= -\frac{1}{\pi}\frac{\Delta}{\left(\omega-\left(\epsilon_f+U\phi_{-\sigma}\right)\right)^2+\left(\Delta\right)^2}\,.\end{aligned} \tag{3.15}$$

To determine the mean field parameters self consistently one may evaluate the f particle numbers per spin n_σ^f

$$\begin{aligned}n_\sigma^f &= \int_{-\infty}^{0} d\omega\rho_f^\sigma(\omega)\\ &= -\frac{\Delta}{\pi}\int_{-\infty}^{0} d\omega\frac{1}{\left(\omega-\left(\epsilon_f+U\phi_{-\sigma}\right)\right)^2+\left(\Delta\right)^2}\\ &= -\frac{1}{\pi}\int_{-\infty}^{-\frac{\left(\epsilon_f+U\phi_{-\sigma}\right)}{\Delta}} d\chi\frac{1}{\chi^2+1}\\ &= \frac{1}{\pi}\mathrm{arccot}\left(\frac{\epsilon_f+U\phi_{-\sigma}}{\Delta}\right)\,.\end{aligned} \tag{3.16}$$

It is convenient to introduce an occupancy $n^f =< \sum_\sigma n_\sigma^f >$ and a magnetization $M_f =< n_\uparrow^f - n_\downarrow^f >$. The mean field equations then become

$$n^f = \frac{1}{\pi}\sum_\sigma \mathrm{arccot}\left(\frac{\epsilon_f+\frac{U}{2}\left(n_f-\sigma M_f\right)}{\Delta}\right) \tag{3.17}$$

$$M_f = \frac{1}{\pi}\sum_\sigma \sigma\mathrm{arccot}\left(\frac{\epsilon_f+\frac{U}{2}\left(n_f-\sigma M_f\right)}{\Delta}\right) \tag{3.18}$$

The mean field equations eq. (3.18) enable us to calculate the density of states of the f-electrons eq. (3.14) explicitly. To do so the following iteration may be applied:

1. Guess starting order parameters $\phi_\uparrow^{(0)}$ and $\phi_\downarrow^{(0)}$.
2. Calculate the density of states $\rho_f^{\sigma,(i)}$ for each spin by using equation eq. (3.15).
3. Calculate the occupation number $n_f^{(i)}$ and the magnetization $M_f^{(i)}$ using equation eq. (3.18).
4. Check if the $n_f^{(i)} = n_f^{(i-1)}$ and $M_f^{(i)} = M_f^{(i-1)}$. If the occupation number and magnetization is not changing any more within a certain accuracy the iteration has converged. If not start again from 1) with new $\phi_\uparrow^{(i)} = \frac{1}{2}\left(n_f^{(i)}+M_f^{(i)}\right)$ and $\phi_\downarrow^{(i)} = \frac{1}{2}\left(n_f^{(i)}-M_f^{(i)}\right)$.

It should be mentioned that the mean field self-consistency converges in all parameter regions. The convergence is slowest in the vicinity of the critical interaction strength U_c. Starting order parameters of $< n_\downarrow^f >= 0.8$ and $< n_\uparrow^f >= 0.2$ as well as a mixing scheme for the order parameter

$$\Phi_i = (1-\chi)\Phi_{i-1} + \chi\Phi_i^{\mathrm{suggested}}\,,$$

where the mixing parameter χ was taken to be 0.75, to obtain convergence in all parameter regions, within ten to twenty iterations (see fig. 3.1 (mid left)).
One more quantity worth investigating is the critical interaction strength U_c for which a local moment will form. We set the magnetization to $M_f = 0^+$ in eq. (3.18) and replace the second equation with its derivative with respect to M_f.

$$\begin{aligned}n^f &= \frac{2}{\pi}\mathrm{arccot}\left(\frac{\epsilon_f+\frac{U_c}{2}n^f}{\Delta}\right)\\ 1 &= \frac{U_c}{\Delta\pi}\frac{1}{1+\left(\frac{\epsilon_f+\frac{U_c}{2}n^f}{\Delta}\right)^2}\end{aligned}$$

Rewriting the first of these equations

$$\frac{\epsilon_f + \frac{U_c}{2} n^f}{\Delta} = \cot\left(\frac{\pi n^f}{2}\right)$$

and inserting into the second yields

$$U_c = \pi\Delta\left(1 + \cot\left(\frac{\pi n^f}{2}\right)\right) \tag{3.19}$$

The impurity density of states $\rho_f^\sigma(\omega)$ for different interaction strengths U, in the particle-hole symmetric case, is examined in the mean field approximation. The density of states of the s-electrons was taken from a semi-infinite, one-dimensional, tight-binding chain eq. (3.23). The hybridization used was $\Delta = 0.1$. This resembles the setup used in the more sophisticated CPT/VCA treatment of the SIAM in later sections. The mean field spectrum undergoes an unphysical crossover to a magnetically polarized solution at $\frac{U_c}{\Delta} = \pi(1 + \cot(\frac{\pi}{2})) = \pi$ (see eq. (3.19)). This observed splitting into spin up and spin down components is unphysical and can be traced back to be a remnant of the mean field approximation. The spectra, indicating a phase-transition, caused by a zero-dimensional impurity are therefore unphysical. To make it explicit, the mean field treatment predicts a quantum phase transition, which is not there. Nevertheless a comparison of the, often applied, approximation for the hybridization self-energy $\Sigma_{\text{hybridization}}$ eq. (3.10) with the numerically exact expression of $\Sigma_{\text{hybridization}}$ eq. (3.9) was undertaken. In fig. 3.1 (bottom left) the impurity density of states is shown as it was obtained applying the approximation eq. (3.10), for various values of interaction strength U. In fig. 3.1 (bottom right) the same is shown for the numerically exact expression of $\Sigma_{\text{hybridization}}$ eq. (3.9). It may be observed that as long as the spectrum consists of a single peak at the Fermi energy ($U < U_c$), the results obtained with approximate $\Sigma_{\text{hybridization}}$ eq. (3.10) are identical to those obtained with the numerically exact expression of $\Sigma_{\text{hybridization}}$ eq. (3.9). As soon as the peaks split, the approximate self-energy starts to deviate. A comparison of the spectra obtained with the two different treatments of the hybridization self-energy is shown in fig. 3.1 (mid right). Note that the sum rule eq. (2.16) is fulfilled for all curves although the results obtained with the exact hybridization self-energy have a higher amplitude than those obtained within the approximation. The splitting (gap) of the spin up and spin down components as a function of interaction strength U is shown in fig. 3.1 (top left) for both ways of treating the hybridization self-energy. The order-parameters n^f, M^f, $< n_\downarrow^f >$ and $< n_\uparrow^f >$ are visualized in as a function of interaction strength U in fig. 3.1 (top right), using the approximate $\Sigma_{\text{hybridization}}$ as well as the exact $\Sigma_{\text{hybridization}}$. The result for a mean field crossover diagram is shown in sec. 3.3.10 together with the CPT/VCA result. These mean field results will be used in sec. 4.5 to get an idea of the non-equilibrium behavior of a quantum dot. Having a rough idea of the physics of the SIAM we proceed by a more sophisticated treatment of the SIAM in terms of CPT/VCA.

3.3. CPT/VCA for the single impurity Anderson model

To apply this approach to the SIAM we start by splitting the physical model under consideration into appropriate pieces (see fig. 3.2), which will serve as reference systems. Here we consider a reference system consisting of two parts. One part, consisting of a cluster of size L, which contains the interacting impurity site

$$\hat{\mathcal{H}}_{\text{cluster}} = \hat{\mathcal{H}}^{L-1}_{\text{conduction}} + \hat{\mathcal{H}}_{\text{impurity}} + \hat{\mathcal{H}}_{\text{hybridization}} \,, \tag{3.20}$$

and a second part, the environment, which contains the rest of the conduction band

$$\hat{\mathcal{H}}_{\text{environment}} = \hat{\mathcal{H}}^{\infty}_{\text{conduction}} \,. \tag{3.21}$$

The original Hamiltonian may now be rewritten as

$$\hat{\mathcal{H}}_{\text{SIAM}} = \hat{\mathcal{H}}_{\text{cluster}} + \hat{\mathcal{H}}_{\text{environment}} + \mathrm{T}_{\text{inter}} \,. \tag{3.22}$$

Here $\mathrm{T}_{\text{inter}}$ is the part of T describing the hopping from cluster to environment, which is the only term not included in the reference system. For the SIAM the two bare Green's functions $\mathrm{G}'_{\text{cluster}}$ and G'_{env} needed for eq. (2.2) may be evaluated separately. Because $\mathrm{G}'_{\text{cluster}}$ is representable by a discrete set of poles, the Q-matrix formalism (see sec. 2.2.2) is used. G'_{env} has a branch cut along the real axis and is not Q-matrix representable. Therefore, for the SIAM, the version of CPT as discussed in sec. 2.1.5 applies.

The cluster Green's function $\mathrm{G}'_{\text{cluster}}$ is determined by exact diagonalization of eq. (3.20). Open boundary

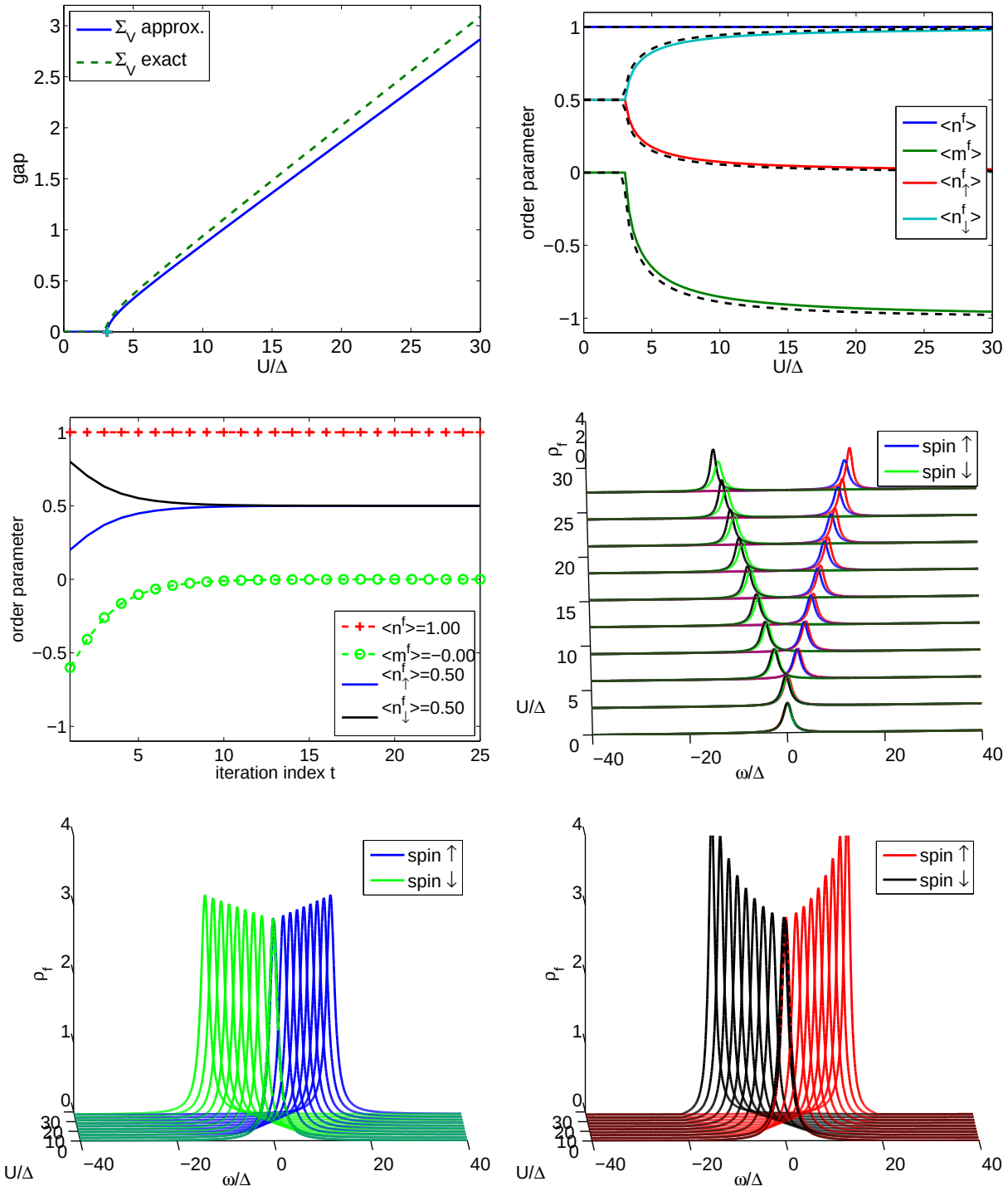

Figure 3.1.: Results obtained by the mean field treatment of the SIAM in the particle-hole symmetric case. The parameters used here were $V = 0.3162$, ϵ_s and $t = 1$. (Top Left) Unphysical splitting of the mean field spin up and spin down components in the density of states as a function of interaction strength U. The cross marks the analytical result for the transition eq. (3.19). (Top Right) Order parameters as a function of interaction strength U. The result for the approximate hybridization self-energy (Σ_V is short for $\Sigma_{\text{hybridization}}$) is plotted in color, while the result for the exact hybridization self-energy is indicated in dashed black. (Mid Left) The evolution of the order parameters of a single run using $\frac{U}{\Delta} = 2$. (Mid Right) Single-particle spectrum as a function of interaction strength U. A comparison for results obtained with the approximate and the exact hybridization self-energy is shown. Again the exact results are plotted in black. (Bottom Left) Single-particle spectrum as a function of interaction strength U obtained with the approximate hybridization self-energy. (Bottom Right) Single-particle spectrum as a function of interaction strength U obtained with the exact hybridization self-energy.

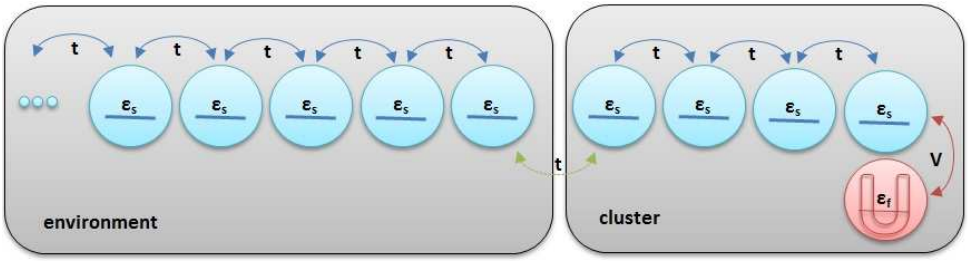

Figure 3.2.: Illustration of the single impurity Anderson model. The model consists of a chain of non-interacting sites with nearest neighbor hopping t and on-site energy ϵ_s. An impurity site may be added to one of the sites representing a second orbital with on-site energy ϵ_f and local Coulomb interaction U. This orbital hybridizes with the conduction electrons via a hybridization matrix element V. The infinite non-interacting chain is truncated at some site L yielding a cluster of variable size including the impurity site and a chain of non-interacting sites. These decomposed systems are in the end coupled via a hopping element t.

conditions are used throughout this work. The Lanczos algorithm is applied to find the groundstate and a Band Lanczos method to obtain the Green's function as described in sec. 2.2. The Green's function of the environment $\mathrm{G}'_{\mathrm{env}}$ is given analytically by the Green's function of a semi-infinite tight binding chain [113]

$$\begin{aligned} \mathrm{g}_{\mathrm{env},i,j}(z) &= f_{0,i-j}(z) - f_{0,i+j}(z) \\ f_{i,j}(z) &= \frac{-i\ \mathrm{sign}\left(\Im \mathrm{m} z\right)}{\sqrt{4|t|^2-(z-\epsilon_s)^2}} \left(- \frac{z-\epsilon_s}{2|t|} \right. \\ &\quad \left. + i\ \mathrm{sign}\left(\Im \mathrm{m} z\right) \sqrt{1-\left(\frac{z-\epsilon_s}{2|t|}\right)^2} \right)^{|i-j|}, \end{aligned} \tag{3.23}$$

where $f_{i,j}$ is the retarded / advanced Green's function of the infinite tight binding chain if the imaginary part of ω is positive / negative. It should be noted that the density of states obtained from this Green's function has a semi-circular shape and may be expressed as

$$\rho_s(\omega) = -\frac{1}{\pi} \Im \mathrm{m} \left(\mathrm{g}_{\mathrm{env},i,j}(\omega + i0^+) \right) = \Re \mathrm{e} \left(\frac{\sqrt{4t^2-(\omega-\epsilon_s)^2}}{2\pi t^2} \right). \tag{3.24}$$

The CPT/VCA calculations are for numerical convenience performed with hopping $t = 1$ and hybridization $V = 0.3162$ which yields $\Delta = 0.1$. However we plot all quantities in units of Δ. The on-site energy ϵ_s is taken to be zero unless explicitly stated.
First we discuss the choice of the variational parameters used in VCA for this model (see sec. 3.3.1). The influence of the position of the impurity within the finite cluster part of the reference system is explained in sec. 3.3.2. We start our discussion of the CPT/VCA results in sec. 3.3.3 by investigating the two-site problem (Anderson molecule) analytically and performing a semi-analytic CPT/VCA. This serves also the purpose of making the reader familiar with the CPT/VCA procedure using a small reference system, where all quantities may be expressed on paper. Then the question of dimensionality of the model is discussed in sec. 3.3.6 by presenting results for an impurity embedded in a two- and three- dimensional bath. We explore the influence of the structure of the environment in sec. 3.3.4 by deforming the bath's density of states. The question of how large the cluster part of the reference system has to be chosen will be discussed in sec. 3.3.5. The possible use of very large cluster parts of the reference system is discussed in sec. 3.3.7. Then we turn to the actual physical results of the model. Several benchmarking dynamic quantities of the SIAM were evaluated. In the following sections, results for the impurity density of states will be presented and compared to NRG and DMRG data. We will elaborate on the strengths and weaknesses of the method as well as the comparison of CPT to VCA. Furthermore, we will discuss the relation between $\mathrm{VCA}_{\mathrm{SC}}$, where the variational parameters are determined self consistently via eq. (2.27) and VCA_{Ω}, where the variational parameters are defined at the stationary point of the grand potential. We will show that the Kondo resonance is reproduced within the framework of CPT/VCA and that the variational results fulfill certain analytic relations like the Friedel sum rule (eq. (3.45)). The method will be shown to provide reasonably accurate results in a wide range of parameter regimes of the model. Low

energy properties related to the Kondo temperature T_K will be discussed in context with renormalization group results. The imaginary frequency Green's function and self-energy will be compared to CT-QMC results. A modified reference system, with explicitly broken spin symmetry is examined in sec. 3.3.13. We start out by discussing the choice of variational parameters within VCA.

3.3.1. Choice of variational parameters

In VCA one can, in principle, optimize all possible single-particle parameters which are present in the original model, as well as additional ones. By adding bath sites not present in the original model, one includes dynamical contributions to the cluster Green's function. The numerical difficulty increases with the number of variational parameters. For the $\mathrm{VCA_{SC}}$ case a multidimensional root finding algorithm has to be adopted. For the VCA_Ω case, a saddle point in many dimensions has to be located. Since the allowed set of variational parameters limits the search space for the self-energies one will find a solution in this restricted space only. It is therefore desirable to vary as many single particle quantities as possible. A balance has to be found between a large space of available self energies and numerically feasible multidimensional algorithms. Many works have addressed the question of which parameters are the most necessary to vary and how the choice of variational parameters will influence or limit the results [26]. As discussed in refs. [46, 114], it is important to include an overall chemical potential as a variational parameter in order to preserve thermodynamic consistency. As a compromise, we will take two variational parameters $\mathsf{x} = \{\epsilon_f, \epsilon_s\}$, which covers the overall chemical potential. Note that this amounts to shifting an overall on-site energy in the whole cluster plus an extra independent shift at the correlated site. For the variation of on-site energies we observe the grand potential Ω to be maximal at the stationary point which is in agreement with results for other models. Further parameters in the SIAM are the hopping t and the hybridization V. As discussed for example in ref. [115], the variation of hopping parameters is not straightforward. For the VCA_Ω approach, we observe a maximum of Ω at $\Delta V = -V$ in the center of two symmetric stationary points (see fig. 3.5 (right)). The two symmetric lying minima are equivalent and are due to the fact that the self-energy is an even power of V. As one tunes the parameters away from particle hole-symmetry this stationary point is lost in the crossover region from the Kondo plateau to a doubly or unoccupied impurity (see sec. 3.3.9). In this parameter region the hopping t and hybridization V are probably not appropriate to be used as variational parameters within VCA_Ω.
In the following, we always choose the set $\mathsf{x} = \{V\}$ or $\mathsf{x} = \{V, t\}$ for calculations at particle-hole symmetry since the variation of on-site energies will always yield zero deviations from the physical parameters and thus reproduce the CPT result here. For all other parameter regions it is sufficient to consider $\mathsf{x} = \{\epsilon_f, \epsilon_s\}$ as variational parameters.
Since the cluster part of the reference system is a finite system, we expect spurious effects depending on the location of the impurity within the cluster. How the position of the impurity within the cluster influences the results is discussed in the next section.

3.3.2. Even-Odd Effect - choice of the impurity position

CPT/VCA rely on the Green's function of a cluster of size L which is obtained by exact diagonalization. Due to this fact it is unavoidable that some effects of the finite size cluster affect the solution of the full system. (Except in the case of vanishing interaction strength ($U = 0$).) Therefore suitable clusters have to be chosen on a basis of physical results. Some aspects of this are discussed by Balzer *et al.* [114] in the context of DMFT and VCA and by Hand *et al.* [116] in the context of DMRG. In this work we consider clusters of even size only. For these systems the groundstate does in general not suffer from spin degeneracy. Furthermore, the spatial position of the impurity is important. This can be inferred from the bath's density of states, which vanishes for $\omega = 0$ at every second site. It may also be seen in the structure of the groundstate, for which the size of the degenerate sectors alternates with the geometrical size of the cluster. In the forthcoming calculations we always place the impurity at the far end of the infinite chain, although essentially the same results are achieved by attaching it to site two, four, etc. inside the chain. We start out our discussion of the physical results by treating an Anderson molecule in isolation and then carrying its solution over to a CPT/VCA reference system. This enables a semi-analytical treatment in terms of CPT and VCA. Then the more sophisticated evaluation using numeric CPT/VCA for larger reference systems will follow.

3.3.3. Semi-analytical expressions for VCA of the two-site problem

The particle-hole symmetric two-site SIAM is considered here in detail to gain a better understanding of the behavior of CPT/VCA. The ground-state energy is obtained by diagonalization. A solution for the 2×2 cluster Green's function G' is presented as well as an expression for the CPT/VCA Green's

function G after coupling to a semi-infinite chain. The only non vanishing natural variational parameter for this system is the hybridization V. Expressions for the self-energy $\Sigma(\Delta V)$, the grand potential $\Omega(\Delta V)$ and the grand potential derivative $\frac{d\Omega(\Delta V)}{d\Delta V}$ are found. Finally the optimal cluster parameter $V'_{\text{stat.}}(U) = V + \Delta V_{\text{stat.}}(U)$, the effective mass $m^*(U)$ (see sec. 3.3.11) and the Kondo temperature $T_K(U)$ (see sec. 3.3.11) are obtained as a function of interaction-strength U.
Consider a correlated site described by annihilation and creation operators f_σ and $f_\sigma^\dagger$ with Coulomb interaction U and on-site energy ϵ_f coupled to a non-interacting site with corresponding annihilation and creation operators c_σ and $c_\sigma^\dagger$ and on-site energy ϵ_s. The Hamiltonian for this system is given by

$$\begin{aligned}\hat{\mathcal{H}}_{\text{2site}} &= U\,\hat{n}_f^\uparrow \hat{n}_f^\downarrow + \epsilon_f \sum_\sigma f_\sigma^\dagger f_\sigma + \epsilon_s \sum_\sigma c_\sigma^\dagger c_\sigma - (V + \Delta V) \sum_\sigma \left(f_\sigma^\dagger c_\sigma + c_\sigma^\dagger f_\sigma \right) \\ &= U\,\hat{n}_f^\uparrow \hat{n}_f^\downarrow - \frac{U}{2} \sum_\sigma \hat{n}_f^\sigma - V' \sum_\sigma \left(f_\sigma^\dagger c_\sigma + c_\sigma^\dagger f_\sigma \right) . \end{aligned} \tag{3.25}$$

In the second line the transition to the particle-hole symmetric case was made by setting $\epsilon_s = 0$ and $\epsilon_f = -\frac{U}{2}$. For CPT $V' = V$ the parameter of the original model. For VCA $V'_{\text{stat.}}(U) = V + \Delta V\text{stat.}(U)$ where $\Delta V\text{stat.}(U)$ is determined via the stationary point of the grand potential Ω within VCA_Ω (see sec. 2.3.1) or self consistently via single particle expectation values within VCA_{SC} (see sec. 2.3.4).
The two-site Hamiltonian will be coupled to a semi-infinite non-interacting environment

$$\hat{\mathcal{H}}_{\text{env.}} = -t \sum_{<ij>} \sum_\sigma \left(c_\sigma^\dagger c_\sigma + c_\sigma^\dagger c_\sigma \right) , \tag{3.26}$$

by CPT/VCA via

$$\hat{\mathcal{H}}_{\text{ce}} = -t \sum_\sigma \left(c_{3,\sigma}^\dagger c_\sigma + c_\sigma^\dagger c_{3,\sigma} \right) ,$$

where c_3 denotes the first site of the semi-infinite chain eq. (3.26) and c the uncorrelated site in the cluster 3.25.
The CPT equation for the Green's function defines the variational parameters

$$\begin{aligned}\mathrm{G}^{-1} &= \mathrm{G}'^{-1} - \mathrm{T} \\ &= \omega - \left(\hat{\mathcal{H}}_{\text{2site}} + \mathrm{T} \right) .\end{aligned}$$

So T consists of of the inter-cluster hopping and the term which has been subtracted from the reference system eq. (3.25) ΔV:

$$\begin{aligned}\mathrm{T} &= \mathrm{T}^{\text{CPT}} + \mathrm{T}^{\text{VCA}} , \\ \mathrm{T}^{\text{CPT}} &= \hat{\mathcal{H}}_{\text{ce}} , \\ \mathrm{T}^{\text{VCA}} &= \Delta V \sum_\sigma \left(f_\sigma^\dagger c_\sigma + c_\sigma^\dagger f_\sigma \right) .\end{aligned}$$

The matrix form of T is explicitly given by

$$\mathrm{T} = \begin{pmatrix} 0 & \Delta V & 0 \\ \Delta V & 0 & -t \\ 0 & -t & 0 \end{pmatrix} . \tag{3.27}$$

Ground state energy

As a first step the ground state energy for this system shall be obtained by diagonalization of the Hamiltonian eq. (3.25). To make work easy, it is advisable to find noninteracting subspaces by investigating the symmetries of this system. The Hamiltonian conserves the number of particles

$$\hat{\mathcal{N}} = \sum_i \sum_\sigma \hat{n}_i^\sigma = \sum_\sigma \left(\hat{n}_f^\sigma + \hat{n}_c^\sigma \right) .$$

To show this we evaluate

$$\begin{aligned}[\hat{\mathcal{H}}_{2\text{site}}, \hat{\mathcal{N}}] = U \sum_{\sigma'} [\hat{n}_f^{\uparrow}\hat{n}_f^{\downarrow}, \left(\hat{n}_f^{\sigma'} + \hat{n}_c^{\sigma'}\right)] \\ - \frac{U}{2} \sum_{\sigma} \sum_{\sigma'} [\hat{n}_f^{\sigma}, \left(\hat{n}_f^{\sigma'} + \hat{n}_c^{\sigma'}\right)] \\ - V' \sum_{\sigma} \sum_{\sigma'} [\left(f_\sigma^\dagger c_\sigma + c_\sigma^\dagger f_\sigma\right), \left(\hat{n}_f^{\sigma'} + \hat{n}_c^{\sigma'}\right)] \,. \end{aligned} \tag{3.28}$$

Using the identities eq. (2.45), the elementary fermionic commutators eq. (2.44), the commutators eq. (2.41), eq. (2.42), eq. (2.43) and

$$\begin{aligned}[c_i^\dagger c_j, \hat{n}_k] = [c_i^\dagger c_j, c_k^\dagger c_k] = -[c_k^\dagger, c_i^\dagger c_j]c_k - c_k^\dagger [c_k, c_i^\dagger c_j] \\ = -\left(\{c_k^\dagger, c_i^\dagger\}c_j - c_i^\dagger \{c_k^\dagger, c_j\}\right) c_k - c_k^\dagger \left(\{c_k, c_i^\dagger\}c_j - c_i^\dagger \{c_k, c_j\}\right) \\ = \delta_{jk} c_i^\dagger c_j - \delta_{ik} c_i^\dagger c_j \,. \end{aligned} \tag{3.29}$$

on eq. (3.28) it follows immediately that

$$[\hat{\mathcal{H}}_{2\text{site}}, \hat{\mathcal{N}}] = 0 \,.$$

The total spin projection $\hat{S}_z$ is defined as

$$\hat{S}_z = \frac{1}{2} \sum_i \left(\hat{n}_i^{\uparrow} - \hat{n}_i^{\downarrow}\right) \,.$$

In the same manner as above it is easy to show that the Hamiltonian conserves the total spin projection

$$[\hat{\mathcal{H}}_{2\text{site}}, \hat{S}_z] = 0 \,.$$

In addition the Hamiltonian commutes with the total Spin $\hat{\mathbf{S}}^2$.
Therefore the many-particle basis may be constructed respecting these symmetries. This results in non-interacting subspaces for $(N = 0, S_z = 0)$, $(N = 1, S_z = \pm\frac{1}{2})$, $(N = 2, S_z = 0, \pm 1)$, $(N = 3, S_z = \pm\frac{1}{2})$, $(N = 4, S_z = 0)$. Since the Hamiltonian is particle-hole symmetric it suffices to investigate the $N = 0$ $(N = 4)$, $N = 1$ $(N = 3)$ and $N = 2$ subspaces:

- The $N = 0$ $(N = 4)$ subspace
  is spanned by $|0,0\rangle$ $(|\uparrow\downarrow,\uparrow\downarrow\rangle)$ where the naming convention is $|s, f\rangle$. The corresponding matrix element is $\langle 0,0|\,\hat{\mathcal{H}}_{2\text{site}}\,|0,0\rangle = 0$. So the eigenenergies E_i^{N,S_z} and eigenvectors $|\Psi\rangle_i^{N,S_z}$ are given by

$$\begin{aligned}|\Psi\rangle_0^{00} &= |0,0\rangle \;, \quad E_0^{00} = 0 \\ |\Psi\rangle_0^{40} &= |\uparrow\downarrow,\uparrow\downarrow\rangle \;, \quad E_0^{40} = 0\end{aligned}$$

- The $N = 1$ $(N = 3)$ subspace
  is spanned by $\{|\uparrow, 0>, |0,\uparrow>\}$ $(\{|\uparrow,\uparrow\downarrow>, |\uparrow\downarrow,\uparrow>\})$ (and the spin symmetric states). The corresponding matrix elements can be read off straight forwardly from the Hamiltonian:

	$\lvert\uparrow,0>$	$\lvert 0,\uparrow>$
$\lvert\uparrow,0>$	0	$-V'$
$\lvert 0,\uparrow>$	$-V'$	$-\frac{U}{2}$

The eigenenergies E_i^{N,S_z} and eigenvectors $|\Psi\rangle_i^{N,S_z}$ are given by

$$|\Psi\rangle_0^{1,+\frac{1}{2}} = -\frac{U-\sqrt{U^2+16V'^2}}{4V'}|\uparrow,0> + |0,\uparrow> \ , \quad E_0^{1,+\frac{1}{2}} = -\frac{1}{4}(U+\sqrt{U^2+16V'^2})$$
$$|\Psi\rangle_1^{1,+\frac{1}{2}} = -\frac{U+\sqrt{U^2+16V'^2}}{4V'}|\uparrow,0> + |0,\uparrow> \ , \quad E_1^{1,+\frac{1}{2}} = -\frac{1}{4}(U-\sqrt{U^2+16V'^2})$$
$$|\Psi\rangle_0^{1,-\frac{1}{2}} = -\frac{U-\sqrt{U^2+16V'^2}}{4V'}|\downarrow,0> + |0,\downarrow> \ , \quad E_0^{1,-\frac{1}{2}} = -\frac{1}{4}(U+\sqrt{U^2+16V'^2})$$
$$|\Psi\rangle_1^{1,-\frac{1}{2}} = -\frac{U+\sqrt{U^2+16V'^2}}{4V'}|\downarrow,0> + |0,\downarrow> \ , \quad E_1^{1,-\frac{1}{2}} = -\frac{1}{4}(U-\sqrt{U^2+16V'^2})$$
$$|\Psi\rangle_0^{3,+\frac{1}{2}} = -\frac{U-\sqrt{U^2+16V'^2}}{4V'}|\uparrow,\uparrow\downarrow> + |\uparrow\downarrow,\uparrow> \ , \quad E_0^{3,+\frac{1}{2}} = -\frac{1}{4}(U+\sqrt{U^2+16V'^2})$$
$$|\Psi\rangle_1^{3,+\frac{1}{2}} = -\frac{U+\sqrt{U^2+16V'^2}}{4V'}|\uparrow,\uparrow\downarrow> + |\uparrow\downarrow,\uparrow> \ , \quad E_1^{3,+\frac{1}{2}} = -\frac{1}{4}(U-\sqrt{U^2+16V'^2})$$
$$|\Psi\rangle_0^{3,-\frac{1}{2}} = -\frac{U-\sqrt{U^2+16V'^2}}{4V'}|\downarrow,\uparrow\downarrow> + |\uparrow\downarrow,\downarrow> \ , \quad E_0^{3,-\frac{1}{2}} = -\frac{1}{4}(U+\sqrt{U^2+16V'^2})$$
$$|\Psi\rangle_1^{3,-\frac{1}{2}} = -\frac{U+\sqrt{U^2+16V'^2}}{4V'}|\downarrow,\uparrow\downarrow> + |\uparrow\downarrow,\downarrow> \ , \quad E_1^{3,-\frac{1}{2}} = -\frac{1}{4}(U-\sqrt{U^2+16V'^2})$$

- The $N=2$ subspace
is spanned by $\{|\uparrow,\uparrow>, |\downarrow,\downarrow>, |\uparrow,\downarrow>, |\downarrow,\uparrow>, |0,\uparrow\downarrow>, |\uparrow\downarrow,0>\}$. The corresponding matrix elements are:

	$\|\uparrow,\uparrow>$	$\|\downarrow,\downarrow>$	$\|\uparrow,\downarrow>$	$\|\uparrow\downarrow,0>$	$\|0,\uparrow\downarrow>$	$\|\downarrow,\uparrow>$
$\|\uparrow,\uparrow>$	$-\frac{U}{2}$					
$\|\downarrow,\downarrow>$		$-\frac{U}{2}$				
$\|\uparrow,\downarrow>$			$-\frac{U}{2}$	$-V$	$-V$	
$\|0,\uparrow\downarrow>$			$-V$	0		$-V$
$\|\uparrow\downarrow,0>$			$-V$		0	$-V$
$\|\downarrow,\uparrow>$				$-V$	$-V$	$-\frac{U}{2}$

Here one can identify the three triplet states

$$|\Psi\rangle_0^{2,+1} = |\uparrow,\uparrow> \ , \quad E_0^{2,+1} = -\frac{U}{2}$$
$$|\Psi\rangle_0^{2,-1} = |\downarrow,\downarrow> \ , \quad E_0^{2,-1} = -\frac{U}{2}$$
$$|\Psi\rangle_0^{2,0} = |\downarrow,\uparrow> - |\uparrow,\downarrow> \ , \quad E_0^{2,0} = -\frac{U}{2} \ .$$

Note that the minus sign in the last triplet state arises due to the minus sign when exchanging two fermions. The other three states are

$$|\Psi\rangle_1^2 = |0,\uparrow\downarrow> - |\uparrow\downarrow,0> \ , \quad E_1^2 = 0$$
$$|\Psi\rangle_2^2 = |\uparrow,\downarrow> - \frac{U-\sqrt{U^2+64V'^2}}{8V'}|\uparrow\downarrow,0> - \frac{U-\sqrt{U^2+64V'^2}}{8V'}|0,\uparrow\downarrow> + |\downarrow,\uparrow> \ ,$$
$$E_2^2 = -\frac{1}{4}(U+\sqrt{U^2+64V'^2})$$
$$|\Psi\rangle_3^2 = |\uparrow,\downarrow> - \frac{U+\sqrt{U^2+64V'^2}}{8V'}|\uparrow\downarrow,0> - \frac{U+\sqrt{U^2+64V'^2}}{8V'}|0,\uparrow\downarrow> + |\downarrow,\uparrow> \ ,$$
$$E_3^2 = -\frac{1}{4}(U-\sqrt{U^2+64V'^2}) \ .$$

The energy levels of the two-site model (Anderson molecule) are plotted in fig. 3.3 for various parameters. There one can nicely see the effects of hybridization and interaction. The plots show the behavior of degeneracies and level (anti-) crossings. For positive U the groundstate energy is found in the $N=2$ sector and is given by

$$E_0 = -\frac{1}{4}\left(U+\sqrt{U^2+64V'^2}\right) \ .$$

We will next turn to the construction of the system's Green's function.

Cluster Green's function

The cluster Green's function G' may be obtained from the Lehmann representation using the results of the previous section. Here we pursue a different often very useful way. We construct the cluster Green's function from the Green's function of the correlated site f by using the equation of motion technique. It is always possible to construct all elements of G_{ij} if the Green's functions of the correlated sites are known exactly.
Schönhammer and Brenig calculated the Green's function of the correlated site for this model perturbativeley and showed that their expression becomes exact in the limit of vanishing bandwidth [90]. This is exactly the case considered here, where the impurity site is coupled to a single non-interacting site, providing a bath with vanishing bandwidth. They obtained

$$G'_{ff}(z) = \frac{1}{z - \Gamma'(z) - \Sigma'(z)} ,$$

where the hybridization $\Gamma'(z)$ in our case is given by

$$\Gamma'(z) = \frac{V'^2}{z} ,$$

and the self-energy $\Sigma'(z)$ is given by

$$\Sigma'(z) = \frac{\frac{U^2}{4}}{z - 9\Gamma'(z)} . \tag{3.30}$$

The G'_{ff} is the $1,1$ element of G'_{ij}. Since we are considering a two-site system the other elements may be constructed by solving the Green's function of a one-site chain G'^0_{ss} and coupling it via V' to the f-site. The Green's function of the free site is given by

$$G'^0_{ss}(z) = \frac{1}{z} . \tag{3.31}$$

G'_{ij} may be then be obtained from a Dyson-like equation

$$\begin{aligned} G'_{fs} &= G'^0_{fs} + G'_{f\alpha} H_{\alpha\beta} G'^0_{\beta s} \\ &= G'^0_{fs} + G'_{ff} H_{ff} G'^0_{fs} + G'_{ff} H_{fs} G'^0_{ss} + G'_{fs} H_{sf} G'^0_{fs} + G'_{fs} H_{ss} G'^0_{ss} . \end{aligned}$$

$H_{\alpha\beta}$ denotes the off-diagonal single-particle terms of the Hamiltonian eq. (3.25)

$$H_{\alpha\beta} = \begin{pmatrix} 0 & -V' \\ -V' & 0 \end{pmatrix} .$$

Since $H_{\alpha\beta}$ contains only off-diagonal elements and $G'^0_{fs} = 0$ we are left with:

$$\begin{aligned} G'_{fs}(z) &= G'_{ff}(z) H_{fs} G'^0_{ss}(z) \\ &= -V' G'_{ff}(z) G'_{ss}(z) . \end{aligned}$$

Due to symmetry $G'_{sf}(z) = G'_{fs}(z)$. The last missing element is obtained as follows

$$\begin{aligned} G'_{ss} &= G'^0_{ss} + G'_{s\alpha} H_{\alpha\beta} G'^0_{\beta s} \\ &= G'^0_{ss} + G'_{sf} H_{fs} G'^0_{ss} \\ &= G'^0_{ss} + V'^2 G'^0_{ss} G'_{ff} G'^0_{ss} . \end{aligned}$$

This general procedure of obtaining all elements of the interacting cluster Green's function from the Green's function of the interacting site (which has to be obtained exactly by some method beforehand for a system of length L) and the matrix Green's function of a free chain of length $L-1$ is outlined in

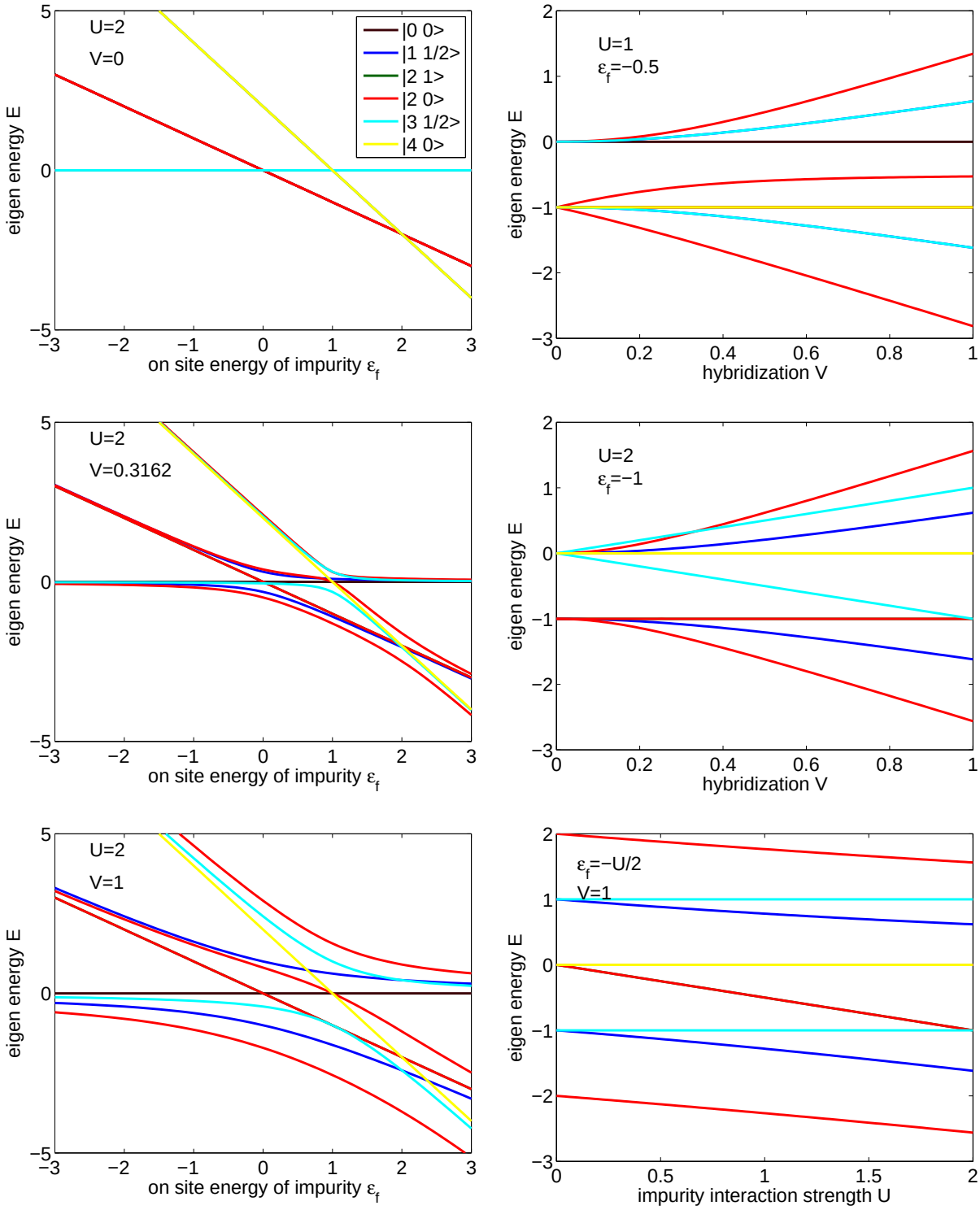

Figure 3.3.: Energy levels of the Anderson molecule as a function of the model parameters. The legend displayed in the upper left figure is valid for all plots. (Left column) Asymmetric model for fixed interaction strength U and hybridization V as a function of on-site energy ϵ_f. (Right Column top and mid) Symmetric model for fixed interaction strength U as a function of hybridization V. (Right Column top) Symmetric model for fixed hybridization V as a function of interaction strength U.

app. E. The Green's function of the semi-infinite environment is given by

$$G'_{ee}(z) = \frac{z - i\,\mathrm{sign}\,(\Im m z)\sqrt{4t^2 - z^2}}{2t^2}\,.$$

The cluster Green's function for the two-site Anderson system and environment is finally given by

$$G'(z) = \begin{pmatrix} \frac{1}{z-\Gamma'(z)-\Sigma'(z)} & -\frac{\frac{V'}{z}}{z-\Gamma'(z)-\Sigma'(z)} & 0 \\ -\frac{\frac{V'}{z}}{z-\Gamma'(z)-\Sigma'(z)} & \frac{1-\frac{\Sigma'(z)}{z}}{z-\Gamma'(z)-\Sigma'(z)} & 0 \\ 0 & 0 & \frac{z-i\,\mathrm{sign}\,(\Im m z)\sqrt{4t^2-z^2}}{2t^2} \end{pmatrix}. \tag{3.32}$$

Next we will use the CPT equation to obtain the Green's function of the total system.

CPT/VCA Green's function

For the CPT/VCA procedure it is more convenient to use the inverse $G'^{-1}(z)$

$$G'^{-1}(z) = \begin{pmatrix} z - \Sigma'(z) & V' & 0 \\ V' & z & 0 \\ 0 & 0 & G'^{-1}_{ee}(z) \end{pmatrix}. \tag{3.33}$$

Here T is the inter-cluster hopping matrix including the variational parameter ΔV for VCA. The inverse of the total Green's function is then given by

$$\begin{aligned} G^{-1}(z) &= G'^{-1}(z) - T \\ &= \begin{pmatrix} z - \Sigma'(z) & V & 0 \\ V & z & t \\ 0 & t & G'^{-1}_{ee}(z) \end{pmatrix}. \end{aligned}$$

After some algebra one may extract the total Green's function of the correlated site

$$\begin{aligned} G_{ff}(z) &= \frac{zG'^{-1}_{ee}(z) - t^2}{(z - \Sigma'(z))(zG'^{-1}_{ee}(z) - t^2) - V^2 G'^{-1}_{ee}(z)} \\ &= \frac{1}{z - V^2\left(\frac{1}{z - t^2 G'_{ee}}\right) - \Sigma'(z)} \\ &= \frac{1}{z - V^2\left(\frac{2}{z + i\,\mathrm{sign}\,(\Im m z)\sqrt{4t^2 - z^2}}\right) - \Sigma'(z)} \\ &= \frac{1}{z - V^2\left(\frac{z - i\,\mathrm{sign}\,(\Im m z)\sqrt{4t^2 - z^2}}{2t^2}\right) - \Sigma'(z)} \\ &= \frac{1}{z - V^2 G'_{ee}(z) - \Sigma'(z)} \\ &= \frac{1}{z - \Gamma(z) - \Sigma'(z)}\,. \end{aligned}$$

Note that due to the CPT/VCA approximation the self-energy stays the self energy of the cluster! The only term changing from the cluster to the total Green's function, is the hybridization to the environment. So instead of the hybridization to an isolated site $\Gamma'(z) = V'^2 G'^0_{ss}$ the Green's function now depends on the hybridization to an infinite chain $\Gamma(z) = V^2 G'_{ee}$. Furthermore the variational parameter ΔV appears in the self energy $\Sigma'(z)$ only.
To perform a VCA calculation, an expression for the grand potential is needed.

Grand Potential $\Omega(\Delta V)$

The grand potential Ω is given by (see eq. (2.23))

$$\Omega(\Delta V) = \omega'_0(\Delta V) + \mathrm{tr}\,(T(\Delta V)) - \frac{1}{\pi}\int_0^\infty d\omega \Re e\left(\mathrm{tr}\left(\ln\left(\mathbb{1} - T(\Delta V)G'(i\omega, \Delta V)\right)\right)\right)\,.$$

Plugging in the cluster groundstate eq. (3.31), the cluster Green's function eq. (3.33) and the matrix T (eq. (3.27)) one obtains a semi-analytic expression for the grand potential $\Omega(U, V, \Delta V, t)$

$$\begin{aligned}
\Omega(U,V,\Delta V,t) = \frac{1}{4}\left(-U - \sqrt{U^2 + 64V')^2}\right) - \frac{2}{\pi}\int_0^\infty d\omega \ln\Bigg(\frac{1}{\mathcal{N}_1(\omega)} \\
\Big(72V^4 + U^2w^2 + 44V^2w^2 + 4w^4 + 36\Delta V^2\left(2V^2 + w^2\right) + 72\Delta VV\left(2V^2 + w^2\right) \\
+ w\sqrt{4t^2 + w^2}\left(36\Delta V^2 + U^2 + 72\Delta VV + 4\left(9V^2 + w^2\right)\right)\Big)\Bigg), \\
\mathcal{N}_1(\omega) = 2\Big(36\Delta V^4 + 144\Delta V^3V + 36V^4 + U^2w^2 + 40V^2w^2 + 4w^4 \\
+ 8\Delta V^2\left(27V^2 + 5w^2\right) + 16\Delta V\left(9V^3 + 5Vw^2\right)\Big).
\end{aligned}$$

The grand potential $\Omega(U, \Delta V)$ is shown in fig. 3.5 (right) for $t = 1.0$ and $V = 0.3162$. To find its stationary point, the derivative with respect to ΔV is needed.

Stationary point of the grand potential $\Omega(\Delta V)$

The stationary point of Ω with respect to ΔV is given by the derivative

$$\begin{aligned}
\frac{d\,\Omega(\Delta V)}{d\,(\Delta V)} &= \nabla_{\Delta V}\omega_0'(\Delta V) + \nabla_{\Delta V}\mathrm{Tr}\,\left(T(\Delta V)\right) - \nabla_{\Delta V}\frac{1}{\pi}\int_0^\infty d\omega\,\mathfrak{Re}\left(\mathrm{tr}\,\left(\ln\left(\mathbb{1} - \mathrm{T}(\Delta V)\mathrm{G}'(i\omega,\Delta V)\right)\right)\right) \\
&= \nabla_{\Delta V}\omega_0'(\Delta V) - \frac{1}{\pi}\int_0^\infty d\omega\,\mathfrak{Re}\left(\mathrm{tr}\,\left(\nabla_{\Delta V}\ln\left(\mathbb{1} - \mathrm{T}(\Delta V)\mathrm{G}'(i\omega,\Delta V)\right)\right)\right) \\
&= \nabla_{\Delta V}\omega_0'(\Delta V) - \frac{1}{\pi}\int_0^\infty d\omega\,\mathfrak{Re}\Bigg(\mathrm{tr}\Big(\left(\mathbb{1} - \mathrm{T}(\Delta V)\mathrm{G}'(i\omega,\Delta V)\right)^{-1}\left(\nabla_{\Delta V}\mathrm{T}(\Delta V)\mathrm{G}'(i\omega,\Delta V)\right) \\
&\quad + \left(\mathbb{1} - \mathrm{T}(\Delta V)\mathrm{G}'(i\omega,\Delta V)\right)^{-1}\left(\mathrm{T}(\Delta V)\nabla_{\Delta V}\mathrm{G}'(i\omega,\Delta V)\right)\Big)\Bigg).
\end{aligned}$$

The second term in the first line vanishes because T (eq. (3.27)) has off-diagonal elements only. Upon plugging in the cluster groundstate eq. (3.31), the cluster Green's function eq. (3.33) and the matrix T

(eq. (3.27)) one obtains a semi-analytic expression for the derivative of the grand potential Ω

$$\begin{aligned}\frac{d\Omega}{d(\Delta V)} = \frac{-16V'}{\sqrt{U^2+64V'^2}} + \frac{16V'}{\pi}\int_0^\infty d\omega\,\frac{1}{\mathcal{N}_2(\omega)}\Bigg(&648V^2V'^4 \\ &+18\left(18\Delta V^4+72\Delta V^3V+26V^4+2\Delta VV\left(U^2+44V^2\right)+\Delta V^2\left(U^2+116V^2\right)\right)w^2 \\ &+\left(72\Delta V^2+U^2+144\Delta VV+80V^2\right)w^4+4w^6 \\ &+\sqrt{4t^2+w^2}\left(4w^5+w^3\left(U^2+72V'^2\right)+w\left(18V'^2\left(U^2+18V'^2\right)\right)\right)\Bigg),\end{aligned} \tag{3.34}$$

$$\begin{aligned}\mathcal{N}_2(\omega) = \left(2592V^2V'^6\right)+\Bigg(&36V'^2\Bigg(36\Delta V^4+144\Delta V^3V+3U^2V^2+124V^4 \\ &+2\Delta VV\left(U^2+160V^2\right)+\Delta V^2\left(U^2+304V^2\right)\Bigg)\Bigg)w^2 \\ &+\Bigg(1584\Delta V^4+U^4+6336\Delta V^3V+84U^2V^2+2192V^4 \\ &+4\Delta V^2\left(19U^2+2528V^2\right)+8\Delta V\left(19U^2V+944V^3\right)\Bigg)w^4 \\ &+\left(8\left(38\Delta V^2+U^2+76\Delta VV+42V^2\right)\right)w^6+16w^8 \\ &+\sqrt{4t^2+w^2}\Bigg(w\left(36V'^4\left(U^2+36V'^2\right)\right)+w^5\left(8\left(U^2+38V'^2\right)\right)+16w^7 \\ &+w^3\Bigg(1584\Delta V^4+U^4+6336\Delta V^3V+76U^2V^2+1584V^4 \\ &+\Delta V^2\left(76U^2+9504V^2\right)+8\Delta V\left(19U^2V+792V^3\right)\Bigg)\Bigg).\end{aligned} \tag{3.35}$$

Setting the derivative to zero one obtains a nonlinear integral equation. An analytic evaluation of the integral is not possible. The roots may be obtained numerically. The integrand of eq. (3.34) is shown in fig. 3.4. The derivative of the grand potential eq. (3.34) is plotted for various values of U in fig. 3.5 (left). The root in the center at $\Delta V = -V$ is unphysical because it would yield a cluster solution corresponding to an atomic limit and therefore will never be able to reproduce the thermodynamic limit with increasing cluster size. Furthermore careful examination of eq. (3.34) shows that the equation breaks down for $\Delta V = -V$, because all ΔV drop out. The evolution of V' with U is shown in figure fig. 3.5 (right). Here we directly try to get a handle on the low energy properties by calculating the effective mass, which is inversely proportional to the Kondo temperature.

Effective Mass

The effective mass is defined in eq. (3.48). Inserting the self-energy for the two-site system eq. (3.30) one obtains

$$\begin{aligned}\frac{m^*(U)}{m^*(0)} &= 1-\frac{U^2}{4}\frac{d}{d\omega}\mathrm{Im}\left(\frac{i\omega}{-\omega^2-9V'^2}\right)\Bigg|_{\omega=0^+} \\ &= 1+\frac{U^2}{4}\frac{d}{d\omega}\left(\frac{\omega}{\omega^2+9V'^2}\right)\Bigg|_{\omega=0^+} \\ &= 1+\frac{1}{36}\left(\frac{U}{V'}\right)^2.\end{aligned} \tag{3.36}$$

Note that for $U = 0$ the effective mass is one as it is supposed to be. Furthermore one sees that within this approximation (self energy of the two site cluster), the Kondo temperature which is inversely proportional to the effective mass becomes proportional to

$$T_K(U) \propto \left(\frac{V'_{\mathrm{stat.}}(U)}{U}\right)^2.$$

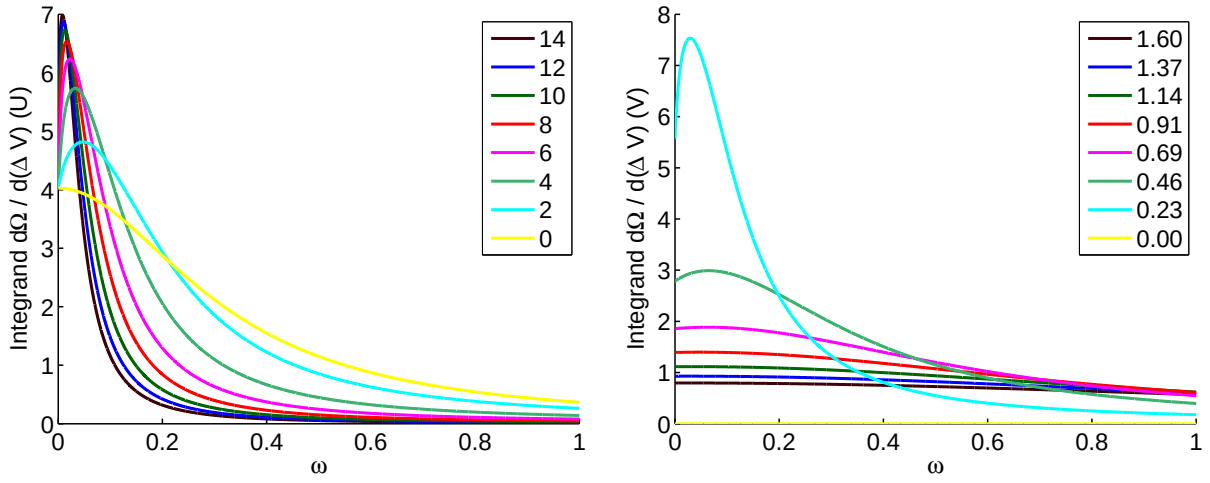

Figure 3.4.: Integrand for the grand potential derivative as a function of energy ω for various values of interaction strength U/t (see legend) (for fixed $V = 0.3162$, $\Delta V = 0$, $t = 1$) (left) and for various values of the hybridization V (for fixed $U/t = 2$, $\Delta V = 0$, $t = 1$) (right).

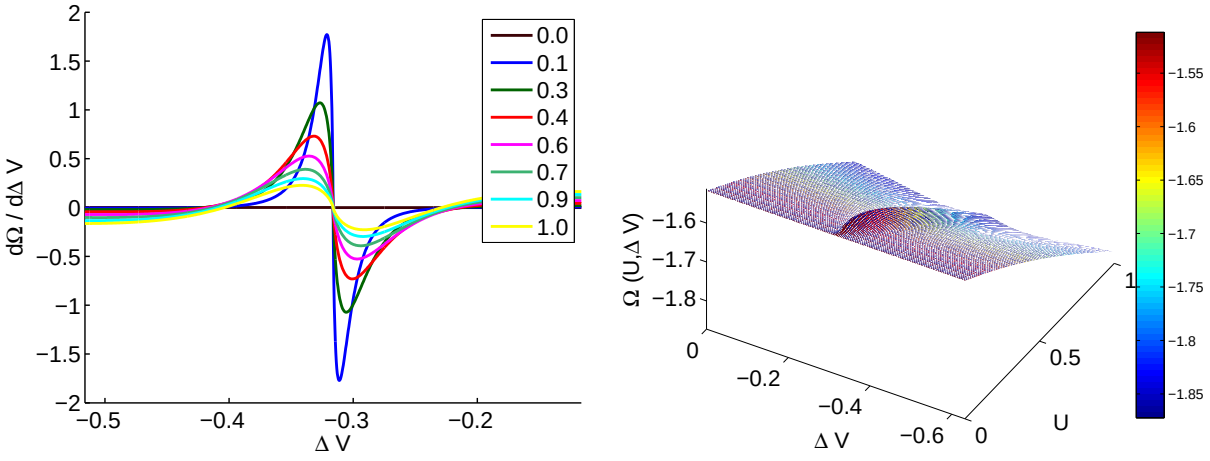

Figure 3.5.: (Left) The derivative of the grand potential eq. (3.34) as a function of ΔV ($t = 1, V = 0.3162$). The root in the center is unphysical in the thermodynamic limit for various values of interaction-strength U/t (see legend). (Right) The grand potential $\Omega(U, \Delta V)$ for hopping $t = 1.0$ and hybridization $V = 0.3162$. One can see three stationary points for each value of interaction strength U. One maximum at $\Delta V = -V$, which is unphysical (see text). And two symmetric minima which correspond to the same physical situation.

Unfortunately the cluster parameter V'_{stat}, which makes the Grand Potential stationary, cannot be determined analytically but a numerical determination of the roots of eq. (3.34) is feasible. This results in a perfect exponential behavior of $m^*(U)$ and $T_K(U)$. The exponent may be obtained by an exponential fit ($R^2 = 1$) and is given by

$$T_K \propto e^{-\gamma \frac{\pi}{8\Delta} U} ,$$

with

$$\gamma = 0.6511 .$$

The effective mass is plotted in fig. 3.7 (right). As a reference the Bethe Ansatz result for T_K^-1 and values obtained by FRG [100] are plotted. The factor $\alpha = 1$ except for the VCA data $\alpha = \frac{1}{\gamma}$ to account for the mismatch in the exponent. The issue of obtaining an exponential scale but not the correct exponent for the functional dependence on U is observed in various methods (see for example variational wavefunctions where the issue was cured by introducing a better Ansatz by Schönhammer [117] or FRG [118]).
After showing that VCA_Ω is capable of creating an exponential scale in U, it is interesting to investigate the behavior of VCA_{SC}.

Self consistent VCA

Here we attempt to obtain the VCA_{SC} solution for the two-site problem. The only variational parameter is ΔV and therefore we determine the expectation value of $< f^\dagger c >$ self consistently. The hopping expectation value is given by

$$< f^\dagger c >= -\frac{2}{\pi} \int_0^\infty d\omega \, \text{G}_{12}(i\omega) .$$

Evaluation of this expectation value in the cluster yields

$$< f^\dagger c >_{\text{cluster}} = -\frac{2}{\pi} \int_0^\infty d\omega \, \frac{4(\Delta V + V)\left(9(\Delta V + V)^2 + w^2\right)}{36(\Delta V + V)^4 + \left(U^2 + 40(\Delta V + V)^2\right) w^2 + 4w^4} . \tag{3.37}$$

Evaluation of this expectation value in the total system gives

$$< f^\dagger c >_{\text{CPT}} = -\frac{2}{\pi} \int_0^\infty d\omega \, \frac{8V}{8V^2 + \frac{w(U^2+36(\Delta V+V)^2+4w^2)\left(w+\sqrt{4t^2+w^2}\right)}{9(\Delta V+V)^2+w^2}} . \tag{3.38}$$

Upon requiring the two expectation values to coincide

$$< f^\dagger c >_{\text{cluster}} \overset{!}{=} < f^\dagger c >_{\text{CPT}} , \tag{3.39}$$

the optimal value of ΔV is obtained.
The numerical evaluation of eq. (3.39) as a function of $V' = V + \Delta V$ is shown for $U = 1$ and $t = 1$ in fig. 3.6 (top). A comparison of the hopping expectation value in the cluster eq. (3.37) and after coupling to the environment eq. (3.38) is shown in fig. 3.6 (bottom). It is immediately obvious that VCA_{SC} does not fulfill the same limits as VCA_Ω for $U \to 0$. In VCA_Ω the grand potential becomes flat in this limit and no stationary point can be found. In VCA_{SC} however the two expectation values do not coincide in this limit. However the equation breaks down at this point. The optimal value for the cluster parameter V' is shown in fig. 3.7 (left) and yield no satisfactory behavior. The effective mass (fig. 3.7 (right)) obtained with those values of V' does not show an exponential dependence on U.

This concludes the discussion of the two-site problem. We now proceed by investigating the effects of the environment density of states on the cluster part of the reference system.

3.3.4. Comparing a flat band to a semi-circular density of states of the environment

The density of states, created by dissecting the one-dimensional tight-binding chain at any site, has a semi-circular shape. The corresponding Green's function may be evaluated analytically (see eq. (3.23)) and is shown in fig. 3.8 (left). The parameters chosen for the plot were $\epsilon_s = 0$ and $t = 1$.
In this section the influence of the shape of the density of states of the bath on the results shall be evaluated. For that purpose the 'natural' semi-circular density of states of the model is replaced by a flat

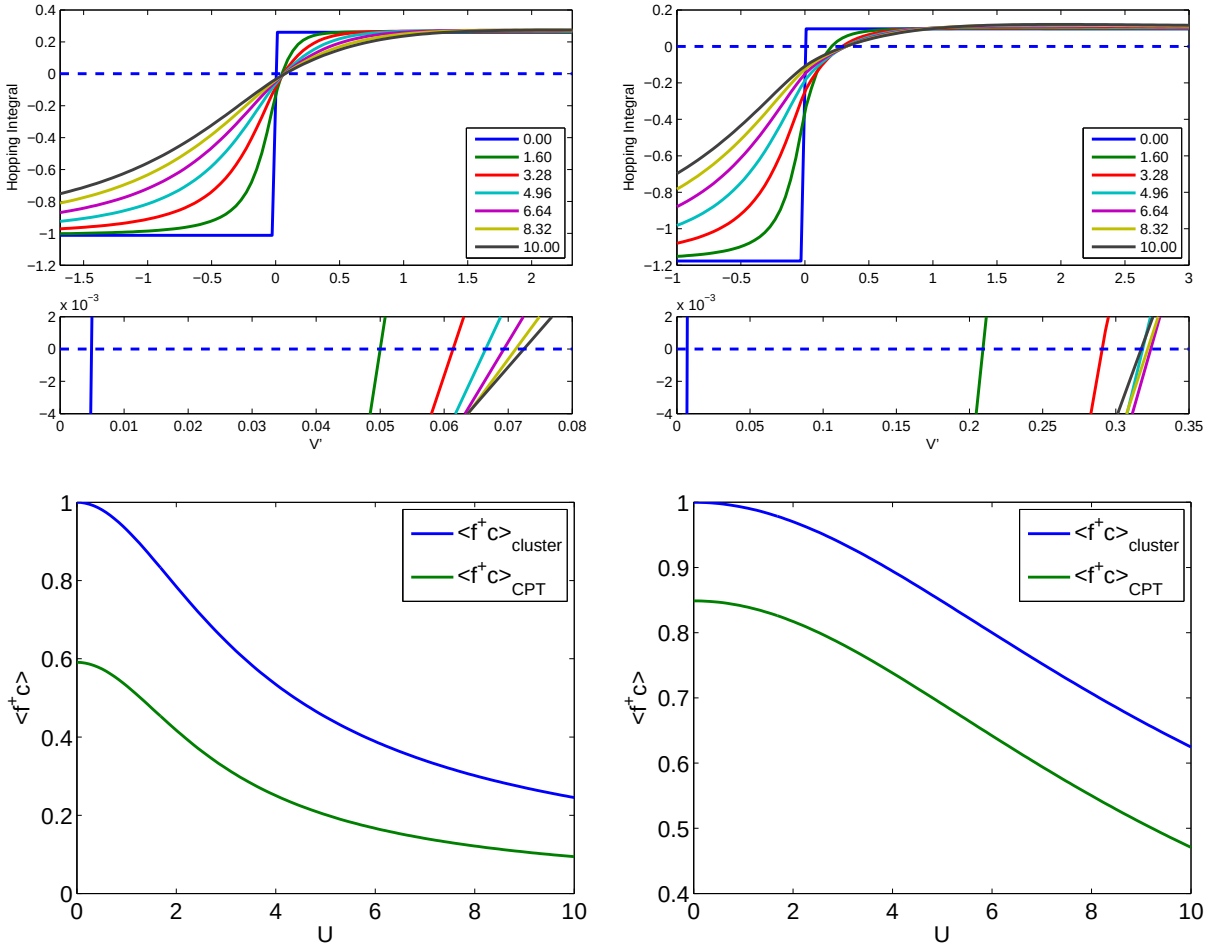

Figure 3.6.: Self consistent VCA results. (Top row) Numerical evaluation of eq. (3.39) as a function of $V' = V + \Delta V$ for $t = 1$ and various U (see legend). The roots indicate the optimal cluster parameter. (Bottom row) The cluster- eq. (3.37) and CPT eq. (3.38) expectation values of the hopping from the impurity to the chain as a function of U/t (see legend) for $t = 1$. (Left Column) $V = 0.3162$, (Right Column) $V = 1.0$.

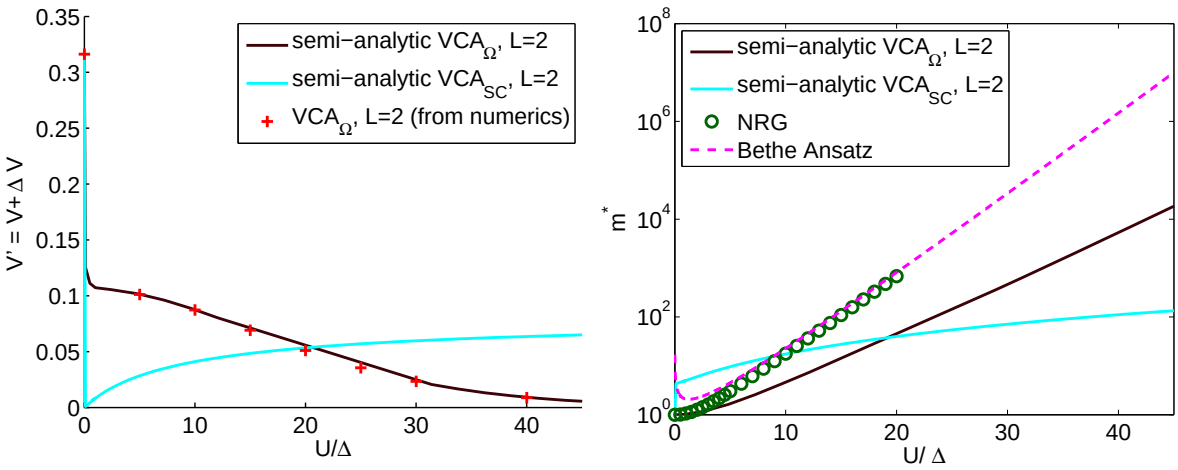

Figure 3.7.: Behavior of the variational parameter and the effective mass. (Left) Optimal parameter V' of the reference system as obtained by the semi-analytical equations for VCA_Ω eq. (3.34) and $\mathrm{VCA}_{\mathrm{SC}}$ eq. (3.39). As a reference the $L = 2$ data of our numerical simulation is shown too. (Right) The effective mass eq. (3.48) obtained by the optimized parameter V' of the reference system (see left figure). Additionally shown is the Bethe-Ansatz [89] eq. (3.46) and NRG [100] result as a reference.

band

$$A_{\mathrm{flat}}(\omega) = \begin{cases} \frac{1}{2D} & -D < \omega < D \\ 0 & \text{else} \end{cases} ,$$

where D denotes the half-bandwidth and the constant is chosen to respect the sum rule eq. (2.16). The Green's function for this density of states may be constructed by first inverting eq. (3.43) which yields the imaginary part $\Im\mathrm{m}\left(\mathrm{G}_{\mathrm{flat}}(z)\right) = -\frac{\pi}{2D}$ within the band. Then one may use Kramers-Kronig relations [1]

$$\Re\mathrm{e}\left(\mathrm{G}_{\mathrm{flat}}(\omega)\right) = \frac{1}{\pi}\mathcal{P}\int_{-\infty}^{\infty} \frac{\Im\mathrm{m}\left(\mathrm{G}_{\mathrm{flat}}(\omega')\right)}{\omega' - \omega}\, d\omega' ,$$

to obtain the real part. The Green's function of the flat band therefore is given by

$$\mathrm{G}_{\mathrm{flat}}(z) = -\frac{1}{2D}\ln\left(\frac{z-D}{z+D}\right) ,$$

In the following this density of states of the environment will be compared to the semi-circular one. Therefore the half-bandwidth is chosen to be $D = \frac{\pi}{2}t$ for the flat density of states, to obtain the same Δ as in the semi-circular case (see eq. (3.5)). The Green's function of the flat band is shown in fig. 3.8 (left). CPT results for the impurity density of states, for a $L = 8$-site cluster, are shown in fig. 3.8 (mid, right). The plots show curves for different values of interaction strength U (using $\Delta = 0.1$). The data in the middle shows results obtained by using the semi-circular tight-binding density of states, while the right plot shows data using the flat band. The spectra are very similar. Especially in the low energy region, there is no difference, since they depend predominantly on the value of the environmental density of states at the Fermi energy. Several other quantities (like the effective mass or the static-spin susceptibility) were evaluated for both kinds of environment giving more or less equivalent results.
The cluster part of the reference system is of finite length. To examine the severity of this approximation spin-spin and density correlation functions are evaluated in the next section.

3.3.5. Estimating the necessary extent of the reference system: spin/density correlations

In this section an attempt is made to estimate the necessary extent of the cluster part of the reference system to achieve good results within CPT/VCA. Calculations of static expectation values (see sec. 3.3.9) revealed, that much smaller clusters suffice in the parameter region where the impurity is essentially zero-

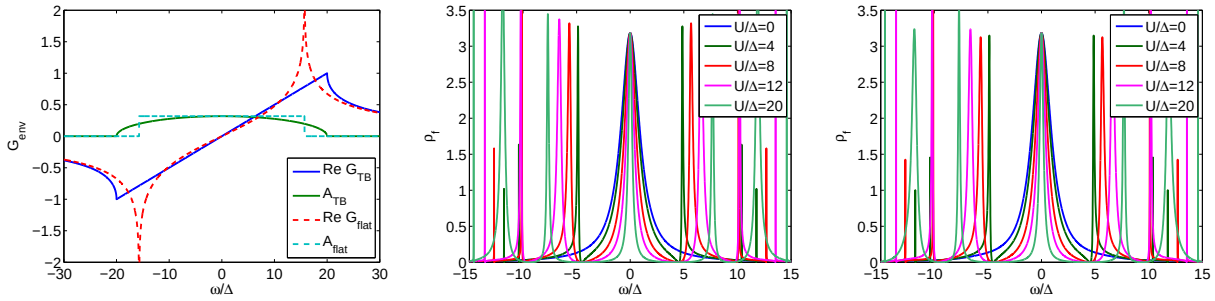

Figure 3.8.: (Left) Density of states and real part of the Green's function of the environment. Shown is the "natural" density of states of a semi-infinite tight binding chain (semi-circular) as well as the flat density of states examined in this section. Note that here the x-axis was scaled with $\Delta = 0.1$ although this parameter does not enter in this calculation. (Mid) Single-particle spectral function for the particle-hole symmetric SIAM at various interaction-strengths U/Δ (see legend). Further parameters used were $V = 0.3162$, $t = 1$ and $0^+ = 10^{-6}$. The bath's density of states used was the semi-circular DOS of the semi-infinite tight binding chain. (Right) The same but calculated using a flat DOS in the environment.

or double occupied. In the Kondo- and the crossover region large clusters are expected to be necessary, because the CPT results look far from converged for cluster sizes examined here. In the following the spin-spin and charge-charge correlations inside the reference system are calculated, which are expected to give a hint on the necessary size of the clusters.
To evaluate the spin-spin correlation function

$$< \hat{\mathbf{S}}_\mathbf{i}\, \hat{\mathbf{S}}_\mathbf{j} > = < \underbrace{\hat{S}_i^z\, \hat{S}_j^z}_{\hat{Z}} + \underbrace{\hat{S}_i^x\, \hat{S}_j^x + \hat{S}_i^y\, \hat{S}_j^y}_{\hat{F}} > \ , \tag{3.40}$$

for the SIAM, we transform this expression to one involving fermionic operators (and number operators) instead of spins. Using

$$\hat{S}^z = \frac{1}{2}\left(\hat{n}^\uparrow - \hat{n}^\downarrow\right) \ ,$$

first operator $\hat{Z}$ transforms to

$$\hat{Z} = \frac{1}{4}\left(\hat{n}_i^\uparrow - \hat{n}_i^\downarrow\right)\left(\hat{n}_j^\uparrow - \hat{n}_j^\downarrow\right) \ .$$

Expressing the x and y components of the spin by spin-ladder operators

$$\hat{S}^+ = \hat{S}^x + i\hat{S}^y = c^{\uparrow\dagger} c^\downarrow \tag{3.41}$$

$$\hat{S}^- = \hat{S}^x - i\hat{S}^y = c^{\downarrow\dagger} c^\uparrow \ , \tag{3.42}$$

the second part of eq. (3.40) $\hat{F}$ takes the form

$$\hat{F} = \frac{1}{2}\left(\hat{S}_i^- \hat{S}_j^+ + \hat{S}_i^+ \hat{S}_j^-\right) \ .$$

Representing the spin-ladder operators by fermionic operators eq. (3.42) one arrives at the fermionic representation of $\hat{F}$

$$\hat{F} = \frac{1}{2}\left(c_i^{\downarrow\dagger} c_i^\uparrow \ c_j^{\uparrow\dagger} c_j^\downarrow \ + c_i^{\uparrow\dagger} c_i^\downarrow \ c_j^{\downarrow\dagger} c_j^\uparrow \ \right) \ .$$

Furthermore the density-density correlation function $< n_i n_j >$ is examined, which consists of four Fermi-operators.
The typical behavior of the spin-spin vector, spin-spin z and density-density correlations as a function of distance away from the impurity is shown in fig. 3.9 (left), for the non-interacting case in a ten-site cluster. The local values at the impurity can be calculated easily and are $< S_0^{z2} >= 0.125$ and $< \mathbf{S}_0^2 >= 0.375$. A plot of the spin-spin vector correlation $< \mathbf{S}_0 \mathbf{S}_{\text{end}} >$ of a large parameter region of the SIAM is shown

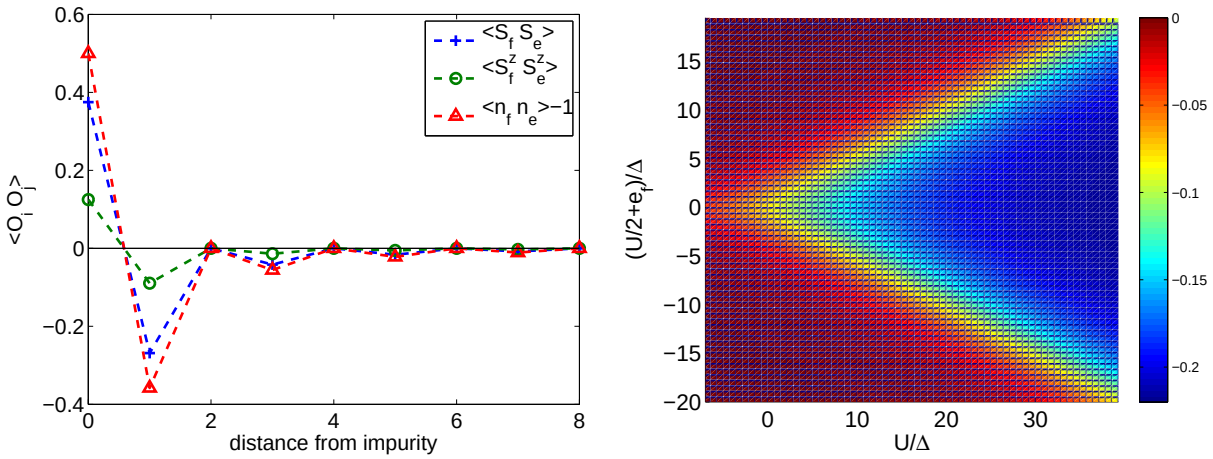

Figure 3.9.: (Left) The spin-spin vector, spin-spin z and density-density correlations as a function of distance away from the impurity are shown. Note that the density-density correlations are visualized as $< n_i n_j > -1$. The data is shown, as a representative for the typical behavior of the correlators, for an interaction strength $U = 0$ in a $L = 10$ site cluster. (Right) The spin-spin vector correlation: $< \mathbf{S}_0 \mathbf{S}_{\text{end}} >$ between the impurity and the site farthest away from the impurity inside the cluster is shown in all parameter regions. The interaction strength for this calculations was $\frac{U}{\Delta} = 2$, the cluster length $L = 6$.

in fig. 3.9 (right). This means the correlation of the impurity with the site farthest away from it is measured. The interaction strength used was $\frac{U}{\Delta} = 2$. For details of the parameter regions of the SIAM see sec. 3.3.10. As is clearly visible from the figure, the correlations have already faded away in the regions where the impurity is zero- or doubly occupied and are still there in the Kondo- and crossover regime. Similar calculations for larger systems (up to $L = 16$) showed essentially the same behavior. Based on an extrapolation in system size L of the spin-spin correlation functions we estimate the need of ≈ 50-site clusters in the Kondo regime of the SIAM for CPT. This discussion does not apply to VCA, where the situation is entirely different and much smaller clusters are sufficient as will be shown in the forthcoming discussion. This behavior can be well understood from the involved physics. In the Kondo regime below a temperature scale T_K, the impurities local moment gets screened by the conduction electrons to make up a singlet state. The question of how many electrons contribute to the screening and how large this screening cloud is, is still open today. Many concepts have been suggested but up to now controversial theoretical predictions exist [8, 119]. New ideas may require very different ways of thinking [120]. It has never been possible to measure this extent in experiment. Bulk measurements are much too less sensitive to detect this length scale $\xi_K = \frac{T_K}{v_F}$ (v_F denotes the Fermi velocity), which typically behaves like

$$\chi(r) = \chi_0 + \frac{\cos(2k_F r)}{r^2} f\left(\frac{r}{\xi_K}\right)$$

These experiments measure for example the Knight-shift, but the $\frac{1}{r^2}$ dependence of the susceptibility renders the parameter ξ_K invisible. Experiments on nano-devices up to now have been fruitless because of the extent of the screening cloud into the leads. Very recent scanning tunneling microscopy (STM) based measurements only can give hints [121].
We model the SIAM by an infinite tight-binding chain. The effects of embedding an impurity in higher dimensions is investigated in the next section.

3.3.6. Effects of an impurity embedded in higher dimensions

In this work the SIAM is modeled by a one-dimensional chain. The effects of embedding the impurity in two- or three dimensions are studied here within CPT. The two- or three dimensional bath is obtained by a mapping of the one-dimensional chain to an effective higher dimensional model, which is only possible in the case of a single impurity. This process, involving a rescaling of the hopping parameters in the chain, is outlined in detail in app. F.
In fig. 3.10, the impurity density of states is shown for an impurity embedded in different dimensions. The results were obtained using CPT based on $L = 10$-site clusters. The result for one-, two-, and three dimensions shows the same characteristic features. Therefore we conclude, that dimensionality does not

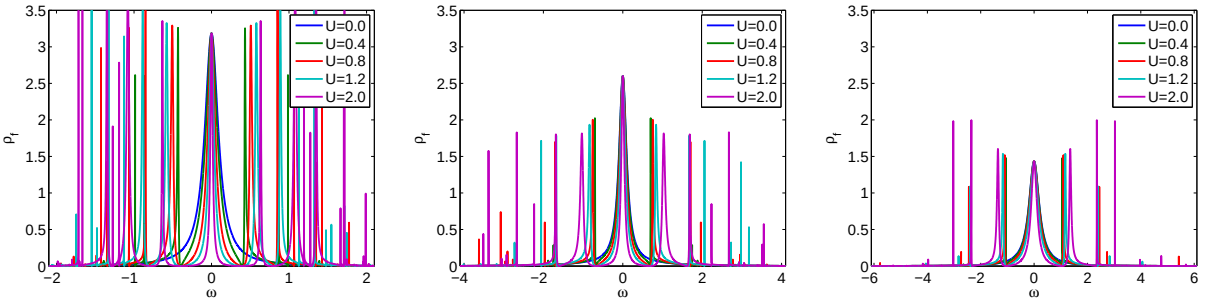

Figure 3.10.: Local density of states in the impurity obtained by CPT. The calculations were done for an interaction strength of $U = 0.0, 0.4, 0.8, 1.2$ and 2.0, a hybridization of $V = 0.3162$ and a hopping of $t = 1$. The cluster-size used was $L = 10$ sites and the numerical broadening $0^+ = 10^{-6}$. (Left) An impurity embedded in a one-dimensional tight-binding system. (Mid) An impurity embedded in a two-dimensional tight-binding system. (Right) An impurity embedded in a three-dimensional tight-binding system.

play a critical role in these kinds of calculations. Note that a scaling of energies with Δ was not done in this section since Δ depends on the density of states (see eq. (3.5)) of the conduction electrons at the Fermi-energy, which is very different in a one-, two- and three-dimensional tight-binding system. This is the reason why the Kondo-resonance in the three plots has a different height in each, although they all fulfill their respective Friedel sum rule eq. (3.45).

The finite size of the cluster part of the reference system is limited to 16-sites within our Band Lanczos treatment. A method which enables accessing larger systems is assessed in the next section.

3.3.7. Using larger reference systems: MPS Lanczos results

The memory requirements of the Band Lanczos cluster solver limit the size of the cluster part of the reference system to 16-sites for the SIAM. The Matrix product state Lanczos method described in sec. 2.2.4 would be a candidate cluster solver for larger systems. This promising method, however is still under development by P. Dargel [45]. In this section an overview of the current status of the ongoing work to merge this method with CPT/VCA shall be given.

The Q-matrices and corresponding excitation energies for the SIAM on six to twenty sites were calculated by Piet Dargel using the MPS Lanczos method. The cluster solution of the single-particle spectral function for a six- and twelve site cluster is shown in fig. 3.12 (left), the corresponding CPT solution for the infinite system in fig. 3.12 (right). One can see that for larger system-sizes, the sum-rule eq. (2.16) is not fulfilled any more by the MPS method. A comparison to six to twelve site Band Lanczos results is shown in fig. 3.11. Shown is the single-particle spectral function of the impurity site for the total system. For small systems the Band Lanczos and the MPS Lanczos results agree. For larger systems, not accessible to Band Lanczos, the MPS Lanczos produces a spurious result in the vicinity of $\omega = 0$ due to missing weight in the Q-matrices. As we are interested especially in the behavior of the low energy region, no further results based on this cluster solver will be presented in the forthcoming discussion. However this method is a promising tool for future extensions of CPT/VCA.

After these preliminary discussions, we now turn to the actual physics of the SIAM within CPT/VCA.

3.3.8. Spectral properties

The single-particle spectral function A^{σ}_{ii} is obtained from the retarded Green's function $\mathrm{G}^{\sigma,\mathrm{ret}}_{ii}$ (ref. [27])

$$A^{\sigma}_{ii}(\omega) = -\frac{1}{\pi}\,\mathfrak{Im}\,\mathrm{G}^{\sigma,\mathrm{ret}}_{ii}(\omega)\,. \tag{3.43}$$

The diagonal element at the impurity site $A^{\sigma}_{ff}(\omega)$ describes the impurity density of states $\rho^{\sigma}_{f}(\omega)$. A physical property of the SIAM which poses a challenge to numerical methods is the Kondo-Abrikosov-Suhl resonance often referred to as Kondo peak [3]. It arises in the parameter regime where the magnetic moment of the impurity is screened by the conduction electrons to form a singlet state [112]. The particle-hole symmetric model lies in the center of this Kondo region. This quasiparticle excitation is for example not captured in mean field approaches (see sec. 3.2). With increasing interaction strength U the numerical solution becomes increasingly challenging.

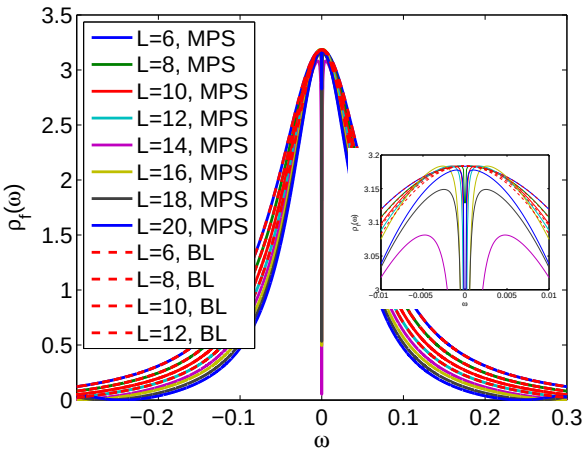

Figure 3.11.: Local single-particle spectral function as a function of ω. For interaction strength $\frac{U}{\Delta} = 8$, on-site energy $\frac{\epsilon_f}{\Delta} = -4$ and a numerical broadening of $0^+ = 10^{-6}$. The CPT results based on a Band Lanczos cluster solver for system sizes $L = 6$ to $L = 12$ are denoted BL. The CPT results based on a MPS Lanczos cluster solver for system sizes $L = 6$ to $L = 20$ are denoted MPS. For small systems the Band Lanczos and the MPS Lanczos results agree. For larger systems, not accessible to Band Lanczos, the MPS Lanczos produces a spurious result in the vicinity of $\omega = 0$ due to missing weight in the Q-matrices. This behavior is expected to be cured in the near future because the method is still under development.

In this section we elaborate on the results for the density of states in the particle-hole symmetric case. Results for the single-particle spectral function eq. (3.43) of the impurity site are shown in fig. 3.13. As a reference, the spectra obtained with NRG and DMRG from Peters [104] are plotted. Renormalization group approaches like NRG are especially suited to reproduce the low energy quasi particle excitations of this model and therefore serve as a reference for our data. The CPT spectral weight at $\omega = 0$ appears too broad in the plot in comparison with the NRG result. This is partly due to a large numerical broadening of $0^+ = 0.05$. Due to the nature of the CPT method we cannot expect it to reproduce the low energy spectrum as well as RG calculations do. The height of the Kondo resonance is too small in this figure because of the large 0^+ which was used to compare to DMRG data only. However the height converges with $0^+ \to 10^{-6}$ to the result predicted by scattering theory (see sec. 3.3.9). The energetically higher excitations like the Hubbard bands located at $\omega \approx -\epsilon_f$ and $\omega \approx -\epsilon_f + U$ develop more and more with increasing length of the cluster part of the reference system L. A comparison of the center of gravity for those developing bands of the $L = 14$ site CPT result and the $L = 50$ site DMRG result are in good qualitative agreement. There are spurious structures in the spectral density, originating from the cluster Green's function of the finite system, preventing continuous bands to form. We would like to note that the accurate determination of the Green's function of the reference system is of prime importance. An inaccuracy in pole-positions or pole-weights for very small but non-vanishing weights will yield spurious artifacts in the spectra in the vicinity of $\omega = 0$ as shown in sec. 3.3.7.
To improve upon the result of CPT we considered the hopping matrix element t and the hybridization matrix element V as variational parameters. The parameters used for the evaluation of the reference system were determined with two different methods. VCA_Ω results are depicted in the plot for a $L = 10$ site cluster. As shown in the figure this method strongly reduces the finite size peaks in the Hubbard bands. The width of the Hubbard bands is reproduced correctly for high values of U where the FWHM within VCA is given by $\approx 1.9\Delta$. This comes very close to the expected 2Δ [90, 122] of the atomic bands. This method improves the spectral properties of the Kondo resonance with respect to CPT, bringing it closer to the $L = 50$ site DMRG result. The data obtained using the self consistent VCA approach $\mathrm{VCA}_{\mathrm{SC}}$ agree very well with the result based on VCA_Ω. One should note that the two broad Lorentzian high energy peaks (in VCA_Ω as well as $\mathrm{VCA}_{\mathrm{SC}}$) consist of many excitations which will be revealed upon repeating this calculation with smaller 0^+. The low computational effort of CPT/VCA proofs advantageous at calculating spectra. The VCA procedure (for a twelve site cluster) usually converges in minutes to hours on a standard workstation PC, while more demanding numerical methods often need days to a week to converge. Furthermore, the spectra are exactly determined from the Lehmann representation and no ill-posed analytical continuation is required in comparison to methods working in imaginary time or imaginary frequency space. To our knowledge the most accurate spectra available for this model so far are published in ref. [123].

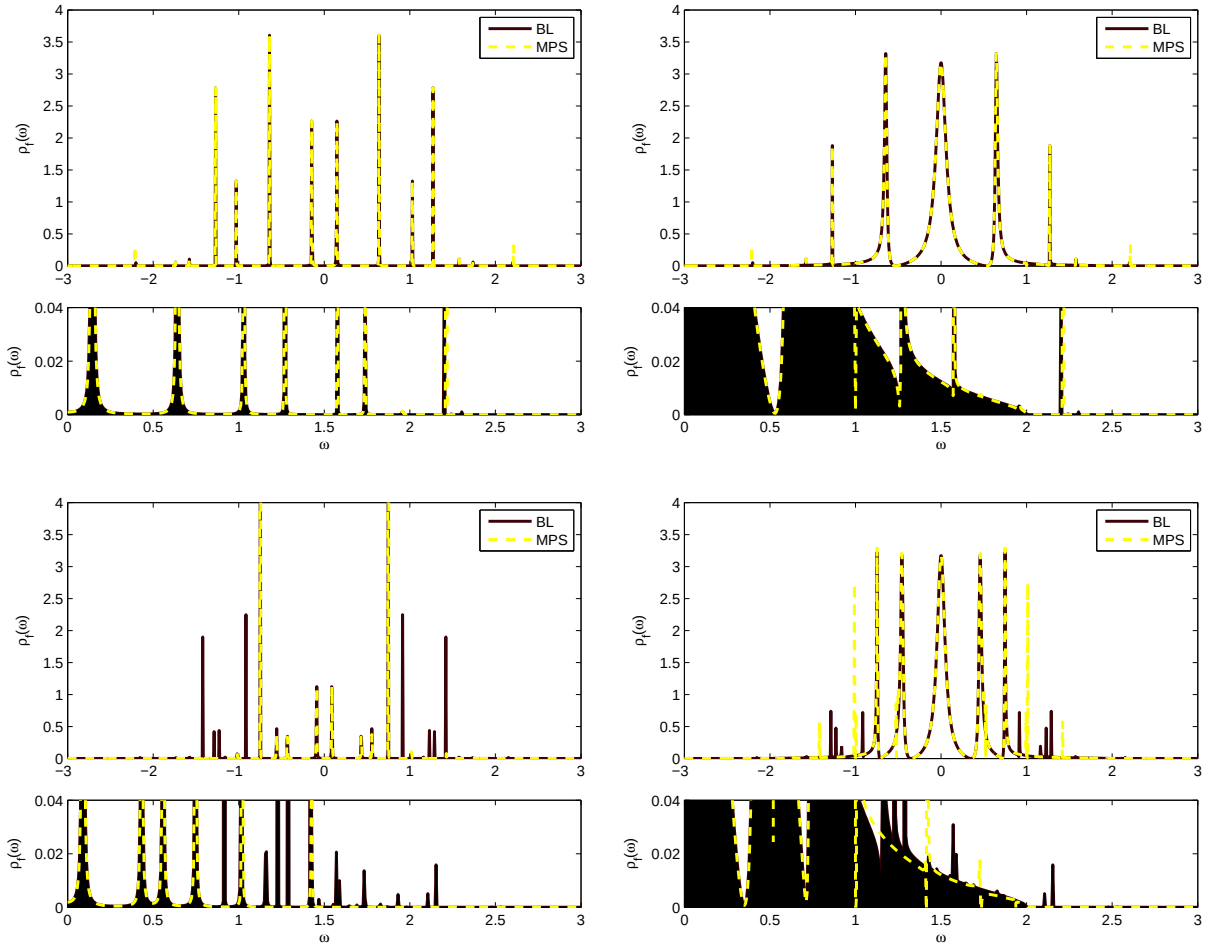

Figure 3.12.: Cluster- and CPT solution of a six- and a twelve-site interacting cluster for the single-particle spectral function of the SIAM. The left column shows the cluster-, the right column, the CPT result. The top row shows the $L = 6$-site results, while the bottom row shows the $L = 12$-site results. The black curves indicate the results obtained by a Band Lanczos cluster solver - the yellow, dashed lines those obtained by a MPS Lanczos solver. Further parameters used were $V = 0.3162$, $t = 1$ and $0^+ = 10^{-6}$.

A spatially resolved image of the spectral function, calculated with CPT, for the parameter set used in fig. 3.13 (c) is shown in fig. 3.14 (left). The qualitative picture would be the same in VCA, merely the structures are slightly shifted. This increased picture reveals how the perturbation introduced by the impurity is fading away slowly in an alternating fashion. At every second site away from the impurity a dip at $\omega = 0$ is present, which is usually referred to as Fano dip.

A zoom to the Kondo peak in the local density of states of the impurity is shown in fig. 3.14 (right) for different values of interaction strength U, in the particle-hole symmetric case, obtained by VCA_Ω. The pinning of the height of the Kondo resonance may be observed, as well as an exponential narrowing of its width. A more detailed look on the spectral region of the Kondo resonance is provided in fig. 3.15. The CPT/VCA_Ω data is compared to NRG and FRG data as well as results obtained from a restricted Hartree-Fock calculation from Karrasch *et al.* [100]. The CPT/VCA results are plotted for lengths of the cluster part of the reference system $L = 2, 4, 6, 8$ and 10 for two different sets of parameters. The results for higher L are always located towards the center of the figure. The results corresponding to the resonance at $\omega = 0$ were obtained for the particle-hole symmetric model. For this set of parameters we used the hybridization V as a variational parameter. The second peak shown centered around $\omega/\Delta \approx 0.8$ corresponds to a parameter set right at the border of the Kondo region. The variational parameters used away from particle-hole symmetry are $\mathsf{x} = \{\epsilon_f, \epsilon_s\}$. One can see that the CPT result is not converged for the $L = 10$ site cluster yet. In contrast, the VCA_Ω result seems to converge much faster. Although in the plot it looks like the VCA result does not improve much upon a restricted Hartree-Fock calculation, in the following we will show that CPT/VCA yields results in all parameter regimes of the SIAM which cannot be reproduced within a mean field treatment (see sec. 3.2).

The variational parameters obtained for the two sets of parameters shown in fig. 3.15 (left) are presented in fig. 3.14 (right). In addition to the VCA_Ω parameters, which were used for the results above, the variational parameters obtained in $\mathrm{VCA}_{\mathrm{SC}}$ are also depicted. We plotted the difference of the parameter of the reference system x' to the physical parameter x: $\Delta\mathsf{x}$. All parameters appear to converge to zero with increasing length of the cluster part of the reference system L. Notice that the self consistent approach always leads to a $\Delta\mathsf{x}$ of greater magnitude with respect to VCA_Ω. Remarkably, the spectrum obtained by VCA_Ω and $\mathrm{VCA}_{\mathrm{SC}}$ for the parameter set $\mathsf{x} = \{\epsilon_f, \epsilon_s\}$ is in very good agreement although the variational parameters are rather different. The most striking difference is that the self consistent approach yields a negative $\Delta\epsilon_f$ while the Ω based VCA yields a positive $\Delta\epsilon_f$. This is however compensated by the different $\Delta\epsilon_s$. Using the hybridization V as a variational parameter, the ΔV obtained by VCA_Ω and $\mathrm{VCA}_{\mathrm{SC}}$ agree rather well. Remarkably, the resulting density of states is very different, which shows that the calculation is extremely sensitive to this parameter.

Overall one can conclude that VCA reproduces the medium and high energy regions of the spectrum reasonably well. The VCA result improves enormously upon the CPT data. In general, the results from VCA_Ω and $\mathrm{VCA}_{\mathrm{SC}}$ agree very well with each other. Next we turn to the examination of static expectation values.

3.3.9. Impurity density of states and occupation

The occupation of the impurity site is given at temperature $T = 0$ by

$$< n_\sigma^f > = \frac{1}{2} + \frac{1}{\pi} \int_0^\infty d\omega \, \mathrm{Re}\, \mathrm{G}_{ff}^\sigma(i\omega) \, . \tag{3.44}$$

This integral may be evaluated from the imaginary frequency Green's function, which in turn is directly accessible within CPT/VCA.

To see whether CPT/VCA are good approximations in all parameter regions of the SIAM, we vary the on-site energy of the impurity ϵ_f at fixed interaction strength U. The local impurity density of states at the chemical potential ($\omega = \mu = 0$) and the impurity occupation number are plotted for various lengths of the cluster part of the reference system $L = 2, 4, 6$ and 8 for the same model parameters. The VCA_Ω result is shown in fig. 3.16 (left), the CPT data in fig. 3.17 (left) and in fig. 3.16 (right) a $\mathrm{VCA}_{\mathrm{SC}}$ calculation. We start out by discussing the VCA_Ω result (fig. 3.16 (left)). The variational parameters x used within VCA_Ω are the on-site energy of the impurity ϵ_f and the on-site energies of the uncorrelated cluster sites ϵ_s. The density of states $\rho_f(0)$ displays a pronounced plateau which is related to the existence of a quasiparticle peak (Kondo resonance) pinned at the chemical potential. The parameter regions leading to an empty ($\epsilon_f < 0$) or to a doubly occupied ($\epsilon_f > U$) impurity do not show the Kondo resonance, as expected. In the half filled region which lies in between, virtual spin fluctuations lead to a pronounced quasi particle peak at the chemical potential. We observe that the result converges with increasing length of the cluster part of the reference system L to the physically expected result. Due to the variational parameters considered, the deviations of the results as a function of L are rather small as compared to CPT where the results

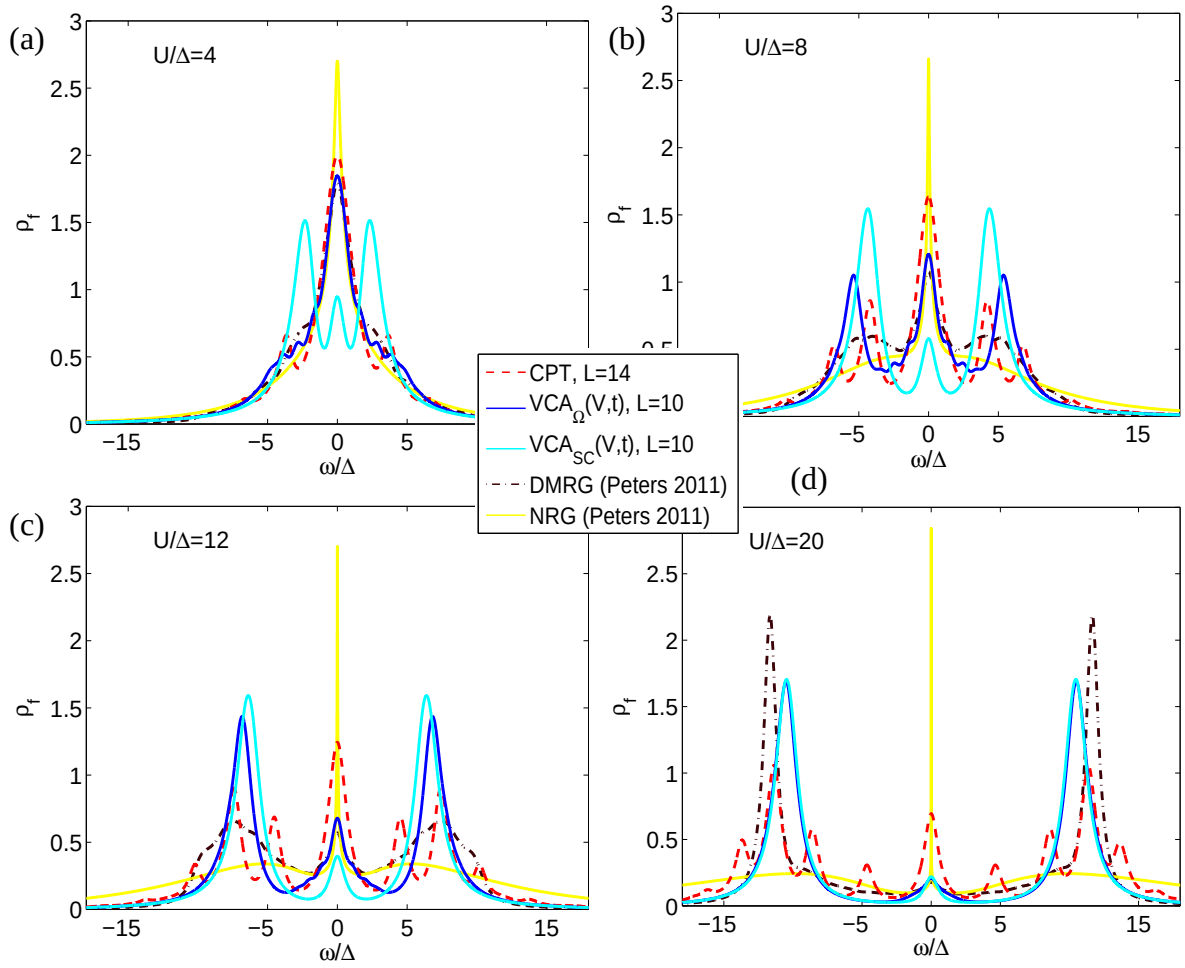

Figure 3.13.: Spectral function at the impurity site at particle-hole symmetry for different interaction strengths U. The interaction strengths shown are $U/\Delta = 4$ in the upper left figure (a), $U/\Delta = 8$ in the upper right figure (b), $U/\Delta = 12$ in the lower left figure (c) and $U/\Delta = 20$ in the lower right figure (d). Each plot shows the results obtained by CPT for a length of the cluster part of the reference system of $L = 14$ (dashed-red), VCA_Ω with two variational parameters: the hopping t and the hybridization V which are determined by the stationary point of the grand potential Ω at a length of the cluster part of the reference system of $L = 10$ (blue), $\mathrm{VCA}_{\mathrm{SC}}$ with the same variational parameters determined self consistently at a length of the cluster part of the reference system of $L = 10$ (cyan). All results have been obtained for a large numerical broadening $0^+ = 0.05$. As a reference the NRG and DMRG results of Peters [104] are plotted in yellow and dash-dotted-dark brown respectively.

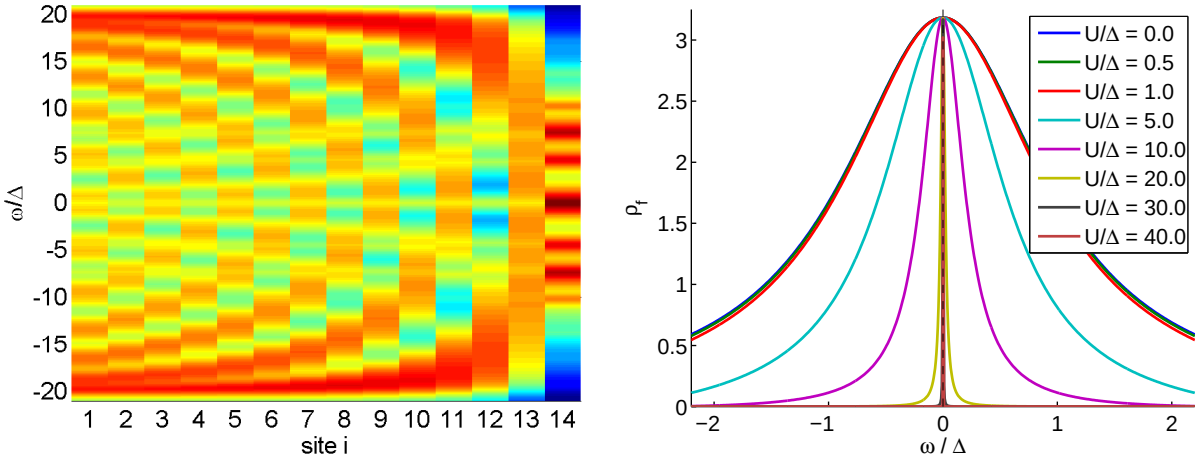

Figure 3.14.: (Left) The local density of states eq. (3.43) is shown resolved in real space. The spectrum was obtained using CPT on a $L = 14$ site cluster. The impurity parameters were $U/\Delta = 12$, $\epsilon_f/\Delta = -6$ and the numerical broadening was set to $0^+ = 0.05$. The spectrum shown in fig. 3.13 (c) corresponds to the data shown for site 14 where the impurity is located. (Right) Zoom to the region of the Kondo peak in the local density of states of the impurity site. The spectra are plotted for several values of interaction strength $U/\Delta = [0, \ldots, 40]$. The curves were obtained for the particle-hole symmetric case, $\Delta = 0.1$, for $0^+ = 10^{-6}$ using VCA_Ω.

change significantly with increasing size of the reference system (see fig. 3.17 (left)). It is difficult to estimate the size of the reference system which is necessary to reach full convergence. We expect CPT calculations in the empty or doubly occupied regions to converge rather fast (within a few sites) while calculations in the Kondo regime, and particularly in the crossover region, may fully converge only at larger sizes ($L \approx 50$) of the reference system (see ref. [116] as well as sec. 3.3.5). This is inferred from the spin-spin correlation function in the cluster which is observed to decay sufficiently fast outside the Kondo plateau (i.e. it is effectively zero at the boundary of the cluster) but shows long range correlations inside the plateau. The $\mathrm{VCA}_{\mathrm{SC}}$ results are obtained with one variational parameter $\mathsf{x} = \{\epsilon_f\}$. The reason for not using $\mathsf{x} = \{\epsilon_f, \epsilon_s\}$ again, is that the result is almost the same as the one obtained with VCA_Ω (see fig. 3.16 (left)). However in some (small) parameter regions the numerical evaluation becomes difficult. The data shown in fig. 3.16 (right) shows a clear improvement as compared to CPT but does not reach the quality of the VCA_Ω result in terms of convergence in system size. Note that for $\mathrm{VCA}_{\mathrm{SC}}$ only one variational parameter was considered as compared to two in the VCA_Ω calculation.
The Friedel sum rule (FSR) [124, 125, 89] provides an exact relation between the extra states induced below the Fermi energy by a scattering center and the scattering phase shift. It also holds true for interacting systems. This gives a relation between the f occupation $< n_\sigma^f >$, and the density of states:

$$\rho_{f,\sigma}(0) = \frac{N_f}{\pi\Delta} \sin^2\left(\frac{\pi < n_\sigma^f >}{N_f}\right) . \tag{3.45}$$

Here N_f denotes the degeneracy of the f orbital and $< n_\sigma^f >$ its mean occupation. In our case $N_f = 2$ and the mean occupation in the Kondo regime $< n^f > \approx 1$. Note that the Friedel sum rule represents the analogon of Luttinger's theorem [126] in the theory of Fermi-liquids [127]. This is why the physics of the impurity is often referred to as local Fermi liquid behavior. Since both of these quantities can be evaluated independently, we can check the validity of the Friedel sum rule in our approximation. Results are shown in fig. 3.16 applied to the $L = 8$ site VCA_Ω results. The VCA_Ω results fulfill the Friedel sum rule almost in the whole Kondo region. At the crossover to a zero or doubly occupied impurity the Friedel sum rule is not fulfilled exactly any more but approximated very well. In the region farther outside it again is perfectly fulfilled. The variational parameters of VCA are crucial to fulfill the Friedel sum rule as can be seen from a CPT calculation (fig. 3.17) which violates it in all parameter regions. It appears as if VCA_Ω with variational parameters $\mathsf{x} = \{\epsilon_f, \epsilon_s\}$ naturally drives the system to fulfill this condition. The $\mathrm{VCA}_{\mathrm{SC}}$ result (fig. 3.16 (right)) violates the sum rule too. This is not a feature of $\mathrm{VCA}_{\mathrm{SC}}$ in general but rather has to do with the choice of variational parameters, which was just $\mathsf{x} = \{\epsilon_f\}$ in this case. The $\mathrm{VCA}_{\mathrm{SC}}$ result for two variational parameters $\mathsf{x} = \{\epsilon_f, \epsilon_s\}$ looks qualitatively like the respective VCA_Ω result.

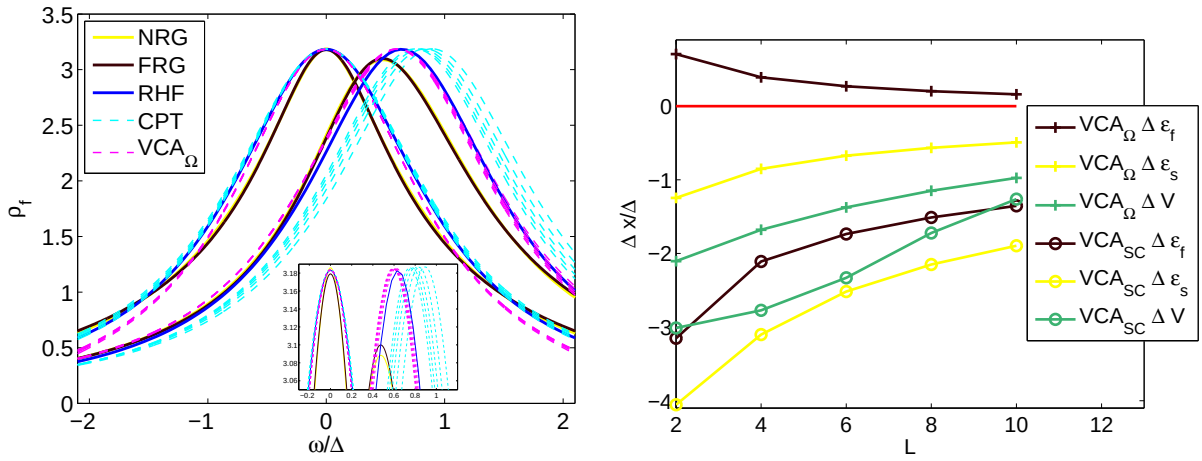

Figure 3.15.: (Left) Magnification of the Kondo resonance in the density of states of the impurity site. Shown are calculations at two different sets of parameters. The resonance at $\omega = 0$ corresponds to the particle-hole symmetric case: $U/\Delta = 20$, $\epsilon_f/\Delta = -10$, while the resonance away from zero corresponds to a set of parameters right at the edge of the Kondo region: $U/\Delta = 20$, $\epsilon_f/\Delta = 0$. For comparison we show NRG (yellow) and FRG (dark brown) data as well as results obtained from a restricted Hartree-Fock calculation (blue) from Karrasch *et al.* [100] (The NRG results are partially hidden by the FRG results.). The CPT result (cyan) is shown for lengths of the cluster part of the reference system $L = 2, 4, 6, 8$ and 10. Results for higher L are always located towards the center of the plot. In the particle-hole symmetric case VCA_Ω (magenta) was performed with variational parameters $\mathsf{x} = \{V\}$ for $L = 2, 4, 6, 8$ and 10. Away from particle-hole symmetry VCA_Ω was performed with variational parameters $\mathsf{x} = \{\epsilon_f, \epsilon_s\}$ for the same lengths of the cluster part of the reference system L. For the CPT/VCA calculations a numerical broadening of $0^+ = 10^{-6}$ was used. The inset shows a zoom to the top region of the peaks. (Right) Magnification of the Kondo resonance in the density of states of the impurity site. Shown are calculations at two different sets of parameters. The resonance at $\omega = 0$ corresponds to the particle-hole symmetric case: $U/\Delta = 20$, $\epsilon_f/\Delta = -10$, while the resonance away from zero corresponds to a set of parameters right at the edge of the Kondo region: $U/\Delta = 20$, $\epsilon_f/\Delta = 0$. For comparison we show NRG (yellow) and FRG (dark brown) data as well as results obtained from a restricted Hartree-Fock calculation (blue) from Karrasch *et al.* [100] (The NRG results are partially hidden by the FRG results.). The CPT result (cyan) is shown for lengths of the cluster part of the reference system $L = 2, 4, 6, 8$ and 10. Results for higher L are always located towards the center of the plot. In the particle-hole symmetric case VCA_Ω (magenta) was performed with variational parameters $\mathsf{x} = \{V\}$ for $L = 2, 4, 6, 8$ and 10. Away from particle-hole symmetry VCA_Ω was performed with variational parameters $\mathsf{x} = \{\epsilon_f, \epsilon_s\}$ for the same lengths of the cluster part of the reference system L. For the CPT/VCA calculations a numerical broadening of $0^+ = 10^{-6}$ was used. The inset shows a zoom to the top region of the peaks. (Right) Evolution of the variational parameters for the data shown in fig. 3.15. Shown is the difference of the parameters of the reference system x' to the physical parameter x: $\Delta\mathsf{x} = \mathsf{x}' - \mathsf{x}$. Parameters obtained by VCA_Ω (crosses) are compared to those obtained by $\mathrm{VCA}_{\mathrm{SC}}$ (circles). The variational parameters $\Delta\epsilon_f$ (dark brown) and $\Delta\epsilon_s$ (yellow) correspond to the calculation away from particle-hole symmetry in fig. 3.15 while the parameter ΔV (olive) corresponds to the calculation at particle-hole symmetry. Lines are only guides to the eye.

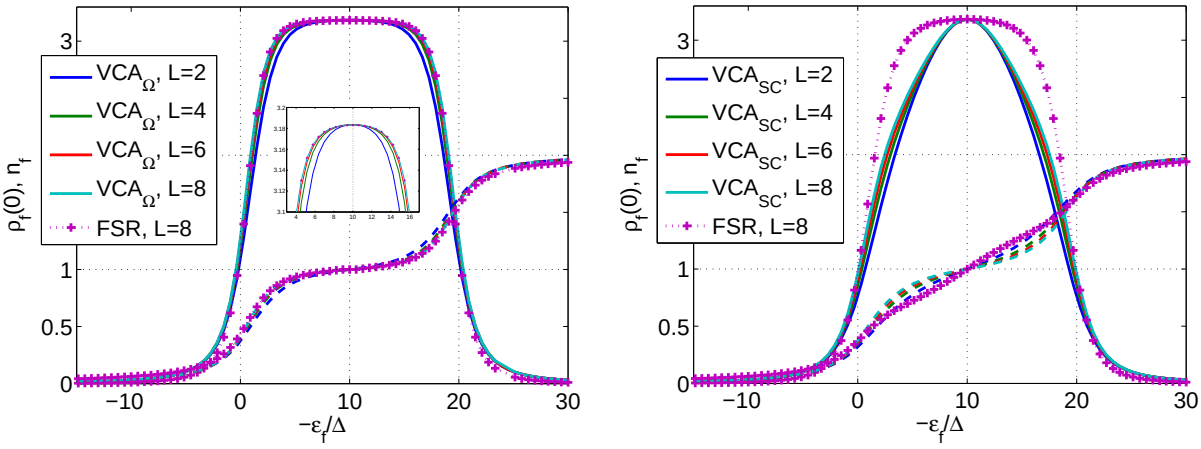

Figure 3.16.: (Left) Density of states of the impurity site (solid lines) obtained via VCA_Ω at $\omega = 0$ and average occupation of the impurity (dashed lines) for different lengths of the cluster part of the reference system $L = 2, 4, 6$ and 8 (blue, green, red and cyan) as a function of the impurity on-site energy ϵ_f. The Coulomb interaction U is kept constant at $U/\Delta = 20$. The numerical broadening used is $0^+ = 10^{-6}$. The set of single particle parameters considered for variation within VCA_Ω is $\mathsf{x} = \{\epsilon_f, \epsilon_s\}$. Note that here the point $\epsilon_f = -\frac{U}{2}$ corresponds to the particle-hole symmetric case. The Friedel sum rule (eq. (3.45)) was applied to the $L = 8$ result (dotted-violet). It is fulfilled to a very good approximation in the Kondo region and far outside of it. Small deviations from the Friedel sum rule arise at the crossover region to an empty or doubly occupied impurity. The inset shows a zoom to the Kondo plateau. (Right) Density of states of the impurity site (solid lines) obtained via $\mathrm{VCA}_{\mathrm{SC}}$ at $\omega = 0$ and average occupation of the impurity (dashed lines) for different lengths of the cluster part of the reference system $L = 2, 4, 6$ and 8 (blue, green, red and cyan) as a function of the impurity on-site energy ϵ_f. The Coulomb interaction U is kept constant at $U/\Delta = 20$. The numerical broadening used is $0^+ = 10^{-6}$. The set of single particle parameters considered for variation within $\mathrm{VCA}_{\mathrm{SC}}$ is $\mathsf{x} = \{\epsilon_f\}$. Note that here the point $\epsilon_f = -\frac{U}{2}$ corresponds to the particle-hole symmetric case. The Friedel sum rule (eq. (3.45)) was applied to the $L = 8$ result (dotted-violet). It is fulfilled outside of the Kondo region only.

Scanning the interaction strength U at fixed impurity on-site energy ϵ_f confirms the presence of the Kondo behavior. Shown in fig. 3.17 (right) are results obtained with VCA_Ω using the same variational parameters $\mathsf{x} = \{\epsilon_f, \epsilon_s\}$ as above. In the weakly correlated part ($U/\Delta \lesssim 5$) the density of states at the chemical potential is low. The intermediate region ($5 \lesssim U/\Delta \lesssim 15$) signals the crossover to the Kondo regime. For larger U the Kondo regime is reached with an impurity occupation of $< n^f > \approx 1$, which may be inferred from the Friedel sum rule. In the inset of the figure, the CPT result for the same lengths of the cluster part of the reference system L are shown. The CPT results are by far not converged for the cluster sizes considered here. This emphasizes the importance of the variational parameters.
The results in fig. 3.16 and fig. 3.17 (right) agree very well with those of calculations based on X-operator technique exercised by Lobo *et al.* [107]. In their work a strong coupling perturbation theory is applied starting from the Anderson molecule as a basis and using the Friedel sum rule as a condition to fix the position of an infinitely narrow conduction band.
The results of this section clearly show that VCA is able to capture the physics of the SIAM in every parameter region. The improvement obtained by going over from CPT to VCA is crucial to fulfill exact analytic relations. The results of this chapter are extended in the next section by constructing a crossover diagram.

3.3.10. Crossover diagram

To delve into the CPT/VCA results for the whole parameter range of the SIAM a "phase diagram" is presented in this section. This is to be understood to be a mere scan of the parameters U and ϵ_f because the model does not undergo a phase transition, unlike indicated in the mean field results presented in sec. 3.2. The density of states of the impurity at the chemical potential $\rho_f(0)$ is shown in fig. 3.18 in a density plot. The left result was obtained using VCA_Ω, the result shown in the right by CPT. This plot essentially shows the height of the Kondo resonance as a function of interaction strength and on-site

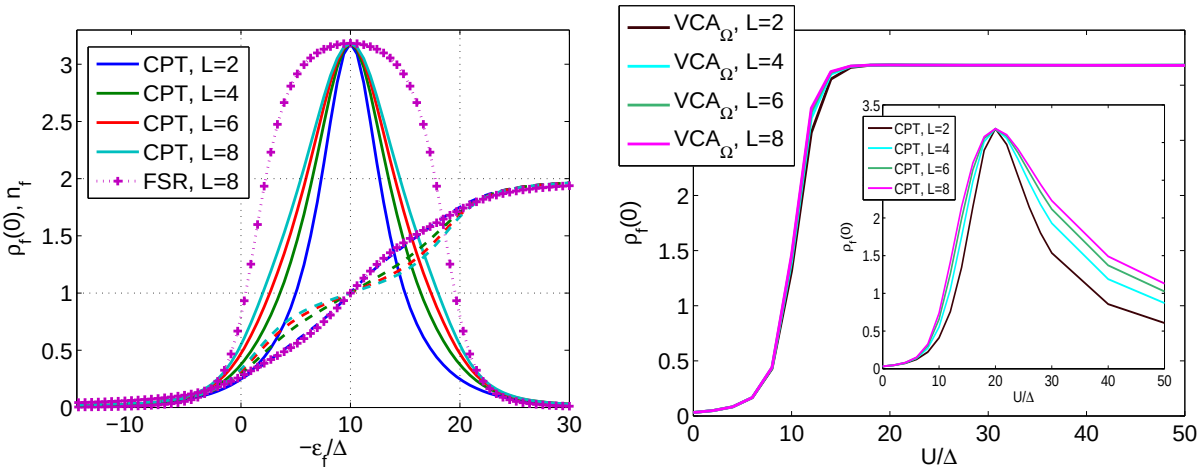

Figure 3.17.: (Left) Density of states of the impurity site (solid lines) obtained via CPT at $\omega = 0$ and average occupation of the impurity (dashed lines) for different lengths of the cluster part of the reference system $L = 2, 4, 6$ and 8 (blue, green, red and cyan) as a function of the impurity on-site energy ϵ_f. The Coulomb interaction U is kept constant at $U/\Delta = 20$. The numerical broadening used is $0^+ = 10^{-6}$. Note that here the point $\epsilon_f = -\frac{U}{2}$ corresponds to the particle-hole symmetric case. The Friedel sum rule (eq. (3.45)) was applied to the $L = 8$ result (dotted-violet). It is drastically violated. However the results are far from converged for the small lengths of the cluster part of the reference system considered here. (Right) Density of states of the impurity site at $\omega = 0$ for different lengths of the cluster part of the reference system $L = 2, 4, 6$ and 8 (dark brown, cyan, olive and magenta) as a function of the interaction strength U. The impurity on-site energy ϵ_f is kept constant at $\epsilon_f/\Delta = -10$. The numerical broadening is chosen to be $0^+ = 10^{-6}$. The set of single particle parameters considered for variation within VCA_Ω is $\mathsf{x} = \{\epsilon_f, \epsilon_s\}$. The inset shows the CPT results.

energy of the impurity. The different regimes of the SIAM, as obtained by an atomic limit calculation (see sec. 3.1), are indicated by black lines. These lines divide the physics into regions where the impurity is doubly, singly or not occupied. In the singly occupied region ($\frac{U}{2} > |\epsilon_f + \frac{U}{2}|$) local moments and their screening is expected to appear. This region which bestrides the cone enclosed by black lines is the region where Kondo physics may take place within this approximation. The parameter regions where the impurity is empty or doubly occupied lie above and below this cone. More sophisticated methods will lead to a smearing out of the border of these regions and introduce a crossover area with competing effects. A boundary expected between a single resonance and a local moment behavior where the single resonance is split into two for spin up and spin down respectively is given by mean field theory (see sec. 3.2). The mean field boundary is obtained from eq. (3.19). The plot shows that the Kondo plateau is reproduced very well by VCA_Ω. The Friedel sum rule eq. (3.45) is fulfilled in all parameter regions in contrast to the CPT result, which clearly shows a weak behavior. The VCA_Ω results are almost converged for lengths of the cluster part of the reference system $L \approx 6$. Increasing L yields better results in the crossover region. Results obtained by means of CPT do not reproduce the Kondo plateau very well for small length of the cluster part of the reference system. We estimate that CPT needs a length of the cluster part of the reference system of $L \approx 50$ to reproduce the Kondo plateau as good as VCA with $L = 6$ sites. The spurious spectral weight arising in the plot in some regions of $U < 0$ may arise as a numerical artifact of the VCA procedure.

The average impurity occupation for the same parameter region is shown in fig. 3.19. The result obtained with VCA_Ω (fig. 3.19 (left)) clearly shows the Kondo plateau where the impurity is singly occupied. The parameter regions of a doubly occupied or empty impurity lead to a density of states in the impurity which is zero at the chemical potential (compare to fig. 3.18). The CPT result (fig. 3.19 (right)) again shows, that CPT would need much larger cluster sizes. A similar behavior is also found at examining the spin-spin correlations of the cluster part of the reference system (see fig. 3.9 (right)). Note that cuts at certain parameter values through the plots: fig. 3.18 and fig. 3.19 are presented in fig. 3.16 (left) and fig. 3.17 (left) for a more detailed overview. The results of this section have been obtained using VCA_Ω with variational parameters $\mathsf{x} = \{\epsilon_f, \epsilon_s\}$. It should be noted that using only $\mathsf{x} = \{\epsilon_f\}$ already yields good results. As mentioned in sec. 3.3.9, CPT needs quite large lengths of the cluster part of the reference system L to converge to the VCA results. Having shown that VCA produces overall good results in all

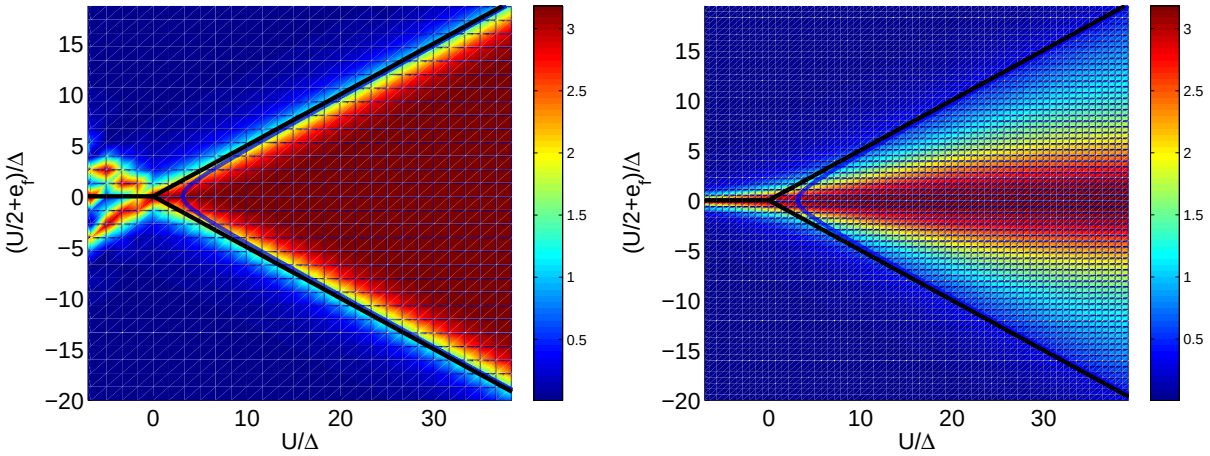

Figure 3.18.: In the plot a "phase diagram" of the SIAM is shown. The quantity on the z-axis is the density of states in the impurity ρ_f at $\omega = 0$ (i.e. the height of the Kondo resonance). The black line indicates the different regions obtained from an atomic limit calculation. In the right cone local moments are to be expected. While in the upper region the impurity is expected to be empty and in the lower half to be doubly occupied. The blue curve shows the onset of a magnetic state as obtained by a mean field treatment (see text). (Left) The results where obtained with VCA_Ω for a set of variational parameters $\mathsf{x} = \{\epsilon_f, \epsilon_s\}$, a length of the cluster part of the reference system of $L = 6$ sites and $0^+ = 10^{-6}$. (Right) The CPT result for the same parameters.

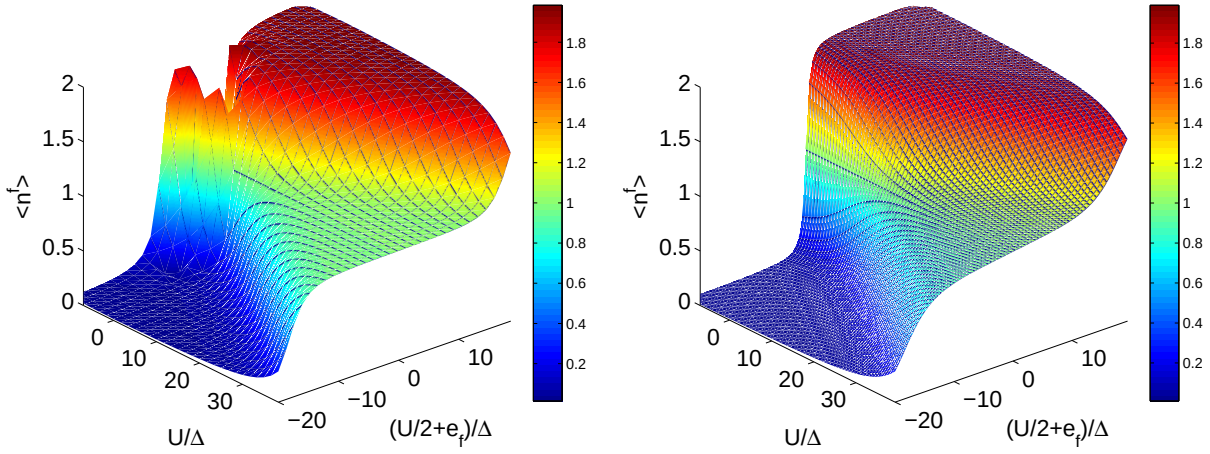

Figure 3.19.: Average particle density in the impurity $< n^f >$ as a function of U and ϵ_f for the same parameters as in fig. 3.18. (Left) The VCA_Ω result. (Right) The CPT result.

parameter regions for the general features of the spectra, we turn to the much harder accessible case of the low energy properties.

3.3.11. Low energy properties, Kondo Temperature

In this section we examine the low energy properties of the symmetric SIAM. In the strong coupling limit a single scale, the Kondo temperature T_K, governs the low energy physics. This scale may be extracted from the width of the Kondo resonance in the local density of states.
The Kondo temperature T_K is known from Bethe Ansatz results for the particle-hole symmetric SIAM [7, 128]

$$T_K = \sqrt{\frac{\Delta U}{2}}\, e^{-\gamma \frac{\pi}{8\Delta} U} \ , \ \gamma = 1 \ . \tag{3.46}$$

This scale which is inversely proportional to the spin-flip rate of the impurity divides the physics of the SIAM into two regions. A local moment behavior of the impurity, where the spin is free and a low temperature region where the local spin and the conduction electrons become entangled and form a singlet state [111].
Quantities which depend inversely on T_K are the effective mass m^* and the static spin susceptibility χ_m. We investigate and compare the results for the scale T_K obtained from the direct determination of T_K (from the full width at half maximum and the spectral weight of the Kondo resonance) and the inverse quantities m^* and χ_m. We find that the results of all four measurements turn out to yield the correct qualitative behavior in VCA_Ω. However in a region where the dependence of T_K is exponentially dependent on the interaction strength U the exponential prefactor is not predicted correctly. Therefore we introduce a scaling factor γ eq. (3.46) which turns out to be the same for all four ways of determining T_K. In particular this factor is independent of the set of parameters used. The scaling factor may be calculated semi-analytically for a reference system consisting of a two site cluster and the semi-infinite environment within VCA_Ω and $\mathrm{VCA}_{\mathrm{SC}}$ ($\mathsf{x} = \{V\}$) (see sec. 3.3.3). The calculation for VCA_Ω leads to an integral expression for the stationary point of the grand potential Ω with respect to ΔV from which the optimal ΔV can be obtained numerically (see sec. 3.3.3). The Kondo scale may be determined from the so obtained values of $V'(U) = \Delta V(U) + V$ by

$$T_K(U) \propto \left(\frac{V'(U)}{U} \right)^2 \ . \tag{3.47}$$

This leads to a perfect exponential behavior with an exponent defined in eq. (3.46) where

$$\gamma = 0.6511 \ .$$

In the following subsections the numerical results obtained by VCA_Ω will be plotted in semi-logarithmic plots over a scaled x-axis: $\alpha \frac{U}{\Delta}$, where $\alpha = \frac{1}{\gamma}$ for the VCA_Ω results. The issue of obtaining an exponential scale but not the correct exponent for the functional dependence on U is common to various approximate methods (for example variational wavefunctions where the issue was cured by introducing an extended Ansatz by Schönhammer [117], saddle-point approximations of a functional integral approach [129] or FRG [118]). A faint analogy may be drawn here to Gutzwiller approximation, where an exponential energy scale in U arises by a renormalized hybridization parameter V [9], which seems also to be the case for VCA_Ω.
The self-consistent calculation for $\mathrm{VCA}_{\mathrm{SC}}$ also leads to an integral expression for the determination of ΔV. This expression is obtained by requiring the expectation values of the hopping from the impurity site to the first site in the chain in the cluster to be the same as the expectation value in the full solution. This procedure does not yield an exponential scale in U. The optimal cluster parameter V' shows spurious behavior as a function of U (see sec. 3.3.3). We conclude that $\mathrm{VCA}_{\mathrm{SC}}$ with $\mathsf{x} = \{V\}$ cannot reproduce the low energy properties of the SIAM, while VCA_Ω yields the correct behavior apart from a factor.

Effective Mass - Quasiparticle Renormalization

The effective mass m^* is defined as the quasiparticle renormalization [100]

$$\begin{aligned}\frac{m^*(U)}{m^*(0)} &= 1 - \left.\frac{d[\operatorname{Im}\Sigma^\sigma_{ff}(i\omega,U)]}{d\omega}\right|_{\omega=0^+} \\ &= \left.\frac{d[\operatorname{Im}\mathrm{G}^\sigma_{ff}(i\omega,U)]}{d\omega}\right|_{\omega=0^+} \times \\ &\left(\left.\frac{d[\operatorname{Im}\mathrm{G}^\sigma_{ff}(i\omega,0)]}{d\omega}\right|_{\omega=0^+}\right)^{-1},\end{aligned} \tag{3.48}$$

where we introduced the dependence on the interaction strength U explicitly. In the Kondo regime, this quantity becomes inversely proportional to the Kondo temperature.
We want to answer the question whether the Kondo scale is captured by CPT/VCA or not. Therefore we compare the functional form and the exponent obtained from the effective mass and the analytic result for T_K eq. (3.46). The result for the effective mass obtained within VCA_Ω is shown in fig. 3.20 (left). The variational parameter used was $\mathsf{x} = \{V\}$. The functional form is reproduced well by VCA_Ω (i.e. it starts out quadratically and goes over to an exponential behavior in the Kondo region). However the exponent $(\frac{\pi}{8\Delta})$ is not reproduced correctly. VCA_Ω yields a lower exponent of $\approx (\gamma\frac{\pi}{8\Delta})$. The factor γ is defined in sec. 3.3.3, determined from a semi-analytical calculation of T_K within VCA_Ω. This additional factor is the same for all initial parameters (within the Kondo regime), it is particularly independent of Δ. Therefore the x-axis for the CPT/VCA results is scaled by $\alpha = \frac{1}{\gamma}$ to see that the functional form of the effective mass matches the NRG result [100] to a very good approximation. The VCA results are already converged for small cluster sizes of $L = 6$ while the CPT results converge rather slowly. An attempt was made to extrapolate the CPT data to $L \to \infty$. It is interesting to observe that this extrapolated curve coincides nicely with the VCA result (L=6) in the low U region. Note that for this quantity the VCA result is almost independent of the length of the cluster part of the reference system as will be motivated in sec. 3.3.12.

Kondo Spectral Weight and Half Width

Since the height of the Kondo resonance is fixed by the Friedel sum rule eq. (3.45) the width and the weight (area) of the peak are proportional to the Kondo temperature T_K. Obtaining the spectral weight or full width at half maximum (FWHM) of the Kondo resonance from the spectrum introduces a large uncertainty. Nevertheless we made an attempt, to get an idea of the behavior of T_K. We fixed the spectral weight by the first minimum to the left and to the right of the central peak. In general the effective mass and static spin susceptibility will yield more reliable results but it is instructive to compare these four ways of determining T_K.
Shown in fig. 3.20 (right) is the evolution of the spectral weight and the FWHM of the Kondo resonance with increasing interaction strength U. The data were calculated using VCA_Ω with a variational parameter $\mathsf{x} = \{V\}$ for the particle-hole symmetric SIAM. For the results shown in the plot the x-axis of the VCA result has been scaled by the same factor α as in the previous section for easier comparison to the Bethe Ansatz result.

Static spin susceptibility

The static spin susceptibility χ_m is given by the linear response to an applied magnetic field B in z direction

$$\chi_m(U) = -\left.\frac{d\left(\langle n_{f\uparrow}\rangle - \langle n_{f\downarrow}\rangle\right)}{dB}\right|_{B=0}. \tag{3.49}$$

In the Kondo regime this quantity too becomes inversely proportional to the Kondo temperature. For the calculations in this section we introduce an additional spin dependent term in the impurity Hamiltonian eq. (3.3)

$$\hat{\mathcal{H}}_{\text{magnetic}} = \sum_\sigma \sigma \frac{B}{2} f^\dagger_\sigma f_\sigma. \tag{3.50}$$

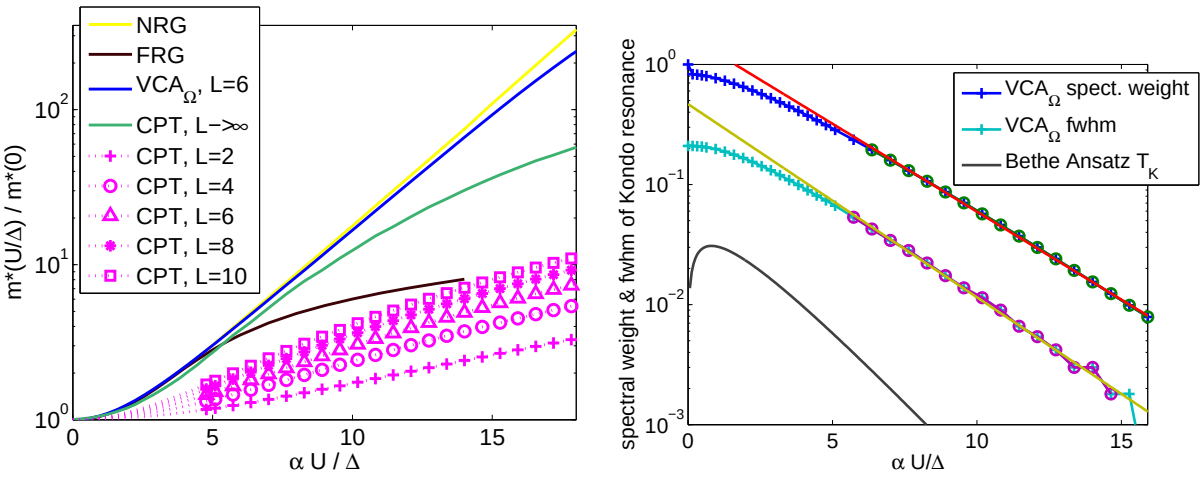

Figure 3.20.: (Left) Effective mass m^* of the Kondo resonance eq. (3.48) as a function of interaction strength U. We plot CPT results for lengths of the cluster part of the reference system $L = 2, 4, 6, 8$ and 10 (magenta), the to $L \to \infty$ extrapolated CPT result (olive), as well as VCA_Ω results (blue). The data points for the CPT result in the low U region are not shown to avoid messing up the plot. The variational parameter used for the VCA_Ω result was $\mathsf{x} = \{V\}$. The VCA_Ω data was obtained for a reference system of length $L = 6$. For CPT as well as VCA_Ω we used a numerical broadening of $0^+ = 10^{-6}$. For comparison the results obtained by NRG (yellow) and FRG (dark brown) are shown [100]. The factor α on the x-axis is $\alpha = 1$ for NRG and FRG data and $\alpha = \frac{1}{\gamma}$ for CPT as well as VCA_Ω results (see text). (Right) VCA_Ω results for the spectral weight (blue) and full width at half maximum (olive) of the Kondo resonance as a function of interaction strength U. The variational parameter used was $\mathsf{x} = \{V\}$. A length of the cluster part of the reference system of $L = 6$ sites and a numerical broadening of $0^+ = 10^{-6}$ were used for this calculation. Data points marked with a circle were used for the fit of the exponential function in the Kondo region. The black line shows the Kondo temperature T_K as obtained by Bethe Ansatz calculations eq. (3.46). The factor α on the x-axis is $\alpha = 1$ for Bethe Ansatz data and $\alpha = \frac{1}{\gamma}$ for VCA_Ω data (see text).

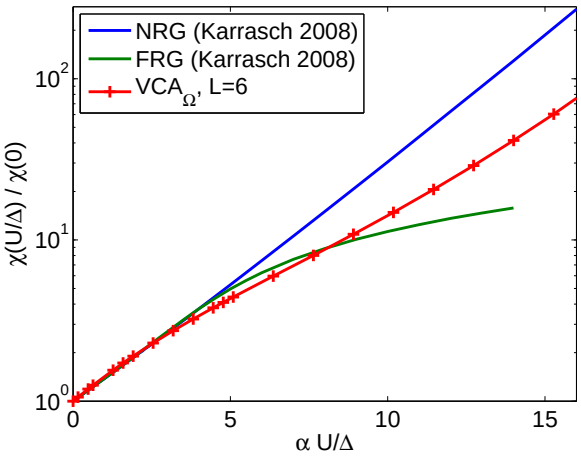

Figure 3.21.: The static spin susceptibility χ_m eq. (3.49) is shown as a function of interaction strength U. The variational parameter used was $\mathsf{x} = \{V\}$. The data were obtained for $L = 6$ sites and $0^+ = 10^{-6}$. For comparison the results obtained by NRG (blue) and FRG (green) are shown [100]. The factor α on the x-axis is $\alpha = 1$ for NRG as well as FRG results and $\alpha = \frac{1}{\gamma}$ for VCA_Ω data (see text).

The static spin susceptibility χ_m as obtained with VCA_Ω is shown in fig. 3.21. The variational parameter used was $\mathsf{x} = \{V\}$. As in the two preceding sections the x-axis was scaled by α for the VCA_Ω data. As a reference the results of NRG and FRG [100] are shown. The behavior of the VCA result is good for small interaction strength U. The VCA result shown for $L = 6$ sites is already converged while the CPT result would require much larger systems.

We would like to highlight that VCA reproduces an energy scale T_K. Results from direct calculation of T_K and calculation of the effective mass m^* and the static spin susceptibility χ_m yield the correct functional form but not the right exponent. The results of this section are further explored in the next paragraph, when the result for the CPT/VCA self-energy is compared to CT-QMC data.

3.3.12. Benchmarking CPT/VCA against continuous time Quantum Monte Carlo

In this section we compare CPT/VCA results to QMC data. We obtained the Monte Carlo results using the continuous time Quantum Monte Carlo (CT-QMC) code of the TRIQS [130] toolkit and its implementation of the hybridization expansion (CT-HYB) [131] algorithm using Legendre polynomials [132]. This method enables access to very low temperatures and is especially suited to obtain low energy properties [19]. The CT-QMC data provides statistically exact and reliable results to test our data.
All CT-QMC calculations were done for a single impurity orbital at $U = 0.8$ and $\epsilon_f = -0.4$. We used a semicircular hybridization function with half bandwidth $D = 2$ and $V = 0.3162$. This setup corresponds to the same model under investigation here. The value for the interaction strength $U = 0.8$ was chosen because of the relatively low expected Kondo temperature of $\beta_K = \frac{1}{T_K} \approx 100$. For all calculations 1.2×10^9 MC updates where conducted, with a sweep size of 100 updates, plus a 10% thermalization period.
To ensure that the Kondo resonance is correctly reproduced by CT-QMC we evaluated the Matsubara Green's function for various values of inverse temperature β. The height of the Kondo resonance is given by the Friedel sum rule eq. (3.45) to be $\Im\mathrm{m}(G_{ff}(i\omega = 0)) = -10$ for the parameters used here ($\Delta = 0.1$). To obtain $\Im\mathrm{m}(G_{ff}(i\omega = 0))$ we extrapolate twice, first in $i\omega \to 0$ for each β, then we use these results and extrapolate to $T \to 0$. The extrapolation to $i\omega \to 0$ is done linearly using the first two Matsubara frequencies. The imaginary part of $\mathrm{G}_{ff}(i\omega)$ and the extrapolated value to $i\omega \to 0$ are shown in the inset of fig. 3.22 (left) for $\beta \in [10, 1200]$. Those extrapolated values are plotted as a function of temperature (fig. 3.22 (left)). These data points are then extrapolated to $T \to 0$ using a fit by a rational model function. The result clearly shows the onset of the Kondo resonance when the temperature is lowered below the Kondo temperature T_K. The extrapolation to $T = 0$ shows very good agreement ($\Im\mathrm{m}(G_{ff}(i\omega = 0)) \approx -10.1$) with the result expected from the Friedel sum rule within the uncertainty. It is important to note that the CT-QMC results converge very nicely in β. Although for higher β lower Matsubara frequencies become available, the overall shape of the Green's function does not change significantly.
Therefore we may compare the $T = 0$ CPT/VCA results for the Green's function and self-energy to the

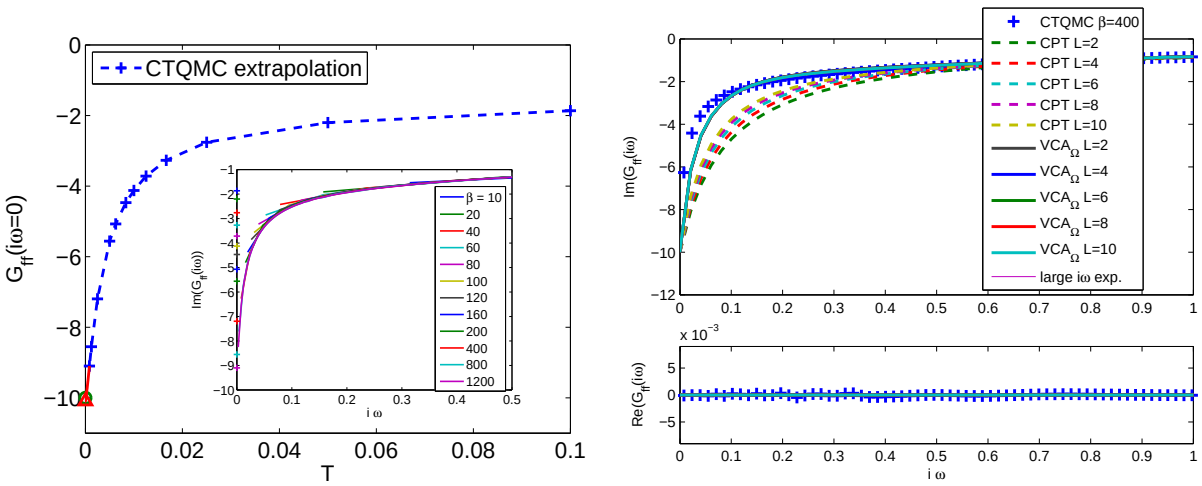

Figure 3.22.: (Left) CT-QMC result for the imaginary part of the impurity Green's function extrapolated to $i\omega = 0$. An extrapolation to zero temperature is attempted, which yields a good agreement with the result predicted by the Friedel sum rule (green circle) within the uncertainty (red triangle). The inset shows the imaginary part of the impurity Green's function for various β (see legend) and the extrapolated points at $i\omega = 0$. (Right) Comparison of the Matsubara impurity Green's function $G_{ff}(i\omega)$ obtained by CT-QMC ($\beta = 400$), CPT and VCA$_\Omega$. The CPT/VCA results were obtained for lengths of the cluster part of the reference system of $L = 2, 4, 6, 8$ and 10. The real part shown in the lower part of the figure is zero. The Friedel sum rule prediction of $\Im\mathrm{m}(G_{ff}(i\omega = 0)) = -10$ is fulfilled by all methods. The legend of this figure serves as well as legend for fig. 3.23 (left) and fig. 3.23 (right). That is why the last entry (large $i\omega$ exp.) is displayed in the legend but is missing in the graph of this figure.

CT-QMC data. The Matsubara Green's functions of the impurity site $G_{ff}(i\omega)$ obtained by CT-QMC ($\beta = 400$), CPT and VCA are shown in fig. 3.22 (right). We use $\beta = 400$ as a compromise between low temperatures and still reliable CT-QMC results (within manageable computation time). The $\beta = 400$ result was obtained using 65 Legendre coefficients. A detailed analysis has shown that this number is sufficient to get high frequency moments of the self-energy Σ accurately. The VCA$_\Omega$ results were obtained with one variational parameter $\mathsf{x} = \{V\}$ for $U = 0.8$, $\Delta = 0.1$ and $0^+ = 10^{-6}$ in the particle-hole symmetric case. For the CPT calculation we used the same parameters. For both methods we considered lengths of the cluster part of the reference system of $L = 2, 4, 6, 8$ and 10. The imaginary part of the CPT result converges with increasing length of the cluster part of the reference system to the expected result. The VCA result lies near the CT-QMC data but underestimates the slope of the curve at low $i\omega$. The VCA result provides a huge improvement upon CPT for the lengths of the cluster part of the reference system shown here. The real part of $G_{ff}(i\omega)$ is exactly zero within CPT/VCA as it is supposed to be. Note that the value of $G_{ff}(i\omega = 0)$ which is fixed by the Friedel sum rule is exactly reproduced within CPT and VCA for the particle-hole symmetric case. The same is shown for the self-energy of the impurity site $\Sigma_{ff}(i\omega)$ in fig. 3.23 (right). From the imaginary part of $\Sigma_{ff}(i\omega)$ one can infer the convergence of the CPT/VCA result with larger length of the cluster part of the reference system L. The real part of the self-energy $\Re\mathrm{e}(\Sigma_{ff}(i\omega) = \mu = -e_f = \frac{U}{2} = 0.4)$ is again exactly reproduced within CPT/VCA.
In the following, we discuss the self-energy $\Sigma(i\omega)$ for the two interesting cases of very low and very high Matsubara frequency. We start out by conducting an expansion of the self-energy $\Sigma(z)$ for high Matsubara frequencies ($z = i\omega \to \infty$) which shall be outlined here briefly. The self-energy matrix is defined by

$$\begin{aligned}\Sigma(z) &= \mathrm{G}_0^{-1} - \mathrm{G}^{-1} \\ &= z - \mathrm{T} - \mathrm{G}^{-1} \,.\end{aligned}$$

Here T is the one-particle part of the Hamiltonian. In the particle-hole symmetric case considered here it contains all the hoppings as well as the on-site energy of the impurity $\epsilon_f = -\frac{U}{2}$. We conduct a series expansion in powers of z^{-1} of $\Sigma(z)$. Apart from the real constant T_{ii} all z-dependent terms of $\Sigma_{ii}(z)$ are anti-symmetric in z. Therefore even powers in $z^{\pm 2l}$, $l > 0$ vanish. Expanding the Green's function $\mathrm{G}(z)$

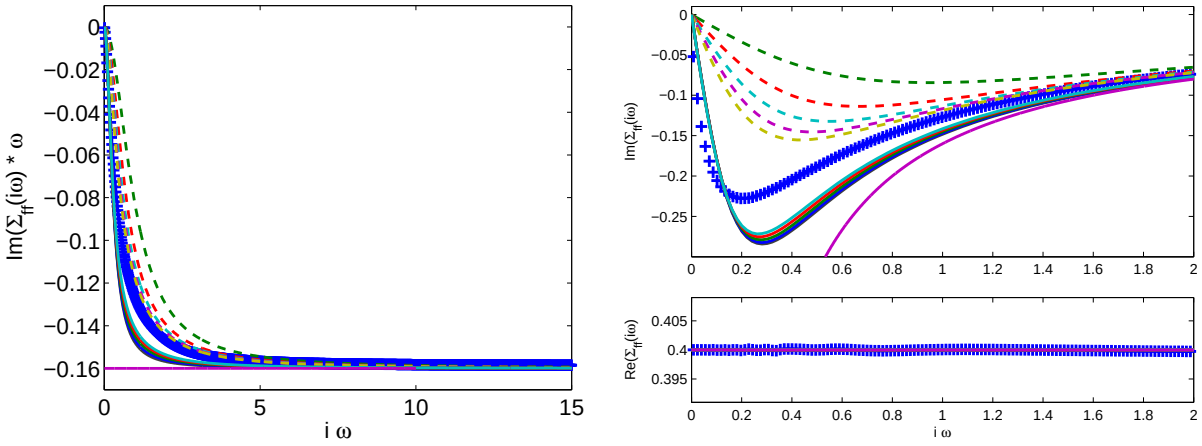

Figure 3.23.: (Left) Comparison of the self-energy of the impurity $\Sigma_{ff}(i\omega)$ times energy ω obtained by CT-QMC ($\beta = 400$), CPT and VCA_Ω. The CPT/VCA results were obtained for lengths of the cluster part of the reference system of $L = 2, 4, 6, 8$ and 10. CPT as well as VCA_Ω become exact for high Matsubara frequencies. The legend for this figure is the same as for fig. 3.22 (right) and is displayed there. (Right) Comparison of the imaginary part of the self-energy of the impurity $\Im\text{m}(\Sigma_{ff}(i\omega))$ obtained by CT-QMC ($\beta = 400$), CPT and VCA_Ω. The CPT/VCA results were obtained for lengths of the cluster part of the reference system of $L = 2, 4, 6, 8$ and 10. An expansion of $\Sigma(i\omega)$ for large $i\omega$ eq. (3.51) is additionally shown (straight line at $-\left(\frac{U}{2}\right)^2$). CPT/VCA always reproduces the exact self-energy for high Matsubara frequencies. The legend for this figure is the same as for fig. 3.22 and is displayed there.

yields for the self-energy $\Sigma(z)$

$$\begin{aligned}
\Sigma(z) &= -\mathrm{T} - z \sum_{m=1}^{\infty} (-1)^m X^m \,, \\
X &= \sum_{n=1}^{\infty} z^{-n} C_n \,, \\
(C_n)_{ij} &= \langle \Psi_0 | a_i \ (\Delta\hat{\mathcal{H}})^n a_j^\dagger | \Psi_0 \rangle \\
&\quad + (-1)^n \ \langle \Psi_0 | a_j^\dagger (\Delta\hat{\mathcal{H}})^n a_i \, | \Psi_0 \rangle \ ,
\end{aligned}$$

where $\Delta\hat{\mathcal{H}} = \hat{\mathcal{H}} - \omega_0$. Collecting powers of z yields a cumulant-like expansion for the self-energy $\Sigma(z)$

$$\begin{aligned}
\Sigma(z) &= \sum_{n=1}^{\infty} z^{-n} \Sigma_n \ , \text{ where} \\
\Sigma_0 &= -T + C_1 \ , \text{ and} \\
\Sigma_1 &= C_2 - C_1^2 \ .
\end{aligned}$$

Here we consider the zeroth and first order in z^{-1} only and obtain for $\Sigma(i\omega)$

$$\Sigma_{ff}(i\omega) = \frac{U}{2} - \frac{i}{\omega} \left(\frac{U}{2}\right)^2 + \mathcal{O}\left(\frac{1}{i\omega}\right)^3 \ , \tag{3.51}$$

where the self-energy at the impurity site Σ_{ff} is the only non-vanishing matrix element of Σ_{ij}. This result is plotted as a reference in fig. 3.23 (right). Due to the nature of the CPT/VCA approximation these methods always yield the exact self-energy for high Matsubara frequency as shown in fig. 3.23 (left). The low energy properties examined in the previous section depend basically on the slope of the Matsubara Green's function at $(i\omega) = 0^+$. The results shown in fig. 3.22 (right) and fig. 3.23 (right) show that this slope is underestimated by CPT/VCA in comparison to CT-QMC, at least at the small lengths of the cluster part of the reference system available. The qualitative picture however shows a good agreement with the expected physics.

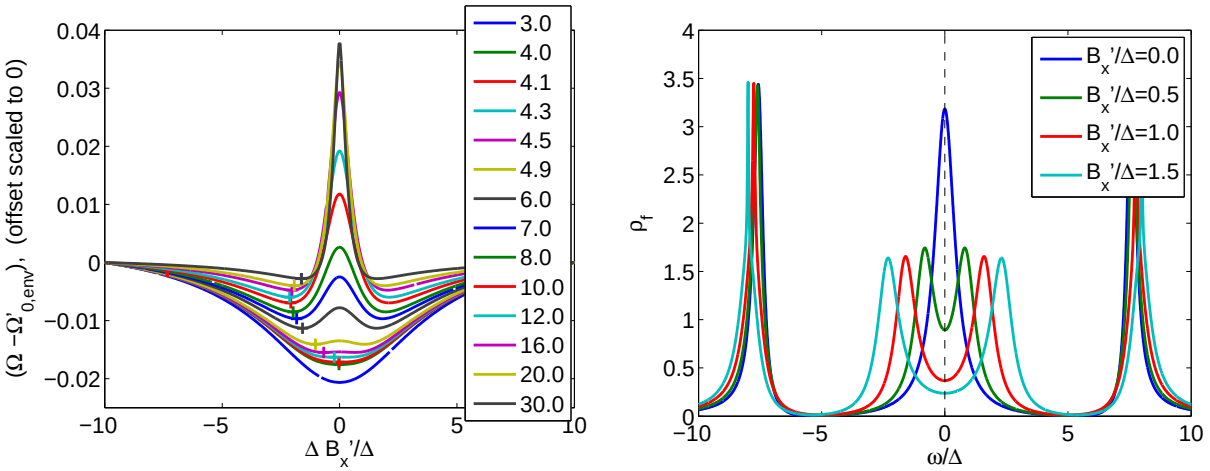

Figure 3.24.: (Left) Grand potential $\Omega - \Omega'_{0,env}$ (eq. (D.18)) as a function of the interaction strength U/Δ (see legend). The data was obtained by studying a $L = 4$ site cluster coupled to an infinite lead. The numerical broadening used was $0^+ = 10^{-6}$. The crosses indicate the respective minimum of the grand potential. There exists a critical $U_c/\Delta \approx 4.3$ above which a finite B'_x is preferred by the system. (Right) The splitting of the Kondo resonance caused by an applied magnetic field in x direction is shown for different values of the auxiliary field B'_x. The plots were obtained using VCA (i.e. the physical field B_x is always zero). Instead of taking the parameter B'_x at the stationary point of the grand potential (this value would be $B'_x/\Delta \approx 1.9$ for the parameters used) we explicitly plug in a fixed value for B'_x. The length of the cluster part of the reference system used was $L = 6$ for the model parameters $U/\Delta = 12$. The numerical broadening used was $0^+ = 10^{-6}$.

The above results suggest a possible application of VCA as an impurity solver for zero temperature DMFT. The results would not suffer from a bath truncation error as in exact diagonalization based DMFT. A big advantage would be the low demand on computational power of VCA and the qualitatively correct local density of states. To round the discussion up, a symmetry breaking field is introduced in the reference system in hope for better results.

3.3.13. Introducing a symmetry breaking field

We explore the possibility to improve the VCA_Ω results achieved by varying the internal single particle parameters of the model by introducing a symmetry breaking 'spin flip field' at the impurity site. The term added to the impurity Hamiltonian eq. (3.3)

$$\hat{\mathcal{H}}_{\mathrm{flip}} = B_x \left(f_\uparrow^\dagger f_\downarrow + f_\downarrow^\dagger f_\uparrow \right) , \tag{3.52}$$

explicitly breaks the conservation of spin in the cluster solution. We are interested in the model with a physical parameter $B_x = 0$ so this variable may only attain a finite value as a variational parameter B'_x in the reference system. This is motivated by the actual physics of the impurity at which conduction electrons undergo spin flip scattering. Our findings indicate that any finite value of B'_x splits the Kondo resonance and has thus to be discarded on physical grounds for the physical system under investigation. While this prevents the application of this field to improve the VCA results, it gives very nice insight in the physics of the SIAM as described by CPT/VCA. We find that a critical interaction strength U depending on the length of the cluster part of the reference system exists, which separates solutions which would prefer a finite B'_x from those which would prefer $B'_x = 0$. The critical interaction strength for $L = 4$ is given by $U_c/\Delta \approx 4.3$. The grand potential $\Omega - \Omega'_{0,env}$ is plotted for various interaction strengths U in fig. 3.24 (left). For an analogous calculation for $L = 6$ site clusters a value of $U_c/\Delta \approx 4.1$ is achieved. The mean field result would yield a critical interaction strength $U_c/\Delta = \pi$ for the parameters used here. We interpret this value as a signature of the onset of local moment behavior. The values for U_c are of course not to be taken literally, they depend very much on the finite size of the cluster under investigation. However, the fact that a critical U exists, signals that the essential physics of the SIAM is reproduced by our approach.

The splitting of the Kondo resonance caused by a non-zero variational field B'_x is shown in fig. 3.24 (right). The value of $U/\Delta = 12$ used for this calculation lies in the region above U_c where the system

prefers a nonzero field B'_x. This ends the discussion of the CPT/VCA results in equilibrium. In the next section we turn to the non-equilibrium case.

4. Non-equilibrium transport through a strongly-correlated quantum dot

Since the early 1990's the field of (then) bulk Kondo physics was enriched by the study of artificial nano-scale structures, exhibiting similar physics in a much more control- and tune-able way [133, 134, 135]. Numerous experimental studies [10, 136, 137, 138, 138] established a new field for both equilibrium Kondo physics as well as non-equilibrium phenomena in those devices. One especially remarkable device providing such a playground for quantum impurity models is a quantum dot [139]. These small units may be used in a single-electron transistor setup, exhibiting Coulomb blockade effects. Quantum dots, sometimes referred to as artificial atoms, resemble the physics of a magnetic impurity in a metal, when connected to metal leads by tunneling barriers. In a metal the magnetic moment of the impurity, above the Kondo temperature T_K provides a local moment, usually in a, singly occupied, narrow f-orbital. Lowering the temperature below T_K, the screening of this moment leads to the remarkable Kondo physics. Quantum dots, with an odd number of electrons, are capable of resembling this behavior as shown in fig. 4.1. The great advantage of artificial nano structures is, that each parameter may be controlled experimentally. A quantum dot, connected to left-, and right leads, as well as a gate electrode, may be modeled by the SIAM. The tunnel couplings to the leads V_L and V_R, are the analogues of the hybridization matrix elements of f- and s-electrons in a bulk impurity system and may be controlled by the gate voltage. The energy levels of the dot and correlation effects may be engineered by using different materials, sizes and geometries of the dot. Such devices are subjected to strong correlations because of the macroscopically entangled states arising from virtual spin flip scattering [10].

The non-equilibrium behavior of such systems under bias poses an unsolved issue even today. Early works ref. [140, 141, 142, 143] gave some essential insight into the basic non-equilibrium physics. A good overview of semi-classical approaches is presented in the book by Richter [144]. A sound theoretical base of the non-equilibrium Kondo physics was developed during the last twenty years ref. [145, 146, 147, 148, 149]. Qualitative results for any bias voltage are extremely hard to obtain because it is expected, that the dot stays in the strong coupling regime also at high bias voltages [150] ($V_{\text{bias}} > T_K$). Several ideas to tackle the interacting non-equilibrium problem are presented in ref. [151]. A comparison of many body perturbation theory and time dependend density functional theory is available in ref. [152]. The involved time scales are discussed for example in ref. [153]. Some progress was made in recent years using non-equilibrium FRG [154, 155, 156], QMC [157, 158], dual-fermion approaches [159, 160] and with the introduction of scattering Bethe Ansatz [161, 162]. The applicability of a master-equation was explored in ref. [163]. DMRG was used to get insight into one-dimensional problems ref. [164, 165]. Recently it was noted that the logarithmic discretization used in NRG causes problems, when one wants to predict the long-time behavior of non-equilibrium systems [166]. In this publication we do not consider any additional charging

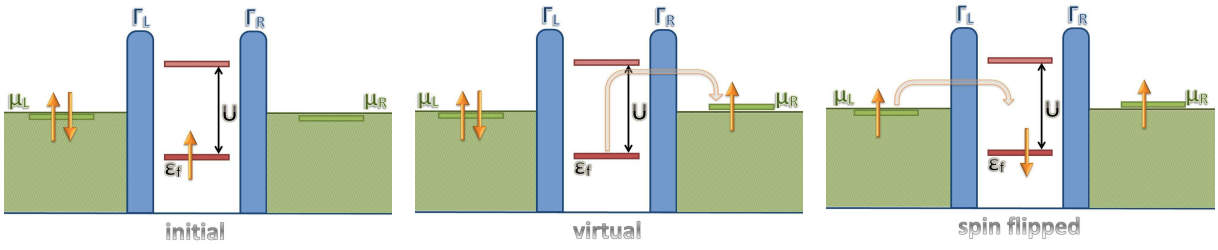

Figure 4.1.: Schematic energy diagram of a quantum dot (reproduced from ref. [10]). The spin-degenerate level of the dot is singly occupied. A depopulation as well as a double-occupation of the dot is energetically unfavorable. The tunnel couplings to the left and right lead are denoted Γ_L and Γ_R. Those leads consist of Fermi seas filled up to their respective chemical potential μ_L and μ_R. A possible virtual spin flip event, which is the essence of the Kondo effect, is depicted here. (Left) Initial state of the quantum dot: single-occupation. (Mid) The dot's electron may tunnel off the correlated region in a virtual process. (Right) It is replaced by an electron of another spin flavor. Another process for such an event may be a virtual double-occupation.

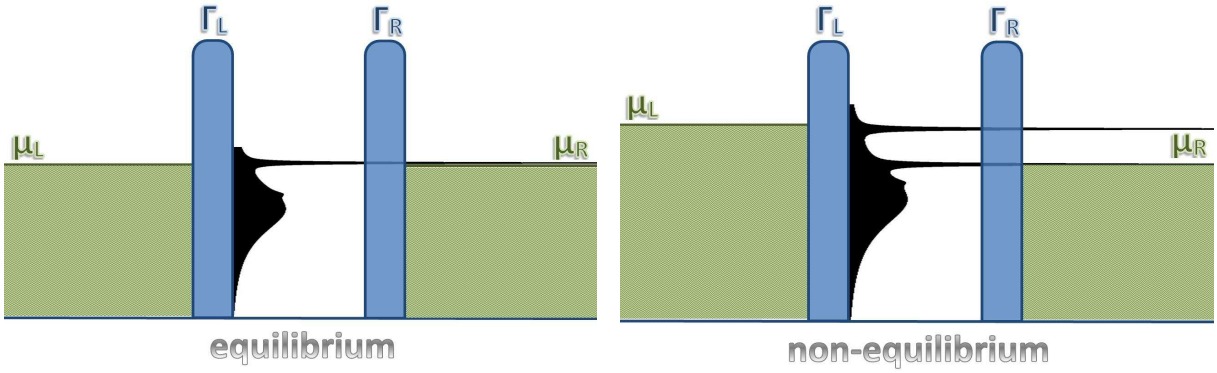

Figure 4.2.: Density of states in a quantum dot (reproduced from ref. [10]). The Kondo effect reveals itself as a characteristic resonance in the local density of states of the quantum dot. (Left) In an equilibrium situation the resonance is located at the Fermi-energy. (Right) In a non-equilibrium situation the Kondo peak splits into two, one pinned at the chemical potential of the left lead, and one pinned at the chemical potential of the right lead.

effects, which are important for a real device. A study of such effects and the involved screening and relaxation time scales was done in ref. [167] using perturbative methods. Very recent results obtained by a non-equilibrium extension of the FRG for the interacting resonant level model became available in ref. [168].
The expected non-equilibrium behavior is pictured in fig. 4.2. A splitted Kondo resonance is pinned at the chemical potentials of the respective leads [169].
In this chapter we use the non-equilibrium formulation of VCA (see sec. 2.4) to obtain non-equilibrium properties of the SIAM in the strongly correlated regime. Results for the effective distribution function are presented in sec. 4.2. An expression for the current in the non-interacting case is obtained in sec. 4.3. The linear-response current in the Kondo-regime will be discussed in sec. 4.4. A comparison of the CPT/VCA results to mean field theory is presented in sec. 4.5. Finally results for the current and density of states as obtained by CPT/VCA are discussed in sec. 4.6. The behavior of the VCA variational parameters will be discussed there. All parameter regions of the SIAM will be explored and also systems with asymmetric coupling to left and right leads will be investigated. We start out by presenting the model of a quantum dot within CPT/VCA in sec. 4.1.

4.1. Modeling of a quantum dot system out of equilibrium

To obtain non-equilibrium properties for the quantum dot system, the SIAM out of equilibrium has to be solved, as explained in the last section. The non-equilibrium VCA may be applied to this problem in splitting the infinite system into three parts (see fig. 4.3). A left (uncorrelated) lead, which is modeled by a semi-infinite tight-binding chain (see eq. (3.23)). A central correlated region, which consists of a SIAM (see eq. (3.1)) in real space on a finite size cluster. And a right lead, which is again modeled by a semi-infinite tight-binding chain. Note that it is crucial that the leads (reservoirs) are of infinite size, otherwise no steady state will be reached. The procedure of splitting is similar to the one considered in the equilibrium case and is described in sec. 3.3. The Green's functions of the reference system are obtained as in the equilibrium case. However here a two by two Keldysh Green's function is used (see sec. 2.4). The cluster part of the reference system, this time, consists of the impurity, sitting in the middle of the cluster. The sites to the left of the impurity belong formally to the left lead (and therefore have on-site energies ϵ_L and chemical potential μ_L). The sites to the right of the impurity belong to the right lead and have the respective parameters. In increasing the size of the cluster part of the reference system symmetrically to the left and right of the impurity, we treat more and more sites of the leads exactly, which would ultimately converge to the exact solution of the total system when $L \to \infty$. Practical system sizes however are limited again to $L \leq 16$. A bias voltage may be applied by shifting the chemical potential and the on-site energies of the leads simultaneously. This is always done in an asymmetric manner: $\mu_L = \epsilon_L = -\epsilon_R = -\mu_R = \frac{V_{\text{bias}}}{2}$. Note again that the uncorrelated sites in the cluster which are situated to the left (right) of the impurity formally belong to the lead and therefore also have on-site energies of $\epsilon_L(\epsilon_R)$. To maintain particle-hole symmetry we are therefore limited to clusters with an odd-number of sites $L = 3, 5, 7, 9, 11, 13$ and 15. Observations showed that every second of these systems $L = 5, 9$ and 13 suffers from a finite-size gap, which closes with increasing cluster size. This arises due to

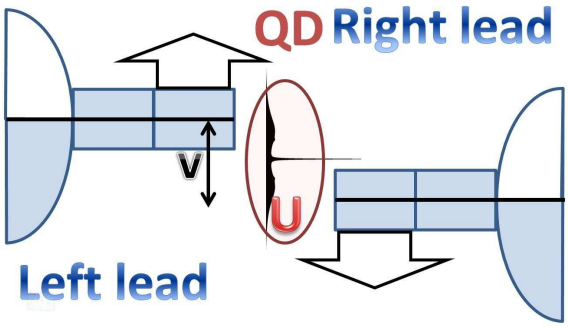

Figure 4.3.: A quantum dot is modeled within VCA by the SIAM. The reference system consists of three parts: A left (uncorrelated) lead, which is modeled by a semi-infinite tight-binding chain. A central correlated region, which consists of a SIAM in real space on a finite size cluster. And a right lead, which is again modeled by a semi-infinite tight-binding chain.

the fact that an even number of sites sits to the right as well as to the left of the impurity. Therefore in the following only $L = 3, 7$ and 11 site clusters will be used.

The effective distribution function will be discussed in the next section.

4.2. Effective distribution function

The effective distribution function was defined in eq. (2.48). We start out by analytically evaluating it for a generic system. Suppose we have again a semi-infinite left lead l, a finite size, central (interacting) region c and a semi-infinite right lead r. To evaluate the effective distribution function we need to obtain the retarded, advanced and Keldysh components of the total Green's function in the central region. The cluster Green's function in Keldysh space is given in block form

$$\widetilde{\mathrm{G}}' = \begin{pmatrix} \mathrm{G}_l'^R & & & \mathrm{G}_l'^K & & \\ & \mathrm{G}_c'^R & & & \mathrm{G}_c'^K & \\ & & \mathrm{G}_r'^R & & & \mathrm{G}_r'^K \\ & & & \mathrm{G}_l'^A & & \\ & & & & \mathrm{G}_c'^A & \\ & & & & & \mathrm{G}_r'^A \end{pmatrix},$$

where R, K and A denote retarded, Keldysh and advanced Green's functions respectively. In general each Green's function in this expression again is a matrix in site/spin space. Coupling the environments to the leads by CPT eq. (2.2) requires the inverse cluster Green's function $\widetilde{\mathrm{G}}'^{-1}$ and the inter-cluster hopping matrix in Keldysh space

$$\widetilde{\mathrm{G}}'^{-1} = \begin{pmatrix} \mathrm{G}_l'^{R-1} & & & -\mathrm{G}_l'^{R-1}\mathrm{G}_l'^K\mathrm{G}_l'^{A-1} & & \\ & \mathrm{G}_c'^{R-1} & & & -\mathrm{G}_c'^{R-1}\mathrm{G}_c'^K\mathrm{G}_c'^{A-1} & \\ & & \mathrm{G}_r'^{R-1} & & & -\mathrm{G}_r'^{R-1}\mathrm{G}_r'^K\mathrm{G}_r'^{A-1} \\ & & & \mathrm{G}_l'^{A-1} & & \\ & & & & \mathrm{G}_c'^{A-1} & \\ & & & & & \mathrm{G}_r'^{A-1} \end{pmatrix}, \quad \widetilde{\mathrm{T}} = \begin{pmatrix} & t & & t & & \\ t & & t & & & \\ & t & & & & \\ & & & & t & \\ & & & t & & t \\ & & & & t & \end{pmatrix}.$$

The CPT equation $\widetilde{\mathrm{G}}^{-1} = \widetilde{\mathrm{G}}'^{-1} - \widetilde{\mathrm{T}}$, yields the total Green's function in Keldysh space. The Keldysh component is given by

$$\widetilde{\mathrm{G}}^K = \begin{pmatrix} \frac{\mathrm{G}_l'^A\mathrm{G}_l'^R t^2\left(\mathrm{G}_c'^K+\mathrm{G}_c'^A\mathrm{G}_c'^R\mathrm{G}_r'^K t^2\right)+\mathrm{G}_l'^K\left(-1+\mathrm{G}_c'^A\mathrm{G}_r'^A t^2\right)\left(1-t^2\mathrm{G}_c'^R\mathrm{G}_r'^R\right)}{\left(1-t^2\mathrm{G}_c'^A(\mathrm{G}_l'^A+\mathrm{G}_r'^A)\right)\left(-1+\mathrm{G}_c'^R(\mathrm{G}_l'^R+\mathrm{G}_r'^R)t^2\right)} & \frac{t\left(\mathrm{G}_c'^K\mathrm{G}_l'^R+\mathrm{G}_c'^A\left(\mathrm{G}_l'^K\mathrm{G}_r'^R-\mathrm{G}_l'^K\mathrm{G}_r'^R\right)t^2\right)}{\left(-1+\mathrm{G}_c'^A(\mathrm{G}_l'^A+\mathrm{G}_r'^A)t^2\right)\left(-1+\mathrm{G}_c'^R(\mathrm{G}_l'^R+\mathrm{G}_r'^R)t^2\right)} \\ \frac{t\left(\mathrm{G}_c'^K\mathrm{G}_l'^A+\mathrm{G}_c'^R\mathrm{G}_l'^K+\mathrm{G}_c'^A\mathrm{G}_c'^R\left(-\mathrm{G}_l'^K\mathrm{G}_r'^A+\mathrm{G}_l'^A\mathrm{G}_r'^K\right)t^2\right)}{\left(1-t^2\mathrm{G}_c'^A(\mathrm{G}_l'^A+\mathrm{G}_r'^A)\right)\left(1-t^2\mathrm{G}_c'^R(\mathrm{G}_l'^R+\mathrm{G}_r'^R)\right)} & \frac{\mathrm{G}_c'^K+\mathrm{G}_c'^A\mathrm{G}_c'^R\left(\mathrm{G}_l'^K+\mathrm{G}_r'^K\right)t^2}{\left(1-t^2\mathrm{G}_c'^A(\mathrm{G}_l'^A+\mathrm{G}_r'^A)\right)\left(1-t^2\mathrm{G}_c'^R(\mathrm{G}_l'^R+\mathrm{G}_r'^R)\right)} \\ \frac{t^2\left(\mathrm{G}_c'^A\mathrm{G}_l'^A\mathrm{G}_r'^K+\mathrm{G}_c'^K\mathrm{G}_l'^A\mathrm{G}_r'^R+\mathrm{G}_c'^R\mathrm{G}_l'^K\mathrm{G}_r'^R-\mathrm{G}_c'^A\mathrm{G}_c'^R(\mathrm{G}_l'^A\mathrm{G}_l'^R\mathrm{G}_r'^K+\mathrm{G}_l'^K\mathrm{G}_r'^A\mathrm{G}_r'^R)t^2\right)}{\left(1-t^2\mathrm{G}_c'^A(\mathrm{G}_l'^A+\mathrm{G}_r'^A)\right)\left(1-t^2\mathrm{G}_c'^R(\mathrm{G}_l'^R+\mathrm{G}_r'^R)\right)} & \frac{\mathrm{G}_c'^K\mathrm{G}_r'^R t+\mathrm{G}_c'^A t\left(\mathrm{G}_r'^K-\mathrm{G}_c'^R\mathrm{G}_l'^R\mathrm{G}_r'^K t^2+\mathrm{G}_c'^R\mathrm{G}_l'^K\mathrm{G}_r'^R t^2\right)}{\left(-1+\mathrm{G}_c'^A(\mathrm{G}_l'^A+\mathrm{G}_r'^A)t^2\right)\left(-1+\mathrm{G}_c'^R(\mathrm{G}_l'^R+\mathrm{G}_r'^R)t^2\right)} \end{pmatrix} \tag{4.1}$$

$$\begin{pmatrix} \frac{t^2\left(\mathrm{G}_c'^A\mathrm{G}_l'^K\mathrm{G}_r'^A+\mathrm{G}_c'^K\mathrm{G}_l'^R\mathrm{G}_r'^A+\mathrm{G}_c'^R\mathrm{G}_l'^R\mathrm{G}_r'^K-\mathrm{G}_c'^A\mathrm{G}_c'^R(\mathrm{G}_l'^A\mathrm{G}_l'^R\mathrm{G}_r'^K+\mathrm{G}_l'^K\mathrm{G}_r'^A\mathrm{G}_r'^R)t^2\right)}{\left(-1+\mathrm{G}_c'^A(\mathrm{G}_l'^A+\mathrm{G}_r'^A)t^2\right)\left(-1+\mathrm{G}_c'^R(\mathrm{G}_l'^R+\mathrm{G}_r'^R)t^2\right)} \\ \frac{t\left(\mathrm{G}_c'^K\mathrm{G}_r'^A+\mathrm{G}_c'^R\left(\mathrm{G}_r'^K+\mathrm{G}_c'^A(\mathrm{G}_l'^K\mathrm{G}_r'^A-\mathrm{G}_l'^A\mathrm{G}_r'^K)t^2\right)\right)}{\left(-1+\mathrm{G}_c'^A(\mathrm{G}_l'^A+\mathrm{G}_r'^A)t^2\right)\left(-1+\mathrm{G}_c'^R(\mathrm{G}_l'^R+\mathrm{G}_r'^R)t^2\right)} \\ \frac{\mathrm{G}_r'^A\mathrm{G}_r'^R t^2\left(\mathrm{G}_c'^K+\mathrm{G}_c'^A\mathrm{G}_c'^R\mathrm{G}_l'^K t^2\right)+\mathrm{G}_r'^K\left(-1+\mathrm{G}_c'^A\mathrm{G}_l'^A t^2\right)\left(-1+\mathrm{G}_c'^R\mathrm{G}_l'^R t^2\right)}{\left(-1+\mathrm{G}_c'^A(\mathrm{G}_l'^A+\mathrm{G}_r'^A)t^2\right)\left(-1+\mathrm{G}_c'^R(\mathrm{G}_l'^R+\mathrm{G}_r'^R)t^2\right)} \end{pmatrix}. \tag{4.2}$$

The retarded/advanced components are

$$\widetilde{\mathrm{G}}^{R/A} = \begin{pmatrix} \frac{\mathrm{G}_l'^{R/A}\left(1-t^2\mathrm{G}_c'^{R/A}\mathrm{G}_r'^{R/A}\right)}{1-t^2\mathrm{G}_c'^{R/A}(\mathrm{G}_l'^{R/A}+\mathrm{G}_r'^{R/A})} & \frac{t\mathrm{G}_c'^{R/A}\mathrm{G}_l'^{R/A}}{1-t^2\mathrm{G}_c'^{R/A}(\mathrm{G}_l'^{R/A}+\mathrm{G}_r'^{R/A})} & \frac{t^2\mathrm{G}_c'^{R/A}\mathrm{G}_l'^{R/A}\mathrm{G}_r'^{R/A}}{1-t^2\mathrm{G}_c'^{R/A}(\mathrm{G}_l'^{R/A}+\mathrm{G}_r'^{R/A})} \\ \frac{t\mathrm{G}_c'^{R/A}\mathrm{G}_l'^{R/A}}{1-t^2\mathrm{G}_c'^{R/A}(\mathrm{G}_l'^{R/A}+\mathrm{G}_r'^{R/A})} & \frac{\mathrm{G}_c'^{R/A}}{1-t^2\mathrm{G}_c'^{R/A}(\mathrm{G}_l'^{R/A}+\mathrm{G}_r'^{R/A})} & \frac{t\mathrm{G}_c'^{R/A}\mathrm{G}_r'^{R/A}}{1-t^2\mathrm{G}_c'^{R/A}(\mathrm{G}_l'^{R/A}+\mathrm{G}_r'^{R/A})} \\ \frac{t^2\mathrm{G}_c'^{R/A}\mathrm{G}_l'^{R/A}\mathrm{G}_r'^{R/A}}{1-\mathrm{G}_c'^{R/A}t^2(\mathrm{G}_l'^{R/A}+\mathrm{G}_r'^{R/A})} & \frac{t\mathrm{G}_c'^{R/A}\mathrm{G}_r'^{R/A}}{1-t^2\mathrm{G}_c'^{R/A}(\mathrm{G}_l'^{R/A}+\mathrm{G}_r'^{R/A})} & \frac{\mathrm{G}_r'^{R/A}\left(1-t^2\mathrm{G}_c'^{R/A}\mathrm{G}_l'^{R/A}\right)}{1-t^2\mathrm{G}_c'^{R/A}(\mathrm{G}_l'^{R/A}+\mathrm{G}_r'^{R/A})} \end{pmatrix}.$$

The effective distribution function p_{eff} is given by $p_{\mathrm{eff}} = \frac{1}{2} - \frac{\mathrm{G}_c^K}{2\left(\mathrm{G}_c^R - \mathrm{G}_c^A\right)}$ (see eq. (2.48)). Here we consider the first definition, where all Green's functions are evaluated at a specific site.

$$p_{\mathrm{eff}} = \frac{\mathrm{G}_c'^A + \mathrm{G}_c'^K - \mathrm{G}_c'^R + t^2\mathrm{G}_c'^A\mathrm{G}_c'^R(\mathrm{G}_l'^A + \mathrm{G}_l'^K - \mathrm{G}_l'^R + \mathrm{G}_r'^A + \mathrm{G}_r'^K - \mathrm{G}_r'^R)}{2\left(\mathrm{G}_c'^A - \mathrm{G}_c'^R + t^2\mathrm{G}_c'^A\mathrm{G}_c'^R(\mathrm{G}_l'^A - \mathrm{G}_l'^R + \mathrm{G}_r'^A - \mathrm{G}_r'^R)\right)} \tag{4.3}$$

From here on we consider the central region to consist of a single-non-interacting site, although the discussion is also valid for multi-site interacting central regions. The cluster Green's functions before coupling (at zero temperature), are then given by (see eq. (2.39))

$$\mathrm{G}_c'^{R/A}(\omega) = \frac{1}{\omega \pm i0^+} \tag{4.4}$$

$$\mathrm{G}_{c/l/r}'^{R/A/K}(\omega) = \left(\mathrm{G}_{c/l/r}'^R(\omega, \epsilon_{c/l/r}) - \mathrm{G}_{c/l/r}'^A(\omega, \epsilon_{c/l/r})\right)\mathrm{sign}(\omega - \mu_{c/l/r})\,. \tag{4.5}$$

Plugging eq. (4.4) and eq. (4.5) into eq. (4.3) and collecting terms $\left(\mathrm{G}_{c/l/r}'^R - \mathrm{G}_{c/l/r}'^A\right) = 2i\Im\mathrm{m}(\mathrm{G}_{c/l/r}'^R) = -2\pi i\rho_{c/l/r}$ one obtains

$$p_{\mathrm{eff}} = \frac{\pi t^2\left(\rho_l + \rho_r - \rho_l\mathrm{sign}(\omega-\mu_l) - \rho_r\mathrm{sign}(\omega-\mu_r))\right) + (0^+ - 0^+\mathrm{sign}(\omega-\mu_c))}{2\left(\pi t^2(\rho_l+\rho_r) + 0^+\right)}\,.$$

Upon taking the limit $0^+ \to 0$, one sees that all contributions of the cluster drop out

$$p_{\mathrm{eff}}(\omega, V_{\mathrm{bias}}) = \frac{1}{2} - \frac{1}{2}\,\frac{\rho_l(\omega,\epsilon_l)\mathrm{sign}(\omega-\mu_l) + \rho_r(\omega,\epsilon_r)\mathrm{sign}(\omega-\mu_r)}{\rho_l(\omega,\epsilon_l) + \rho_r(\omega,\epsilon_r)}\,. \tag{4.6}$$

This shows that the effective distribution function at zero temperature, defined via one site of the central region, does not depend on the central region at all. More importantly it does not depend on the interaction U, but solely on the applied bias voltage $V_{\mathrm{bias}} = \mu_l - \mu_r$ with $\epsilon_l = \mu_l$ and $\epsilon_r = \mu_r$. Furthermore it is purely real as it is to be expected for a distribution function. It reduces to the Fermi-Dirac distribution in the limit $V_{\mathrm{bias}} = 0$.
An explicit result for a non-interacting tight-binding system under bias which consists of two semi-infinite leads and a single-site central region is plotted in fig. 4.4. The densities of states for the left and right lead, needed for the evaluation of eq. (4.6) are given in eq. (3.23). This generic behavior does not change with increased system size and is independent of the cluster parameters including interaction, as mentioned before. Note that the top point of the trapezoid-shaped structure in the lower part of fig. 4.4 at $\frac{V_{\mathrm{bias}}}{\Delta} = 40$ occurs exactly at the point where the density of states of the left and right lead stop overlapping.
Using the basic results for the Green's function obtained here, a reference expression for the current of a non-interacting system will be presented in the next section.

4.3. Current in the non-interacting case

The current in the non-interacting case ($U = 0$), for both spin directions, may be evaluated using the formula for the current eq. (2.47) and the Keldysh Green's function G_{lc}^K and G_{cl}^K evaluated in eq. (4.2)

$$\begin{aligned} j = \int_{-\infty}^{\infty} d\omega\,\Re\mathrm{e}\Bigg(-\frac{(\mathrm{G}_l'^A - \mathrm{G}_l'^R)V^2}{\mathcal{N}}\Bigg(&-2i0^+\mathrm{sign}(\omega-\mu_c) + 2i0^+\mathrm{sign}(\omega-\mu_l) \\ &+ V^2(\mathrm{G}_r'^A(-\mathrm{sign}(\omega-\mu_r) + \mathrm{sign}(\omega-\mu_l)) + \mathrm{G}_r'^R(-\mathrm{sign}(\omega-\mu_l) + \mathrm{sign}(\omega-\mu_r)))\Bigg)\Bigg) \\ \mathcal{N} = 2\pi\left(0^+ + i\left((\mathrm{G}_l'^R + \mathrm{G}_r'^R)V^2 - \omega\right)\right)&\left(0^+ - i(\mathrm{G}_l'^A + \mathrm{G}_r'^A)V^2 + i\omega\right)\,, \end{aligned}$$

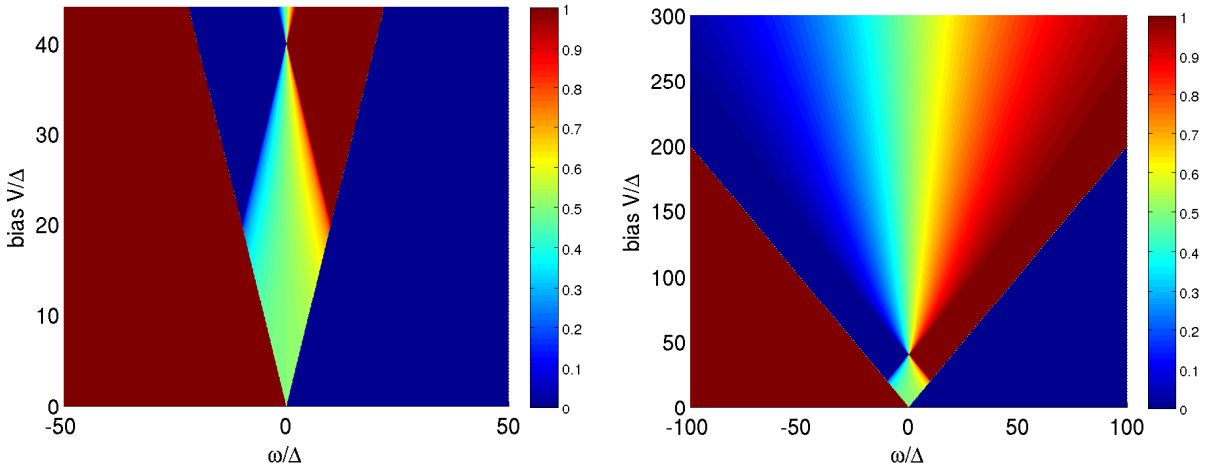

Figure 4.4.: Effective distribution function eq. (4.6) for a tight-binding chain under bias. The hopping t is chosen to be one. A bias of $V_{\text{bias}} = \mu_l - \mu_r$, with $\epsilon_l = \mu_l$ and $\epsilon_r = \mu_r$, was applied by anti-symmetrically shifting the chemical potentials of the left and right lead starting from zero. The axis are scaled with $\Delta = 0.1$, to make comparison to other plots more easy. (Left) Zoom to the relevant parameter region of this work. (Right) The same but for a larger parameter space.

which may be simplified by taking the limit $0^+ \to 0$

$$\begin{aligned} j &= 2\pi V^4 \int_{-\infty}^{\infty} d\omega \, \frac{\rho_l \rho_r (\text{sign}(\omega - \mu_l) - \text{sign}(\omega - \mu_r))}{\left((\mathrm{G}_l'^A + \mathrm{G}_r'^A)V^2 - \omega\right)\left((\mathrm{G}_l'^R + \mathrm{G}_r'^R)V^2 - \omega\right)} \\ &= 4\pi V^4 \int_{\mu_l}^{\mu_r} d\omega \, \frac{\rho_l \rho_r}{\left((\mathrm{G}_l'^A + \mathrm{G}_r'^A)V^2 - \omega\right)\left((\mathrm{G}_l'^R + \mathrm{G}_r'^R)V^2 - \omega\right)} , \end{aligned} \tag{4.7}$$

All currents in this thesis will be given in units of hopping $t = 1$. The expression in the integrand is purely real, because $\mathrm{G}^R = (\mathrm{G}^A)^\dagger$. Here the left/right Green's functions of the environment are given in eq. (3.23). It is interesting to compare this result to ref. [170], where an expression for the current through an interacting region is derived. The current under bias is obtained from this expression by setting $\frac{V_{\text{bias}}}{2} = \epsilon_l = \mu_l = -\mu_r = -\epsilon_r$. The current under doping is obtained by setting $\frac{d}{2} = \mu_l = -\mu_r =$ and $\epsilon_r = \epsilon_l = 0$. These two currents are plotted in fig. 4.5. One can clearly see the effects of the leads' bands in the biased case.

As a reference value for CPT/VCA calculations, the linear response current in the Kondo-regime will be derived in the next section.

4.4. Linear response in the Kondo regime

According to ref. [140, 81], the conductance may be calculated using a Landauer-type formula generalized to interacting systems

$$\sigma = \frac{i\, e^2}{\hbar} \sum_\sigma \int_{-\infty}^{\infty} \frac{d\omega}{2\pi} \frac{dp_{\text{FD}(\omega,\mu,\beta)}}{d\omega} \frac{\Gamma_L^\sigma(\omega)\Gamma_R^\sigma(\omega)}{\Gamma_L^\sigma(\omega) + \Gamma_R^\sigma(\omega)} 2i\Im\mathrm{m}\left(\mathrm{G}^\sigma(\omega + i0^+)\right) . \tag{4.8}$$

This formula is valid for proportional leads $\Gamma_L(\omega) = \alpha\Gamma_R(\omega)$ in a steady-state situation. Here $-\frac{1}{\pi}\Im\mathrm{m}\left(\mathrm{G}^\sigma(\omega + i0^+)\right)$ is the interacting density of states in the system. Γ_i^σ are the hybridizations with the $i = L, R$ left and right lead

$$\Gamma_i^\sigma(\omega) = 2\pi \sum_k |V_k^\sigma|^2 \, \delta(\omega - \omega_k^\sigma) .$$

As always we use units of $e = \hbar = 1$. We are interested in the zero temperature conductance for a particle-hole symmetric system with chemical potential $\mu = \epsilon_F = 0$ and symmetric leads $\Gamma_L(\omega) = \Gamma_R(\omega)$. Therefore the derivative of the Fermi-Dirac distribution function $p_{\text{FD}}(\omega, \mu, \beta)$ reduces to $\delta(\epsilon_F = 0)$. The coupling

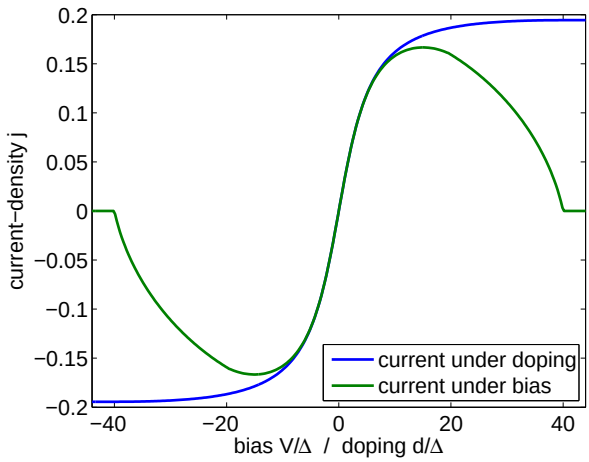

Figure 4.5.: Current under bias/doping in the non-interacting case obtained by eq. (4.7). The model parameters were hybridization $V = 0.3162$ and hopping $t = 1$. The current is given in units of hopping $t = 1$.

of one site to symmetric leads by a local hopping V gives a spin independent hybridization function

$$\Gamma_{L(R)} = \Gamma(\omega) = \pi V^2 \rho_{L(R)}(\omega) \,, \tag{4.9}$$

where $\rho(\omega)$ is the local density of states of the first site of the non-interacting lead (i.e. here a semicircular LDOS of a semi-infinite tight binding chain). Plugging all this information into eq. (4.8) the conductance for both spin channels is given by

$$\begin{aligned}\sigma &= 2i \int_{-\infty}^{\infty} \frac{d\omega}{2\pi}\, \delta(0) \frac{\Gamma(\omega)}{2} (-\pi) \left(-\frac{1}{\pi} \Im\mathrm{m}\left(\mathrm{G}(\omega + i0^+)\right)\right) \\ &= \Gamma(0) \Im\mathrm{m}\left(\mathrm{G}(i0^+)\right) \,.\end{aligned}$$

The hybridization at the Fermi energy, for the semi-infinite tight binding chain (hopping t), is given by

$$\Gamma(0) = \pi V^2 \frac{1}{t\pi} = \frac{V^2}{t} = \Delta \,.$$

For a symmetric impurity the height of the Kondo resonance at $\omega = 0$ is given by $\frac{1}{\pi\Delta}$. So

$$-\frac{1}{\pi} \Im\mathrm{m}\left(\mathrm{G}(\omega + i0^+)\right) = \frac{1}{\pi\Delta} \,.$$

This result is only valid in the Kondo regime at zero temperature and for very small bias voltages. Therefore we are left with a linear-response conductance (for both spin channels) of

$$\sigma = \frac{1}{\pi} \,, \tag{4.10}$$

which remarkably is independent of all system parameters $(\Delta, t, V, ...)$ and especially independent of the interaction strength U, as long as the system is in the Kondo regime. This of course arises from the pinning and constant height of the Kondo peak. Note that this is exactly the result for the conductance quantum

$$\sigma_0 = \frac{2e^2}{h} = \frac{e^2}{\pi\hbar} \,,$$

which reproduces in units of $e = \hbar = 1$ the above result 4.10.
Although mean field theory produces qualitatively wrong results for the SIAM (see sec. 3.2), it is interesting to compare CPT/VCA to some other technique before proceeding further.

4.5. Doped leads: A comparison of cluster perturbation theory to mean field results

In this section we examine the case of lead-doping (instead of applying a bias voltage). In this case the bands of the leads do not shift altogether ($\epsilon_{l,r} = 0$), only the chemical potentials of the leads are shifted in an asymmetric manner with doping $\frac{d}{2} = \mu_l = -\mu_r$. This can be achieved, for example, by introducing dopants into the lead material, or by applying pressure to suitable materials. This case is interesting, because it allows for comparison to a specific form of the Meir-Winegreen-Lee formula [140, 81]. This form is obtained by rewriting eq. (4.8) for our purpose here

$$j = i \sum_\sigma \int_{-\infty}^{\infty} \frac{d\omega}{2\pi} \left(p_{\mathrm{FD},L}(\omega,\mu,\beta) - p_{\mathrm{FD},R}(\omega,\mu,\beta)\right) \frac{\Gamma_L^\sigma(\omega)\Gamma_R^\sigma(\omega)}{\Gamma_L^\sigma(\omega)+\Gamma_R^\sigma(\omega)} 2i\Im\mathrm{m}\left(\mathrm{G}^\sigma(\omega+i0^+)\right) ,$$

which is again only valid for the case of a bias voltage in the wide band limit, or the case of doping with arbitrary bands. Inserting eq. (4.9) and the Fermi-Dirac distributions at zero temperature eq. (D.1) one obtains for the current

$$j = \pi V^2 \sum_\sigma \int_{-\mu_L}^{\mu_R} d\omega\, \rho_E(\omega)\rho_f^\sigma(\omega) . \tag{4.11}$$

To arrive at this expression, we assumed that the right and left leads have an equal density of states ρ_E. The current therefore is given essentially by the density of states in the interacting site ρ_f^σ.
To obtain a rough estimate for the current, the mean field results for the interacting impurity ρ_f^σ are used (see sec. 3.2). As noted there, the mean field single-particle spectra are qualitatively wrong. Furthermore, using the density of states ρ_f^σ from the mean field equations gives an equilibrium density of states which is not a good approximation for large doping. Results for the current under doping are shown in fig. 4.6 (left) with the approximate hybridization self-energy and fig. 4.6 (right) with the exact hybridization self-energy. Note that all currents are evaluated in both spin channels. This approach provides a starting point to compare more sophisticated methods to.
In the following the mean field results for the current obtained by eq. (4.11) are compared to CPT results of $L = 3, 7$ and 11 site clusters in fig. 4.7. The mean field currents are obtained by eq. (4.11) using the mean field density of states eq. (3.15). The CPT currents are obtained by eq. (2.47) using the CPT procedure. The current was obtained by CPT as well as MF for various values of interaction-strength U in the particle-hole symmetric case. The hybridization was chosen to be $V = 0.3162$ and the hopping in the chain was $t = 1$. As can be seen from the plots, CPT performs dramatically better than MF because it correctly reproduces the Kondo resonance. The CPT results show a pronounced finite-size structure. It is however questionable if CPT is a good approximation for large doping, because the CPT self-energy again does not "know of" the non-equilibrium situation. This point may be cured by introducing a self-consistent feedback as it is done in non-equilibrium VCA in the next section. As the results in equilibrium suggest, VCA with variational parameters $\mathsf{x} = \{V, t\}$ may strongly reduce the CPT finite-size effect (see fig. 3.13 and discussion there). It is interesting to note that the integration in eq. (4.11) is essentially over a semi-circle from $\rho_E(\omega)$ times a Lorentz peak at $\omega = 0$ from $\rho_f^\sigma(\omega)$. This is true as long as the mean field solution does not break the symmetry. The semi-circle may be approximated by a flat band of height $\frac{1}{\pi t}$, because away from $\omega = 0$, $\rho_f^\sigma(\omega)$ is essentially zero. Putting this into eq. (4.11) and examining the case of large doping ($\mu_L = -\mu_R$ greater than the bandwidth) the current takes the value of 2Δ. After comparing CPT/VCA to mean field results, we turn to the more interesting and more difficult case of a strongly correlated quantum dot under bias.

4.6. A biased quantum dot: CPT/VCA results

Here we consider a correlated quantum dot which is coupled to two leads (left, right). To study the performance of CPT/VCA we split the reference system into three parts: left lead, interacting region and right lead. The interacting region consists of the correlated site and additional uncorrelated sites to the left and to the right of it which belong to the leads but are treated within the diagonalization of the cluster - thereby creating a better approximation. The chemical potential of the left lead μ_L as well as the on-site energy ϵ_L are set equal. To apply a bias voltage to the device this parameter is then scanned from zero to some value and the corresponding parameter for the right lead is tuned in exactly the negative direction asymmetrically. So we have $\mu_L = \epsilon_L = -\epsilon_R = -\mu_R = \frac{V_{\mathrm{bias}}}{2}$. Note that the uncorrelated sites in the cluster which are situated to the left (right) of the impurity formally belong to the lead and therefore also have on-site energies of $\epsilon_L(\epsilon_R)$.

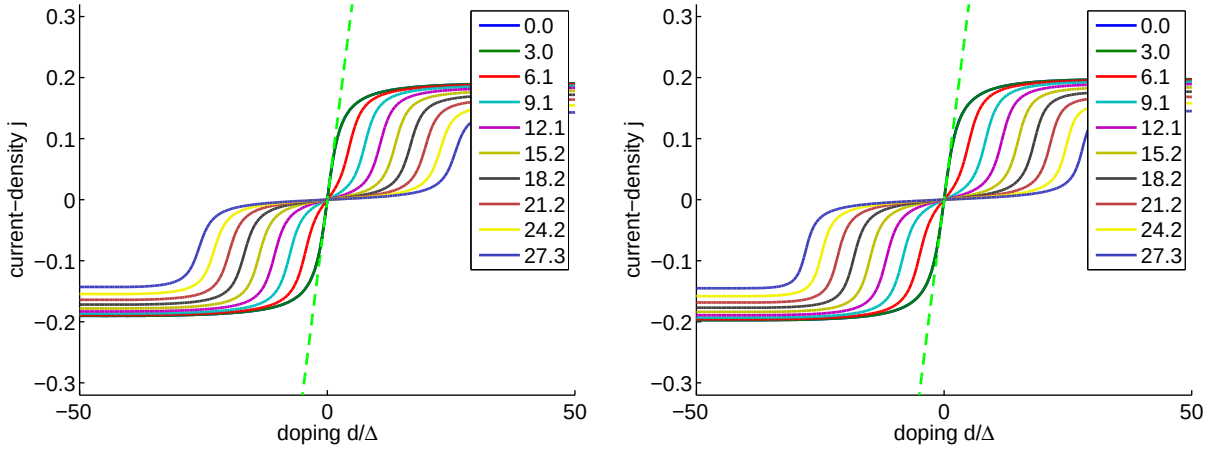

Figure 4.6.: Mean field results, in the particle-hole symmetric case, for the current under doping obtained by eq. (4.11). The legend indicates different values of interaction strength $\frac{U}{\Delta}$. The hybridization was chosen to be $V = 0.3162$ and the hopping in the chain was $t = 1$. A spurious mean field gap opens at the critical interaction strength $\frac{U_c}{\Delta} = 3.14$. (Left) Results obtained using the approximate MF hybridization self-energy. (Right) Results obtained using the exact MF hybridization self-energy.

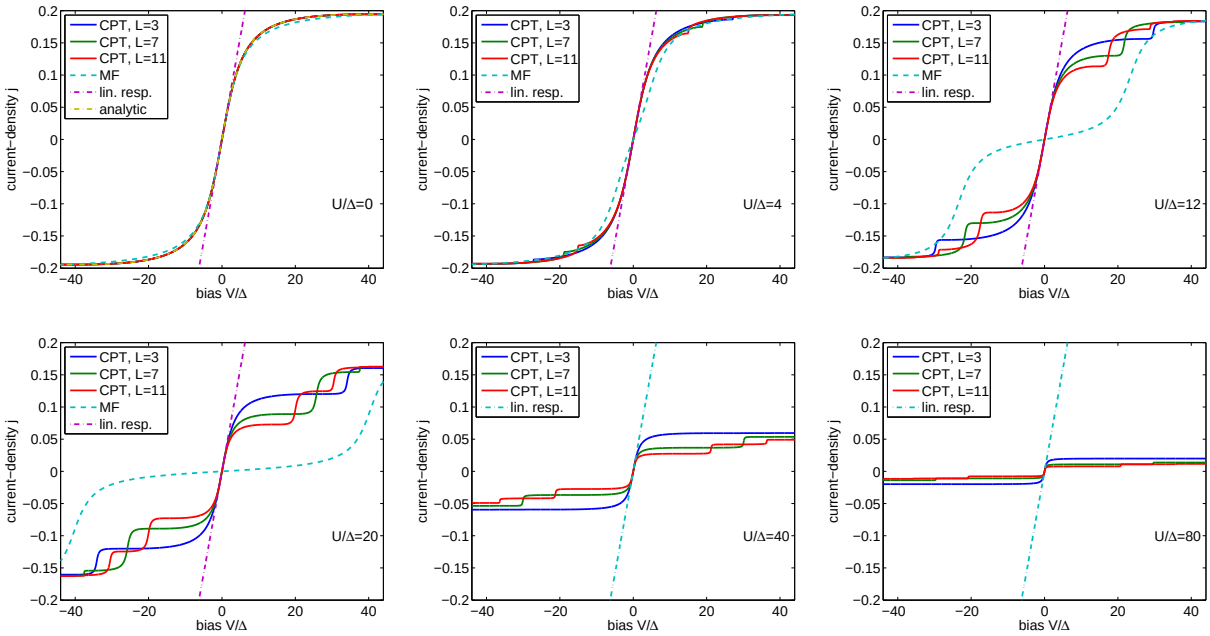

Figure 4.7.: Comparison of the CPT and MF currents under doping. Shown are the CPT results for $L = 3, 7$ and 11 site clusters as well as the MF results using the exact hybridization self-energy. All curves are for particle-hole symmetric parameters. The hybridization was chosen to be $V = 0.3162$ and the hopping in the chain was $t = 1$. The plots from top, left to bottom right show results for interaction strength $\frac{U}{\Delta} = 0, 4, 12, 20, 40$ and 80. The linear response result, valid in the Kondo regime, eq. (4.10) is also indicated. The analytic result for $U = 0$ was calculated using eq. (4.7).

In the following CPT and non-equilibrium VCA calculations are performed for the SIAM under bias. The non-equilibrium VCA results in this chapter were calculated with one variational parameter $\mathsf{x} = \{\Delta t\}$. This variational offset was added to all hoppings, in the cluster ($t' = t + \Delta t$) as well as the hybridization ($V' = V + \Delta t$) to the correlated site, uniformly. The variational parameter is fixed by requiring the average over all expectation values in the cluster to coincide with the corresponding average in the total system after coupling to the leads. All calculations were done for three different sizes of the cluster part of the reference system $L = 3, 7$ and 11. The hybridization parameter was chosen to be $V = 0.3162$ and the hopping to be $t = 1$, which yields again $\Delta = 0.1$. All calculations were done in three parameter regions. In the particle-hole symmetric case: $\epsilon_f = -\frac{U}{2}$ (Kondo regime), in a parameter region where the impurity is zero-occupied: $\epsilon_f = -\frac{U}{2}+2U$ and in a parameter region, where the impurity is doubly-occupied: $\epsilon_f = -\frac{U}{2} - U$. Different values of interaction-strength $\frac{U}{\Delta} = 4, 8, 12$ and 20 where investigated in each of these cases. Results for the behavior of the variational parameters will be given, as well as data obtained for the current and the non-equilibrium density of states.

4.6.1. Behavior of the variational parameters

The resulting parameter-shift $\Delta t = t' - t$ is shown for different interaction strengths $\frac{U}{\Delta}$ and cluster sizes L in fig. 4.8 in the particle-hole symmetric case: $\epsilon_f = -\frac{U}{2}$ (Kondo regime). The same data is shown in fig. 4.9 in a parameter region where the impurity is zero-occupied: $\epsilon_f = -\frac{U}{2} + 2U$ and in fig. 4.10 in a parameter region, where the impurity is doubly-occupied: $\epsilon_f = -\frac{U}{2} - U$. A similar behavior for all interaction strengths is observed.

4.6.2. Current

The current-density eq. (2.46) (for both spin channels) is examined here, for different values of the interaction strength $\frac{U}{\Delta} = 4, 8, 12$ and 20. The current was measured between the left lead and the first site of the system and it was checked that the continuity equation is fulfilled. This is achieved by calculating the current with $0^+ = 0$.
The current for a singly-occupied impurity is plotted in fig. 4.11. The CPT/VCA current yields the correct linear response current for small bias voltages. It is interesting to observe, that VCA always departs sooner from the linear response behavior than CPT with increasing interaction strength U. This is to be expected due to an exponential thinning of the Kondo resonance with increasing U [171]. The linear response current is independent of the interaction strength U in the Kondo regime. This is due to the fact, that CPT as well as VCA respect the Friedel sum rule in the particle hole symmetric case. The current under bias goes to zero as soon as the bands of the leads stop overlapping (here at $V_{\text{bias}}/\Delta = 40$). In those cases, where this happens before reaching this bias voltage, the vanishing of the current is due to effects in the dot. As expected non-equilibrium VCA strongly suppresses the finite-size effects of the cluster. This is also seen in equilibrium where VCA leads to the formation of continuous Hubbard bands while CPT yields more separated peaks for small system sizes (see fig. 3.13 and discussion there). For lower interaction strengths (see for example $U/\Delta = 4$), the CPT/VCA results for different cluster sizes coincide almost. For large interaction strength (see for example $U/\Delta = 20$) they depart from each other, respecting the linear response and high voltage limits. A pronounced two-peak structure seems to evolve for the non-equilibrium VCA $L = 7$ result with increasing interaction-strength U. The maximum current decreases monotonically with interaction-strength U.
The current for a zero-occupied impurity is plotted in fig. 4.12. As one can see by comparing to the linear response current of the Kondo regime, the current here is much smaller than in the Kondo regime. It is remarkable that the CPT and VCA results for all cluster sizes lie almost on top of each other. Note that in this case each plot has a differently scaled y-axis.
The current for a doubly-occupied impurity is plotted in fig. 4.13. Again the current is much smaller than in the Kondo regime and CPT and VCA perform very similar.

4.6.3. Density of states

The local density of states in the impurity is shown in fig. 4.14 for the particle-hole symmetric case, for $L = 3, L = 7$ and $L = 11$ site clusters respectively. The LDOS is plotted in a density plot as a function of energy ω (horizontal) and applied bias voltage (vertical). The splitting of the Kondo resonance, which resides at $\omega = 0$ for zero bias, is observed in both CPT and non-equilibrium VCA. In the non-equilibrium situation the Kondo resonance splits into two peaks. A linear splitting, depending on interaction strength U, is observed in non-equilibrium VCA. For high voltages the LDOS seems to saturate. Note that the

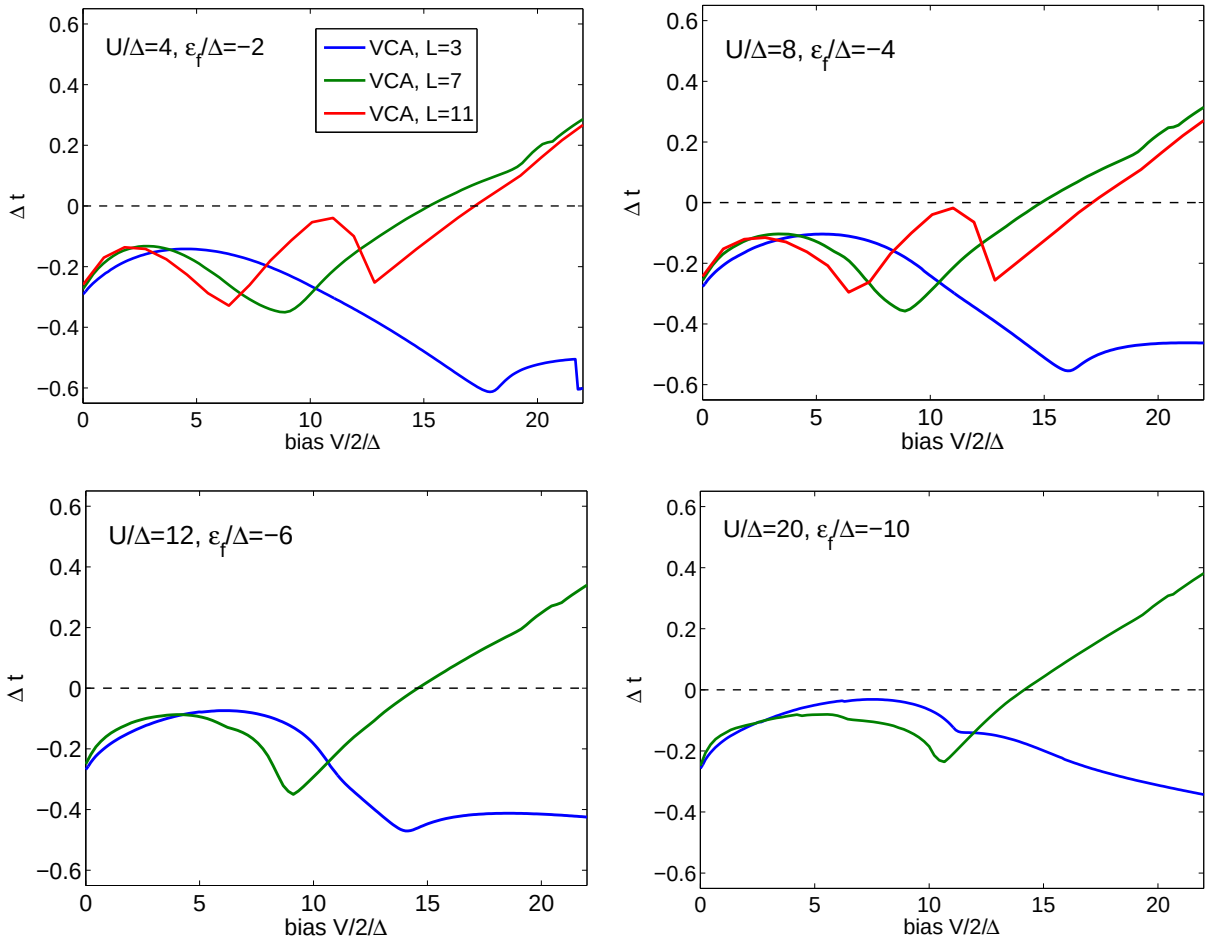

Figure 4.8.: Behavior of the non-equilibrium VCA variational parameter $\mathsf{x} = \{\Delta t\}$, $\Delta t = t' - t$ as a function of bias voltage. Shown are results for system-sizes $L = 3, 7$ and 11 in each plot. The figures from top, left to bottom, right are for different interaction-strengths $\frac{U}{\Delta} = 4, 8, 12$ and 20. These results are for the singly-occupied impurity: $\epsilon_f = -\frac{U}{2}$. The hybridization was chosen to be $V = 0.3162$ and the inter-chain hopping $t = 1$. Note that the $L = 11$-site VCA data for $\frac{U}{\Delta} = 12$ and 20 is missing due to repeated trouble with the file system at lengthy calculations.

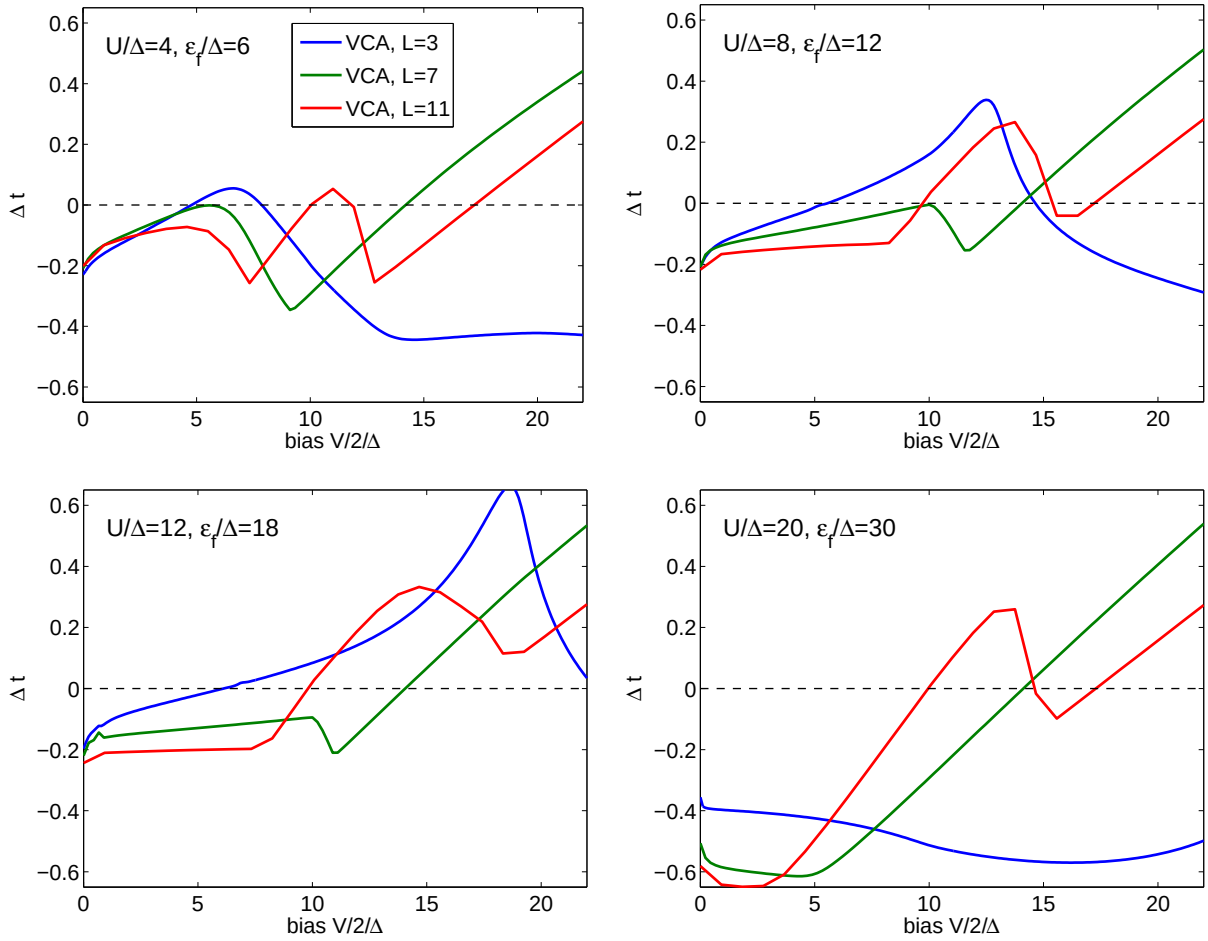

Figure 4.9.: Behavior of the non-equilibrium VCA variational parameter $\mathsf{x} = \{\Delta t\}$, $\Delta t = t' - t$ as a function of bias voltage. Shown are results for system-sizes $L = 3, 7$ and 11 in each plot. The figures from top, left to bottom, right are for different interaction-strengths $\frac{U}{\Delta} = 4, 8, 12$ and 20. These results are for the zero-occupied impurity: $\epsilon_f = -\frac{U}{2} + 2U$. The hybridization was chosen to be $V = 0.3162$ and the inter-chain hopping $t = 1$.

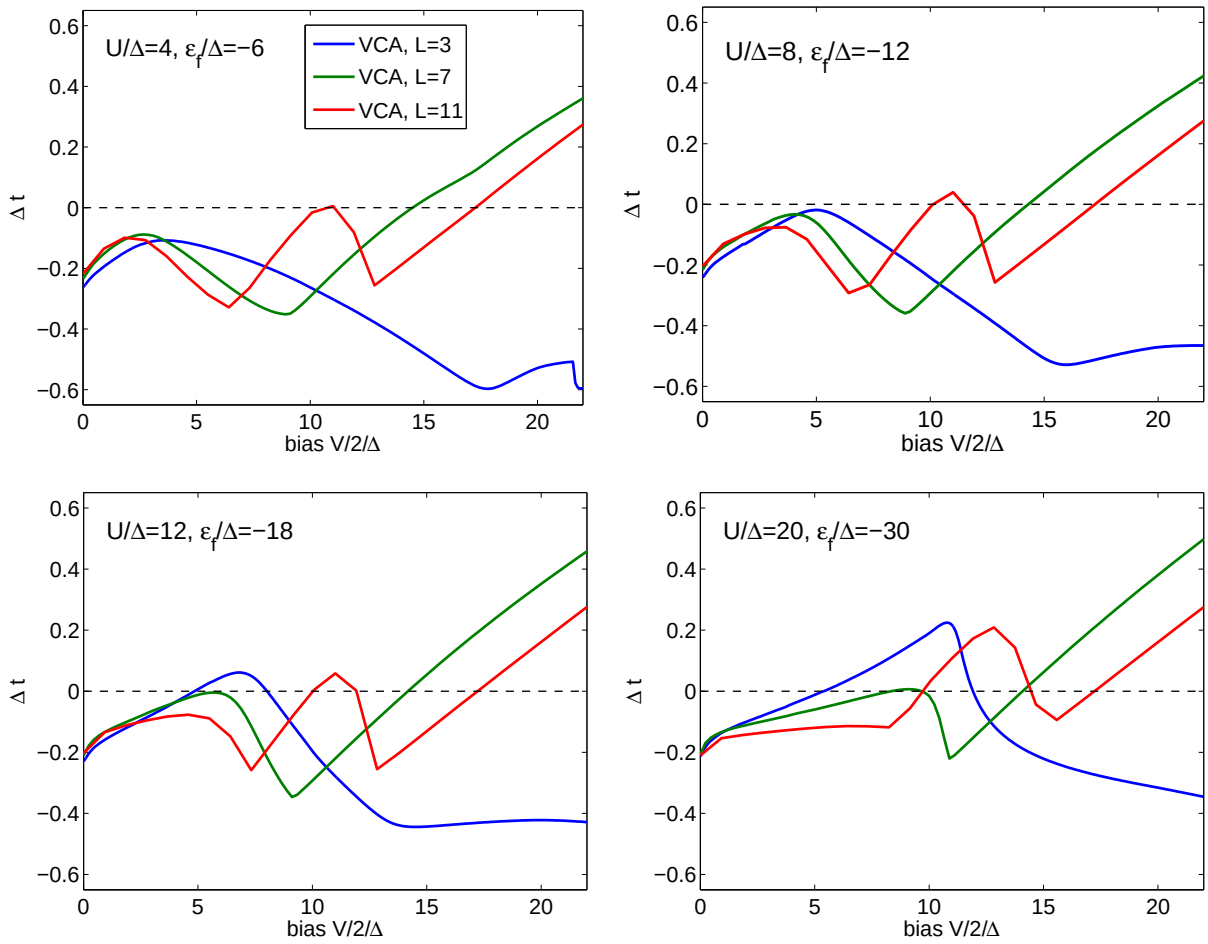

Figure 4.10.: Behavior of the non-equilibrium VCA variational parameter $\mathsf{x} = \{\Delta t\}$, $\Delta t = t' - t$ as a function of bias voltage. Shown are results for system-sizes $L = 3, 7$ and 11 in each plot. The figures from top, left to bottom, right are for different interaction-strengths $\frac{U}{\Delta} = 4, 8, 12$ and 20. These results are for the doubly-occupied impurity: $\epsilon_f = -\frac{U}{2} - U$. The hybridization was chosen to be $V = 0.3162$ and the inter-chain hopping $t = 1$.

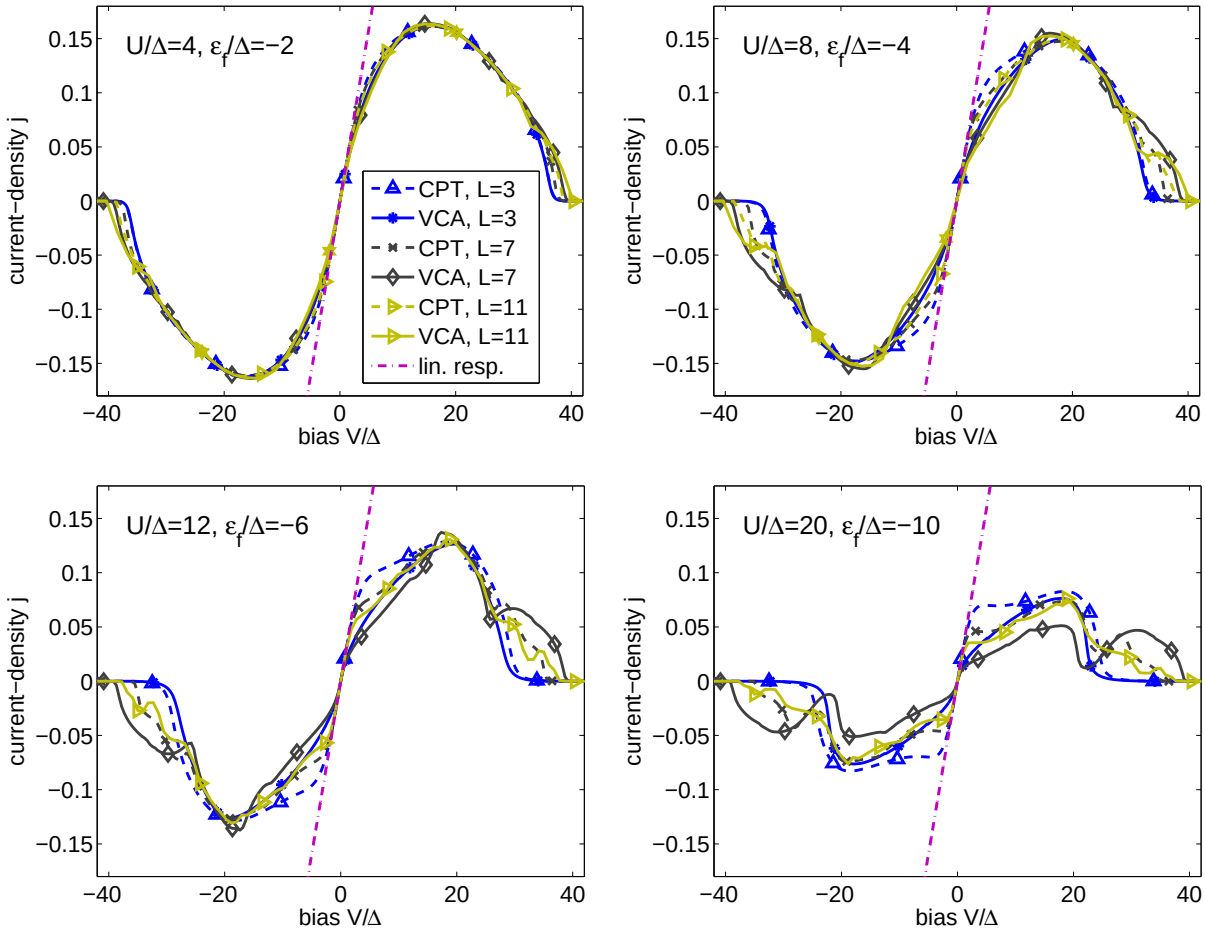

Figure 4.11.: Non-equilibrium VCA current under bias. Shown are results for system-sizes $L = 3, 7$ and 11 in each plot. The figures from top, left to bottom, right are for different interaction-strengths $\frac{U}{\Delta} = 4, 8, 12$ and 20. These results are for the singly-occupied impurity: $\epsilon_f = -\frac{U}{2}$. The hybridization was chosen to be $V = 0.3162$ and the inter-chain hopping $t = 1$. The linear-response result for the current, valid for this setup, is shown in addition. Note that the $L = 11$-site VCA data for $\frac{U}{\Delta} = 12$ and 20 is missing due to repeated trouble with the file system at lengthy calculations.

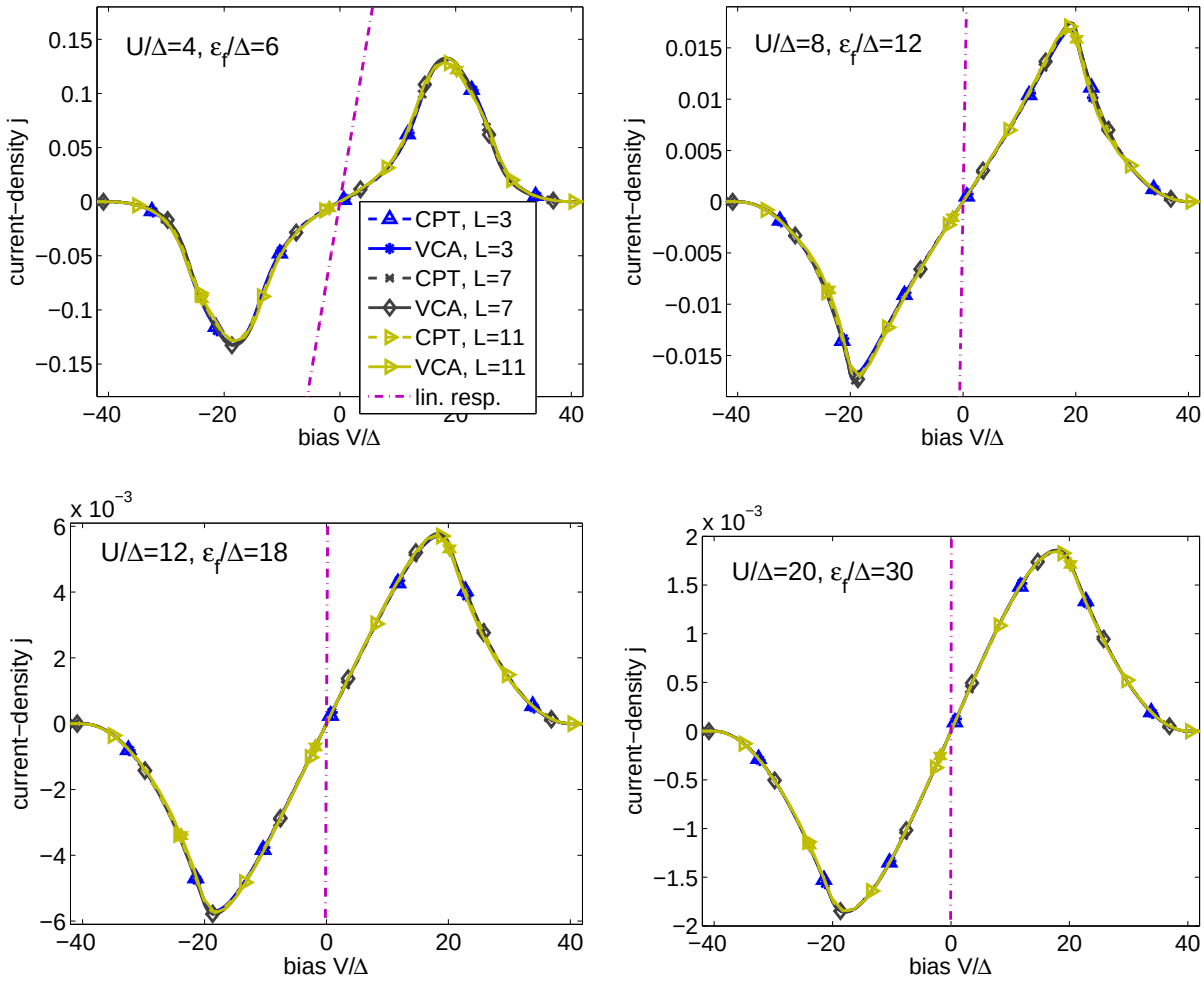

Figure 4.12.: Non-equilibrium VCA current under bias. Shown are results for system-sizes $L = 3, 7$ and 11 in each plot. The figures from top, left to bottom, right are for different interaction-strengths $\frac{U}{\Delta} = 4, 8, 12$ and 20. Note that the linear-response result for the current in the Kondo regime is indicated as a guide for the eye. This device is not in the Kondo regime. Also note the different scale on the y-axis. These results are for the zero-occupied impurity: $\epsilon_f = -\frac{U}{2} + 2U$. The hybridization was chosen to be $V = 0.3162$ and the inter-chain hopping $t = 1$.

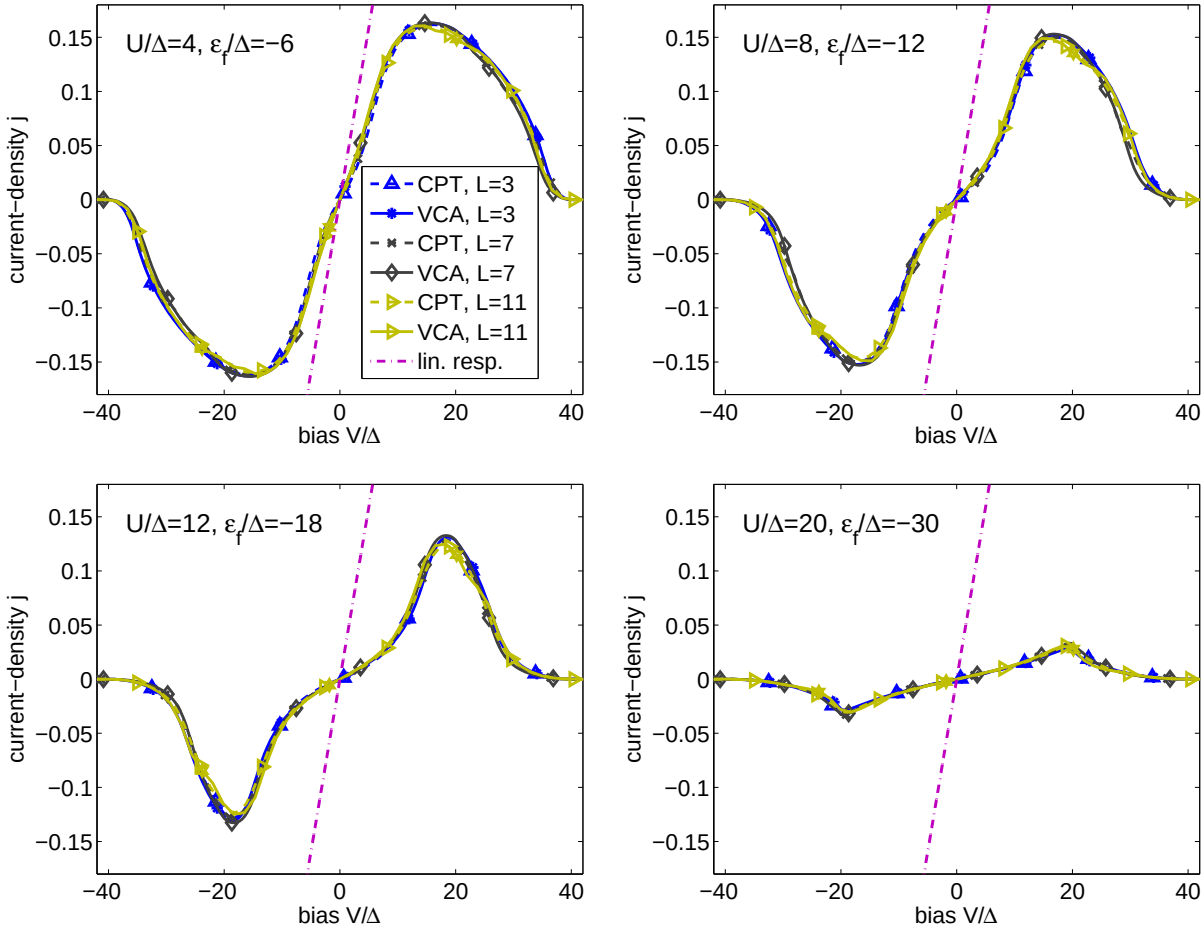

Figure 4.13.: Non-equilibrium VCA current under bias. Shown are results for system-sizes $L = 3, 7$ and 11 in each plot. The figures from top, left to bottom, right are for different interaction-strengths $\frac{U}{\Delta} = 4, 8, 12$ and 20. Note that the linear-response result for the current in the Kondo regime is indicated as a guide for the eye. This device is not in the Kondo regime. These results are for the doubly-occupied impurity: $\epsilon_f = -\frac{U}{2} - U$. The hybridization was chosen to be $V = 0.3162$ and the inter-chain hopping $t = 1$.

$L = 11$-site VCA results look a bit broader, which is due to the lower resolution of the images. While the CPT results produce a periodic structure in bias voltage, the VCA data shows a linear splitting of the Kondo peak up to a saturation region.
The local density of states in the impurity is shown in fig. 4.15 in the zero-occupied case. The local density of states in the impurity is shown in fig. 4.16 in the doubly-occupied case. In the zero- and doubly-occupied case, the DOS shows one of the Hubbard bands. Otherwise it looks pretty unspectacular. As already mentioned when discussing the current, in these parameter regions CPT and VCA yield similar results for all cluster sizes.

After examining these three distinct parameter sets, i.e. a singly-, doubly-, and un-occupied impurity, in detail, a wider picture resolving the whole parameter space of the SIAM shall be presented.

4.6.4. Current in all parameter regions

In this section the current through the dot under bias is analyzed as a function of the impurity on-site energy ϵ_f at fixed interaction strength U. The three cases studied in detail in the last section are of course included. By sweeping ϵ_f and calculating the current under bias at each ϵ_f, it is possible to study the behavior of the current in the different parameter regimes of the SIAM. Due to demanding computational time needed for these calculations, we limit ourselves to $L = 3$-site CPT/VCA here. The whole procedure and parameters are virtually identical to those used in the last section. The results for the current as a function of bias voltage and on-site energy are shown in fig. 4.17 for interaction strengths $U/\Delta = 4$ and 8 and in fig. 4.18 for interaction strengths $U/\Delta = 12$ and 20. In both figures CPT and VCA results for $L = 3$ and $\Delta = 0.1$ are shown. As noted already previously the differences between CPT and VCA for low interaction strength (see $U/\Delta = 4$) are rather small. However going to larger interaction strength they become large (see $U/\Delta = 20$). Note that this is the three-site result, so no two-peak structure develops in the VCA current, as seen in fig. 4.11. It is interesting to observe that in all cases the largest current is obtained exactly at the crossover points from the Kondo to the un- or doubly occupied impurity (these regions are marked by black-dashed lines in the plots). It is also interesting that the VCA procedure yields a much more uniform current upon variation of the on-site energy in the Kondo regime as the CPT calculation does. This result undermines once more that outside of the Kondo plateau CPT and VCA yield virtually the same result for all system sizes.

Next we briefly touch upon the case of different couplings to the two leads: $\Gamma_L \neq \Gamma_R$.

4.6.5. Asymmetric tunneling to the leads

In this section the effects of an asymmetric coupling of the dot to the left and right lead are explored. A coupling to the leads is chosen of $V_L = \frac{V}{1.5}$ and $V_R = 1.5V$ where $V = 0.3162$. The hopping everywhere else in the chain is $t = 1$ and a value for $\Delta = 0.1$ is calculated using V. The results for the current, variational parameters and density of states are shown in fig. 4.19 for $U/\Delta = 4$, in fig. 4.20 for $U/\Delta = 8$, in fig. 4.21 for $U/\Delta = 12$ and in fig. 4.22 for $U/\Delta = 20$. As predicted in ref. [169] under bias the Kondo resonance splits into two components with different weight. The one with higher weight located at the chemical potential of the lead which couples stronger. A pinning of the resonances at the respective chemical potentials of the leads cannot be observed here. However the effect of more weight in the peak closer to the chemical potential of the stronger coupling lead is predicted. It is interesting to observe in the density of states, that there seems to be a crossover to totally different behavior at some bias voltages. These crossovers are not due to problems with degeneracy when finding the cluster solution. Since in the whole thesis all calculations are done grand canonically and the degeneracy of the groundstate is taken care of (see eq. (2.13)). I suspect these crossovers to arise due to cluster symmetry, finite size and boundary conditions. Such crossovers occur more often for larger clusters. The CPT density of states for low bias voltages does not look very promising. However the VCA result does. It yields a reasonable density of states also in the low bias region. Furthermore it reduces the amount of spurious crossovers to a minimum. There is however a narrow region at medium bias voltages where the VCA result undergoes some crossovers. This can also be seen in the behavior of the variational parameters and the current. The current in this region most probably cannot be trusted. It is furthermore interesting that the VCA current is in most parameter regions larger than the CPT current.

This concludes the discussion about non-equilibrium VCA. We now turn to the description of Graphene with magnetic vacancies.

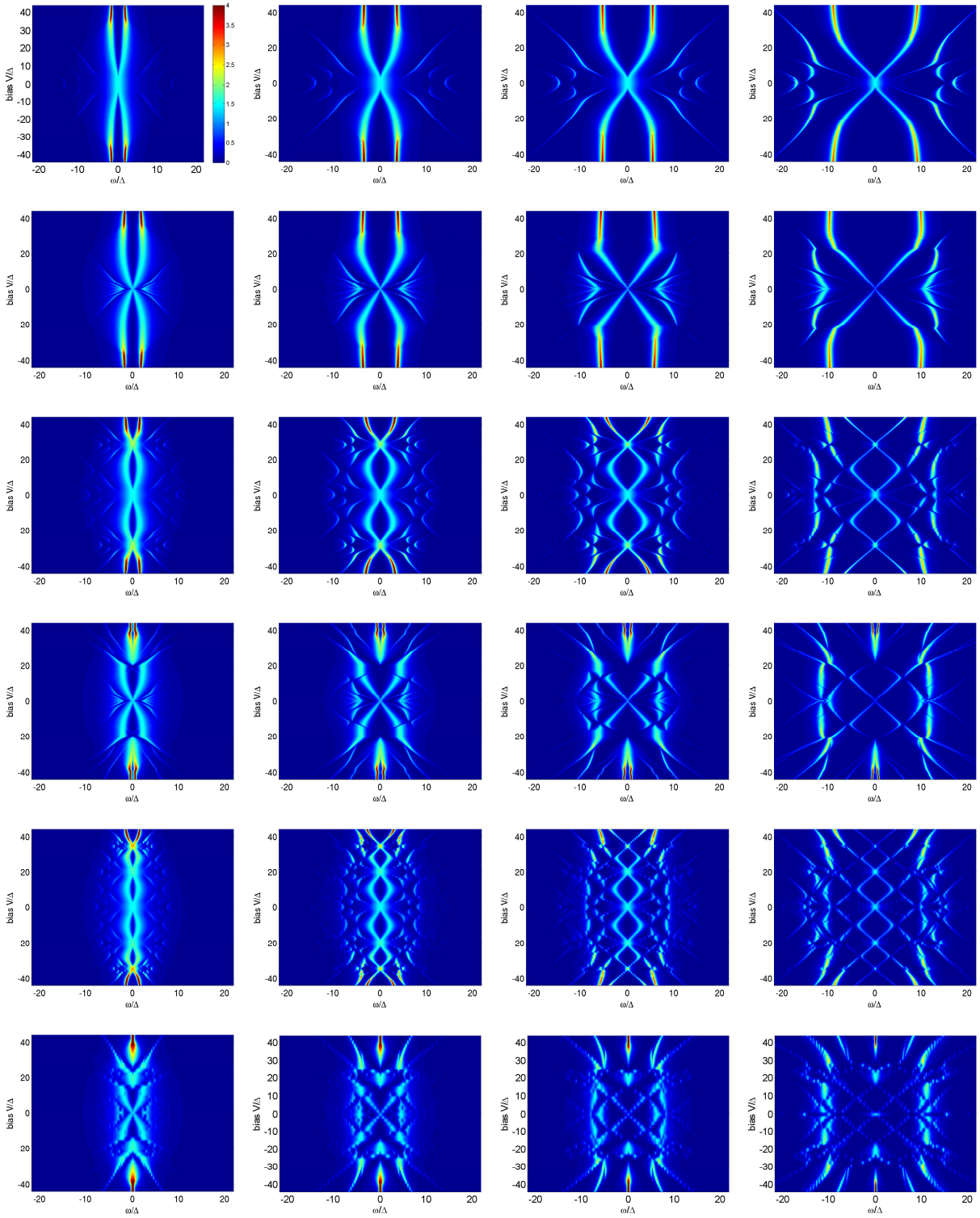

Figure 4.14.: Local density of states in the impurity for sizes of the cluster part of the reference system of $L = 3, 7$ and 11 as a function of the applied bias voltage. The results shown are for the singly-occupied impurity. Note that zero bias voltage amounts to the equilibrium situation. The maximum peak height in the high bias area may be up to three times as high as indicated in the colorbar. The colorbar was chosen to resolve also the finer structures at low bias. The sum rule eq. (2.16) is fulfilled at each applied bias voltage. From left-column to right-column the interaction strength increases: $\frac{U}{\Delta} = 4, 8, 12,$ and 20. (First row) CPT result for $L = 3$. (Second row) Non-equilibrium VCA result for $L = 3$. (Third row) CPT result for $L = 7$. (Fourth row) Non-equilibrium VCA result for $L = 7$. (Fifth row) CPT result for $L = 11$. (Sixth row) Non-equilibrium VCA result for $L = 11$.

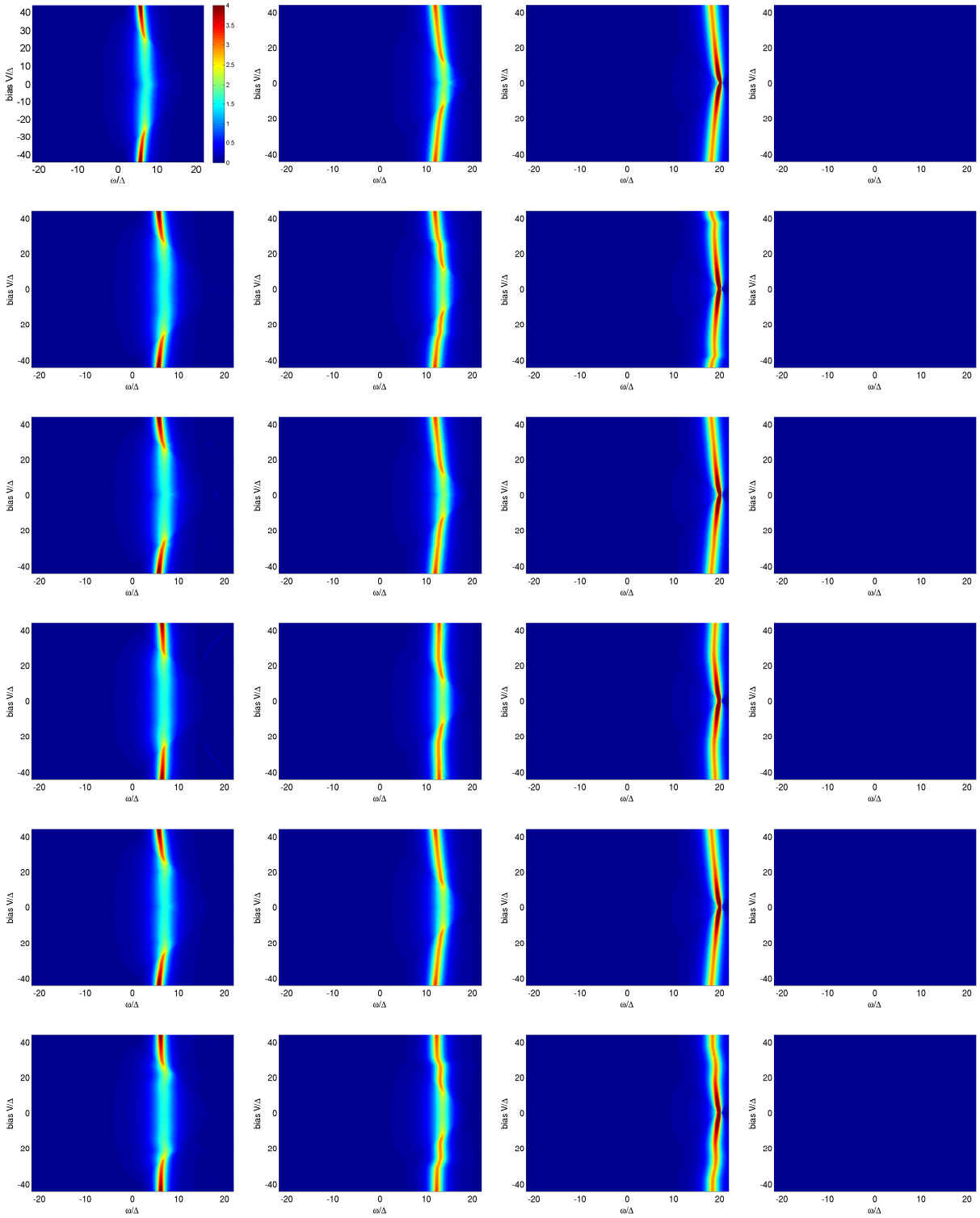

Figure 4.15.: Local density of states in the impurity for sizes of the cluster part of the reference system of $L = 3, 7$ and 11 as a function of the applied bias voltage. The results shown are for the zero-occupied impurity. Note that zero bias voltage amounts to the equilibrium situation. The maximum peak height in the high bias area may be up to three times as high as indicated in the colorbar. The colorbar was chosen to resolve also the finer structures at low bias. The sum rule eq. (2.16) is fulfilled at each applied bias voltage. From left-column to right-column the interaction strength increases: $\frac{U}{\Delta} = 4, 8, 12,$ and 20. (First row) CPT result for $L = 3$. (Second row) Non-equilibrium VCA result for $L = 3$. (Third row) CPT result for $L = 7$. (Fourth row) Non-equilibrium VCA result for $L = 7$. (Fifth row) CPT result for $L = 11$. (Sixth row) Non-equilibrium VCA result for $L = 11$.

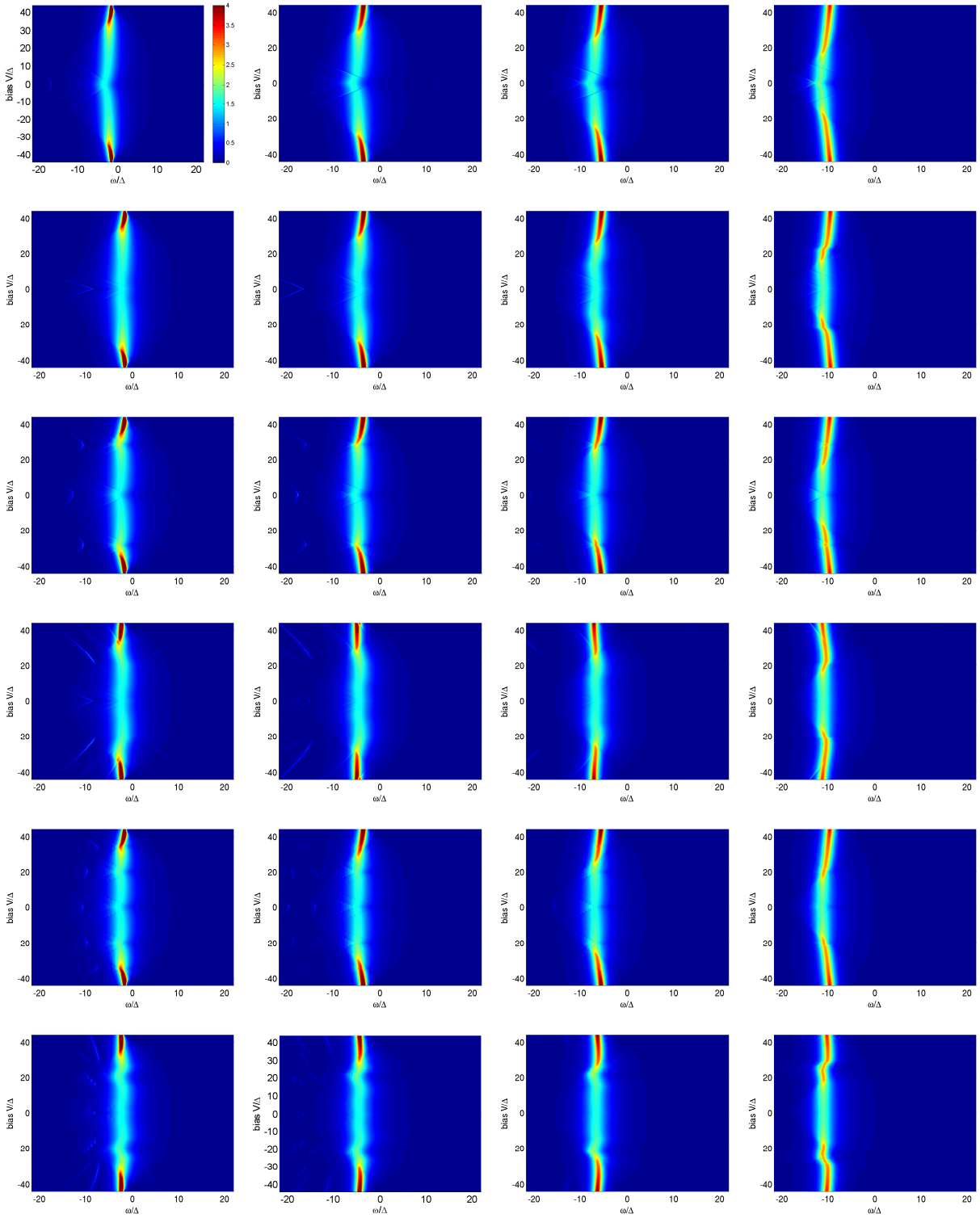

Figure 4.16.: Local density of states in the impurity for sizes of the cluster part of the reference system of $L = 3, 7$ and 11 as a function of the applied bias voltage. The results shown are for the doubly-occupied impurity. Note that zero bias voltage amounts to the equilibrium situation. The maximum peak height in the high bias area may be up to three times as high as indicated in the colorbar. The colorbar was chosen to resolve also the finer structures at low bias. The sum rule eq. (2.16) is fulfilled at each applied bias voltage. From left-column to right-column the interaction strength increases: $\frac{U}{\Delta} = 4, 8, 12,$ and 20. (First row) CPT result for $L = 3$. (Second row) Non-equilibrium VCA result for $L = 3$. (Third row) CPT result for $L = 7$. (Fourth row) Non-equilibrium VCA result for $L = 7$. (Fifth row) CPT result for $L = 11$. (Sixth row) Non-equilibrium VCA result for $L = 11$.

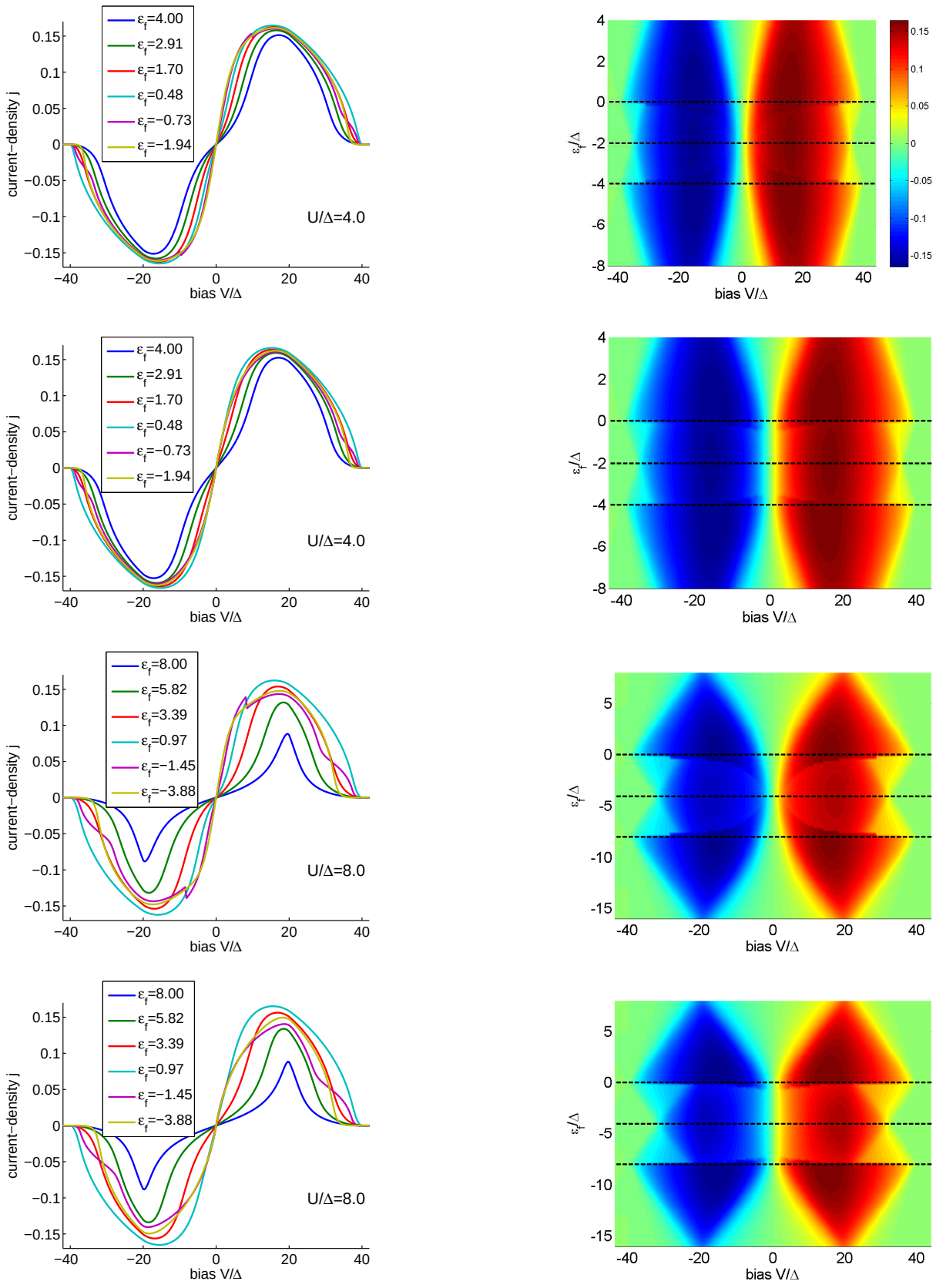

Figure 4.17.: The current under bias is shown as a function of on-site energy ϵ_f at fixed interaction strength U. Thereby the behavior of the current in different parameter regimes of the SIAM is probed. The upper group of four images show results for interaction strength $U/\Delta = 4$. The first row shows the CPT and the second row the VCA $\times = \{\Delta t\}$ result. The lower group of four images show results for interaction strength $U/\Delta = 8$. The CPT result is depicted in the third row, while the VCA results are plotted in the fourth row. (Left column) The current is shown for several selected values of on-site energy ϵ_f. (Right column) The current is shown in a density plot as a function of on-site energy ϵ_f and bias voltage.

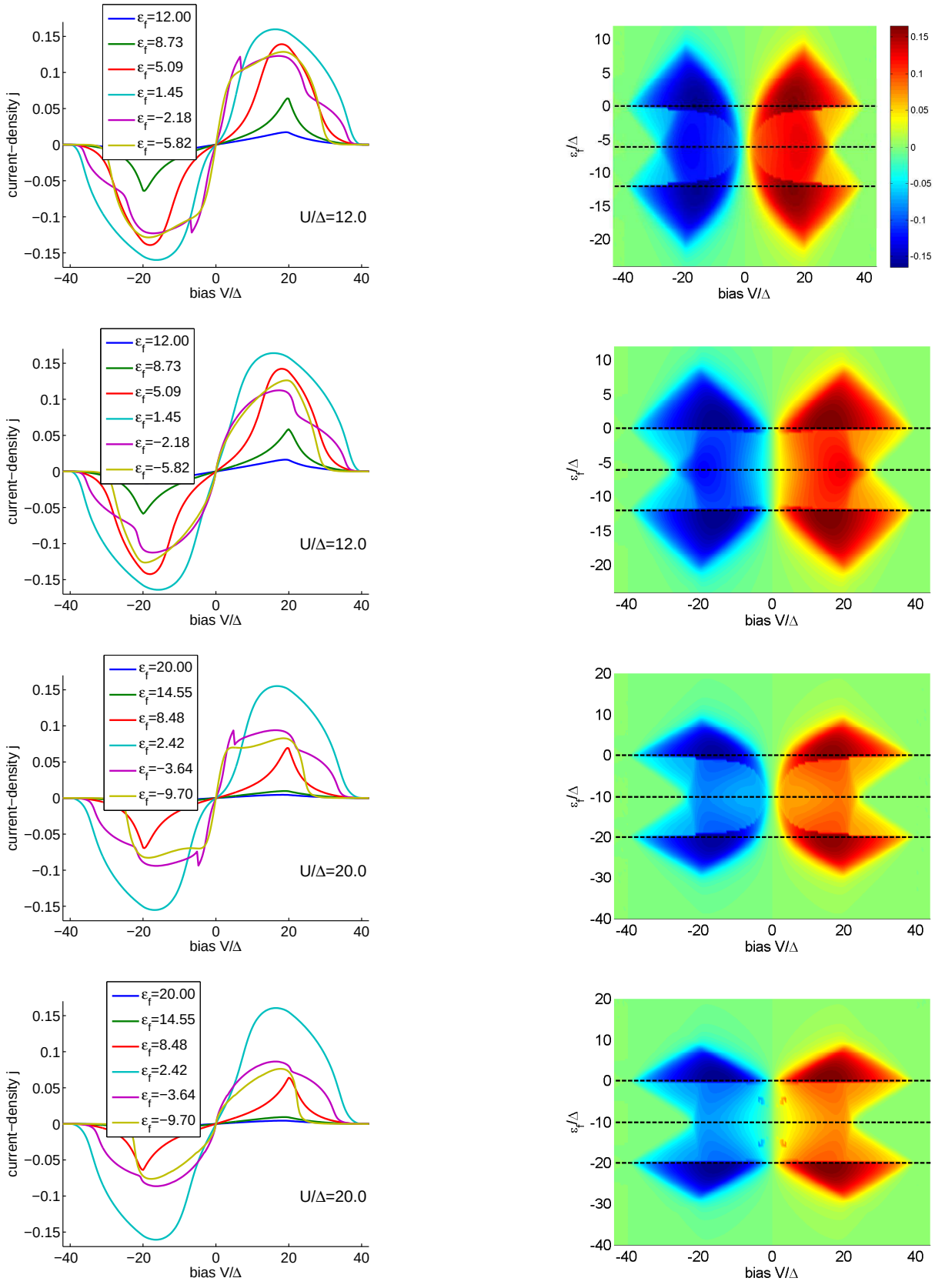

Figure 4.18.: The current under bias is shown as a function of on-site energy ϵ_f at fixed interaction strength U. Thereby the behavior of the current in different parameter regimes of the SIAM is probed. The upper group of four images show results for interaction strength $U/\Delta = 12$. The first row shows the CPT and the second row the VCA $\times = \{\Delta t\}$ result. The lower group of four images show results for interaction strength $U/\Delta = 20$. The CPT result is depicted in the third row, while the VCA results are plotted in the fourth row. (Left column) The current is shown for several selected values of on-site energy ϵ_f. (Right column) The current is shown in a density plot as a function of on-site energy ϵ_f and bias voltage.

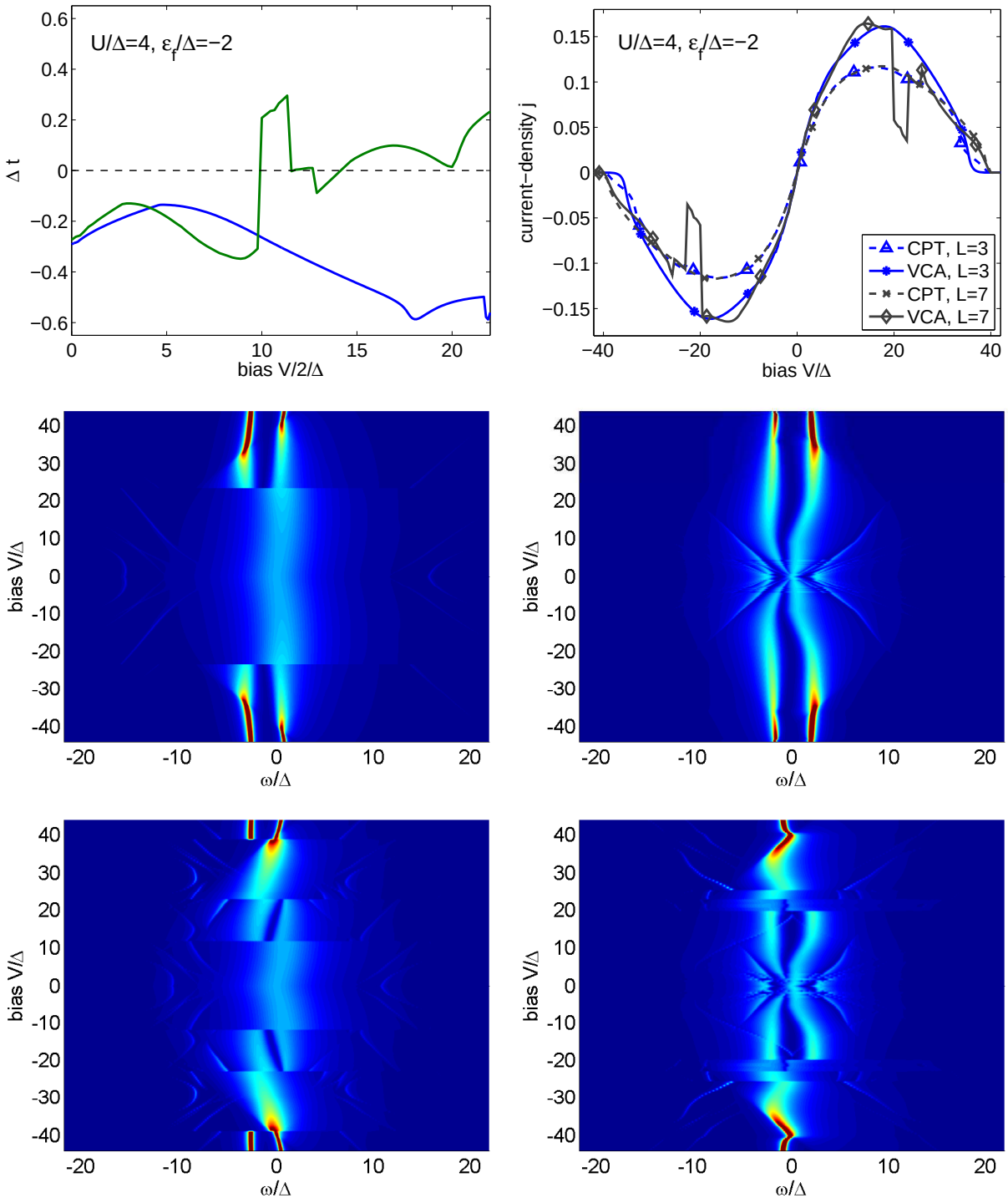

Figure 4.19.: Results for asymmetric coupling to the leads: $V_L = \frac{V}{1.5}$, $V_R = 1.5V$ for an interaction-strength of $U/\Delta = 4$ in the particle-hole symmetric case. All results have been obtained by CPT and VCA for $L = 3$ and 7. (Top left) The behavior of the VCA variational parameter t. (Top right) Current obtained by CPT/VCA. (Mid left) Density of states as obtained by $L = 3$-site CPT. (Mid right) Density of states as obtained by $L = 3$-site VCA. (Bottom left) Density of states as obtained by $L = 7$-site CPT. (Bottom right) Density of states as obtained by $L = 7$-site VCA.

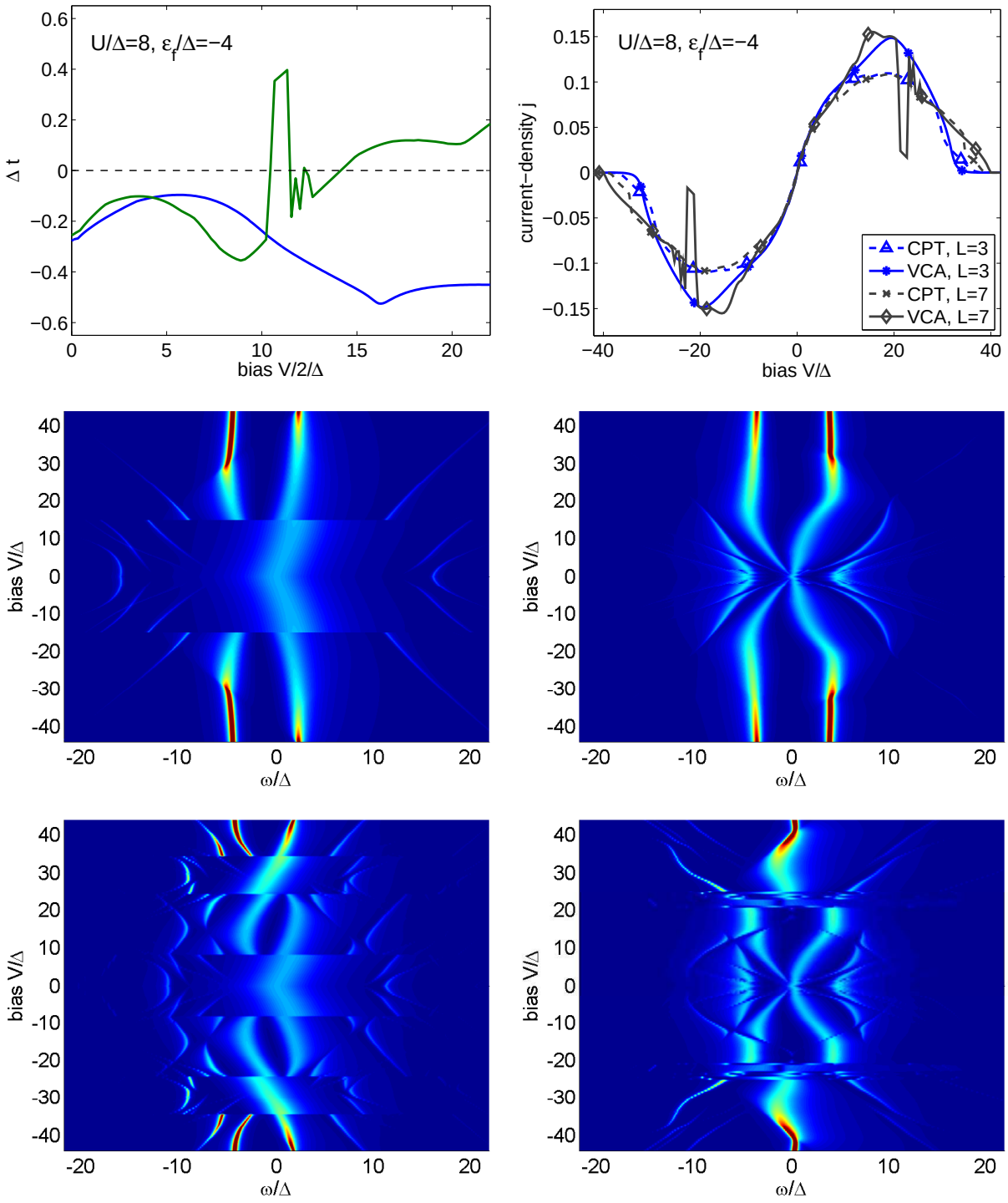

Figure 4.20.: Results for asymmetric coupling to the leads: $V_L = \frac{V}{1.5}$, $V_R = 1.5V$ for an interaction-strength of $U/\Delta = 8$ in the particle-hole symmetric case. All results have been obtained by CPT and VCA for $L = 3$ and 7. (Top left) The behavior of the VCA variational parameter t. (Top right) Current obtained by CPT/VCA. (Mid left) Density of states as obtained by $L = 3$-site CPT. (Mid right) Density of states as obtained by $L = 3$-site VCA. (Bottom left) Density of states as obtained by $L = 7$-site CPT. (Bottom right) Density of states as obtained by $L = 7$-site VCA.

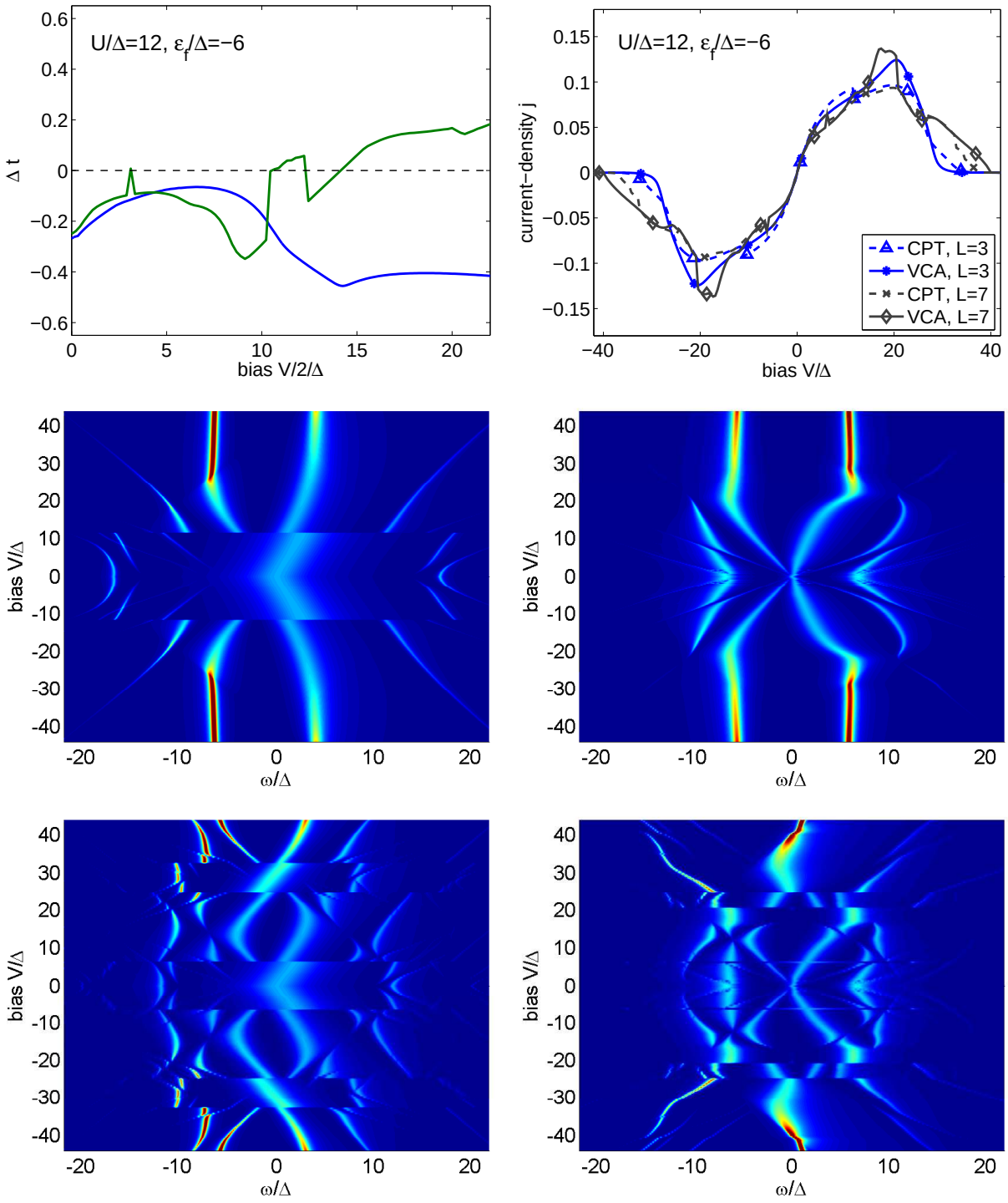

Figure 4.21.: Results for asymmetric coupling to the leads: $V_L = \frac{V}{1.5}$, $V_R = 1.5V$ for an interaction-strength of $U/\Delta = 12$ in the particle-hole symmetric case. All results have been obtained by CPT and VCA for $L = 3$ and 7. (Top left) The behavior of the VCA variational parameter t. (Top right) Current obtained by CPT/VCA. (Mid left) Density of states as obtained by $L = 3$-site CPT. (Mid right) Density of states as obtained by $L = 3$-site VCA. (Bottom left) Density of states as obtained by $L = 7$-site CPT. (Bottom right) Density of states as obtained by $L = 7$-site VCA.

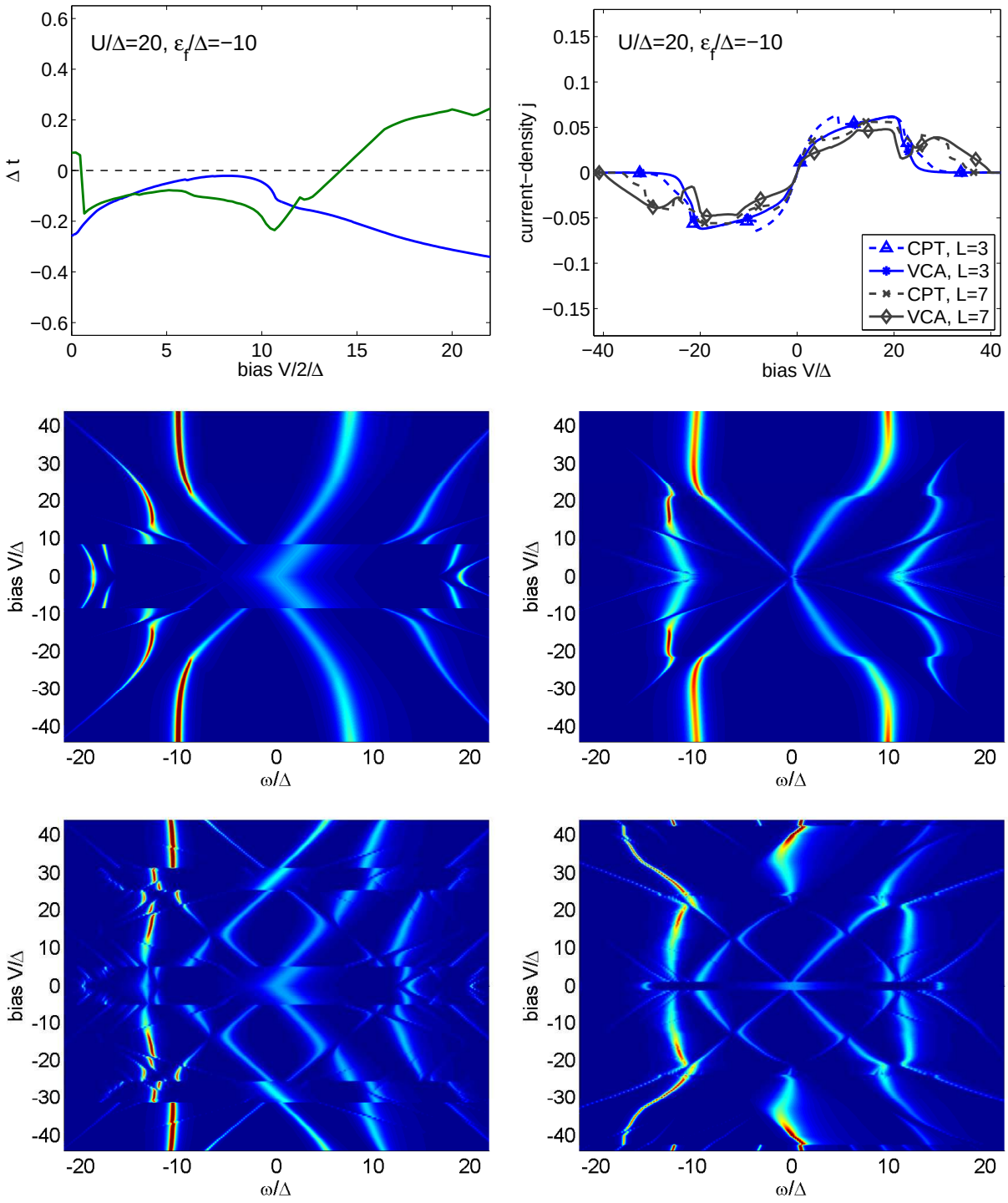

Figure 4.22.: Results for asymmetric coupling to the leads: $V_L = \frac{V}{1.5}$, $V_R = 1.5V$ for an interaction-strength of $U/\Delta = 20$ in the particle-hole symmetric case. All results have been obtained by CPT and VCA for $L = 3$ and 7. (Top left) The behavior of the VCA variational parameter t. (Top right) Current obtained by CPT/VCA. (Mid left) Density of states as obtained by $L = 3$-site CPT. (Mid right) Density of states as obtained by $L = 3$-site VCA. (Bottom left) Density of states as obtained by $L = 7$-site CPT. (Bottom right) Density of states as obtained by $L = 7$-site VCA.

5. Magnetic vacancies in Graphene

A single layer of Graphite, one allotrope of carbon, is named Graphene. Graphene consists of a single layer of carbon atoms, packed in a honeycomb lattice, with a carbon-carbon distance of $a = 0.142\,\mathrm{nm}$. This remarkable two-dimensional material, developed into one of the hottest topics in research during the last years. This can be attributed both to the amazing fundamental phenomena and the promising future applications. The interest in Graphene was furthermore fueled by the Nobel price in physics 2010, which was awarded to Geim and Novoselov for the production and isolation of this, previously thought unstable, material [172, 173]. Graphene is a playground for fascinating physics like the quantum Hall effect, Dirac fermions and Klein tunneling. It has remarkable mechanical and electrical properties. Being a transparent conductor, it is mechanically stronger than steel and stretchable. Both the thermal and electrical conductivity are very high. It is closely related to nano-structures, like fullerenes and carbon-nanowires, which can be thought of as rolled up Graphene. A good review of the electronic properties of Graphene can be found in ref. [174]. A description in terms of a tight-binding Hamiltonian in ref. [175]. The motivation for this work stems from a recent study of another remarkable feature of Graphene. Chen *et al.* found that vacancies, introduced by proton-irradiation, behave like magnetic defects [18]. Therefore a Kondo-like behavior is observed. Such effects have previously been reported in irradiated Graphene [176, 177] and apply as well to magnetic ad atoms on the surface [178, 179, 180]. The theoretical study is however difficult, because in addition to an interacting many-body problem which has to be solved, the material is strongly disordered. A study of what to expect from different forms of defects in Graphene was performed by Ding in ref. [181]. How disorder may be modeled in this material is described in ref. [182]. Some studies of defects in Graphene are available. Magnetic impurities were studied by QMC [183], DMFT [184] and analytic work [185]. The topic was furthermore related to quantum criticality [186]. A mean field/QMC study of the Hubbard model on a honeycomb lattice was performed recently by Feldner *et al.* [187].
In the following we build a model for disordered magnetic vacancies in Graphene. This model is loosely based on the SIAM, which was shown to yield good results within VCA in previous chapters. The new component here is a scheme of incorporating the randomness of disorder. This chapter is organized as follows. First the lattice structure of Graphene will be examined in context with CPT/VCA cluster tilings in sec. 5.1. The superlattice-wavevector transforms for this model are given there too. Then a CPT/VCA extension to random vacancies, a special form of disorder, will be discussed in sec. 5.2. To test the method results for the homogeneous Hubbard model on the Graphene lattice are presented in sec. 5.3. Finally results for the influence of magnetic vacancies in Graphene, on the single-particle spectra, are given in sec. 5.4.

5.1. Cluster decomposition of Graphene

Graphene is a purely two-dimensional material. In this section the decomposition of the Graphene lattice into two-site-, six-site ring- and ten-site double-ring- clusters is presented. These cluster decompositions are needed for CPT as well as the VCA treatment of Graphene. We start out by discussing the lattice structure of Graphene shown in fig. 5.1.

5.1.1. Graphene Lattice γ

The two dimensional Graphene lattice is not a Bravais lattice. This means it cannot be constructed by a one atom unit cell. The smallest unit cell possible is one consisting of two atoms. The Graphene lattice is then built up by placing this two atom element on a triangular lattice. The lattice vectors $\mathbf{R}^\gamma$ of this elementary lattice γ are given by

$$\mathbf{R}_1^\gamma = \frac{a}{\sqrt{3}} \begin{pmatrix} \frac{3}{2} \\ \frac{\sqrt{3}}{2} \end{pmatrix}, \qquad \mathbf{R}_2^\gamma = \frac{a}{\sqrt{3}} \begin{pmatrix} \frac{3}{2} \\ -\frac{\sqrt{3}}{2} \end{pmatrix}, \tag{5.1}$$

where a is the lattice constant, which is set to 1 in this work. This lattice is depicted in fig. 5.2 (left). In literature the lattice vectors of hexagonal type lattices are often given with the lattice constant a scaled

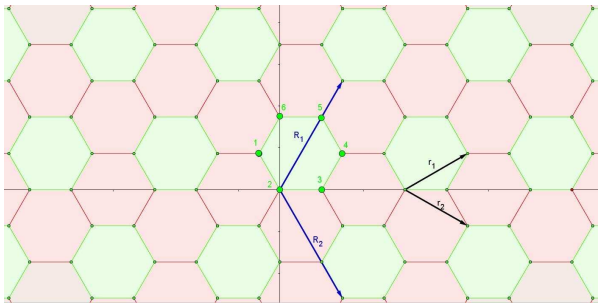

Figure 5.1.: The two dimensional lattice of Graphene. The Bravais lattice is a triangular two dimensional lattice (eq. (5.1)). The black arrows (r_1, r_2) indicate the lattice vectors of the lattice γ. A two site unit cell is attached at each lattice point (eq. (5.2)). Shown is a cluster decomposition into six-site ring clusters (green). The green numbers show the labeling of the sites inside the cluster (eq. (5.2)). The blue arrows (R_1, R_2) indicate the lattice vectors of the superlattice Γ. The Bravais lattice here is a jolted triangular lattice given in eq. (5.1). The lattice constant was chosen to be $a = 1$.

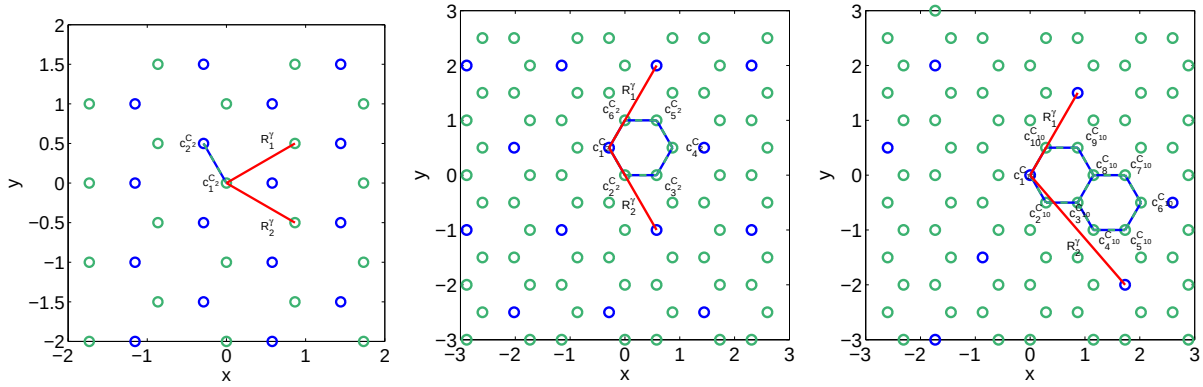

Figure 5.2.: (Left) Lattice of Graphene γ eq. (5.1). The lattice vectors are indicated in red and the two atoms of the unit cell are labeled according to eq. (5.2). (Mid) The lattice of the six-site ring cluster Γ_6 eq. (5.5). The lattice vectors are indicated in red and the six atoms of the unit cell are labeled according to eq. (5.6). (Right) The lattice of the ten-site double ring cluster Γ_{10} eq. (5.9). The lattice vectors are indicated in red and the ten atoms of the unit cell are labeled according to eq. (5.10). The lattice constant was chosen to be $a = 1$.

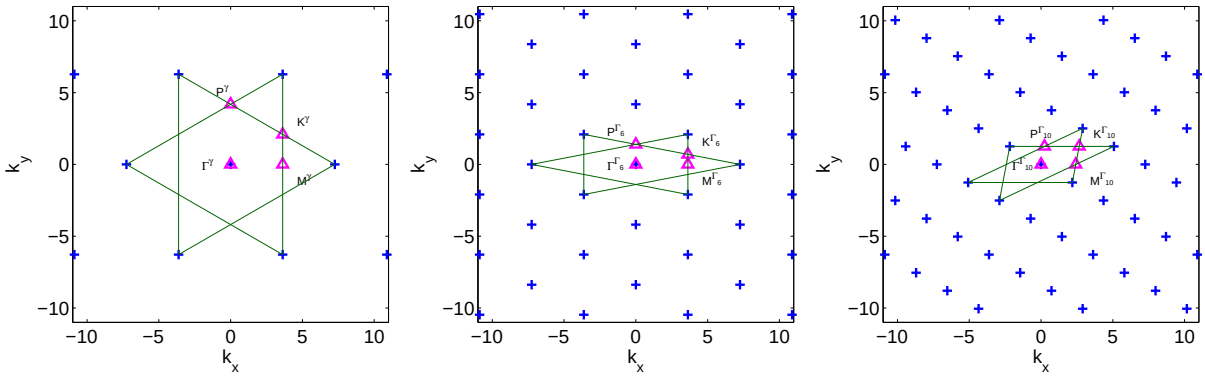

Figure 5.3.: (Left) Reciprocal lattice of Graphene γ (eq. (5.3)). Some special points in the Brillouin zone (purple triangles) are given in eq. (5.4). (Mid) The reciprocal lattice of the superlattice Γ_6 (eq. (5.7)). Special points in the Brillouin zone (purple triangles) are given in eq. (5.8). (Right) The reciprocal lattice of the superlattice Γ_{10} (eq. (5.11)). Special points in the Brillouin zone (purple triangles) are given in eq. (5.12). The lattice constant was chosen to be $a = 1$.

by $\sqrt{3}$. This often leads to confusing factors of $\sqrt{3}$ when one is used to working with the bare a. Here I tried to make a compromise and pull the factor $\sqrt{3}$ explicitly out of the expressions which makes them readable in both conventions. The two atoms in the unit cell C_2 are located at

$$\mathbf{c}_1^{C_2} = \frac{a}{\sqrt{3}} \begin{pmatrix} 0 \\ 0 \end{pmatrix}, \qquad \mathbf{c}_2^{C_2} = \frac{a}{\sqrt{3}} \begin{pmatrix} -\frac{1}{2} \\ \frac{\sqrt{3}}{2} \end{pmatrix}. \tag{5.2}$$

The reciprocal lattice vectors $\mathbf{K}^\gamma$ are given by

$$\mathbf{K}_1^\gamma = \frac{2\pi\sqrt{3}}{a} \begin{pmatrix} \frac{1}{3} \\ \frac{1}{\sqrt{3}} \end{pmatrix}, \qquad \mathbf{K}_2^\gamma = \frac{2\pi\sqrt{3}}{a} \begin{pmatrix} \frac{1}{3} \\ -\frac{1}{\sqrt{3}} \end{pmatrix}. \tag{5.3}$$

The reciprocal lattice and the Brillouin zone are shown in fig. 5.3 (left). Special points in the Brillouin zone are given by

$$\Gamma^\gamma = \begin{pmatrix} 0 \\ 0 \end{pmatrix}, \qquad P^\gamma = \frac{2\pi\sqrt{3}}{a} \begin{pmatrix} 0 \\ \frac{4}{27} \end{pmatrix}, \qquad M^\gamma = \frac{2\pi\sqrt{3}}{a} \begin{pmatrix} \frac{1}{3} \\ 0 \end{pmatrix}, \qquad K^\gamma = \frac{2\pi\sqrt{3}}{a} \begin{pmatrix} \frac{1}{3} \\ \frac{1}{3\sqrt{3}} \end{pmatrix}. \tag{5.4}$$

5.1.2. Six-site ring superlattice Γ_6

We now consider one possible cluster tiling which is motivated by the lattice symmetry. The lattice vectors of the superlattice Γ_6 for six-site ring clusters are given by

$$\mathbf{R}_1^{\Gamma_6} = \frac{a}{\sqrt{3}} \begin{pmatrix} \frac{3}{2} \\ \frac{3\sqrt{3}}{2} \end{pmatrix}, \qquad \mathbf{R}_2^{\Gamma_6} = \frac{a}{\sqrt{3}} \begin{pmatrix} \frac{3}{2} \\ -\frac{3\sqrt{3}}{2} \end{pmatrix}. \tag{5.5}$$

The six atoms in the cluster C_6 are located at

$$\begin{aligned} \mathbf{c}_1^{C_6} &= \frac{a}{\sqrt{3}} \begin{pmatrix} -\frac{1}{2} \\ \frac{\sqrt{3}}{2} \end{pmatrix}, & \mathbf{c}_2^{C_6} &= \frac{a}{\sqrt{3}} \begin{pmatrix} 0 \\ 0 \end{pmatrix}, & \mathbf{c}_3^{C_6} &= \frac{a}{\sqrt{3}} \begin{pmatrix} 1 \\ 0 \end{pmatrix}, \\ \mathbf{c}_4^{C_6} &= \frac{a}{\sqrt{3}} \begin{pmatrix} \frac{3}{2} \\ \frac{\sqrt{3}}{2} \end{pmatrix}, & \mathbf{c}_5^{C_6} &= \frac{a}{\sqrt{3}} \begin{pmatrix} 1 \\ \sqrt{3} \end{pmatrix}, & \mathbf{c}_6^{C_6} &= \frac{a}{\sqrt{3}} \begin{pmatrix} 0 \\ \sqrt{3} \end{pmatrix}. \end{aligned} \tag{5.6}$$

This lattice is depicted in fig. 5.2 (mid). The reciprocal lattice vectors $\mathbf{K}^{\Gamma_6}$ are given by

$$\mathbf{K}_1^{\Gamma_6} = \frac{2\pi\sqrt{3}}{a} \begin{pmatrix} \frac{1}{3} \\ \frac{1}{3\sqrt{3}} \end{pmatrix}, \qquad \mathbf{K}_2^{\Gamma_6} = \frac{2\pi\sqrt{3}}{a} \begin{pmatrix} \frac{1}{3} \\ -\frac{1}{3\sqrt{3}} \end{pmatrix}. \tag{5.7}$$

The reciprocal lattice and the Brillouin zone are shown in fig. 5.3 (mid). Special points in the Brillouin zone are given by

$$\Gamma^{\Gamma_6} = \begin{pmatrix} 0 \\ 0 \end{pmatrix}, \qquad P^{\Gamma_6} = \frac{2\pi\sqrt{3}}{a} \begin{pmatrix} 0 \\ \frac{2}{9\sqrt{3}} \end{pmatrix}, \qquad M^{\Gamma_6} = \frac{2\pi\sqrt{3}}{a} \begin{pmatrix} \frac{1}{3} \\ 0 \end{pmatrix}, \qquad K^{\Gamma_6} = \frac{2\pi\sqrt{3}}{a} \begin{pmatrix} \frac{1}{3} \\ \frac{1}{9\sqrt{3}} \end{pmatrix}. \tag{5.8}$$

5.1.3. Ten-site double ring Superlattice Γ_{10}

Another possible cluster tiling which is motivated by the lattice symmetry is a ten-site double ring cluster. The lattice vectors of the superlattice Γ_{10} are given by

$$\mathbf{R}_1^{\Gamma_{10}} = \frac{a}{\sqrt{3}} \begin{pmatrix} \frac{3}{2} \\ \frac{3\sqrt{3}}{2} \end{pmatrix}, \qquad \mathbf{R}_2^{\Gamma_{10}} = \frac{a}{\sqrt{3}} \begin{pmatrix} 3 \\ -2\sqrt{3} \end{pmatrix}. \tag{5.9}$$

The ten atoms in the cluster C_{10} are located at

$$\begin{aligned} &\mathbf{c}_1^{C_{10}} = \frac{a}{\sqrt{3}} \begin{pmatrix} 0 \\ 0 \end{pmatrix}, \quad \mathbf{c}_2^{C_{10}} = \frac{a}{\sqrt{3}} \begin{pmatrix} \frac{1}{2} \\ -\frac{\sqrt{3}}{2} \end{pmatrix}, \quad \mathbf{c}_3^{C_{10}} = \frac{a}{\sqrt{3}} \begin{pmatrix} \frac{3}{2} \\ -\frac{\sqrt{3}}{2} \end{pmatrix}, \quad \mathbf{c}_4^{C_{10}} = \frac{a}{\sqrt{3}} \begin{pmatrix} 2 \\ -\sqrt{3} \end{pmatrix}, \quad \mathbf{c}_5^{C_{10}} = \frac{a}{\sqrt{3}} \begin{pmatrix} 3 \\ -\sqrt{3} \end{pmatrix}, \\ &\mathbf{c}_6^{C_{10}} = \frac{a}{\sqrt{3}} \begin{pmatrix} \frac{7}{2} \\ -\frac{\sqrt{3}}{2} \end{pmatrix}, \quad \mathbf{c}_7^{C_{10}} = \frac{a}{\sqrt{3}} \begin{pmatrix} 3 \\ 0 \end{pmatrix}, \quad \mathbf{c}_8^{C_{10}} = \frac{a}{\sqrt{3}} \begin{pmatrix} 2 \\ 0 \end{pmatrix}, \quad \mathbf{c}_9^{C_{10}} = \frac{a}{\sqrt{3}} \begin{pmatrix} \frac{3}{2} \\ \frac{\sqrt{3}}{2} \end{pmatrix}, \quad \mathbf{c}_{10}^{C_{10}} = \frac{a}{\sqrt{3}} \begin{pmatrix} \frac{1}{2} \\ \frac{\sqrt{3}}{2} \end{pmatrix}. \end{aligned} \tag{5.10}$$

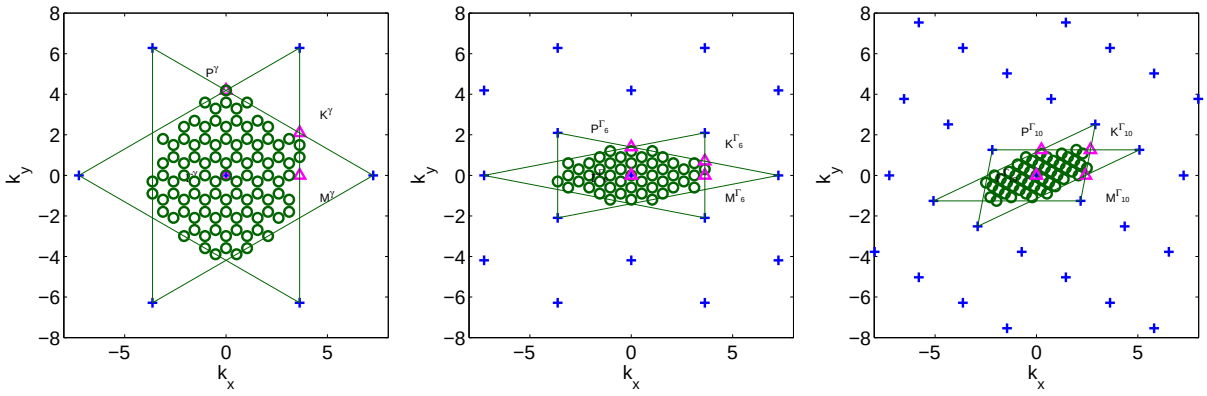

Figure 5.4.: (Left) The reciprocal lattice points of the lattice γ for a 7×7 system with periodic boundary conditions. (Mid) The reciprocal lattice points of the lattice Γ_6 for a 7×7 system with periodic boundary conditions. (Right) The reciprocal lattice points of the lattice Γ_{10} for a 7×7 system with periodic boundary conditions.

This lattice is visualized in fig. 5.2 (right). The reciprocal lattice vectors $\mathbf{K}^{\Gamma_{10}}$ are given by

$$\mathbf{K}_1^{\Gamma_{10}} = \frac{2\pi\sqrt{3}}{a}\begin{pmatrix}\frac{4}{15}\\ \frac{2\sqrt{3}}{15}\end{pmatrix}, \qquad \mathbf{K}_2^{\Gamma_{10}} = \frac{2\pi\sqrt{3}}{a}\begin{pmatrix}\frac{1}{5}\\ -\frac{1}{5\sqrt{3}}\end{pmatrix}. \tag{5.11}$$

The reciprocal lattice and the Brillouin zone are shown in fig. 5.3 (right). Special points in the Brillouin zone are given by

$$\Gamma^{\Gamma_{10}} = \begin{pmatrix}0\\0\end{pmatrix}, \quad P^{\Gamma_{10}} = \frac{2\pi\sqrt{3}}{a}\begin{pmatrix}\frac{1}{45}\\ \frac{\sqrt{3}}{15}\end{pmatrix}, \quad M^{\Gamma_{10}} = \frac{2\pi\sqrt{3}}{a}\begin{pmatrix}\frac{10}{45}\\ 0\end{pmatrix}, \quad K^{\Gamma_{10}} = \frac{2\pi\sqrt{3}}{a}\begin{pmatrix}\frac{11}{45}\\ \frac{\sqrt{3}}{15}\end{pmatrix}. \tag{5.12}$$

After discussing several possible cluster tilings, the reciprocal space of these lattices is to be examined.

5.1.4. Brillouin zones of the Graphene lattices

The **k**-points of the first Brillouin zone are needed for computing integrals in reciprocal space by evaluating sums over **k** dependent quantities (**k** out of the first Brillouin zone). For an infinite system there exist special schemes how to choose special **k**-points [188, 189, 190] representative for the whole system. Sampling **k**-points is not a good option in this case because one wants to compare results obtained by different calculations and one would have to ensure the use of the same sampled **k**-points. We deal with finite lattices (with periodic boundary conditions). Here the **k**-points can be obtained exactly by first creating a mesh of **k**-points along the reciprocal lattice vectors

$$\mathbf{k_p} = \frac{n_1}{N_1}\mathbf{K_1} + \frac{n_2}{N_2}\mathbf{K_2}\,,$$

where N_i is the number of lattice points along reciprocal lattice vector $\mathbf{K_i}$ and n_i runs from $-[\frac{N_i}{2}]$ to $[\frac{N_i}{2}]$. Here [ ] denotes the Gauss bracket. Not all the points $\mathbf{k_p}$ will lie within the first Brillouin zone and some need to be folded back to it. This procedure depends on the shape of the Brillouin zone. The first Brillouin zones of the 2, 6 and 10-site clusters are shown in fig. 5.4. The computational effort of sums in **k**-space may be reduced considerably by taking Brillouin zone symmetries into account.
For CPT/VCA the inter-cluster hopping matrix T is needed in a superlattice wave vector transformed form, which will be discussed in the following.

5.1.5. Superlattice wave vector transform

Considering a lattice γ of infinite extent, the superlattice-wave vector transform of the hopping matrix $\mathrm{T}_{\mathbf{rr'}}$ is given by

$$\begin{aligned}\mathrm{T}_{\mathbf{RR'}}(\tilde{\mathbf{k}}) &= \sum_{\tilde{\mathbf{r}}\in\Gamma} e^{i\tilde{\mathbf{k}}\cdot\tilde{\mathbf{r}}}\ \mathrm{T}_{\mathbf{rr'}} \text{ where } \begin{cases}\mathbf{r} = & \mathbf{R}\\ \mathbf{r'} = & \tilde{\mathbf{r}}+\mathbf{R'}\end{cases},\\ \mathrm{T}_{ij}(\tilde{\mathbf{k}}) &= \sum_{n_1,n_2\in\{-1,0,1\}} e^{i\tilde{\mathbf{k}}\cdot\left(n_1\mathbf{R}_1^\Gamma+n_2\mathbf{R}_2^\Gamma\right)}\ \mathrm{T}_{i,\,j+n_1 \text{ action of } \mathbf{R}_1^\Gamma(j)+n_2 \text{ action of } \mathbf{R}_2^\Gamma(j)}\,,\end{aligned} \tag{5.13}$$

where $\mathbf{r}$ are lattice vectors of the lattice γ, $\mathbf{R}$ are locations inside the cluster and $\tilde{\mathbf{r}}$ are lattice vectors of the superlattice Γ. We now turn to the specific cases of the cluster decompositions discussed above.

5.1.6. One-site Cluster Tiling

Although the unit cell of Graphene consists of two atoms, it is possible to construct single-site clusters by attributing the intra-unit cell hopping to the hopping matrix T and solving the atomic problem for the cluster Green's function. The superlattice is then given by the elementary Graphene lattice γ. The superlattice-wave vector transformed hopping matrix is given by

$$\mathrm{T}_{ij}^{(1)}(\mathbf{k}) = \begin{pmatrix} \Delta\epsilon & -t\left(1+e^{-i\mathbf{k}\cdot\mathbf{R}_2^\gamma}+e^{+i\mathbf{k}\cdot\left(\mathbf{R}_1^\gamma-\mathbf{R}_2^\gamma\right)}\right)\\ -t\left(1+e^{+i\mathbf{k}\cdot\mathbf{R}_2^\gamma}+e^{-i\mathbf{k}\cdot\left(\mathbf{R}_1^\gamma-\mathbf{R}_2^\gamma\right)}\right) & \Delta\epsilon\end{pmatrix}, \tag{5.14}$$

where t is the uniform nearest neighbor hopping matrix element. The quantity $\Delta\epsilon$ is introduced by the VCA procedure as variational parameter.
Note that in the case of one-site clusters no Green's function periodization is necessary.

5.1.7. Two-site Cluster Tiling

The superlattice here again is given by the elementary Graphene lattice γ. For two-site clusters the superlattice-wave vector transformed hopping matrix is given by

$$\mathrm{T}_{ij}^{(2)}(\mathbf{k}) = \begin{pmatrix} \Delta\epsilon & \Delta t - t\left(e^{-i\mathbf{k}\cdot\mathbf{R}_2^\gamma}+e^{+i\mathbf{k}\cdot\left(\mathbf{R}_1^\gamma-\mathbf{R}_2^\gamma\right)}\right)\\ \Delta t - t\left(e^{+i\mathbf{k}\cdot\mathbf{R}_2^\gamma}+e^{-i\mathbf{k}\cdot\left(\mathbf{R}_1^\gamma-\mathbf{R}_2^\gamma\right)}\right) & \Delta\epsilon\end{pmatrix}. \tag{5.15}$$

The quantities $\Delta\epsilon$ and Δt are introduced by the VCA procedure as variational parameters. Note that in the case of two-site clusters no Green's function periodization is necessary.

5.1.8. Six-site Ring Cluster Tiling

For a six-site ring cluster the superlattice is given above by the lattice Γ_6. The superlattice-wave vector transformed hopping matrix is given by

$$\mathrm{T}_{ij}^{(6)}(\mathbf{k}) = \begin{pmatrix} \Delta\epsilon & \Delta t & 0 & -t\,e^{-i\mathbf{k}\cdot\left(\mathbf{R}_1^{\Gamma_6}+\mathbf{R}_2^{\Gamma_6}\right)} & 0 & \Delta t\\ \Delta t & \Delta\epsilon & \Delta t & 0 & -t\,e^{-i\mathbf{k}\cdot\mathbf{R}_1^{\Gamma_6}} & 0\\ 0 & \Delta t & \Delta\epsilon & \Delta t & 0 & -t\,e^{+i\mathbf{k}\cdot\mathbf{R}_2^{\Gamma_6}}\\ -t\,e^{+i\mathbf{k}\cdot\left(\mathbf{R}_1^{\Gamma_6}+\mathbf{R}_2^{\Gamma_6}\right)} & 0 & \Delta t & \Delta\epsilon & \Delta t & 0\\ 0 & -t\,e^{+i\mathbf{k}\cdot\mathbf{R}_1^{\Gamma_6}} & 0 & \Delta t & \Delta\epsilon & \Delta t\\ \Delta t & 0 & -t\,e^{-i\mathbf{k}\cdot\mathbf{R}_2^{\Gamma_6}} & 0 & \Delta t & \Delta\epsilon\end{pmatrix}. \tag{5.16}$$

For six site clusters the general periodization prescription for Green's functions

$$\begin{aligned}\mathrm{G}(\mathbf{k},\omega) &= \frac{1}{N_C}\sum_{\mathbf{R},\mathbf{R'}} e^{-i\mathbf{k}\cdot(\mathbf{R}-\mathbf{R'})}\ \mathrm{G}_{\mathbf{RR'}}(\mathbf{k},\omega)\\ &= \frac{1}{N_C}\sum_{i,j} e^{-i\mathbf{k}\cdot(\mathbf{c}_i-\mathbf{c}_j)}\ \mathrm{G}_{ij}(\mathbf{k},\omega)\,,\end{aligned} \tag{5.17}$$

may be generalized to

$$\mathrm{G}_{\alpha\beta}(\mathbf{k},\omega) = \frac{1}{N_C} \sum_{i\epsilon\alpha} \sum_{j\epsilon\beta} e^{-i\mathbf{k}\cdot(\mathbf{c}_i - \mathbf{c}_j)}\, \mathrm{G}_{ij}(\mathbf{k},\omega)\,, \tag{5.18}$$

where α, β denote the two translationally inequivalent lattice sites of the two-site unit cell C_2 and i and j denote the sites of the cluster under consideration. The specific application to the six-site ring cluster yields

$$\mathrm{G}_{\alpha\beta}(\mathbf{k},\omega) = \frac{1}{N_C} \sum_{i\epsilon\{1,3,5\}} \sum_{j\epsilon\{2,4,6\}} e^{-i\mathbf{k}\cdot\left(\mathbf{c}_i^{\mathrm{C}6} - \mathbf{c}_j^{\mathrm{C}6}\right)}\, \mathrm{G}_{ij}(\mathbf{k},\omega)\,. \tag{5.19}$$

5.1.9. Ten-site Ring Cluster Tiling

For a ten-site ring cluster the superlattice is given above by the lattice Γ_{10}. The superlattice-wave vector transformed hopping matrix is given by

$$\mathrm{T}_{ij}^{(10)}(\mathbf{k}) = \begin{pmatrix} \Delta\epsilon & \Delta t & & & & & & & & \Delta t \\ \Delta t & \Delta\epsilon & \Delta t & & & & & & & \\ & \Delta t & \Delta\epsilon & \Delta t & & & \Delta t & & & \\ & & \Delta t & \Delta\epsilon & \Delta t & & & & & \\ & & & \Delta t & \Delta\epsilon & \Delta t & & & & \\ & & & & \Delta t & \Delta\epsilon & \Delta t & & & \\ & & & & & \Delta t & \Delta\epsilon & \Delta t & & \\ & & \Delta t & & & & \Delta t & \Delta\epsilon & \Delta t & \\ & & & & & & \Delta t & \Delta\epsilon & \Delta t & \\ \Delta t & & & & & & & \Delta t & \Delta\epsilon & \end{pmatrix} +$$

$$+ -t \begin{pmatrix} & & & & & & & & e^{-i\mathbf{k}\cdot\left(\mathbf{R}_1^{\Gamma 10} + \mathbf{R}_2^{\Gamma 10}\right)} & \\ & & & & & & & e^{-i\mathbf{k}\cdot\mathbf{R}_1^{\Gamma 10}} & & \\ & & & & & & e^{-i\mathbf{k}\cdot\mathbf{R}_1^{\Gamma 10}} & & & \\ & & & & & & & & & e^{i\mathbf{k}\cdot\mathbf{R}_2^{\Gamma 10}} \\ e^{+i\mathbf{k}\cdot\left(\mathbf{R}_1^{\Gamma 10} + \mathbf{R}_2^{\Gamma 10}\right)} & & & & & & & & & \\ & & & & & e^{+i\mathbf{k}\cdot\mathbf{R}_1^{\Gamma 10}} & & & & \\ & & & & e^{+i\mathbf{k}\cdot\mathbf{R}_1^{\Gamma 10}} & & & & & \\ & & & & & & & & e^{-i\mathbf{k}\cdot\mathbf{R}_2^{\Gamma 10}} & \end{pmatrix}. \tag{5.20}$$

For ten site clusters the general periodization prescription for Green's functions eq. (5.17) may be generalized to

$$\mathrm{G}_{\alpha\beta}(\mathbf{k},\omega) = \frac{1}{N_C} \sum_{i\epsilon\{1,3,5,7,9\}} \sum_{j\epsilon\{2,4,6,8,10\}} e^{-i\mathbf{k}\cdot\left(\mathbf{c}_i^{\mathrm{C}10} - \mathbf{c}_j^{\mathrm{C}10}\right)}\, \mathrm{G}_{ij}(\mathbf{k},\omega)\,. \tag{5.21}$$

This concludes the basics about the Graphene lattice structure and its cluster decompositions. In the next section a model for randomly positioned magnetic vacancies is introduced.

5.2. Disorder Model for correlated sites

In this section a model for randomly positioned magnetic vacancies in Graphene, within CPT/VCA, is introduced. Disordered systems have previously been described by the SFA [56] and also by VCA [57]. The approach to disorder in this work is based on both these studies and is a direct extension of ref. [57]. Irradiation induced vacancies in Graphene are reported to exhibit local magnetic moment behavior [18]. In the VCA framework, Graphene is modeled by a tight binding Hamiltonian on a honeycomb lattice, described by the one-band Hubbard model parameters ($U = 0$, $\epsilon = 0$, $t = 1$). The magnetic impurities may either be added upon introducing a spin-spin term like in a Kondo Hamiltonian [191] or in a better approximation by related impurity terms like in the SIAM. Here we choose to model the magnetic vacancies as interstitial impurities v, having high interaction strength U_v, an on-site energy which makes the system particle-hole symmetric: $\epsilon_v = -\frac{U_v}{2}$ and a hybridization to the surrounding carbon atoms of

$t_v << t$. Those vacancies are randomly distributed on the Graphene lattice:

$$\hat{\mathcal{H}} = -t \sum_{\langle i,j\rangle\,\sigma}^{L-N^v} c^\dagger_{i\sigma}\, c_{j\sigma} - \frac{U}{2} \sum_{\alpha\sigma}^{N^v} v^\dagger_{\alpha\sigma}\, v_{\alpha\sigma} + U_v \sum_{\alpha}^{N^v} \hat{n}^v_{\alpha\uparrow}\, \hat{n}^v_{\alpha\downarrow} - t_v \sum_{\langle\alpha,i\rangle\,\sigma} \left(c^\dagger_{i\sigma}\, v_{\alpha\sigma} + v^\dagger_{\alpha\sigma}\, c_{i\sigma} \right) .$$

Here the $c^\dagger_{i\sigma}/c_{i\sigma}$ creates/annihilates an electron with spin σ at site i. The operators $v^\dagger_{\alpha\sigma}/v_{\alpha\sigma}$ create/annihilate electrons at the correlated vacancy sites α. This setup corresponds to local moment behavior in the vacancies (impurities) above T_K and Kondo screening below, in accordance with experiment [18]. Since Graphene is a two-dimensional material it is to be expected, that randomly induced vacancies (with local moment behavior) have a similar effect as magnetic adsorbates on Graphene making this approach suitable for the treatment of adsorbates as well. We proceed by discussing how this infinite disordered lattice may be treated within CPT/VCA.
The vacancies are produced by irradiation in a random fashion. This randomness has to be included in the resulting Green's function G. Approaching the problem using CPT/VCA, the solution is based on finite size clusters of length L. The idea is to calculate the cluster Green's function G′ for different classes of vacancy configurations. There will be

$$N_{\mathcal{C}} = L + 1$$

classes C_α corresponding to $\alpha = 0$ up to $\alpha = L$ vacancies inside the cluster. These classes make up the set

$$\mathcal{C} = \{C_\alpha\},\ \alpha \in [0, L] .$$

Each of these classes has a multiplicity of

$$m_\alpha = \binom{L}{\alpha},$$

corresponding to the different possibilities to spread the α vacancies inside the cluster.
For example the vacancy class C_0 denotes clusters with no vacancies present (multiplicity $m_\alpha = 1$), another one may be to have one vacancy in the cluster C_1 (multiplicity $m_\alpha = L$).
Note that this classification of clusters into groups having the same number of impurities, does not mean that clusters within one group have the same properties. Consider as an example a larger cluster with two vacancies. Then the correlations will be strongly dependent on the distance between the two vacancy sites. However this classification makes sense because the probability of finding a cluster will in a first approximation depend only on the number of vacancies in it.
To emulate a disordered lattice with a given concentration of vacancies the classes C_α have to be mixed in an appropriate fashion. It is to be expected, that more vacancies inside the same cluster are less likely. How this is done in practice will be outlined in sec. 5.2.1.
There are two ideas for averaging the solution for the Green's function over the vacancy realizations:

1. Averaging of the cluster Green's function. The ideas presented in ref. [192] have to be extended in two points. Here we consider a weighed average of the cluster Green's function corresponding to different vacancy classes. The second more crucial point has to do with the modeling of the vacancies and the lattice geometry. Since the hopping on the lattice t is uniform, except for hopping into the vacancy $t_v << t$, one has to deal with a different inter-cluster hopping matrix for each disorder configuration! This may only be treated on this level by averaging not only G' but also T. Details of this approach will be described in detail in sec. 5.2.2.

2. Averaging of the total Green's function after CPT/VCA coupling. This is ad-hoc and it will be shown below that this approach does not yield an acceptable result. This approach will be outlined in sec. 5.2.3.

The probability to find a certain amount of vacancies inside one cluster will be discussed in the next paragraph.

5.2.1. Weighing disorder configurations

Each cluster configuration η belongs to a vacancy class C_α. Depending on the multiplicity m_α the normalized reweighing factors are defined as

$$p_\alpha = \frac{w_\alpha}{m_\alpha \sum_{\alpha=1}^{N_\mathcal{C}} w_\alpha} .$$

Any average may then be calculated by multiplying each component by the appropriate p_α and summing over all of them An averaged quantity $\overline{A}$ is calculated as

$$\overline{A} = \frac{1}{\sum_{\alpha=1}^{N_\mathcal{C}} w_\alpha} \sum_{C_\alpha \in \mathcal{C}}^{N_\mathcal{C}} \frac{w_\alpha}{m_\alpha} \sum_{\eta \in C_\alpha}^{m_\alpha} A_\eta . \tag{5.22}$$

The concentration of vacancies is given by the ratio of the number of vacancies N^v and the number of total sites available L

$$P_v = \frac{N^v}{L} = \frac{\sum_{\alpha=1}^{N_\mathcal{C}} \alpha\, w_\alpha}{L \sum_{\alpha=1}^{N_\mathcal{C}} w_\alpha} .$$

Specifying a desired vacancy concentration P_v a probability distribution function for the weights w_α has to be found fulfilling additional constraints:

- All weights have to be positive:

$$w_\alpha > 0 \quad \forall\ \alpha .$$

- For zero vacancy concentration only configurations involving no vacancies may contribute:

$$w_\alpha = 0 \quad \forall\ \alpha > 0 \ \wedge\ w_0 > 0 \text{ if } P_v = 0 .$$

- For a vacancy concentration of one only configurations $\in C_L$ may contribute:

$$w_\alpha = 0 \quad \forall\ \alpha < L \ \wedge\ w_L > 0 \text{ if } P_v = 1 .$$

It is to be expected that for a given vacancy concentration P_v the weight of a cluster of size L having α vacancies present is given by the binomial distribution [193]

$$w_\alpha(L, P_v) = P_v^\alpha (1 - P_v)^{(L-\alpha)} \binom{L}{\alpha} , \tag{5.23}$$

which fulfills the above constraints. The distribution of cluster weights is shown in fig. 5.5 for various values of the desired vacancy concentration and cluster sizes. This in principle would still leave some freedom in weighing different configurations having the same number of vacancies, which is not investigated here. Note that this is an approximation because the scattering off nearest-neighbor vacancies is certainly different from the scattering of two separated vacancies. Next, two examples for weighing clusters will be presented to illustrate the above notation.

Example I: weighing for two-site clusters

Consider a system of two-site clusters $L = 2$. There may exist $\alpha = 0, 1$ or 2 vacancies inside a single cluster. This gives $N_\mathcal{C} = L + 1 = 3$ vacancy classes. The multiplicity of the classes is given by $m_\alpha = [1, 2, 1]$ because there exist two ways to arrange one vacancy in a two-site cluster. The overall number of different cluster configurations is 4 (not taking symmetry into account). One may choose three weights w_α according to

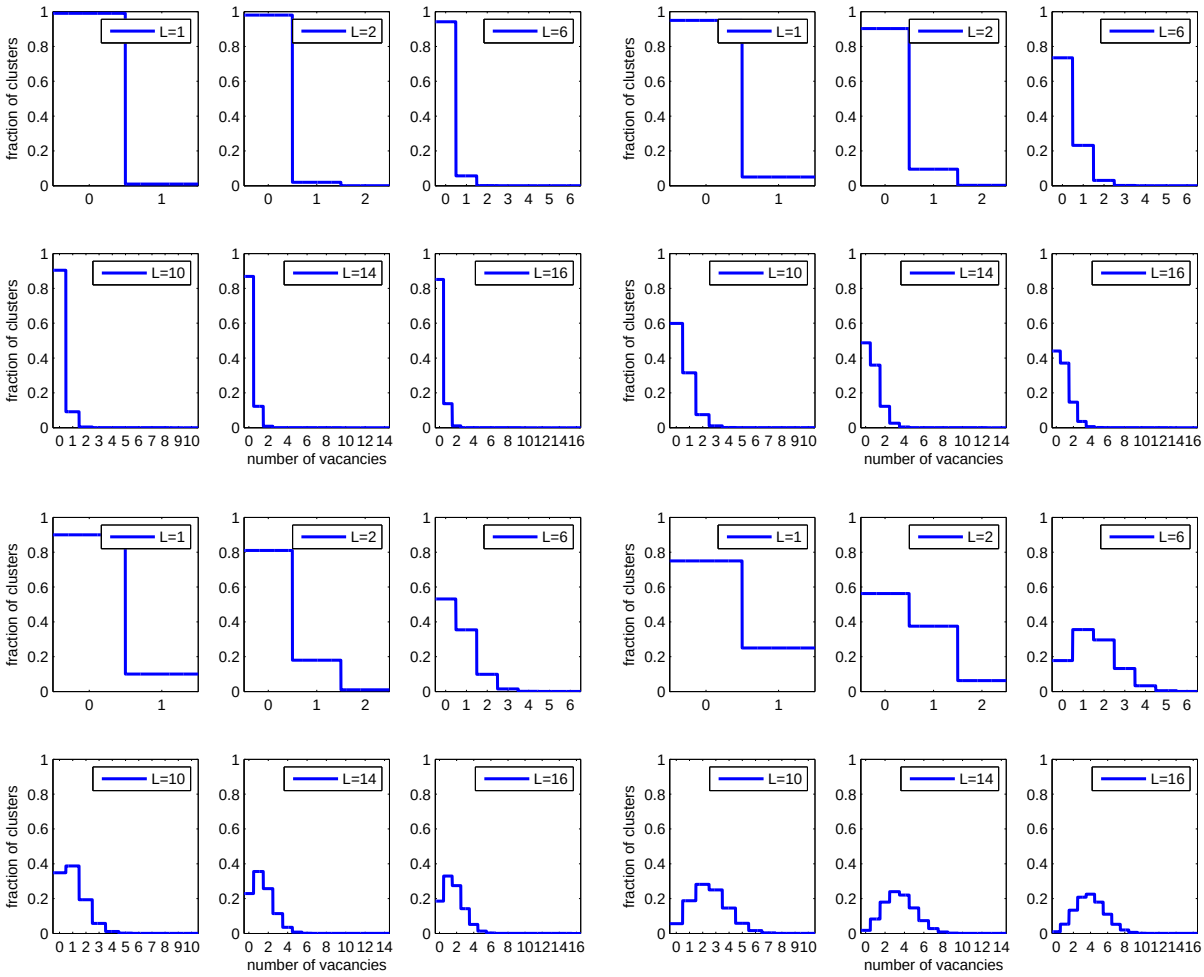

Figure 5.5.: Distribution of cluster weights according to the binomial distribution eq. (5.23) for cluster sizes $L = 1, 2, 6, 10, 14$ and 16 and vacancy concentrations of $P_v = 1\%$ (six pictures in top left corner), $P_v = 5\%$ (six pictures in top right corner), $P_v = 10\%$ (six pictures in bottom left corner), $P_v = 25\%$ (six pictures in bottom right corner). Note that for higher values of P_v the distribution does not decrease monotonically with the number of vacancies per cluster.

eq. (5.23) to obtain the desired impurity concentration P_v

$$P_v = \frac{(w_1 + 2\,w_2)}{2\,(w_0 + w_1 + w_2)}\,.$$

An average quantity is explicitly calculated

$$\begin{aligned}\overline{A} &= \frac{1}{\sum\limits_{\alpha=1}^{N_\mathcal{C}} w_\alpha} \sum_{C_\alpha \in \mathcal{C}}^{N_\mathcal{C}} \frac{w_\alpha}{m_\alpha} \sum_{\eta \in C_\alpha}^{m_\alpha} A_\eta \\ &= \frac{1}{w_0 + w_1 + w_2}\left(\frac{w_0}{1} A_0 + \frac{w_1}{2}\left(A_1^1 + A_1^2\right) + \frac{w_2}{1} A_2\right)\,.\end{aligned}$$

Example II: weighing for six-site clusters

Consider a system of six-site clusters $L = 6$. There may exist $\alpha = 0, 1, 2, 3, 4, 5$ or 6 vacancies inside a single cluster. This gives $N_\mathcal{C} = L + 1 = 7$ vacancy classes. The multiplicity of the classes is given by $m_\alpha = [1, 6, 15, 20, 15, 6, 1]$ corresponding to the number of possibilities to arrange the vacancies inside a six-site cluster. The overall number of different cluster configurations is 64 (not taking symmetry into account). One may choose six weights w_α according to eq. (5.23) to obtain the desired impurity concentration P_v

$$P_v = \frac{(w_1 + 2\,w_2 + 3\,w_3 + 4\,w_4 + 5\,w_5 + 6\,w_6)}{6\,(w_0 + w_1 + w_2 + w_3 + w_4 + w_5 + w_6)}\,.$$

We will now proceed by introducing the averaging of Green's functions for different vacancy configurations within CPT/VCA.

5.2.2. Approach to disorder (I): Averaging on cluster level

Here I will present details for what will be referred to as disorder approach I: averaging on the cluster level. This is the conceptually correct way for averaging as outlined in ref. [56, 57]. The cluster Green's function of a single vacancy configuration is given by

$$\mathrm{G}'_\eta = \mathrm{Q}_\eta\,\mathrm{g}'_\eta\,\mathrm{Q}^\dagger_\eta,\ \eta \in C_\alpha\,. \tag{5.24}$$

The averaged cluster Green's function will then be given by eq. (5.22)

$$\begin{aligned}\overline{\mathrm{G}'} &= \frac{1}{\sum\limits_{\alpha=1}^{N_\mathcal{C}} w_\alpha} \sum_{C_\alpha \in \mathcal{C}}^{N_\mathcal{C}} \frac{w_\alpha}{m_\alpha} \sum_{\eta \in C_\alpha}^{m_\alpha} \mathrm{Q}_\eta\,\mathrm{g}'_\eta\,\mathrm{Q}^\dagger_\eta \\ &= \sum_{C_\alpha \in \mathcal{C}}^{N_\mathcal{C}} \sum_{\eta \in C_\alpha}^{m_\alpha} \left(\sqrt{\frac{w_\alpha}{m_\alpha \sum\limits_{\alpha=1}^{N_\mathcal{C}} w_\alpha}}\,\mathrm{Q}_\eta\right) \mathrm{g}'_\eta \left(\sqrt{\frac{w_\alpha}{m_\alpha \sum\limits_{\alpha=1}^{N_\mathcal{C}} w_\alpha}}\,\mathrm{Q}^\dagger_\eta\right) \\ &= \sum_{C_\alpha \in \mathcal{C}}^{N_\mathcal{C}} \sum_{\eta \in C_\alpha}^{m_\alpha} \tilde{\mathrm{Q}}_\eta\,\mathrm{g}'_\eta\,\tilde{\mathrm{Q}}^\dagger_\eta\,,\end{aligned}$$

where one can read off the definitions of the tilded quantities. This may be rewritten in matrix notation defining

$$\begin{aligned}\tilde{\mathrm{Q}} &= \left(\tilde{\mathrm{Q}}_{\eta=1}, \tilde{\mathrm{Q}}_2, \ldots\right) \\ \tilde{\mathrm{Q}}^\dagger &= \left(\tilde{\mathrm{Q}}^\dagger_1; \tilde{\mathrm{Q}}^\dagger_2; \ldots\right) \\ \tilde{\mathrm{g}'} &= \mathrm{diag}\left(\mathrm{g}'_1, \mathrm{g}'_2, \ldots\right)\,,\end{aligned}$$

in the usual form

$$\overline{\mathrm{G}'} = \tilde{\mathrm{Q}}\,\tilde{\mathrm{g}'}\,\tilde{\mathrm{Q}^\dagger}\,.$$

The CPT/VCA Green's function is then given by

$$\begin{aligned} \mathrm{G} &= \tilde{\mathrm{Q}} \frac{1}{\omega - \left(\tilde{\Lambda} - \tilde{\mathrm{Q}}^\dagger \, \mathrm{T} \, \tilde{\mathrm{Q}}\right)} \tilde{\mathrm{Q}}^\dagger \\ &= \left(\mathbb{1} - \overline{\mathrm{G}'} \, \mathrm{T}\right)^{-1} \overline{\mathrm{G}'} \, , \end{aligned}$$

where

$$\tilde{\Lambda} = \mathrm{diag}\left(\tilde{\Lambda}_1, \tilde{\Lambda}_2, ...\right) \, .$$

Note that here Q may also stand for $\mathrm{Q}_{\mathrm{per}}$ as defined in ch. 2.1.4. An issue with the problem at hand is that T, even in CPT, is different for every vacancy configuration η (not class α). This arises due to the different hoppings into the vacancies t_v, which sit on different sites in each configuration. One way to deal with this would be to average T in the same way as the cluster Green's function is averaged:

$$\overline{\mathrm{T}} = \frac{1}{\sum\limits_{\alpha=1}^{N_\mathcal{C}} w_\alpha} \sum_{C_\alpha \in \mathcal{C}}^{N_\mathcal{C}} \frac{w_\alpha}{m_\alpha} \sum_{\eta \in C_\alpha}^{m_\alpha} \mathrm{T}_\eta \, .$$

The full averaged Green's function within this approximation is given by

$$\overline{\mathrm{G}}_I = \left(\mathbb{1} - \overline{\mathrm{G}'} \, \overline{\mathrm{T}}\right)^{-1} \overline{\mathrm{G}'} \, .$$

Please note again that in this approach all quantities are averaged on cluster level. These averaged quantities $\overline{\mathrm{G}'}$ and $\overline{\mathrm{T}}$ go into one CPT equation eq. (2.2) to yield the total Green's function G.
Next averaging at another level of the calculation is described.

5.2.3. Approach to disorder (II): Averaging of the full Green's function

This approach is not controlled and just for reasons of comparison. Averaging on cluster level, leaves the problem of separately averaging the matrix T. It is interesting to see what happens if each vacancy configuration η is treated with the corresponding T_η at the level of the "CPT-Dyson" equation. However then the averaging has to be done at the level of the CPT/VCA-Green's function G. The cluster Green's function of a single vacancy configuration G'_η is again given by eq. (5.24). A configuration specific matrix T_η is used to calculate a CPT/VCA-Green's function G_η for each configuration

$$\mathrm{G}_\eta^{-1} = \mathrm{G}_\eta'^{-1} - \mathrm{T}_\eta \, .$$

The averaged CPT/VCA-Green's $\overline{\mathrm{G}}$ is then simply given by

$$\begin{aligned} \overline{\mathrm{G}}_{II} &= \frac{1}{\sum\limits_{\alpha=1}^{N_\mathcal{C}} w_\alpha} \sum_{C_\alpha \in \mathcal{C}}^{N_\mathcal{C}} \frac{w_\alpha}{m_\alpha} \sum_{\eta \in C_\alpha}^{m_\alpha} \tilde{\mathrm{Q}}_\eta \frac{1}{\omega - \left(\tilde{\Lambda}_\eta - \tilde{\mathrm{Q}}_\eta \, \mathrm{T}_\eta \, \tilde{\mathrm{Q}}_\eta\right)} \tilde{\mathrm{Q}}_\eta^\dagger \\ &= \frac{1}{\sum\limits_{\alpha=1}^{N_\mathcal{C}} w_\alpha} \sum_{C_\alpha \in \mathcal{C}}^{N_\mathcal{C}} \frac{w_\alpha}{m_\alpha} \sum_{\eta \in C_\alpha}^{m_\alpha} \mathrm{G}_\eta \, . \end{aligned} \tag{5.25}$$

So here the CPT equation is applied to each configuration η and the total Green's functions G_η are then averaged over. The biggest issue, besides it's general uncontrolledness, with this approach is straight forward to see. At least some of the calculated Green's functions G_η will be of the class $\eta \in C_0$. This means that no vacancies are present within the cluster and the spectrum may in general be gapless (while spectra for $\eta \in C_\alpha \; \alpha > 0$ are expected to be gapped). It can now be seen from eq. (5.25) that no matter how many vacancy configurations will be mixed with this $\mathrm{G}_{\eta=0}$ the spectrum will stay gapless. I consider this unphysical. Therefore in the following we will pursue disorder approach (I).
In the next section, results for the homogeneous Hubbard model on a honeycomb lattice are presented and compared to other methods.

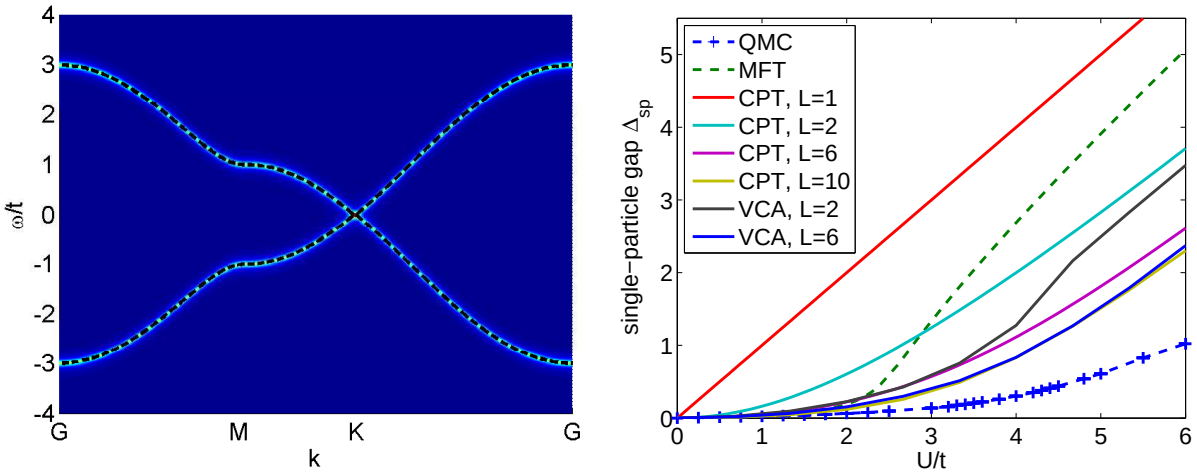

Figure 5.6.: (Left) Density of states of Graphene plotted along a common path in the Brillouin-zone: $\Gamma - M - K - \Gamma$. The result for $U = 0$ (tight binding model) is shown which was calculated for all cluster sizes within CPT and VCA as a check. The black line shows the analytical result for the nearest-neighbor tight-binding dispersion relation of Graphene eq. (5.26). (Right) The gap as a function of interaction strength U obtained by CPT using $1, 2, 6,$ and 10 site clusters as well as with VCA_Ω using 2 and 6 site clusters. The variational parameter used is the hopping t since the model is particle-hole symmetric. As a reference the mean field and QMC results by Feldner *et al.* [187] are plotted.

5.3. Calculations for homogeneous Graphene

In this section the CPT/VCA method shall be tested on the two-dimensional honeycomb lattice. Therefore results for the tight-binding model and the Hubbard model will be presented. First the density of states is discussed. Then the band gap as a function of interaction-strength U will be compared to other methods.

5.3.1. Density of states

In this section results obtained by CPT/VCA are discussed for $L = 1, 2, 6$ and 10 -site clusters. Results for the density of states in the non-interacting case (tight-binding model) reproduce the analytic solution [175]

$$\epsilon(\mathbf{k}) = \epsilon - t * \sqrt{1 + 4\cos(\sqrt{3}k_x\frac{a}{2})\cos(k_y\frac{a}{2}) + \cos(k_y\frac{a}{2})^2}\,, \tag{5.26}$$

as expected for all cluster sizes (see fig. 5.6 (left)). Data for a (homogeneous) Hubbard model is shown in fig. 5.7 for $U = 1$ and $\epsilon = -0.5$, in fig. 5.8 for $U = 2$ and $\epsilon = -1$, in fig. 5.9 for $U = 3$ and $\epsilon = -1.5$ and in fig. 5.10 for $U = 4$ and $\epsilon = -2$. The data was obtained by CPT as well as by VCA_Ω with one variational parameter $\mathsf{x} = \{t\}$. The model is particle-hole symmetric, so a variation of on-site energies would always yield a zero deviation from the physical parameter. An expected band gap opens for all studied cluster sizes. The result for two-site clusters exhibits a much wider band gap as the six-site result. Also the narrowing of the bands, observed for six-site clusters is absent in the two-site result. The six and ten site results look qualitatively similar, while the two site results deviate. It is interesting to note that VCA always tends to predict a smaller gap than CPT. The gap at the K point also becomes less wide for larger cluster sizes. This indicates an overestimation of the gap in CPT/VCA, which is gradually cured by considering larger clusters.

Next the band gap as a function of interaction-strength U as obtained by CPT/VCA will be compared to other methods.

5.3.2. CPT/VCA band gap

The single particle gap is obtained by adding the lowest (in magnitude) positive excitation energy of the total system $\lambda^U_{\mathbf{k}}$ at $\mathbf{k} = K$ and the lowest in magnitude negative excitation energy of the total system $\lambda^L_{\mathbf{k}}$ ($\lambda_{\mathbf{k}}$ is defined in sec. 2.1.4). The gap as a function of interaction strength U, obtained by CPT using

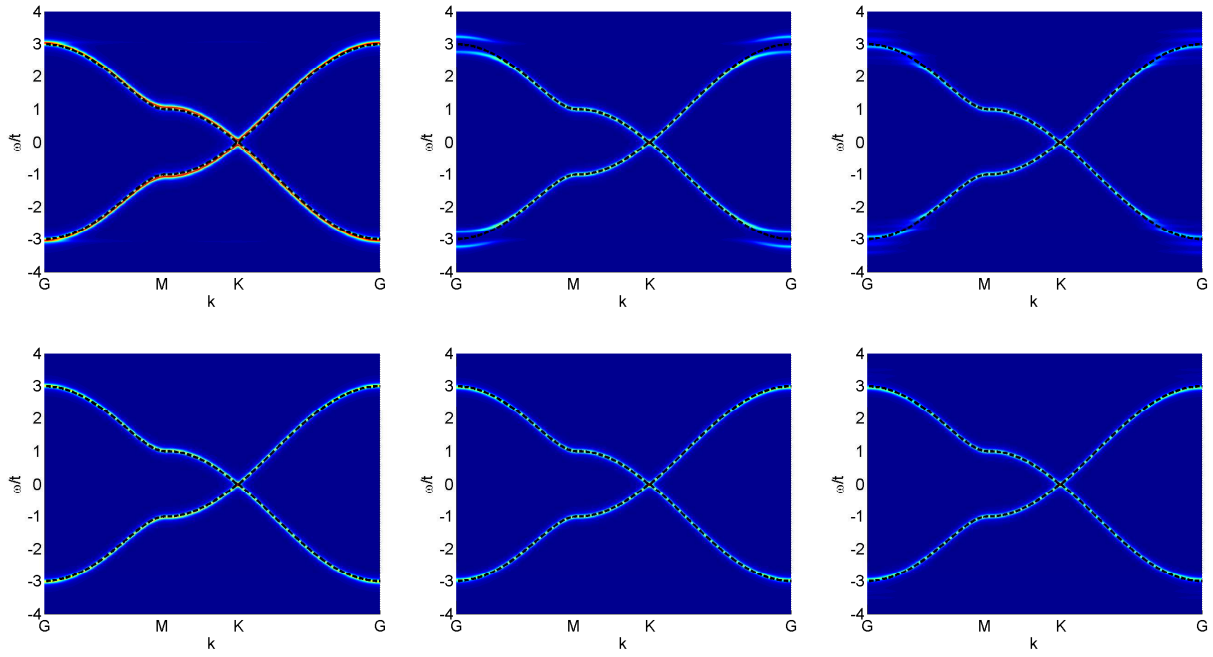

Figure 5.7.: Density of states of Graphene plotted along a common path in the Brillouin-zone: $\Gamma - M - K - \Gamma$. The result for $U = 1$ (Hubbard model) is shown from left to right for $L = 2, 6$ and 10 site clusters. The black line indicates the analytical result for the nearest-neighbor tight-binding dispersion relation of Graphene eq. (5.26). (Top row) Results obtained by CPT. (Bottom row) Data obtained by VCA with variational parameter $\mathsf{x} = \{t\}$.

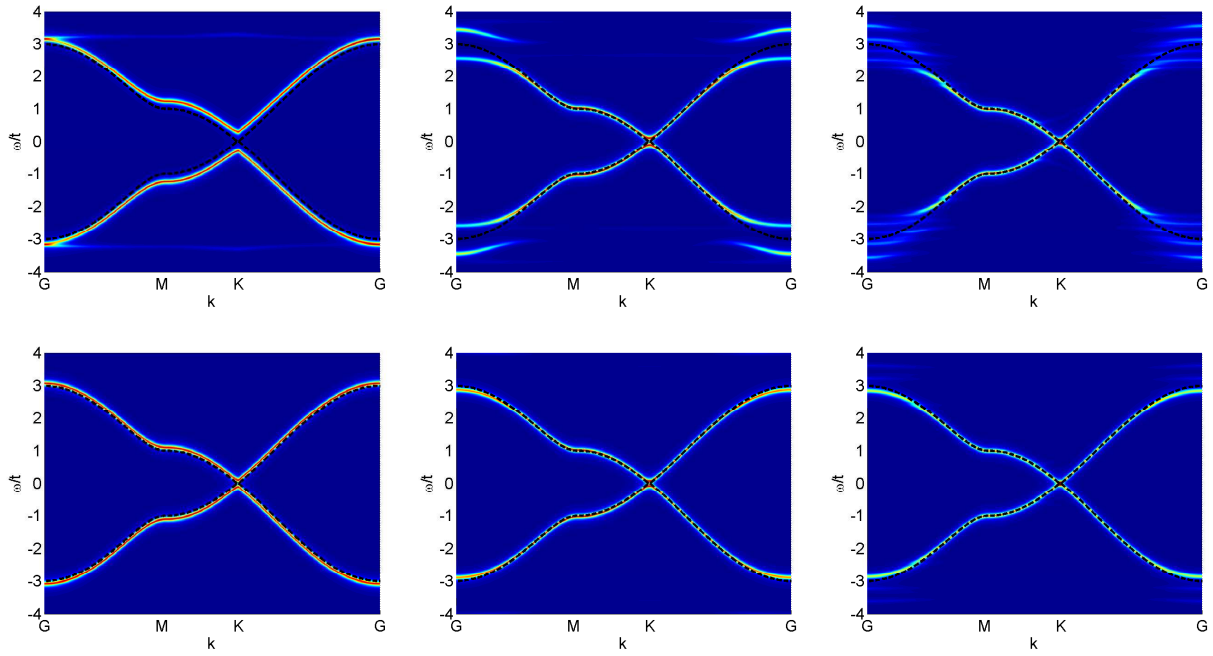

Figure 5.8.: Density of states of Graphene plotted along a common path in the Brillouin-zone: $\Gamma - M - K - \Gamma$. The result for $U = 2$ (Hubbard model) is shown from left to right for $L = 2, 6$ and 10 site clusters. The black line indicates the analytical result for the nearest-neighbor tight-binding dispersion relation of Graphene eq. (5.26). (Top row) Results obtained by CPT. (Bottom row) Data obtained by VCA with variational parameter $\mathsf{x} = \{t\}$.

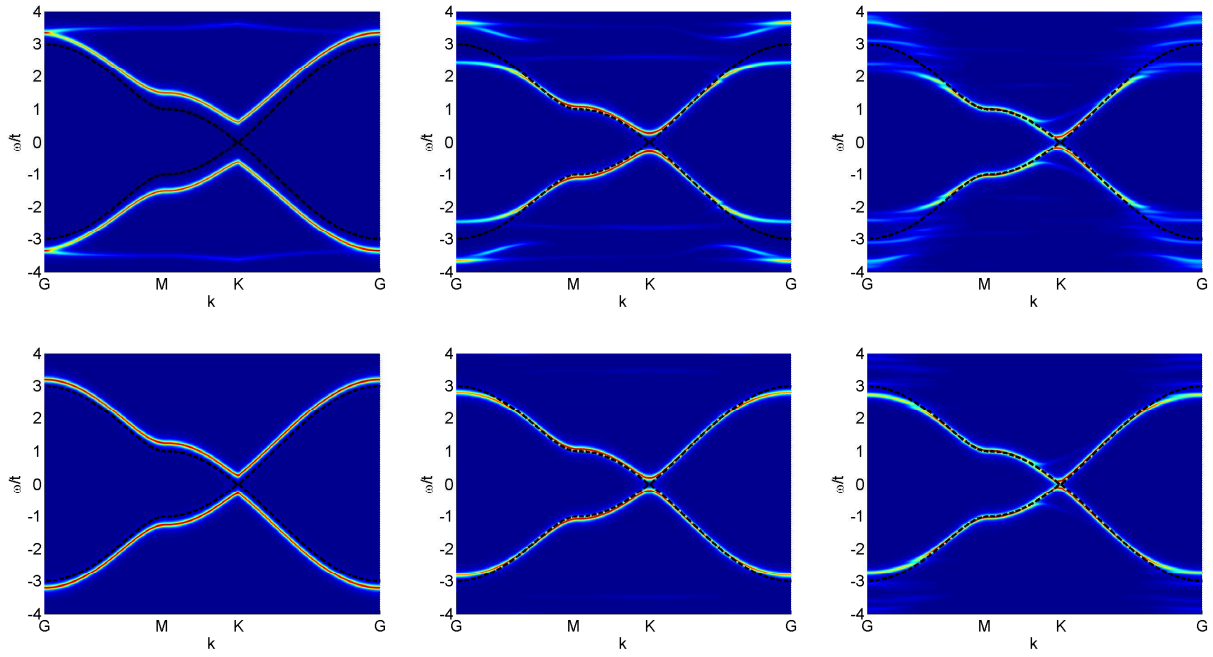

Figure 5.9.: Density of states of Graphene plotted along a common path in the Brillouin-zone: $\Gamma - M - K - \Gamma$. The result for $U = 3$ (Hubbard model) is shown from left to right for $L = 2, 6$ and 10 site clusters. The black line indicates the analytical result for the nearest-neighbor tight-binding dispersion relation of Graphene eq. (5.26). (Top row) Results obtained by CPT. (Bottom row) Data obtained by VCA with variational parameter $\mathsf{x} = \{t\}$.

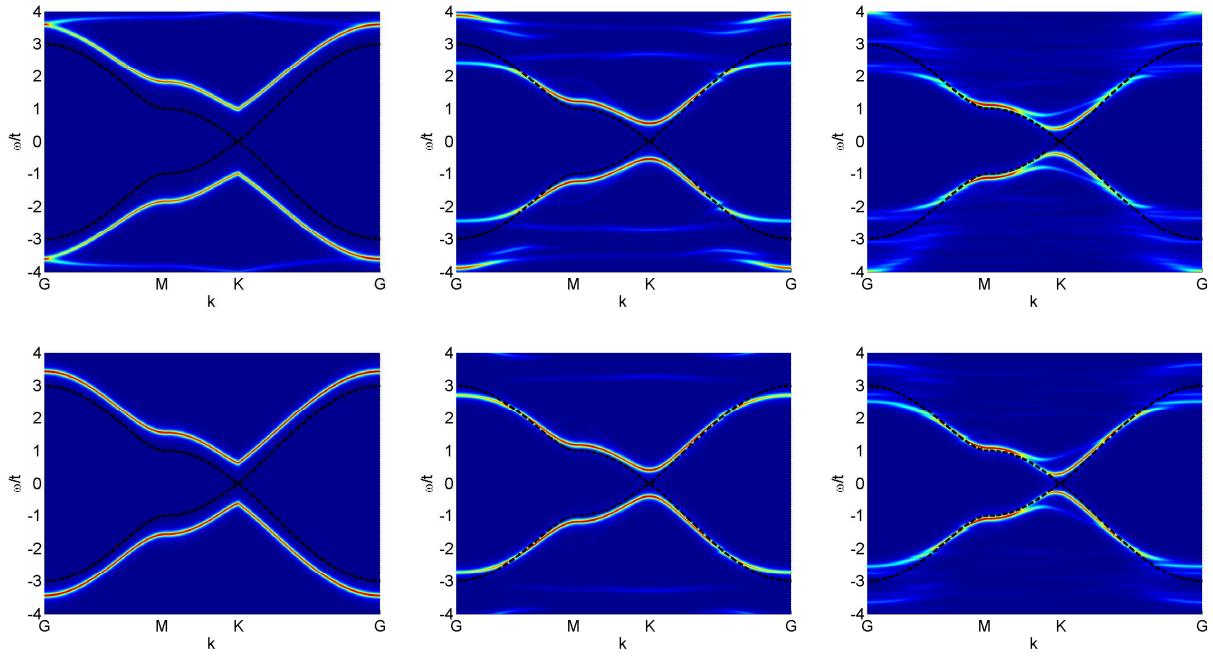

Figure 5.10.: Density of states of Graphene plotted along a common path in the Brillouin-zone: $\Gamma - M - K - \Gamma$. The result for $U = 4$ (Hubbard model) is shown from left to right for $L = 2, 6$ and 10 site clusters. The black line indicates the analytical result for the nearest-neighbor tight-binding dispersion relation of Graphene eq. (5.26). (Top row) Results obtained by CPT. (Bottom row) Data obtained by VCA with variational parameter $\mathsf{x} = \{t\}$.

$1, 2, 6,$ and 10 site clusters as well as with VCA_Ω using 2 and 6 site clusters, is shown in fig. 5.6 (right). The variational parameter used is the hopping t since the model is particle-hole symmetric. The results show convergence to the QMC data. The mean field and QMC data was obtained by Feldner *et al.* in ref. [187]. It is interesting to observe that the VCA result for a certain cluster size almost reaches the quality of the CPT result for the next higher cluster size. After testing CPT/VCA on the homogeneous Hubbard model we proceed by investigating Graphene with random magnetic vacancies.

5.4. Results for Graphene with randomly positioned magnetic vacancies

Graphene with randomly positioned magnetic vacancies, in a given concentration, is studied within the two disorder approaches presented above. The magnetic vacancies are modeled by the system parameters: $t = 1, U_v/t = 2, \epsilon_v = -U_v/2, t_v/t = 0.3162$. Those numbers where chosen because it is to be expected, that a magnetic vacancy behaves like having a strong Coulomb repulsion with a low hopping parameter. Otherwise they are chosen arbitrarily, more realistic values are part of future work.
The data obtained by CPT for the averaged single particle spectral function, within disorder approach I (i.e. averaging on cluster level), is shown in fig. 5.11. Results are shown for vacancy concentrations of $P_v = 1\%, 5\%, 10\%$ and 25%. The mixing of the disorder configurations was done according to a Binomial distribution as outlined in sec. 5.2.1. The calculations were done for cluster sizes of $L = 1, 2, 6$ and 10. The un-natural choice of one-site clusters causes spurious spectra without a vacancy-induced band gap. One may observe two gaps opening in the spectrum away from $\omega = 0$ with increasing vacancy concentration. The case of one-site clusters will be excluded from further discussions here. All other system sizes behave in principle similar. A gap opens at the K point, at the Fermi energy $\epsilon_F = 0$, with increasing vacancy concentration. The gap opens already at low vacancy concentrations of about 1%. In the extreme limit of 25% vacancies the lattice starts to seperate into smaller pieces causing flat disconnected parts in the spectra, like in a dimerized lattice. This basically is a localization phenomenon. It is interesting to observe, that in the $L = 2$-site case the spectrum at the K point starts out almost linearly. The $L = 6$- and 10-site calculations agree on an almost quadratic spectrum at K. This is in accordance with the results for homogeneous Graphene (see sec. 5.3). Furthermore two symmetric, non-dispersing bands of low weight evolve in the vicinty of the Fermi energy, at a vacancy concentration of $\approx 10\%$ in the case of $L = 2-, 6$- and 10-site clusters. The larger the clusters, the more gaps away from the Fermi-energy open. This may be an issue of the Green's function periodization. One can also observe, that the larger the clusters get, the smaller the gap at the Fermi-energy will be predicted. This is in accordance with the result for a homogenous Hubbard model (see fig. 5.6 (right)). There it was shown, that smaller clusters always overestimate the size of the gap in comparison to QMC. The general form of the tight-binding dispersion relation on a honeycomb lattice eq. (5.26) is preserved in the $L = 1-$ and 2-site case. The results obtained by $L = 6-$ and 10-site clusters distort the original dispersion much more. It is interesting to observe that the one-site result and the six-site result agree reasonably well on the position of the induced openings in the band away from $\omega = 0$. Another interesting result however is, that all cluster sizes yield almost the same spectrum at the Γ point. A Kondo-resonance at $\omega = 0$ is not observed.
It may be interesting to compare the results obtained for magnetic vacancies with randomly positioned non-magnetic impurities. These are modeled by the system parameters: $t = 1, U_v/t = 0, \epsilon_v/t = -1, t_v/t = 0.3162$, to be able to compare to the case examined before. The spectra obtained for this setup for the same concentration of impurities and cluster sizes as before are plotted in fig. 5.12. The spectra look quite similar to those obtained before. Therefore we may conclude that the general features of the spectra arise due to the effects of disorder and not a finite interaction strength U at the impurity locations. There are however some details, like in the additionally introduced flat bands in the vicinity of the Fermi-energy. In this case only one of those develops, as opposed to two in the previous case of magnetic vacancies.
As expected results obtained by averaging the total Green's function (disorder approach II) do not yield a physical result (see fig. 5.13). Note that the general features of the spectra obtained for various cluster sizes agree very well qualitatively.

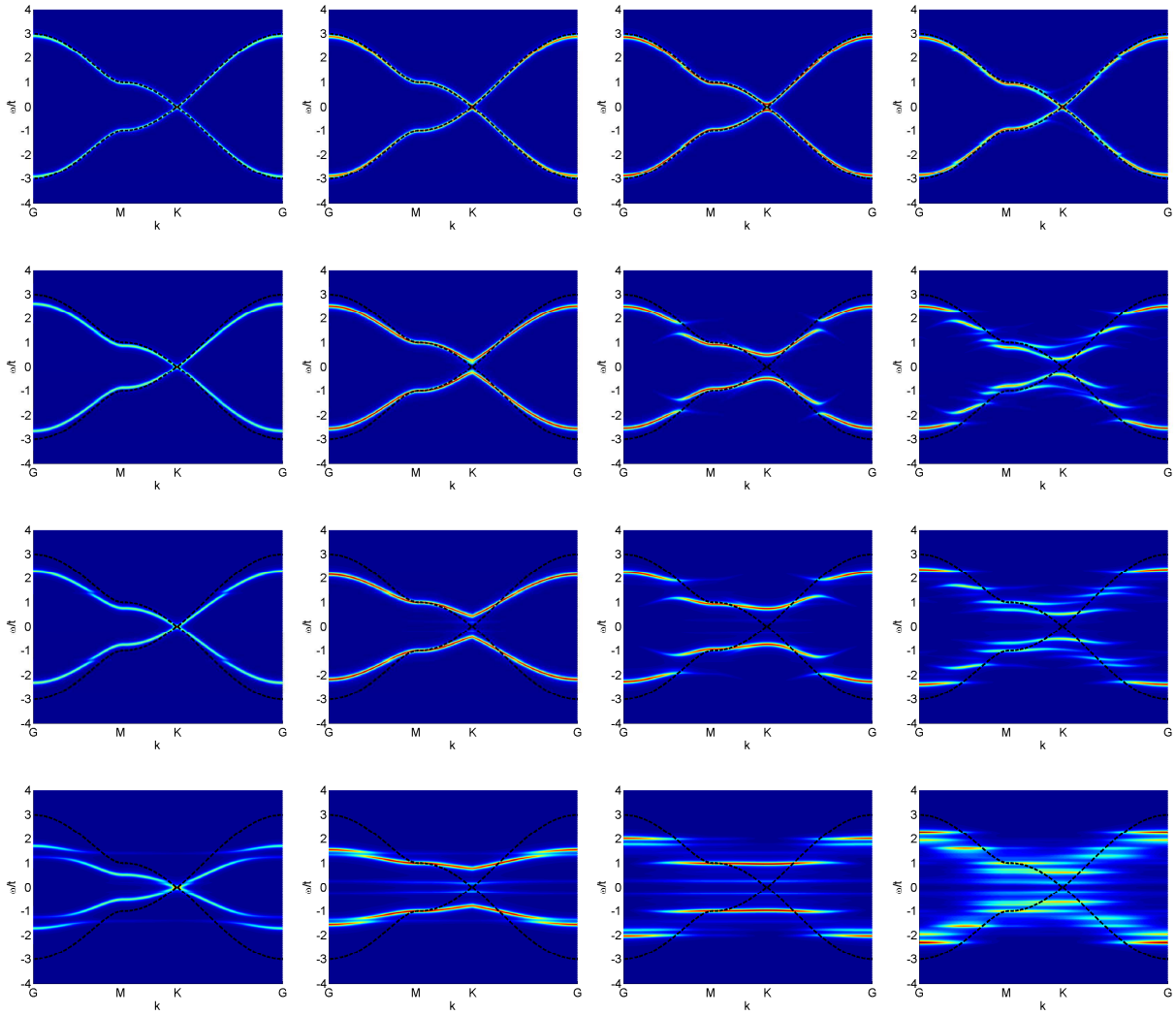

Figure 5.11.: Density of states of Graphene with randomly distributed magnetic vacancies plotted along a common path in the Brillouin-zone: $\Gamma - M - K - \Gamma$. The averaged single particle spectral function obtained by CPT for a vacancy concentration of P_v = 1% (top row), P_v = 5% (second row), P_v = 10% (third row), P_v = 25% (bottom row). Data is shown for cluster sizes of L = 1 (first column), L = 2 (second column), L = 6 (third column) and L = 10 (fourth column). The spectra were calculated by the disorder approach I where the Green's function and single particle hopping matrix is averaged on cluster level. The black line shows the analytical result for the nearest-neighbor tight-binding dispersion relation of Graphene eq. (5.26).

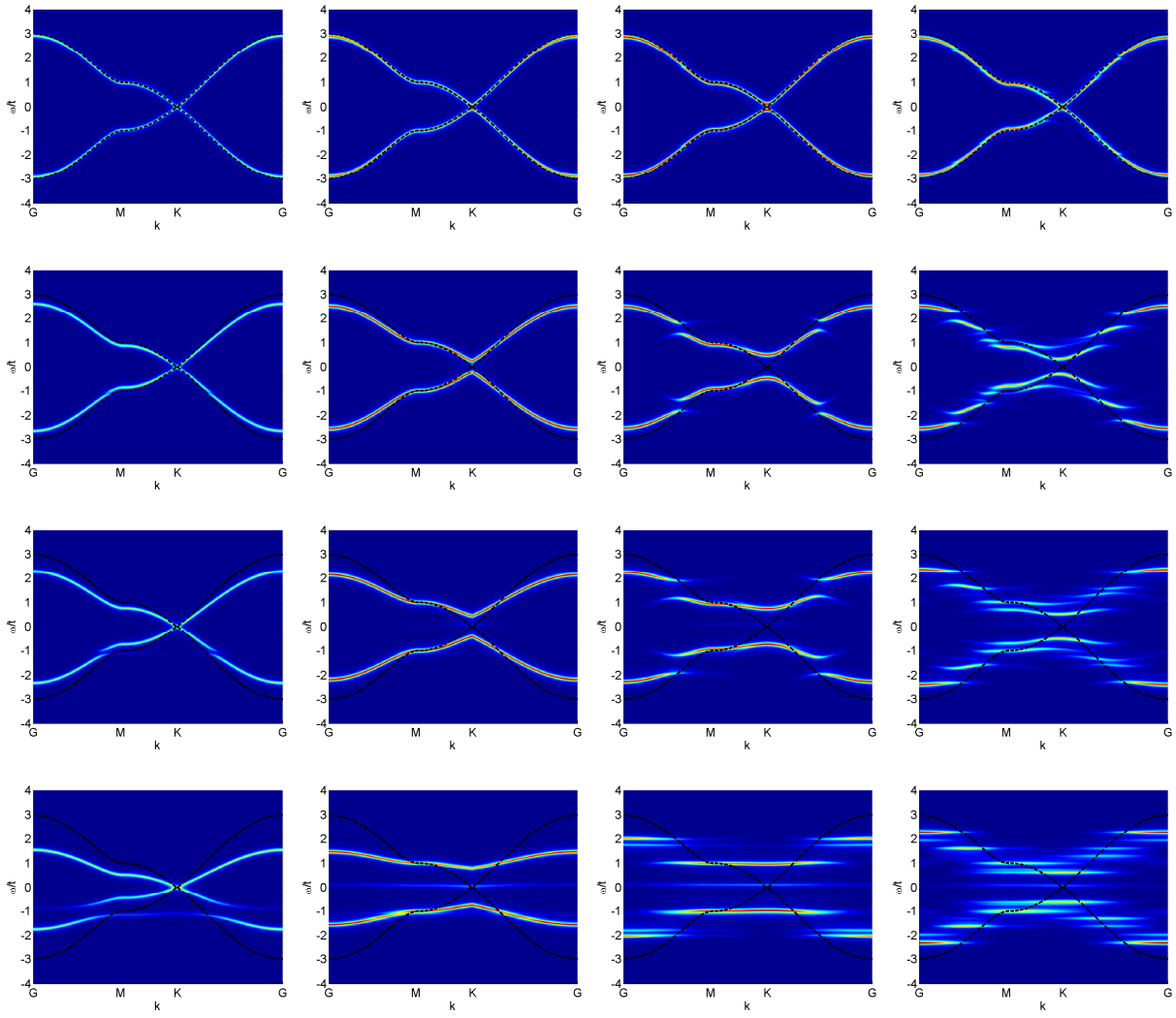

Figure 5.12.: Density of states of Graphene with randomly distributed non-magnetic defects plotted along a common path in the Brillouin-zone: $\Gamma - M - K - \Gamma$. The averaged single particle spectral function obtained by CPT for a vacancy concentration of P_v = 1% (top row), P_v = 5% (second row), P_v = 10% (third row), P_v = 25% (bottom row). Data is shown for cluster sizes of L = 1 (first column), L = 2 (second column), L = 6 (third column) and L = 10 (fourth column). The spectra were calculated by the disorder approach I where the Green's function and single particle hopping matrix is averaged on cluster level. The black line shows the analytical result for the nearest-neighbor tight-binding dispersion relation of Graphene eq. (5.26).

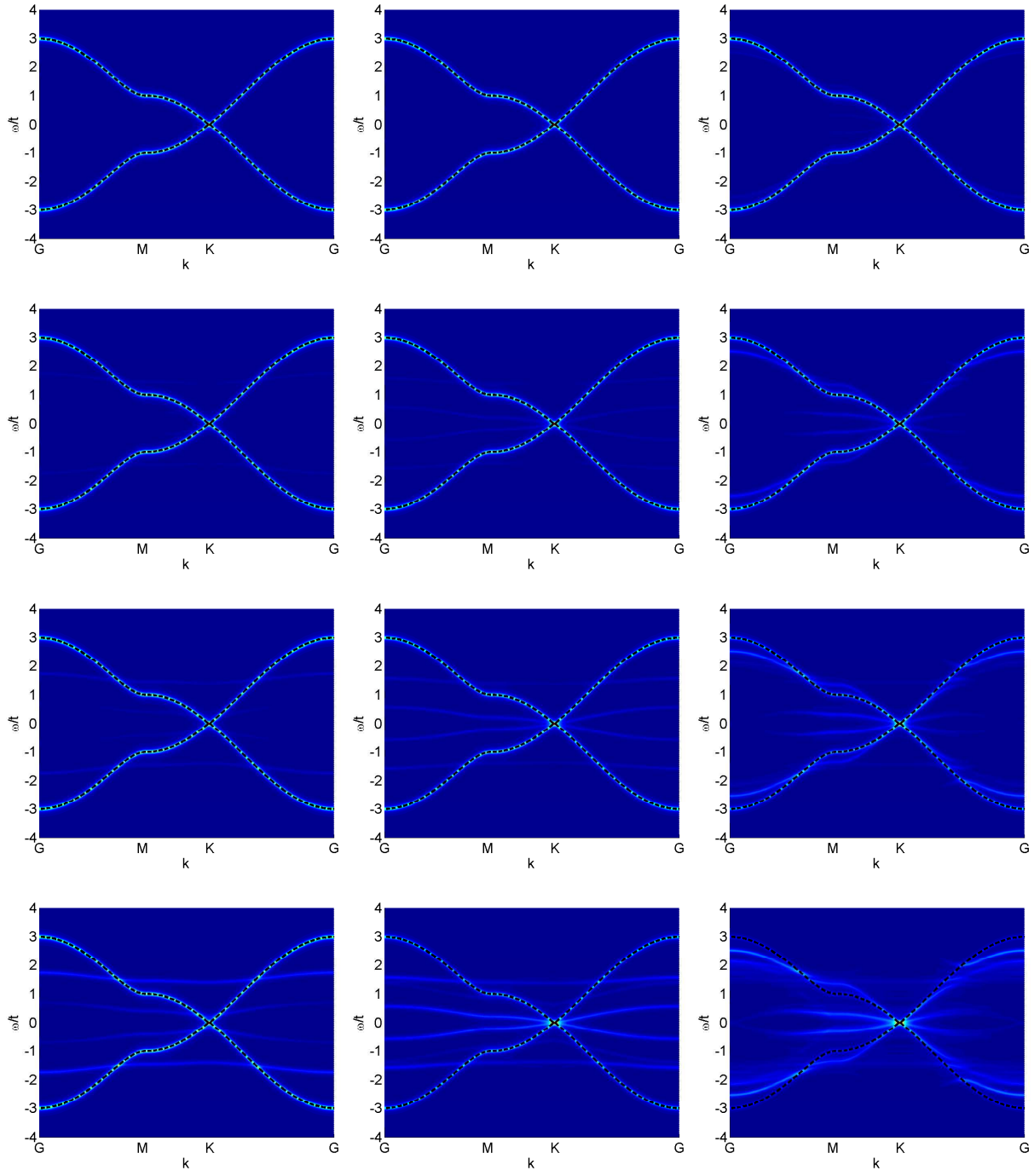

Figure 5.13.: Density of states of Graphene with random randomly distributed magnetic vacancies plotted along a common path in the Brillouin-zone: $\Gamma - M - K - \Gamma$. The averaged single particle spectral function obtained by CPT for a vacancy concentration of P_v = 1% (top row), P_v = 5% (second row), P_v = 10% (third row), P_v = 25% (bottom row). Data is shown for cluster sizes of L = 1 (first column), L = 2 (second column), L = 6 (third column) and L = 10 (fourth column). The spectra were calculated by the disorder approach II where the full Green's function is averaged over. The black line shows the analytical result for the nearest-neighbor tight-binding dispersion relation of Graphene eq. (5.26).

6. Conclusions

In this thesis cluster perturbation theory and the variational cluster approach have been extended and applied to quantum impurity models. Calculations done for the single impurity Anderson model, the building block of the majority of quantum impurity models, yield good results. An expression for the change of the grand potential originating from the coupling of the impurity to the infinite bath was derived. A self consistent formulation of the variational cluster approach, previously introduced in the context of non-equilibrium problems [25], was explored. Results obtained by the self consistent approach show good qualitative agreement with results obtained by VCA based on the grand potential. It was possible to show that the essential physics of the single impurity Anderson model is captured by CPT and VCA. Using VCA, the results converge at moderate cluster sizes while the CPT results require prohibitively large clusters to converge. Comparison to results obtained from Bethe Ansatz, renormalization group approaches and data obtained from X-Operator based calculations shows good agreement for all quantities investigated. VCA_Ω yields qualitatively correct spectral properties for the single impurity Anderson model. It reproduces the Kondo resonance and an exponential scale in interaction strength U. Furthermore the position and width of the Hubbard satellites comes out correct. For the asymmetric model the Friedel sum rule is fulfilled in all parameter regions implying that the Kondo resonance is pinned at the chemical potential in the Kondo region. A close look at the Kondo resonance showed that the variational cluster approach is able to reproduce the resonance and the functional behavior of the Kondo temperature remarkably well. The Kondo temperature is expected to show exponential behavior in interaction strength in the Kondo regime. VCA tends to underestimate the exponent. Comparison of dynamic quantities to continuous time Quantum Monte Carlo shows good agreement. In conclusion VCA is a flexible and versatile method which provides reasonably accurate results with modest computational resources.

Based on the success of VCA in an equilibrium simulation, a non-equilibrium extension of VCA was applied to a strongly-correlated quantum dot. A value for the linear response current in the Kondo regime was determined as well as an expression for the effective distribution function. In the non-equilibrium application again the extension from CPT to VCA proofed to be crucial. We investigated the current and non-equilibrium density of states in all parameter regions. A linear splitting of the Kondo resonance was observed in VCA, as well as an interesting behavior of the steady-state current: A two peak structure evolves for higher interaction-strength in the Kondo regime. Furthermore the current in the Kondo regime is very stable against variations of the model parameters. The highest peak-to-peak current however is observed exactly at the crossover point from the Kondo plateau to the zero- or doubly occupied impurity.

In the third part of this work randomly positioned magnetic vacancies in Graphene were studied using CPT/VCA. This made an extension to a strongly disordered, interacting problem necessary. A scheme for treating vacancies/impurities in a lattice within CPT/VCA was developed and applied. The results for the single-particle spectra and the behavior of the band gap looks promising for future applications. The good behavior of VCA for the SIAM makes an eventual use as a cluster-solver for DMFT appealing.

Acknowledgments

First of all I would like to thank my parents for their love, encouragement and support.
Especially I want to thank my supervisor Prof. Wolfgang von der Linden who guided me through this work with great intuition, suggestions and ideas. I would like to thank Prof. Enrico Arrigoni for co-supervising me, providing lots of valueable ideas and vivid explainations of difficult topics. I thank both of them for spending a lot of time on our discussions, being always available and clarifying all my questions.
I am indebted to Prof. Kurt Schönhammer for giving me the opportunity of a marvelous stay at the University of Göttingen for one month during the time of my thesis. With his help I was able to gain some very valuable understanding of the analytic behavior of my work. I would like to thank the members of the group in Göttingen especially Prof. Thomas Pruschke and Prof. Andreas Honecker for stimulating and interesting discussions. I thank Piet Dargel for interesting discussions and for providing his MPS Lanczos data.
I would like to thank everybody who supported me during my studies, especially Prof. Winfried Kernbichler, who gave me the opportunity to work at the institute very early, and encouraged me all the time. Furthermore I would like to express my gratitude to my colleagues Michael Knap and Markus Aichhorn who were always available for technical questions as well as discussions about the underlying physics. I enjoyed working in the quantum many-body theory group at the Institute of Theoretical and Computational Physics with Christoph Heil, Faruk Geles, Klaus Lang, Benjamin Kollmitzer, Anna Fulterer, Elias Assmann, Hubert Antlinger, Valentin Zauner and Martin Ganahl. For helping me with lots of bureaucratic work I thank Brigitte Schwarz and for keeping our computers going, Andreas Hirczy. Finally for having a good time during our coffee breaks I would like to express my gratitude to Andreas Martitsch, Iris Hehn and Matthias Hasewend. I thank Andreas Martitsch for cooking up a great bst-style scheme for LaTeX references.
I am grateful to R.Peters for providing his DMRG and NRG data shown in fig. 3.13 and to C.Karrasch for providing his FRG and NRG data shown in fig. 3.15, fig. 3.20 and fig. 3.21. For providing the MF and QMC data shown in fig. 5.6 (right) I thank A. Honecker. I thank P. Dargel for applying the matrix product state Lanczos algorithm to several reference systems. The CPT results based on these calculations are shown in fig. 3.11 and fig. 3.12. I thank Olivier Parcollet and Michel Ferrero for important, critical feedback concerning the convergence of the CT-QMC data. Use was made of the CT-QMC code of the TRIQS [130] toolkit.
This work is partly supported by the Austrian Science Fund (FWF) P18551-N16 and financial support came from the Förderungsstipendium of the TU Graz.

Bibliography

[1] W. Nolting. *Grundkurs Theoretische Physik 7: Viel-Teilchen-Theorie (Springer-Lehrbuch).* Springer, 7., aktualisierte aufl. edition (2009). ISBN 3642016057.

[2] P. W. Anderson. *Localized Magnetic States in Metals.* Phys. Rev. **124** (1), 41 (1961).

[3] J. Kondo. *Resistance Minimum in Dilute Magnetic Alloys.* PTP **32** (1), 37–49 (1964).

[4] M. P. Sarachik, E. Corenzwit, and L. D. Longinotti. *Resistivity of Mo-Nb and Mo-Re Alloys Containing 1% Fe.* Phys. Rev. **135**, A1041–A1045 (1964).

[5] A. M. Clogston, B. T. Matthias, M. Peter, H. J. Williams, E. Corenzwit, and R. C. Sherwood. *Local Magnetic Moment Associated with an Iron Atom Dissolved in Various Transition Metal Alloys.* Phys. Rev. **125** (2), 541 (1962).

[6] K. G. Wilson. *The renormalization group: Critical phenomena and the Kondo problem.* Rev. Mod. Phys. **47** (4), 773 (1975).

[7] V. A. Fateev and P. B. Wiegmann. *The exact solution of the s-d exchange model with arbitrary impurity spin S (Kondo problem).* Phys. Lett. A **81** (2-3), 179–184 (1981).

[8] I. Affleck. *The Kondo Screening Cloud.* arXiv:0111321 (2001).

[9] H. Tsunetsugu, M. Sigrist, and K. Ueda. *The ground-state phase diagram of the one-dimensional Kondo lattice model.* Rev. Mod. Phys. **69** (3), 809–864 (1997).

[10] S. M. Cronenwett. *A Tunable Kondo Effect in Quantum Dots.* Science **281** (5376), 540–544 (1998).

[11] D. Loss and D. P. DiVincenzo. *Quantum computation with quantum dots.* Phys. Rev. A **57** (1), 120 (1998).

[12] G. Kotliar, S. Y. Savrasov, K. Haule, V. S. Oudovenko, O. Parcollet, and C. A. Marianetti. *Electronic structure calculations with dynamical mean-field theory.* Rev. Mod. Phys. **78** (3), 865 (2006).

[13] K. Held, I. A. Nekrasov, G. Keller, V. Eyert, N. Blümer, A. K. McMahan, R. T. Scalettar, T. Pruschke, V. I. Anisimov, and D. Vollhardt. *Realistic investigations of correlated electron systems with LDA + DMFT.* Phys. Status Solidi **243** (11), 2599–2631 (2006).

[14] W. Metzner and D. Vollhardt. *Correlated Lattice Fermions in $d = \infty$ Dimensions.* Phys. Rev. Lett. **62**, 324–327 (1989).

[15] A. Georges, G. Kotliar, W. Krauth, and M. J. Rozenberg. *Dynamical mean-field theory of strongly correlated fermion systems and the limit of infinite dimensions.* Rev. Mod. Phys. **68**, 13–125 (1996).

[16] M. Nuss, E. Arrigoni, M. Aichhorn, and W. von der Linden. *Exploring the Kondo physics of the single impurity Anderson model by means of the variational cluster approach.* arXiv:1110.4533 (2011).

[17] M. Kaku. *Physics of the Future: How Science Will Shape Human Destiny and Our Daily Lives by the Year 2100.* Doubleday, first edition edition (2011). ISBN 0385530803.

[18] J.-H. Chen, L. Li, W. G. Cullen, E. D. Williams, and M. S. Fuhrer. *Tunable Kondo effect in graphene with defects.* Nat. Phys. **7** (7), 535–538 (2011).

[19] E. Gull, A. J. Millis, A. I. Lichtenstein, A. N. Rubtsov, M. Troyer, and P. Werner. *Continuous-time Monte Carlo methods for quantum impurity models.* Rev. Mod. Phys **83** (2), 349–404 (2010).

[20] S. Gull and G. Daniell. *Image reconstruction from incomplete and noisy data.* Nature **272** (5655), 686–690 (1978).

[21] J. Skilling. *Classic Maximum Entropy.* Kluwer Academic Publishers, Dordtrecht, 45–52 (1989).

[22] C. Gros and R. Valenti. *Cluster expansion for the self-energy: A simple many-body method for interpreting the photoemission spectra of correlated Fermi systems.* Phys. Rev. B **48** (1), 418 (1993).

[23] Sénéchal, D. Perez, and M. Pioro-Ladriére. *Spectral Weight of the Hubbard Model through Cluster Perturbation Theory.* Phys. Rev. Lett. **84** (3), 522 (2000).

[24] M. Potthoff, M. Aichhorn, and C. Dahnken. *Variational Cluster Approach to Correlated Electron Systems in Low Dimensions.* Phys. Rev. Lett. **91** (20), 206402 (2003).

[25] M. Knap, W. von der Linden, and E. Arrigoni. *Nonequilibrium steady state for strongly-correlated many-body systems: variational cluster approach.* Phys. Rev. B **84** (11), 115145 (2011).

[26] D. Sénéchal. *An introduction to quantum cluster methods.* arXiv:0806.2690 (2008).

[27] J. W. Negele and H. Orland. *Quantum Many-particle Systems.* Westview Press (1998). ISBN 0738200522.

[28] M. Aichhorn. *Ordering Phenomena in Strongly-Correlated Systems: Cluster Perturbation Theory Approaches.* Ph.D. thesis, TU Graz (2004).

[29] M. Knap. *Masters thesis: Quantum many body properties of strongly correlated lattice bosons and polaritons* (2009).

[30] W. Gasser, E. Heiner, and K. Elk. *Method Greenschen Funktionen in Der Festkörper Und Vielteilchenphysik.* Not Avail (2001). ISBN 3527402187.

[31] S. Doniach and E. H. Sondheimer. *Green's Functions for Solid State Physicists.* World Scientific Publishing Company (1998). ISBN 1860940803.

[32] S. Pairault, D. Sénéchal, and A.-M. S. Tremblay. *Strong-Coupling Expansion for the Hubbard Model.* Phys. Rev. Lett. **80** (24), 5389–5392 (1998).

[33] S. Pairault, D. Sénéchal, and A.-M. Tremblay. *Strong-coupling perturbation theory of the Hubbard model.* The European Physical Journal B **16** (1), 21 (2000).

[34] D. Sénéchal, D. Perez, and M. Pioro-Ladriére. *Spectral Weight of the Hubbard Model through Cluster Perturbation Theory.* Phys. Rev. Lett. **84** (3), 522 (2000).

[35] A. L. Fetter and J. D.Walecka. *Quantum Theory of Many- Particle Systems.* McGraw-Hill, New York (1971).

[36] R. P. Feynman, R. B. Leighton, and M. Sands. *The Feynman Lectures on Physics including Feynman's Tips on Physics: The Definitive and Extended Edition.* Addison Wesley, 2 edition (2005). ISBN 0805390456.

[37] J. Hubbard. *Electron Correlations in Narrow Energy Bands.* Proceedings of the Royal Society of London. Series A. **276** (1365), 238 –257 (1963).

[38] C. Lanczos. *An Iteration Method for the Solution of the Eigenvalue Problem of Linear Differential and Integral Operators.* Journal of research of the National Bureau of Standards **45**, 255–282 (1951).

[39] Z. Bai, J. Demmel, J. Dongarra, A. Ruhe, and H. van der Vorst. *Templates for the Solution of Algebraic Eigenvalue Problems: A Practical Guide.* Society for Industrial Mathematics, 1 edition (1987). ISBN 0898714710.

[40] M. G. Zacher, R. Eder, E. Arrigoni, and W. Hanke. *Evolution of the stripe phase as a function of doping from a theoretical analysis of angle-resolved photoemission data.* Phys. Rev. B **65** (4), 045109 (2002).

[41] E. Anderson, Z. Bai, C. Bischof, S. Blackford, J. Demmel, J. Dongarra, J. Du Croz, A. Greenbaum, S. Hammarling, A. McKenney, and D. Sorensen. *LAPACK Users' Guide – Third Edition* (1999).

[42] J. G. F. Francis. *The QR Transformation A Unitary Analogue to the LR Transformation – Part 1.* The Computer Journal **4** (3), 265–271 (1961).

[43] J. G. F. Francis. *The QR Transformation – Part 2.* The Computer Journal **4** (4), 332–345 (1962).

[44] D. S. Watkins. *The QR Algorithm Revisited.* SIAM Review **50** (1), 133 (2008).

[45] P. E. Dargel, A. Honecker, R. Peters, R. M. Noack, and T. Pruschke. *Adaptive Lanczos-vector method for dynamic properties within the density matrix renormalization group.* Phys. Rev. B **83** (16), 161104 (2011).

[46] M. Aichhorn, E. Arrigoni, M. Potthoff, and W. Hanke. *Antiferromagnetic to superconducting phase transition in the hole- and electron-doped Hubbard model at zero temperature.* Phys. Rev. B **74** (2), 024508 (2006).

[47] D. Senechal, P.-L. Lavertu, M.-A. Marois, and A.-M. Tremblay. *Competition between Antiferromagnetism and Superconductivity in High-T c Cuprates.* Phys. Rev. Lett. **94**, 156404 (2005).

[48] M. Aichhorn, E. Arrigoni, M. Potthoff, and W. Hanke. *Phase separation and competition of superconductivity and magnetism in the two-dimensional Hubbard model : From strong to weak coupling.* Phys. Rev. B **76**, 224509 (2007).

[49] M. Aichhorn, H. G. Evertz, and M. Potthoff. *Charge ordering in extended Hubbard models.* Phys. Rev. B **70**, 235107 (2004).

[50] T. Yoshikawa and M. Ogata. *Role of frustration and dimensionality in the Hubbard model on the stacked square lattice: Variational cluster approach.* Phys. Rev. B **79** (144429), 1–7 (2009).

[51] H. Watanabe, T. Shirakawa, and S. Yunoki. *Microscopic Study of a Spin-Orbit-Induced Mott Insulator in Ir Oxides.* Phys. Rev. Lett. **105**, 216410 (2010).

[52] W. Koller and N. Dupuis. *Variational cluster perturbation theory for Bose Hubbard models.* J. Phys.: Condensed Matter **18** (41), 9525–9540 (2006).

[53] M. Balzer and M. Potthoff. *Variational cluster approach to ferromagnetism in infinite dimensions and in one – dimensional chains* (2010). ArXiv:1007.2517.

[54] E. Arrigoni, M. Knap, and W. von der Linden. *Extended self-energy functional approach for strongly-correlated lattice bosons in the superfluid phase.* Phys. Rev. B **84** (1), 014535 (2011).

[55] M. Knap, E. Arrigoni, and W. von der Linden. *Variational cluster approach for strongly-correlated lattice bosons in the superfluid phase.* Phys. Rev. B **83** (13), 134507 (2011).

[56] M. Potthoff and M. Balzer. *Self-energy-functional theory for systems of interacting electrons with disorder.* Phys. Rev. B **75** (12), 125112 (2007).

[57] M. Knap, E. Arrigoni, and W. von der Linden. *Excitations in disordered bosonic optical lattices.* Phys. Rev. A **82** (5), 053628 (2010).

[58] M. Aichhorn, E. Arrigoni, M. Potthoff, and W. Hanke. *Variational cluster approach to the Hubbard model: Phase-separation tendency and finite-size effects.* Phys. Rev. B **74** (23), 235117 (2006).

[59] M. Knap, E. Arrigoni, and W. von der Linden. *Spectral properties of strongly correlated bosons in two-dimensional optical lattices.* Phys. Rev. B **81** (2), 024301 (2010).

[60] K. Seki, R. Eder, and Y. Ohta. *A BCS-BEC crossover in the extended Falicov-Kimball model: Variational cluster approach.* arXiv:1110.3150 (2011).

[61] S. Horiuchi, S. Kudo, T. Shirakawa, and Y. Ohta. *Antiferromagnetism versus Kondo screening in the two-dimensional periodic Anderson model at half filling: Variational cluster approach.* Phys. Rev. B **78** (15), 155128 (2008).

[62] M. Knap, E. Arrigoni, and W. V. D. Linden. *Spectral properties of coupled cavity arrays in one dimension.* Phys. Rev. B **81** (March), 1–16 (2010).

[63] H. Allmaier, L. Chioncel, E. Arrigoni, M. I. Katsnelson, A. I. Lichtenstein, and D. Groot. *Half-metallicity in NiMnSb: a Variational Cluster Approach with ab-initio parameters.* Phys. Rev. B **81** (054422), 1–8 (2009).

[64] N.-H. Tong. *Extended variational cluster approximation for correlated systems.* Phys. Rev. B **72** (11), 115104 (2005).

[65] M. Potthoff. *Self-energy-functional approach to systems of correlated electrons.* Eur. Phys. J. B **32** (4), 429–436 (2003).

[66] M. Potthoff. *Self-energy-functional approach: Analytical results and the Mott-Hubbard transition.* Eur. Phys. J. B **36** (3), 335–348 (2003).

[67] M. Potthoff. *Self-energy-functional theory.* arXiv:1108.2183 (2011).

[68] J. M. Luttinger and J. C. Ward. *Ground-State Energy of a Many-Fermion System. II.* Phys. Rev. **118** (5), 1417 (1960).

[69] M. Potthoff. *Non-perturbative construction of the Luttinger-Ward functional.* Condens. Mat. Phys. **9**, 557 (2006).

[70] W. H. Press, S. A. Teukolsky, W. T. Vetterling, and B. P. Flannery. *Numerical Recipes 3rd Edition: The Art of Scientific Computing.* Cambridge University Press, 3 edition (2007). ISBN 0521880688.

[71] G. Henkelman and H. Jo. *A climbing image nudged elastic band method for finding saddle points and minimum energy paths.* Chem. Phys. **113** (22) (2000).

[72] G. Henkelman and H. Jo. *A dimer method for finding saddle points on high dimensional potential surfaces using only first derivatives.* Chem. Phys. **111** (15) (1999).

[73] J. A. Nelder and R. Mead. *A Simplex Method for Function Minimization.* The Computer Journal **7** (4), 308–313 (1965).

[74] GNU. *GNU Scientific Library: GSL.* http://www.gnu.org/s/gsl/ (2011).

[75] M. Balzer and M. Potthoff. *Non-equilibrium cluster-perturbation theory.* Phys. Rev. B **83** (19), 195132 (2011).

[76] A. Jauho. *Introduction to the Keldysh Nonequilibrium Green Function Technique* (2006).

[77] J. Rammer and H. Smith. *Quantum field-theoretical methods in transport theory of metals.* Rev. Mod. Phys. **58** (2), 323 (1986).

[78] A. Kamenev. *Many-body theory of non-equilibrium systems.* arXiv:0412296 (2004).

[79] J. Viljas. *On the calculation of Green' s functions in nonequilibrium Fermi systems* (2008).

[80] J. Keller and M. Jarrell. *Lecture Notes: The Non-Equilibrium Green Function Method* (2011).

[81] H. Haug and A. Jauho. *Quantum Kinetics in Transport and Optics of Semiconductors.* Springer-Verlag GmbH, 2., corr. printing edition (1996). ISBN 3540616020.

[82] L. V. Keldysh. *Diagram technique for nonequilibrium processes.* Zh. Eksp. Teor. Fiz. (47), 1515 (1965).

[83] J. Schwinger. *Brownian Motion of a Quantum Oscillator.* J.Math. Phys. **2**, 407 (1961).

[84] R. Feynman and F. V. Jr. *The theory of a general quantum system interacting with a linear dissipative system.* Ann. Phys. **24** (0), 118 – 173 (1963).

[85] A. A. Abrikosov, L. P. Gorkov, and F. A. Davis. *Methods of Quantum Field Theory in Statistical Physics.* Dover Pubn Inc (1975). ISBN 0486632288.

[86] G. D. Mahan. *Many particle physics.* Springer, 3 edition (2000). ISBN 0306463385.

[87] M. Gell-Mann and F. Low. *Bound States in Quantum Field Theory.* Phys. Rev. **84**, 350 (1951).

[88] J. Friedel. *On some electrical and magnetic properties of metallic solid solutions.* Can. J. Phys. **34** (12A), 1190–1211 (1956).

[89] A. C. Hewson. *The Kondo Problem to Heavy Fermions.* Cambridge University Press (1997). ISBN 0521599474.

[90] W. Brenig and K. Schönhammer. *On the theory of chemisorption.* Zeitschrift für Physik **267**, 201–208 (1974).

[91] R. Brako and D. M. Newns. *Slowly varying time-dependent local perturbations in metals: a new approach.* J. Phys. C **14** (21), 3065–3078 (1981).

[92] D. C. Langreth and P. Nordlander. *Derivation of a master equation for charge-transfer processes in atom-surface collisions.* Phys. Rev. B **43** (4), 2541 (1991).

[93] I. Affleck. *Quantum Impurity Problems in Condensed Matter Physics.* arXiv:0809.3474 (2008).

[94] F. Steglich, J. Aarts, C. D. Bredl, W. Lieke, D. Meschede, W. Franz, and H. Schäfer. *Superconductivity in the Presence of Strong Pauli Paramagnetism: CeCu2Si2.* Phys. Rev. Lett. **43** (25), 1892 (1979).

[95] P. Coleman. *Heavy Fermions: electrons at the edge of magnetism.* arXiv:0612006 (2006).

[96] K. Yamada and K. Yosida. *Perturbation Expansion for the Anderson Hamiltonian. III* **53** (5), 1286–1301 (1975).

[97] H. Bethe. *Zur Theorie der Metalle.* Zeitschrift für Physik **71** (3-4), 205–226 (1931).

[98] R. Bulla, T. A. Costi, and T. Pruschke. *Numerical renormalization group method for quantum impurity systems.* Rev. Mod. Phys. **80** (2), 395 (2008).

[99] R. Hedden, V. Meden, T. Pruschke, and K. Schönhammer. *A functional renormalization group approach to zero-dimensional interacting systems.* J. Phys.: Condens. Matter **16** (29), 5279–5296 (2004).

[100] C. Karrasch, R. Hedden, R. Peters, T. Pruschke, K. Schönhammer, and V. Meden. *A finite-frequency functional renormalization group approach to the single impurity Anderson model.* J. Phys.: Condens. Matter **20** (34), 345205 (2008).

[101] A. Isidori, D. Roosen, L. Bartosch, W. Hofstetter, and P. Kopietz. *Spectral function of the Anderson impurity model at finite temperatures.* Phys. Rev. B **81** (23), 235120 (2010).

[102] S. Nishimoto and E. Jeckelmann. *Density-matrix renormalization group approach to quantum impurity problems.* J. Phys.: Condens. Matter **16** (4), 613–625 (2004).

[103] S. Nishimoto, F. Gebhard, and E. Jeckelmann. *Dynamical mean-field theory calculation with the dynamical density-matrix renormalization group.* Physica B: Condensed Matter **378-380**, 283–285 (2006).

[104] R. Peters. *Spectral functions for single- and multi-Impurity models using DMRG.* Phys. Rev. B **84** (7), 075139 (2011).

[105] S. Florens and A. Georges. *Slave-rotor mean-field theories of strongly correlated systems and the Mott transitionin finite dimensions.* Phys. Rev. B **70** (3), 035114 (2004).

[106] P. Coleman. *New approach to the mixed-valence problem.* Phys. Rev. B **29** (6), 3035 (1984).

[107] T. Lobo, M. S. Figueira, and M. E. Foglio. *The atomic approach to the Anderson model for the finite U case: application to a quantum dot.* Nanotechnology **21** (27), 274007 (2010).

[108] R. N. Silver, J. E. Gubernatis, D. S. Sivia, and M. Jarrell. *Spectral Densities of the Symmetric Anderson Model.* Phys. Rev. Lett. **65** (4), 496 (1990).

[109] J. E. Hirsch and R. M. Fye. *Monte Carlo Method for Magnetic Impurities in Metals.* Phys. Rev. Lett. **56** (23), 2521 (1986).

[110] M. Caffarel and W. Krauth. *Exact diagonalization approach to correlated fermions in infinite dimensions: Mott transition and superconductivity.* Phys. Rev. Lett. **72** (10), 1545 (1994).

[111] P. Fulde. *Electron Correlations in Molecules and Solids.* Springer, 3rd edition (2003). ISBN 3540593640.

[112] P. Coleman. *Local moment physics in heavy electron systems.* AIP Conference Proceedings **629** (1), 79–160 (2002).

[113] E. N. Economou. *Green's Functions in Quantum Physics.* Springer, 3rd ed. edition (2010). ISBN 3642066917.

[114] M. Balzer, W. Hanke, and M. Potthoff. *Mott transition in one dimension: Benchmarking dynamical cluster approaches.* Phys. Rev. B **77** (4), 045133 (2008).

[115] M. Knap, E. Arrigoni, and W. von der Linden. *Benchmarking the variational cluster approach by means of the one-dimensional Bose-Hubbard model.* Phys. Rev. B **81** (23), 235122 (2010).

[116] T. Hand, J. Kroha, and H. Monien. *Spin Correlations and Finite-Size Effects in the One-Dimensional Kondo Box.* Phys. Rev. Lett. **97** (13), 136604 (2006).

[117] K. Schönhammer. *Variational Ansatz for the Anderson model of chemisorption.* Phys. Rev. B **13** (10), 4336 (1976).

[118] S. Andergassen, T. Enss, C. Karrasch, and V. Meden. *A gentle introduction to the functional renormalization group: the Kondo effect in quantum dots.* Quantum Magnetism edited by B. Barbara, Y. Imry, G. Sawatzky, and P.C.E. Stamp (Springer) (2008).

[119] K. R. Patton, H. Hafermann, S. Brener, A. I. Lichtenstein, and M. I. Katsnelson. *Probing the Kondo screening cloud via tunneling-current conductance fluctuations.* Phys. Rev. B **80** (21), 212403 (2009).

[120] X. Wen. *Quantum Field Theory of Many-body Systems: From the Origin of Sound to an Origin of Light and Electrons.* Oxford University Press, USA, reissue edition (2007). ISBN 019922725X.

[121] H. Pruser, M. Wenderoth, P. E. Dargel, A. Weismann, R. Peters, T. Pruschke, and R. G. Ulbrich. *Long-range Kondo signature of a single magnetic impurity.* Nat. Phys. **7**, 203â206 (2011).

[122] O. Gunnarsson and K. Schönhammer. *Chapter 64: Many-body formulation of spectra of mixed valence systems.* Handbook on the Physics and Chemistry of Rare Earths **10**, 103–163 (1987).

[123] R. Zitko and T. Pruschke. *Energy resolution and discretization artefacts in the numerical renormalization group.* Phys. Rev. B **79** (2009).

[124] J. S. Langer and V. Ambegaokar. *Friedel Sum Rule for a System of Interacting Electrons.* Phys. Rev. **121** (4), 1090 (1961).

[125] D. C. Langreth. *Friedel Sum Rule for Anderson's Model of Localized Impurity States.* Phys. Rev. **150** (2), 516 (1966).

[126] J. M. Luttinger. *Fermi Surface and Some Simple Equilibrium Properties of a System of Interacting Fermions.* Phys. Rev. **119** (4), 1153–1163 (1960).

[127] P. Coleman. *Introduction to Many Body physics.* http://www.physics.rutgers.edu/ coleman/ (2011).

[128] N. Kawakami and A. Okiji. *Exact expression of the ground-state energy for the symmetric anderson model.* Phys. Lett. A **86** (9), 483–486 (1981).

[129] G. Kotliar and A. E. Ruckenstein. *New Functional Integral Approach to Strongly Correlated Fermi Systems: The Gutzwiller Approximation as a Saddle Point.* Phys. Rev. Lett. **57** (11), 1362 (1986).

[130] M. Ferrero and O. Parcollet. *TRIQS: a Toolkit for Research in Interacting Quantum Systems* (2011).

[131] P. Werner and A. J. Millis. *Hybridization expansion impurity solver: General formulation and application to Kondo lattice and two-orbital models.* Phys. Rev. B **74** (15), 155107 (2006).

[132] L. Boehnke, H. Hafermann, M. Ferrero, F. Lechermann, and O. Parcollet. *Orthogonal Polynomial Representation of Imaginary-Time Green's Functions.* Phys. Rev. B **84** (7), 075145 (2011).

[133] K. Marc. *Artificial Atoms.* Physics Today **46** (24), 24 (1993).

[134] R. C. Ashoori. *Electrons in artificial atoms.* Nature **369** (2), 413 (1996).

[135] U. Meirav and E. B. Foxman. *Single-electron phenomena in semiconductors.* Semicond. Sci. Technol. **11**, 255–284 (1996).

[136] D. Goldhaber-Gordon, J. Göres, M. Kastner, H. Shtrikman, D. Mahalu, and U. Meirav. *From the Kondo Regime to the Mixed-Valence Regime in a Single-Electron Transistor.* Phys. Rev. Lett. **81** (23), 5225–5228 (1998).

[137] M. Kastner and D. Goldhaber-Gordon. *Kondo physics with single electron transistors.* Solid State Commun. **119** (4-5), 245–252 (2001).

[138] D. Goldhaber-Gordon, J. Go, and D. Goldhabergordon. *The Kondo effect in a single-electron transistor.* Materials Science and Engineering B **84** (1-2), 17–21 (2001).

[139] S. M. Reimann and M. Manninen. *Electronic structure of quantum dots.* Reviews of Modern Physics **74** (October), 1283–1342 (2002).

[140] Y. Meir, N. S. Wingreen, and P. A. Lee. *Transport through a strongly interacting electron system: Theory of periodic conductance oscillations.* Phys. Rev. Lett. **66** (23), 3048 (1991).

[141] Y. Meir, N. S. Wingreen, and P. A. Lee. *Low-temperature transport through a quantum dot: The Anderson model out of equilibrium.* Phys. Rev. Lett. **70** (17), 2601 (1993).

[142] N. S. Wingreen and Y. Meir. *Anderson model out of equilibrium: Noncrossing-approximation approach to transport through a quantum dot.* Phys. Rev. B **49** (16), 11040 (1994).

[143] A.-P. Jauho, N. S. Wingreen, and Y. Meir. *Time-dependent transport in interacting and noninteracting resonant-tunneling systems.* Phys. Rev. B **50** (8), 5528 (1994).

[144] K. Richter. *Semiclassical Theory of Mesoscopic Quantum Systems.* Springer (1999). ISBN 3540665668.

[145] T. K. Ng and P. A. Lee. *On-Site Coulomb Repulsion and Resonant Tunneling.* Phys. Rev. **61** (15), 1768–1771 (1988).

[146] J. König, J. Schmid, H. Schoeller, and G. Schön. *Resonant tunneling through ultrasmall quantum dots: Zero-bias anomalies, magnetic-field dependence, and boson-assisted transport.* Phys. Rev. B **54** (23), 16820–16837 (1996).

[147] R. Aguado, G. Platero, C. Tejedor, and R. Lopez. *AC Kondo effect in quantum dots.* Physica B **258**, 256–259 (1998).

[148] A. Kaminski and L. I. Glazman. *Universality of the Kondo Effect in a Quantum Dot out of Equilibrium.* Phys. Rev. B **62** (12), 8154–8170 (2000).

[149] F. Heidrich-Meisner, I. González, K. Al-Hassanieh, a. Feiguin, M. Rozenberg, and E. Dagotto. *Nonequilibrium electronic transport in a one-dimensional Mott insulator.* Phys. Rev. B **82** (20), 1–11 (2010).

[150] P. Coleman, C. Hooley, and O. Parcollet. *Is the quantum dot at large bias a weak-coupling problem?* Phy. Rev. Lett. **86** (18), 4088–4091 (2001).

[151] J. Eckel, S. G. Jakobs, and M. Thorwart. *Comparative study of theoretical methods for nonequilibrium quantum transport.* arXiv:1001.3773 (2011).

[152] A. M. Uimonen, E. Khosravi, A. Stan, G. Stefanucci, S. Kurth, R. van Leeuwen, and E. K. U. Gross. *Comparative study of many-body perturbation theory and time-dependent density functional theory in the out-of-equilibrium Anderson model.* Phys. Rev. B **84** (11), 115103 (2011).

[153] L. D. Contreras-Pulido, J. Splettstoesser, M. Governale, J. König, and M. Büttiker. *Time scales in the dynamics of an interacting quantum dot.* arXiv:1111.4135 (2011).

[154] T. Kloss and P. Kopietz. *Non-equilibrium time evolution of bosons from the functional renormalization group.* Phys. Rev. B **83** (20), 205118 (2010).

[155] S. G. Jakobs, M. Pletyukhov, and H. Schoeller. *Nonequilibrium functional renormalization group with frequency-dependent vertex function: A study of the single-impurity Anderson model.* Phys. Rev. B **81** (19), 195109 (2010).

[156] P. Wang and S. Kehrein. *Flow Equation Calculation of Transient and Steady State Currents in the Anderson Impurity Model.* Phys. Rev. B **82** (12), 125124 (2010).

[157] J. E. Han and R. J. Heary. *Imaginary-Time Formulation of Steady-State Nonequilibrium: Application to Strongly Correlated Transport.* Phys. Rev. Lett. **99** (23), 236808 (2007).

[158] A. Dirks, P. Werner, M. Jarrell, and T. Pruschke. *CT-QMC and Maximum Entropy Approach to a Scattering-States Formulation of Strongly Correlated Steady-State Transport.* Journal of Physics: Conference Series **273**, 012150 (2011).

[159] C. Jung, A. Lieder, S. Brener, H. Hafermann, B. Baxevanis, A. Chudnovskiy, A. N. Rubtsov, M. I. Katsnelson, and A. I. Lichtenstein. *Dual fermion approach to non-equilibrium strongly correlated problems.* Annalen der Physik (2010).

[160] E. Mu, C. J. Bolech, and S. Kirchner. *Universal out-of-equilibrium transport in Kondo-correlated quantum dots: a renormalized superperturbation theory on the Keldysh contour* (arXiv:1111.4076).

[161] P. Mehta and N. Andrei. *Nonequilibrium Transport in Quantum Impurity Models: The Bethe Ansatz for Open Systems.* Phys. Rev. Lett. **96** (21), 216802 (2006).

[162] P. Wiegmann. *Towards an exact solution of the Anderson model.* Phys. Lett. A **80** (2-3), 163–167 (1980).

[163] C. Timm. *Tunneling through molecules and quantum dots: Master-equation approaches.* Phys. Rev. B **77** (19), 1–13 (2008).

[164] G. Schneider and P. Schmitteckert. *Conductance in strongly correlated 1D systems: Real-Time Dynamics in DMRG.* arXiv:0601389 1–4 (2006).

[165] A. Bransch. *Conductance of correlated systems: real-time dynamics in finite systems.* arXiv:1004.4178 (2010).

[166] A. Rosch. *Wilson chains are not thermal reservoirs.* arXiv:1110.6514 (2011).

[167] P. Myöhänen, R. Tuovinen, T. Korhonen, G. Stefanucci, and R. van Leeuwen. *Image charge dynamics in time-dependent quantum transport.* arXiv:1111.6104 (2011).

[168] D. M. Kennes, S. G. Jakobs, C. Karrasch, and V. Meden. *A renormalization group approach to time dependent transport through correlated quantum dots.* arXiv:1111.6982 (2011).

[169] A. Schiller and E. Lebanon. *Measuring the out-of-equilibrium splitting of the Kondo resonance.* Phys. Rev. B **65** (3), 035308 (2001).

[170] Y. Meir and N. S. Wingreen. *Landauer Formula for the Current through an Interacting Eelctron Region.* Phys. Rev. Lett. **68** (April), 2512 (1992).

[171] P. Dutt, J. Koch, J. Han, and K. Le Hur. *Effective equilibrium theory of nonequilibrium quantum transport.* Annals of Physics **326** (12), 2963–2999 (2011).

[172] K. S. Novoselov, a. K. Geim, S. V. Morozov, D. Jiang, Y. Zhang, S. V. Dubonos, I. V. Grigorieva, and a. a. Firsov. *Electric field effect in atomically thin carbon films.* Science (New York, N.Y.) **306** (5696), 666–9 (2004).

[173] K. S. Novoselov, D. Jiang, F. Schedin, T. J. Booth, V. V. Khotkevich, S. V. Morozov, and a. K. Geim. *Two-dimensional atomic crystals.* Proceedings of the National Academy of Sciences of the United States of America **102** (30), 10451–3 (2005).

[174] a. H. Castro Neto, N. M. R. Peres, K. S. Novoselov, and a. K. Geim. *The electronic properties of graphene.* Rev. Mod. Phys. **81** (1), 109–162 (2009).

[175] S. Reich, J. Maultzsch, C. Thomsen, and P. Ordejón. *Tight-binding description of graphene.* Phys. Rev. B **66** (3), 1–5 (2002).

[176] P. Esquinazi, D. Spemann, R. Höhne, a. Setzer, K.-H. Han, and T. Butz. *Induced Magnetic Ordering by Proton Irradiation in Graphite.* Physical Review Letters **91** (22), 8–11 (2003).

[177] J. Barzola-Quiquia, P. Esquinazi, M. Rothermel, D. Spemann, T. Butz, and N. García. *Experimental evidence for two-dimensional magnetic order in proton bombarded graphite.* Phys. Rev. B **76** (16), 2–5 (2007).

[178] F. Schedin, a. K. Geim, S. V. Morozov, E. W. Hill, P. Blake, M. I. Katsnelson, and K. S. Novoselov. *Detection of individual gas molecules adsorbed on graphene.* Nat. Mat. **6** (9), 652–5 (2007).

[179] B. Uchoa, L. Yang, S.-W. Tsai, N. Peres, and a. Castro Neto. *Theory of Scanning Tunneling Spectroscopy of Magnetic Adatoms in Graphene.* Phys. Rev. Lett. **103** (20), 1–4 (2009).

[180] B. Uchoa, V. Kotov, N. Peres, and a. Castro Neto. *Localized Magnetic States in Graphene.* Phys. Rev. Lett. **101** (2), 1–4 (2008).

[181] F. Ding. *Theoretical study of the stability of defects in single-walled carbon nanotubes as a function of their distance from the nanotube end.* Phys. Rev. B **72** (24), 1–7 (2005).

[182] V. Pereira, J. Lopes dos Santos, and a. Castro Neto. *Modeling disorder in graphene.* Phys. Rev. B **77** (11) (2008).

[183] F. M. Hu, H.-q. Lin, and J. E. Gubernatis. *Magnetic Impurities in Graphene.* Phys. Rev. B **84** (7), 075414 (2011).

[184] P. Haase, S. Fuchs, T. Pruschke, H. Ochoa, and F. Guinea. *Interactions and magnetic moments near vacancies and resonant impurities in graphene.* Phys. Rev. B **83** (24), 241408 (2011).

[185] Z.-G. Zhu and J. Berakdar. *Magnetic adatoms on graphene in the Kondo regime: an Anderson model treatment.* Phys. Rev. B **84** (16), 165105 (2011).

[186] B. Uchoa, T. Rappoport, and a. Castro Neto. *Kondo Quantum Criticality of Magnetic Adatoms in Graphene.* Phys. Rev. Lett. **106** (1), 4–7 (2011).

[187] H. Feldner, Z. Y. Meng, A. Honecker, D. Cabra, S. Wessel, and F. F. Assaad. *Magnetism of finite graphene samples: Mean-field theory compared with exact diagonalization and quantum Monte Carlo simulations.* Phys. Rev. B **81** (11), 115416 (2010).

[188] S. L. Cunningham. *Special points in the two-dimensional Brillouin zone.* Phys. Rev. B **10** (12), 4988 (1974).

[189] D. J. Chadi and M. L. Cohen. *Special Points in the Brillouin Zone.* Phys. Rev. B **8** (12), 5747 (1973).

[190] H. J. Monkhorst and J. D. Pack. *Special points for Brillouin-zone integrations.* Phys. Rev. B **13** (12), 5188 (1976).

[191] J. R. Schrieffer and P. A. Wolff. *Relation between the Anderson and Kondo Hamiltonians.* Phys. Rev. **149** (2), 149 (1966).

[192] M. Knap, E. Arrigoni, and W. von der Linden. *Excitations in disordered bosonic optical lattices.* Phys. Rev. A **82** (5), 053628 (2010).

[193] M. W. Haverkort, I. S. Elfimov, and G. A. Sawatzky. *Electronic structure and self energies of randomly substituted solids using density functional theory and model calculations.* arXiv:1109.4036 (2011).

[194] W. Kohn and J. M. Luttinger. *Ground-State Energy of a Many-Fermion System.* Phys. Rev. **118** (1), 41 (1960).

[195] K. Jänich. *Funktionentheorie: Eine Einführung.* Springer, 6. aufl. 2. korr. nachdruck 4th printing. edition (2010). ISBN 3540203923.

[196] R. D. Mattuck. *A Guide to Feynman Diagrams in the Many-Body Problem.* Dover Publications, 2 edition (1992). ISBN 0486670473.

[197] A. Nieto. *Evaluating Sums over the Matsubara Frequencies.* Comput. Phys. Commun. **92**, 54 (1995).

[198] P. E. Dargel. *Masters Thesis: Local Density of States of the Single Impurity Anderson Model* (2009).

List of Figures

A. Abbreviations

List of abbreviations (in alphabetical order)

- ARPES ... angle resolved photo emission spectroscopy
- BZ ... Brillouin zone
- CDMFT ... cluster/cellular dynamical mean field theory
- CPT ... cluster perturbation theory
- CT-QMC ... continuous time quantum Monte Carlo
- CT-HYB ... continuous time hybridization expansion quantum Monte Carlo
- DCA ... dynamical cluster approximation
- DMFT ... dynamical mean field theory
- DMRG ... density matrix renormalization group
- DOS ... density of states
- ED ... exact diagonalization
- FRG ... functional renormalization group
- FSR ... Friedel sum rule
- FWHM ... full width at half maximum
- IPES ... inverse photo emission spectroscopy
- LDOS ... local density of states
- MF ... mean field theory
- MPS ... matrix product states
- NRG ... numerical renormalization group
- PES ... photo emission spectroscopy
- PT ... perturbation theory
- QD ... quantum dot
- QMC ... quantum Monte Carlo
- SFA ... self-energy functional approach
- STM ... scanning tunneling microscope
- SIAM ... single impurity Anderson Model
- VCA ... variational cluster approach
- VCA_{Ω} ... variational cluster approach based on the grand potential
- $\mathrm{VCA}_{\mathrm{SC}}$ ... variational cluster approach based on self-consistency

B. Units, Libraries and Infrastructure

In this document units of

$$\hbar = e = k_B = 1 \ ,$$

are used. The reduces Planck's constant is denoted $\hbar$, the (positive) electronic charge e and Boltzmann's constant k_B. The hopping integral for free electrons on a lattice, t is set to one unless otherwise noted.

The numerical calculations done in this work were performed using a self-written program in C++. The program was developed in Eclipse Helios using a GNU C compiler v4.4. Use was made of several libraries for C++: Boost, Lapack, Arpack, Blas and GSL v1.15. A wrapper library for some numerical routines developed by Ralf Gamilscheg and Michael Knap, BoostTools was used. Some parts of the work, especially data evaluation, were done using Matlab v7.11.0. For the CT-QMC calculations I used the TRIQS toolkit. All calculations were done on an Intel quad-core I7, with 16 gigabytes of RAM, operated by a Debian 6.0 Linux system. For this document LaTeX was used.

C. Detailed analysis of the grand potential for infinite reference systems

In the following it will be shown that for a formally infinite system consisting of one or more clusters and an environment a regular expression for the grand potential Ω can be obtained. The part of the system which may be troublesome is hidden in the noninteracting environment of infinite extent which will blow up the trace. We first examine the third part of eq. (2.23)

$$\operatorname{Tr} \ln(-\mathrm{G}) = \ln(\det(-\mathrm{G})) \ . \tag{C.1}$$

To find a practicable notation we write the matrix Green's functions in terms of its elements in block indices, where the index c stands for cluster and the index e for environment. These indices denote blocks which are of infinite extent. To ease the notation the spin index is depressed as it is just a parameter. All infinite terms are those containing $\operatorname{tr} \mathrm{G}'_{ee}$. The idea is to first rewrite the interacting Green's functions $\mathrm{G}_{\alpha\beta}$ ($\alpha, \beta \in [c, e]$) in terms of the noninteracting Green's functions $\mathrm{G}'_{\alpha\beta}$ and the coupling matrix $\mathrm{T}_{\alpha\beta}$. Note that for the problem under consideration here $\mathrm{G}_{\alpha\beta}$ is a full matrix. The Green's function of the reference system $\mathrm{G}'_{\alpha\beta}$ is of course diagonal in block indices. Finally the coupling matrix $\mathrm{T}_{\alpha\beta}$ has in CPT only off diagonal elements, but in VCA a further contribution T_{cc} enters, arising from the variational parameters. We are now going to identify and separate the problematic terms. To see how these terms in the end drop out consider the right hand part of eq. (C.1) in the form

$$X := \ln\left(\det\left(-\begin{pmatrix} \mathrm{G}_{cc} & \mathrm{G}_{ce} \\ \mathrm{G}_{ec} & \mathrm{G}_{ee} \end{pmatrix}\right)\right) ,$$

and insert an identity matrix to the left and to the right of G

$$\begin{aligned} X = \ln\Bigg\{ \det\Bigg[& \begin{pmatrix} \mathbb{1} & 0 \\ 0 & -\mathrm{G}'_{ee} \end{pmatrix} \begin{pmatrix} \mathbb{1} & 0 \\ 0 & -\mathrm{G}'_{ee} \end{pmatrix}^{-1} \times (-1) \\ & \begin{pmatrix} \mathrm{G}_{cc} & \mathrm{G}_{ce} \\ \mathrm{G}_{ec} & \mathrm{G}_{ee} \end{pmatrix} \begin{pmatrix} \mathbb{1} & 0 \\ 0 & -\mathrm{G}'_{ee} \end{pmatrix}^{-1} \begin{pmatrix} \mathbb{1} & 0 \\ 0 & -\mathrm{G}'_{ee} \end{pmatrix} \Bigg] \Bigg\} , \end{aligned}$$

which can be written as

$$\begin{aligned} X = \ln\Bigg\{ & \det\left(-\mathrm{G}'_{ee}\right) \det\begin{pmatrix} -\mathrm{G}_{cc} & \mathrm{G}_{ce}\mathrm{G}'^{-1}_{ee} \\ \mathrm{G}'^{-1}_{ee}\mathrm{G}_{ec} & -\mathrm{G}'^{-1}_{ee}\mathrm{G}_{ee}\mathrm{G}'^{-1}_{ee} \end{pmatrix} \\ & \times \det\left(-\mathrm{G}'_{ee}\right) \Bigg\} . \end{aligned} \tag{C.2}$$

The interacting Green's function $\mathrm{G}_{\alpha\beta}$ is determined in terms of the noninteracting Green's functions $g_{\alpha\beta}$ and the coupling matrix $\mathrm{T}_{\alpha\beta}$ straightforwardly by Dyson's equation

$$\mathrm{G}_{cc} = r_{cc}\,\mathrm{G}'_{cc} \tag{C.3a}$$

$$\mathrm{G}_{ee} = \mathrm{G}'_{ee} + \mathrm{G}'_{ee}\,\mathrm{T}_{ec}\,\mathrm{G}_{cc}\,\mathrm{T}_{ce}\,\mathrm{G}'_{ee} \tag{C.3b}$$

$$\mathrm{G}_{ec} = \mathrm{G}'_{ee}\,\mathrm{T}_{ec}\,\mathrm{G}_{cc} \tag{C.3c}$$

$$\mathrm{G}_{ce} = \mathrm{G}_{cc}\,\mathrm{T}_{ce}\,r_{ee} \ , \tag{C.3d}$$

where the abbreviation r_{cc} has been defined as

$$r_{cc} = \left(\mathbb{1} - \mathrm{G}'_{cc}\,\mathrm{T}_{cc} - \mathrm{G}'_{cc}\,\mathrm{T}_{ce}\,\mathrm{G}'_{ee}\,\mathrm{T}_{ec}\right)^{-1} \ . \tag{C.4}$$

It is important to note that all occurring terms including r_{cc} (which depends just on the projection of G'_{ee} on the finite cluster space) are well behaved under the trace, except for g_{ee} which has infinite trace.

Inserting eqs. (C.3) into eq. (C.2) we obtain

$$\begin{aligned} X =& 2\,\mathrm{Tr}\ln\left(-\mathrm{G}'_{ee}\right) \\ &+ \ln\left(\det\begin{pmatrix} -\mathrm{G}_{cc} & \mathrm{G}_{cc}\,\mathrm{T}_{ce} \\ \mathrm{T}_{ec}\,\mathrm{G}_{cc} & -\mathrm{G}'^{-1}_{ee} - \mathrm{T}_{ec}\,\mathrm{G}_{cc}\,\mathrm{T}_{ce} \end{pmatrix}\right). \end{aligned} \tag{C.5}$$

To get rid of the last troublesome term G'^{-1}_{ee} we rewrite the above expression using Sylvester's theorem

$$\det\left(X + A\,B\right) = \det\left(X\right)\,\det\left(\mathbb{1} + B\,X^{-1}\,A\right)\,, \tag{C.6}$$

which is valid for non singular X. A suitable form of eq. (C.5) is

$$\begin{aligned} X =& 2\,\mathrm{Tr}\ln\left(-\mathrm{G}'_{ee}\right) + \ln\Bigg\{\det\Bigg[\begin{pmatrix} -\mathrm{G}_{cc} & 0 \\ 0 & -\mathrm{G}'^{-1}_{ee} \end{pmatrix} \\ &+ \begin{pmatrix} 0 & \mathrm{G}_{cc} \\ \mathrm{T}_{ec}\,\mathrm{G}_{cc} & -\mathrm{T}_{ec}\,\mathrm{G}_{cc} \end{pmatrix}\begin{pmatrix} \mathbb{1} & 0 \\ 0 & \mathrm{T}_{ce} \end{pmatrix}\Bigg]\Bigg\}. \end{aligned}$$

Applying theorem eq. (C.6) we may write

$$\begin{aligned} X =& 2\,\mathrm{Tr}\ln\left(-\mathrm{G}'_{ee}\right) + \ln\Bigg\{\det\left(-\mathrm{G}_{cc}\right)\,\det\left(-\mathrm{G}'^{-1}_{ee}\right) \\ &\det\Bigg[\mathbb{1} + \begin{pmatrix} 0 & -\mathbb{1} \\ -\underbrace{\mathrm{T}_{ce}\,\mathrm{G}'_{ee}\,\mathrm{T}_{ec}}_{p_{cc}}\,\mathrm{G}_{cc} & +\underbrace{\mathrm{T}_{ce}\,\mathrm{G}'_{ee}\,\mathrm{T}_{ec}}_{p_{cc}}\,\mathrm{G}_{cc} \end{pmatrix}\Bigg]\Bigg\}. \end{aligned}$$

Here we have identified p_{cc} as another well behaved quantity which just depends on the projection of the infinite environment onto the finite cluster. Finally we end up with

$$\begin{aligned} X =& \mathrm{Tr}\ln\left(-\mathrm{G}'_{ee}\right) + \mathrm{Tr}\ln\left(-\mathrm{G}_{cc}\right) + \\ &\mathrm{Tr}\ln\left\{\mathbb{1} + \begin{pmatrix} 0 & -\mathbb{1} \\ -p_{cc}\,\mathrm{G}_{cc} & +p_{cc}\,\mathrm{G}_{cc} \end{pmatrix}\right\}. \end{aligned}$$

The last term vanishes as we see as follows. With the abbreviation $a = p_{cc}\mathrm{G}_{cc}$ it reads

$$\mathrm{Tr}\ln\left\{\mathbb{1} + \begin{pmatrix} 0 & -\mathbb{1} \\ -a & a \end{pmatrix}\right\} = \ln\det\begin{pmatrix} \mathbb{1} & -\mathbb{1} \\ -a & \mathbb{1} + a \end{pmatrix}$$

We use a Schur complement type of decomposition by seeking an upper tridiagonal matrix which applied from the right eliminates the upper right block of the original matrix and only changes the lower right block. In the present case it reads

$$\begin{pmatrix} \mathbb{1} & -\mathbb{1} \\ -a & \mathbb{1} + a \end{pmatrix} \times \begin{pmatrix} \mathbb{1} & \mathbb{1} \\ 0 & \mathbb{1} \end{pmatrix} = \begin{pmatrix} \mathbb{1} & 0 \\ -a & \mathbb{1} \end{pmatrix}.$$

The inverse of a matrix

$$\begin{pmatrix} \mathbb{1} & F \\ 0 & \mathbb{1} \end{pmatrix}^{-1} = \begin{pmatrix} \mathbb{1} & -F \\ 0 & \mathbb{1} \end{pmatrix},$$

and we get

$$\begin{aligned} \ln\det\begin{pmatrix} \mathbb{1} & -\mathbb{1} \\ -a & \mathbb{1} + a \end{pmatrix} &= \ln\det\begin{pmatrix} \mathbb{1} & 0 \\ -a & \mathbb{1} \end{pmatrix} + \ln\det\begin{pmatrix} \mathbb{1} & -\mathbb{1} \\ 0 & \mathbb{1} \end{pmatrix} \\ &= 2\ln(1) = 0. \end{aligned}$$

Adding now the first two terms of equation eq. (2.23) the grand potential Ω is given by

$$\begin{aligned}
\Omega &= \Omega' - \mathrm{Tr}\ln\left(-G'_{ee}\right) - \mathrm{Tr}\ln\left(-G'_{cc}\right) \\
&\quad + \mathrm{Tr}\ln\left(-G'_{ee}\right) + \mathrm{Tr}\ln\left(-G_{cc}\right) + 0 \\
&= \Omega' - \mathrm{Tr}\ln\left(-G'_{cc}\right) + \mathrm{Tr}\ln\left(-G_{cc}\right) + 0 \\
&= \Omega' + \mathrm{Tr}\ln\left(r_{cc}\right) \\
&= \Omega' - \mathrm{Tr}\ln\left(\mathbb{1} - G'_{cc}\tilde{\Sigma}_{cc}\right), \\
\Sigma_{cc} &:= T_{cc} + T_{ce}G'_{ee}T_{ec}\,.
\end{aligned} \tag{C.7}$$

This shows that the infinite environment contributions drop out and we may use eq. (D.18) to obtain a finite value for the grand potential Ω.

D. Evaluation of the grand potential

The goal of this appendix is to find an expression for the grand potential Ω in terms of the Green's functions available in a CPT/VCA approach. The system we have in mind here is a fermionic cluster coupled to a formally infinite environment. The calculation done here in full detail follows [26] closely. Similar calculation for bosonic systems may be found in [52, 29]. The new aspect of this result is that it may be used for formally infinite systems.
The grand potential Ω for fermions can be cast into the form of eq. (2.23) [194, 68, 85]. Where G and G' are the CPT/VCA Green's function and the Green's function of the reference system respectively. Note that for Bosons the minus sign in front of G' and the plus sign in front of G are exchanged. The minus signs inside the logarithms are necessary to meet the convention for the branch cut of the complex logarithmic function in standard numerical methods. The trace Tr denotes a sum over Matsubara frequencies and a sum over lattice sites and spin which is denoted tr

$$Tr \equiv \frac{1}{\beta}\sum_{\omega_n} tr\,.$$

Here $\beta = \frac{1}{k_B T}$ is the inverse temperature. The fermionic Matsubara frequencies $w_n = \frac{(2n+1)\pi}{\beta}$ are defined as the poles of the Fermi-Dirac distribution function [30]

$$p_{FD}(z) = \frac{1}{e^{\beta z}+1}\,. \tag{D.1}$$

The Green's function G is given by

$$\mathrm{G} = \left(\mathbb{1} - \mathrm{G}'\mathrm{T}\right)^{-1}\mathrm{G}'\,, \tag{D.2}$$

within the CPT/VCA approximation. As shown in app. C the expression for Ω in eq. (2.23) is convergent also for the formally infinite reference system considered here. This means that the formally infinite matrices G' and T may be folded back to dimensions $L + c$, where L is the size of the cluster part of the reference system and c is the number of environment sites coupled to the cluster. Therefore we may rewrite the expression for the grand potential (eq. (2.23)) using the CPT/VCA approximation for G (eq. (D.2)) and obtain

$$\begin{aligned}\Omega &= \Omega' + \mathrm{Tr}\,\ln\left(\left(\mathbb{1} - \mathrm{G}'\mathrm{T}\right)^{-1}\right) + \mathrm{Tr}\,\ln\left(-\mathrm{G}'\right) - \mathrm{Tr}\,\ln\left(-\mathrm{G}'\right)\\ &= \Omega' - \mathrm{Tr}\,\ln\left(\mathbb{1} - \mathrm{G}'\mathrm{T}\right)\,.\end{aligned} \tag{D.3}$$

Our goal is to show that this trace is integrable and to cast it into a form which may be calculated efficiently numerically.
We start out by analyzing the asymptotic behavior of the second term in eq. (D.3) which we will refer to as I. Examining the trace

$$I = \mathrm{Tr}\,\ln\left(\mathbb{1} - \mathrm{G}'\mathrm{T}\right) = \frac{1}{\beta}\sum_{\omega_n}\mathrm{tr}\,\ln\left(\mathbb{1} - \mathrm{G}'\mathrm{T}\right)\,, \tag{D.4}$$

and knowing that

$$\mathrm{G}'(\omega) \overset{\omega\to\infty}{\longrightarrow} \frac{1}{\omega}\,,$$

we find that

$$\begin{aligned}\mathrm{tr}\,\ln\left(\mathbb{1} - \mathrm{G}'\mathrm{T}\right) &\overset{\omega\to\infty}{\longrightarrow} \mathrm{tr}\,\ln\left(1 - \frac{T}{\omega}\right)\\ &= \mathrm{tr}\,-\frac{\mathrm{T}}{\omega} - \frac{1}{2}\left(\frac{\mathrm{T}}{\omega}\right)^2 - O\left(\frac{\mathrm{T}}{\omega}\right)^3\\ &\approx -\frac{1}{\omega}\mathrm{tr}\,\mathrm{T} \propto \frac{1}{\omega}\,.\end{aligned}$$

Where we Taylor expanded the logarithm and we used that the matrix T is ω independent. Since the integral of $\frac{1}{\omega}$ diverges, one introduces a convergence factor $e^{i\omega_n 0^+}$.

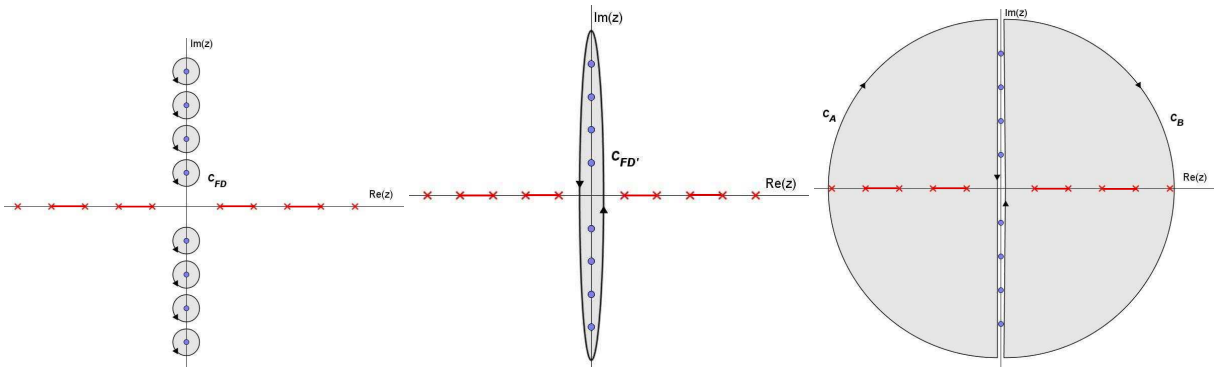

Figure D.1.: Deformation of the integration contour C_{FD} (left) to $C_{FD'}$ (middle). Note that in the process the contour is cut once at infinity and reconnected the other way round to end up with C_{AB} (right).

We are going to replace the sum over Matsubara frequencies by an integral using the residue theorem [195]

$$\oint_C f(z)dz = 2\pi i \sum_p \mathrm{Res}\left(f(z, z_p)\right) \ . \tag{D.5}$$

which is valid for any function f(z) which is meromorphic inside the region C. It was mentioned before that the poles of the Fermi-Dirac distribution eq. (D.1) are the fermionic Matsubara frequencies ω_n. We will now use a common trick from many body theory for sums like this [35, 196]. We construct a function $f(z)$ which has as residuals exactly the integrand we are looking for

$$\frac{1}{2\pi i}\frac{1}{\beta}\mathrm{tr}\,\ln\left(\mathbb{1} - \mathrm{G}'(\mathrm{z})\mathrm{T}\right)e^{z0^+} \ , \tag{D.6}$$

where the integration contour used encloses all poles of the Fermi-Dirac distribution C_{FD} (see figure D.1 (left)). Note that in this context the Fermi-Dirac distribution p_{FD} is sometimes called Matsubara weighing function [197]. Making an educated guess the function f(z) we are looking for is

$$f(z) = -\frac{1}{2\pi i}p_{FD}(z)\mathrm{tr}\,\ln\left(\mathbb{1} - \mathrm{G}'(\mathrm{z})\mathrm{T}\right)e^{z0^+} \ . \tag{D.7}$$

To show this we will calculate the residuals of eq. (D.7) with respect to the poles of the Fermi-Dirac distribution function and end up with eq. (D.6). The residuals are given by

$$\mathrm{Res}\left(f(z,\omega_n)\right) = -\frac{1}{2\pi i}\lim_{z\to\omega_n}\frac{z-\omega_n}{e^{\beta z}+1}\mathrm{tr}\,\ln\left(\mathbb{1} - \mathrm{G}'(\mathrm{z})\mathrm{T}\right)e^{z0^+} \ .$$

The numerator as well as the denominator go to zero in the limit $z \to \omega_n$. By using the theorem of Del'Hospital and differentiating the numerator and the denominator separately with respect to z we obtain

$$\begin{aligned}
\mathrm{Res}\left(f(z,\omega_n)\right) &= -\frac{1}{2\pi i\beta}\lim_{z\to\omega_n}\frac{1}{e^{\beta z}}e^{z0^+}\mathrm{tr}\,\ln\left(\mathbb{1} - \mathrm{G}'(\mathrm{z})\mathrm{T}\right) + \frac{1}{e^{\beta z}}\left(z-\omega_n\right)\left(\frac{\partial}{\partial z}e^{z0^+}\mathrm{tr}\,\ln\left(\mathbb{1} - \mathrm{G}'(\mathrm{z})\mathrm{T}\right)\right) \\
&= -\frac{1}{2\pi i\beta}\mathrm{tr}\,\ln\left(\mathbb{1} - \mathrm{G}'(\omega_n)\mathrm{T}\right)\frac{1}{e^{\beta\omega_n}}e^{\omega_n 0^+} \\
&= \frac{1}{2\pi i}\frac{1}{\beta}\mathrm{tr}\,\ln\left(\mathbb{1} - \mathrm{G}'(\omega_n)\mathrm{T}\right)e^{\omega_n 0^+} \ .
\end{aligned}$$

To end up at the last line we used that $e^{\beta\omega_n} = -1$. So far we replaced the sum over Matsubara frequencies by a complex contour integral and rendered the integral convergent by a convergence factor

$$I = -\frac{1}{2\pi i}\oint_{C_{FD}} dz\,\frac{1}{e^{\beta z}+1}\mathrm{tr}\,\ln\left(\mathbb{1} - \mathrm{G}'(z)\mathrm{T}\right)e^{z0^+} \ . \tag{D.8}$$

Note that the integrand has also poles along the real axis arising from $\mathrm{G}'(z)$.
To evaluate the integral we try to deform the integration contour into something more usable. Some

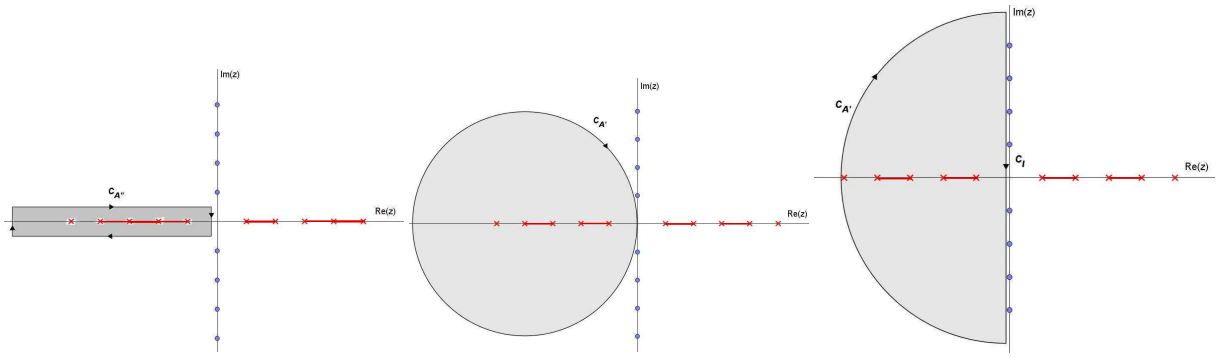

Figure D.2.: Three possible integration contours for the T=0 case. We use contour C_A which is depicted to the far right and can be split into two integrals $C_{A'}$ along an infinite semicircle and C_I along the imaginary axis from $+i\infty$ to $-i\infty$.

possibilities are shown in figure D.1. In some of the proposed contours the limits where cut at infinity and closed the other way round. Having in mind an integration contour C_{AB} like the one in figure D.1 (right), we are interested in the zero temperature result ($\beta \to \infty$). In this limit the Fermi-Dirac distribution goes to zero in the region B ($\mathrm{Re}(z) > 0$) as

$$\begin{aligned}\lim_{\beta\to\infty} \frac{1}{e^{\beta z}+1} &= \lim_{\beta\to\infty} \frac{1}{e^{\beta \mathrm{Re}(z)} e^{\beta \mathrm{Im}(z)}+1} \\ &= \frac{1}{e^{\infty \xi^2} e^{\infty \chi}+1} \to 0\,.\end{aligned}$$

It goes to one in the region A ($\mathrm{Re}(z) < 0$)

$$\begin{aligned}\lim_{\beta\to\infty} \frac{1}{e^{\beta z}+1} &= \lim_{\beta\to\infty} \frac{1}{e^{\beta \mathrm{Re}(z)} e^{\beta \mathrm{Im}(z)}+1} \\ &= \frac{1}{e^{-\infty \xi^2} e^{\infty \chi}+1} \to 1\,.\end{aligned}$$

For zero temperature we are therefore left with only the integration in the negative real half plane. Some possible integration contours are drawn in figure D.2. Choosing the contour C_A and splitting it into two contributions $C_{A'}$ and C_I (see figure D.2 (right)) we evaluate the integral along the infinite semicircle $C_{A'}$ first

$$\begin{aligned}I' &= -\frac{1}{2\pi i} \oint_{C_{A'}} dz\, \frac{1}{e^{\beta z}+1} \mathrm{tr}\, \ln\left(\mathbb{1} - \mathrm{G}'(z)\mathrm{T}\right) e^{z0^+} \\ &= \lim_{R\to\infty} -\frac{1}{2\pi i} \int_{\frac{3}{2}\pi}^{\frac{1}{2}\pi} d\phi\, iRe^{i\phi} \mathrm{tr}\, \ln\left(\mathbb{1} - \mathrm{G}'(Re^{i\phi})\mathrm{T}\right) e^{iRe^{i\phi}0^+}\,.\end{aligned}$$

Where in the integral the substitution $z = \lim_{R\to\infty} Re^{i\phi}$ was done. For large arguments we know that the Green's function G' behaves like $\frac{1}{\omega}$ so we can proceed with

$$\begin{aligned}I' &= -\frac{1}{2\pi} \lim_{R\to\infty} R \int_{\frac{3}{2}\pi}^{\frac{\pi}{2}} d\phi\, e^{i\phi} \mathrm{tr}\, \ln\left(\mathbb{1} - \frac{\mathrm{T}}{Re^{i\phi}}\right) e^{iRe^{i\phi}0^+} \\ &= -\frac{1}{2\pi} \lim_{R\to\infty} R \int_{\frac{3}{2}\pi}^{\frac{\pi}{2}} d\phi\, e^{i\phi} \mathrm{tr}\, -\frac{\mathrm{T}}{Re^{i\phi}} e^{iRe^{i\phi}0^+} \\ &= -\frac{\mathrm{tr}\, T}{2\pi} \lim_{R\to\infty} \int_{\frac{\pi}{2}}^{\frac{3}{2}\pi} d\phi\, e^{iRe^{i\phi}0^+}\,.\end{aligned}$$

From the first to the second line the logarithm was expanded. Next we try to find an estimate for the upper bound of the absolute value of this integral

$$\begin{aligned}
\left| \int_{\frac{\pi}{2}}^{\frac{3}{2}\pi} d\phi \, e^{iRe^{i\phi}0^+} \right| &= \left| \int_{\frac{\pi}{2}}^{\frac{3}{2}\pi} d\phi \, e^{iR(\cos\phi + i\sin\phi)0^+} \right| \\
&\leq \int_{\frac{\pi}{2}}^{\frac{3}{2}\pi} d\phi \left| e^{-R\sin\phi 0^+} \right| \\
&\approx \int_0^{\frac{\pi}{2}} d\phi \left| e^{-\frac{2}{\pi}R\phi 0^+} \right| \\
&= \left| -\frac{\pi}{2R0^+} e^{-\frac{2}{\pi}R\phi 0^+} |_0^{\frac{\pi}{2}} \right| \\
&= \left| \frac{\pi}{2R0^+} \left(1 - e^{-R0^+} \right) \right| . \qquad \text{(D.9)}
\end{aligned}$$

As one can see eq. (D.9) goes to zero for $R \to \infty$ and therefore the integral I′ vanishes. Note that the limit R to infinity has to be executed before the limit 0^+ to zero. The only part of the integral which contributes to I is

$$I = -\frac{1}{2\pi i} \oint_{C_I} dz \, \mathrm{tr} \ln \left(\mathbb{1} - \mathrm{G}'(\mathrm{z})\mathrm{T} \right) e^{z0^+} , \qquad \text{(D.10)}$$

where the contour C_I runs along the imaginary axis from $+i\infty$ to $-i\infty$.
At evaluating the integral numerically the convergence factor e^{z0^+} is very unpleasant. The next step is to get rid of it. We will add to the integrand a function r(z) which has only poles on the outside of the integration contour. These are chosen to lie on the positive real axis in our approach. Furthermore r(z) should behave like $\frac{1}{\omega}$ in the limit $\omega \to \infty$ to cancel the $-\frac{1}{\omega}$ behavior of the integrand. Such a function r(z) may be chosen to be

$$r(z) = \frac{\mathrm{tr}\,\mathrm{T}}{z - \rho} , \qquad \text{(D.11)}$$

where ρ is a large positive real number. The expression for I takes the form

$$I = -\frac{1}{2\pi i} \oint_{C_I} dz \underbrace{\mathrm{tr} \ln \left(\mathbb{1} - \mathrm{G'(z)T} \right) + \frac{\mathrm{T}}{z - \rho}}_{\propto \frac{1}{\omega^2}} . \qquad \text{(D.12)}$$

The added term $r(z)$ will not contribute to the integral as the poles lie outside the region of integration but it will render the integral convergent because the expression within the trace now goes like $\frac{1}{\omega^2}$ as compared to the $\frac{1}{\omega}$ before. Therefore the convergence factor may be dropped.
It is possible to further rewrite the integral using the property of retarded Green's functions

$$\mathrm{G}(-i\omega) = \mathrm{G}^*(i\omega) ,$$

which also holds true for the function r(z). The resulting integral

$$\begin{aligned}
I &= -\frac{1}{2\pi i} \int_{+i\infty}^{-i\infty} d\omega \, \mathrm{tr} \ln \left(\mathbb{1} - \mathrm{G}'(\omega)\mathrm{T} \right) + \frac{\mathrm{T}}{\omega - \rho} \\
&= \frac{1}{2\pi i} \int_{-\infty}^{+\infty} i d\omega \, \mathrm{tr} \ln \left(\mathbb{1} - \mathrm{G}'(i\omega)\mathrm{T} \right) + \frac{\mathrm{T}}{i\omega - \rho} \\
&= \frac{1}{2\pi} (\int_{-\infty}^{0} d\omega \, \mathrm{tr} \ln \left(\mathbb{1} - \mathrm{G}'(i\omega)\mathrm{T} \right) + \frac{\mathrm{T}}{i\omega - \rho} \\
&+ \int_0^{+\infty} d\omega \, \mathrm{tr} \ln \left(\mathbb{1} - \mathrm{G}'(i\omega)\mathrm{T} \right) + \frac{\mathrm{T}}{i\omega - \rho}) \\
&= \frac{1}{2\pi} (\int_0^{\infty} d\omega \, \mathrm{tr} \ln \left(\mathbb{1} - \mathrm{G}'(-i\omega)\mathrm{T} \right) + \frac{\mathrm{T}}{-i\omega - \rho} \\
&+ \int_0^{+\infty} d\omega \, \mathrm{tr} \ln \left(\mathbb{1} - \mathrm{G}'(i\omega)\mathrm{T} \right) + \frac{\mathrm{T}}{i\omega - \rho}) \\
&= \frac{1}{2\pi} \int_0^{\infty} d\omega \, \mathrm{tr} \ln \left(\mathbb{1} - \mathrm{G}'(i\omega)\mathrm{T} \right) + \frac{\mathrm{T}}{i\omega - \rho} + \mathrm{cc} . \qquad \text{(D.13)}
\end{aligned}$$

The integration variable ω was once implicitly negated in this process.
The integral over $r(\omega) + \mathrm{cc}$ may be evaluated having in mind the form of T (see figure D.3)

$$\begin{aligned}
\frac{1}{2\pi}\int_0^\infty d\omega \,\mathrm{tr}\,\frac{\mathrm{T}}{i\omega-\rho}+\frac{\mathrm{T}}{-i\omega-\rho} &= \frac{1}{2\pi}\mathrm{tr}\,\mathrm{T}\int_0^\infty d\omega\,\frac{1}{i\omega-\rho}-\frac{1}{i\omega+\rho}\\
&= \frac{1}{2\pi}\mathrm{tr}\,\mathrm{T}\,(-2\rho)\int_0^\infty d\omega\,\frac{1}{\omega^2+\rho^2}\\
&= -\frac{1}{\pi}\mathrm{tr}\,\mathrm{T}\rho\frac{1}{\rho}\arctan\left(\frac{\omega}{\rho}\right)|_0^\infty\\
&= -\frac{1}{\pi}\mathrm{tr}\,\mathrm{T}\left(\frac{\pi}{2}-0\right)\\
&= -\frac{\mathrm{tr}\,\mathrm{T}}{2}\\
&= -L\Delta\mu\,, \qquad \text{(D.14)}
\end{aligned}$$

where $\Delta\mu$ is the on-site part of T. The trace of T is given by $\mathrm{tr}\,\mathrm{T} = 2L\Delta\mu$ for homogeneous systems, where the factor 2 is due to spin. Here L is the size of the reference system. The value $\Delta\mu$ is the difference of the chemical potential of the reference system to the variational chemical potential in VCA.
Putting everything together we obtain

$$\begin{aligned}
I &= -L\Delta\mu+\frac{1}{2\pi}\int_0^\infty d\omega\,\mathrm{tr}\,\ln\left(\mathbb{1}-\mathrm{TG}'(i\omega)\right)+\mathrm{cc}\\
&= -L\Delta\mu+\frac{1}{2\pi}\int_0^\infty d\omega\,\mathrm{tr}\,2\Re\mathrm{e}\left(\ln\left(\mathbb{1}-\mathrm{TG}'(i\omega)\right)\right)\\
&= -L\Delta\mu+\frac{1}{\pi}\sum_\sigma\int_0^\infty d\omega\ln\left|\det\left(\mathbb{1}-\mathrm{TG}'_{\sigma\sigma}(i\omega)\right)\right|\,. \qquad \text{(D.15)}
\end{aligned}$$

A numerical convergence analysis for integrals of this kind is undertaken in [26]. There it is shown that the convergence is in general very good. The method used to evaluate eq. (D.15) is a Gauss-Legendre integration. The region of integration from zero to infinity is split into three regions. Region one with about twenty points on the interval $[0, \Lambda_1)$ where Λ_1 is the low energy scale of the problem (i.e. the smallest eigenvalue of the hamiltonian, up to some minimum). Region two with about twenty points on the interval $[\Lambda_1, \Lambda_2)$ where Λ_2 is the high energy scale of the problem (i.e. the largest eigenvalue of the hamiltonian up to some maximum). Region three on the interval $[\Lambda_2, \infty)$ where in the integrand one substitutes $u = \frac{1}{\omega}$ and integrates from 0 to Λ_2^{-1}:

$$\frac{1}{\pi}\int_0^{\frac{1}{\Lambda_2}} d\omega\,\omega^{-2}\ln\left|\det\left(\mathbb{1}-\mathrm{TG}'(\frac{i}{\omega})\right)\right|\,. \qquad \text{(D.16)}$$

The integrand vanishes very fast for large arguments and so the contributions from the third region are small.
Finally putting everything together the expression for the grand potential at zero temperature is

$$\begin{aligned}
\Omega &= \Omega' - I\\
&= \omega_0' + \mathrm{tr}\,\mathrm{T} - \frac{1}{\pi}\sum_\sigma\int_0^\infty d\omega\ln\left|\det\left(\mathbb{1}-\mathrm{TG}'_{\sigma\sigma}(i\omega)\right)\right| \qquad \text{(D.17)}\\
&= \omega_0' + L\Delta\mu - \frac{1}{\pi}\sum_\sigma\int_0^\infty d\omega\ln\left|\det\left(\mathbb{1}-\mathrm{TG}'_{\sigma\sigma}(i\omega)\right)\right|\,. \qquad \text{(D.18)}
\end{aligned}$$

To round this discussion up, some interesting comments follow. Note that $\det\left(\mathbb{1}-\mathrm{G}'(i\omega)\mathrm{T}\right) = \det\left(\mathbb{1}-\mathrm{TG}'(i\omega)\right)$ due to Sylvester's theorem. The trace in expression D.18 still includes spin. For systems where the different spins do not couple and G_σ is calculated for one spin σ only a factor 2 may replace the sum over σ. As test for the correct implementation may serve the fact that for non-interacting systems the grand potential has to be a constant in all variational parameters. This arises from the fact that whatever values are chosen for the variational parameters, CPT/VCA yields the exact result. Equation D.18 also permits to see very easily why the noninteracting infinite system will not cause this grand potential to diverge. A full proof for this fact is given in app. C. Consider an infinite noninteracting lead coupled to a finite interacting cluster. The lead part in the Green's function G' will be diagonal and occupy the block of G' from index $L+1$ to ∞. Note also the matrix T (which is now also infinite) will maintain its form (see figure D.3). The matrix $\mathbb{1}-\mathrm{G}'\mathrm{T}$ will be in general a full matrix in the block $[1, L+2]$ if two leads are

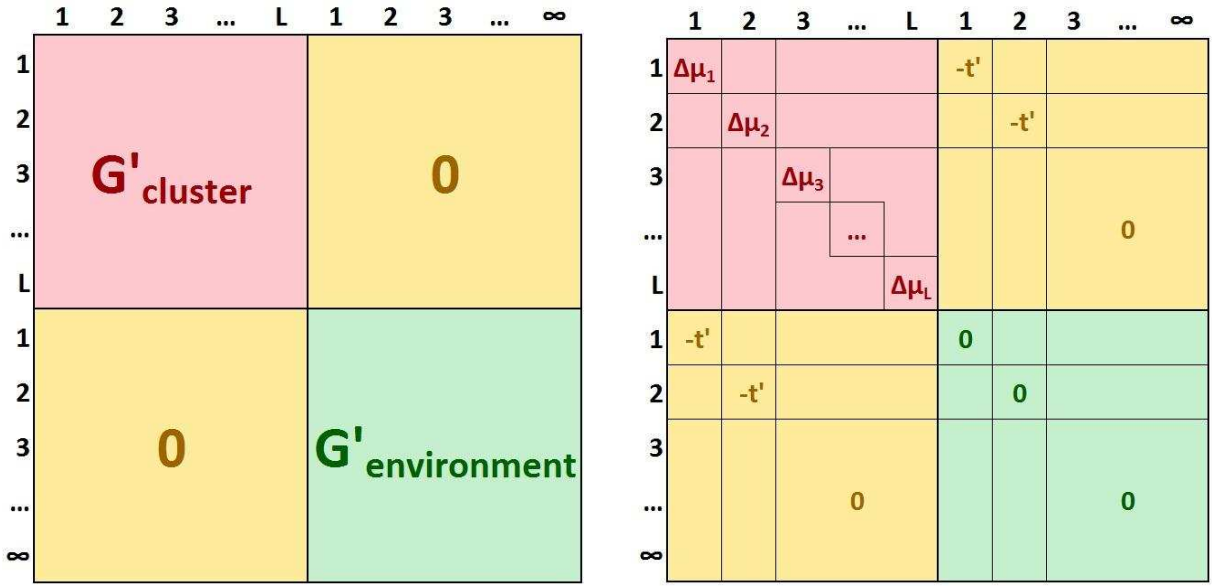

Figure D.3.: Generic form of the matrix representation of the cluster Green's function G' (left) and the inter-cluster hopping matrix T (right).

coupled to the cluster or $[1, L+1]$ if one lead is coupled to the cluster. It will have ones in the diagonal from $[L+2, \infty]$ or $[L+1, \infty]$ and no further off diagonal elements. So taking the log (which is a matrix logarithm) and then the trace will be finite (only zeros will be added up for the infinite non interacting system). This arises of course from the fact that just a finite number of sites of the environment are coupled to the cluster.

E. Obtaining the matrix Green's function from the Green's function of the correlated site

A general procedure for obtaining all elements of the interacting cluster Green's function G'_{ij} from the Green's function of the interacting site G'_{ff} (which has to be obtained exactly by some method beforehand for a system of length L) and the matrix Green's function of a free chain of length $L-1$ $G'_{ss'}$, $s, s' \in [1, ..., L-1]$ is outlined here. A similar discussion using T-matrix representation in **k**-space is given in ref. [198]. We discuss the special case of a single impurity at the far end of a non-interacting chain, but the method is applicable to systems with a finite number of impurities and the generalization is straight forward. The advantage provided by this method is that in any calculation only the local impurity Green's function needs to be calculated. From this Green's function the local Green's function on every other site as well as the off-diagonal terms may be reconstructed.
The $L \times L$ cluster Green's function G'_{ij} is built up successively by making use of the equation of motion method which results in a Dyson-like equation. We start out by creating the block diagonal uncoupled Green's function G'^0_{ij}, where $G'^0_{11} = G'_{ff}$ and $G'^0_{ij} = G'_{ss'}$, $i, j \in [2, ..., L]$. Then one proceeds by obtaining the cluster Green's function by

$$G'_{ij} = G'^0_{ij} + G'^0_{i\alpha} T_{\alpha\beta} G'_{\beta j} \, .$$

Here $T_{\alpha\beta}$ has just an entry $-V$ for the coupling of the impurity to the first site of the chain and the hermitian conjugate. Therefore the equation reduces to

$$\begin{aligned} G'_{ij} &= G'^0_{ij} + G'^0_{i1} T_{12} G'_{2j} + G'^0_{i2} T_{21} G'_{1j} \\ &= G'^0_{ij} - V \left(G'^0_{i1} G'_{2j} + G'^0_{i2} G'_{1j} \right) \, . \end{aligned} \tag{E.1}$$

This looks like an ordinary CPT coupling of an isolated impurity to the first site of some other system. However in this context there is a major difference! The Green's function of the impurity G'_{ff} was already obtained for the specific system of length L under consideration. So we merely reconstruct the other matrix elements, which is exact! It is important to note that we have to proceed iteratively and not by a matrix operation:

1. One starts out at the impurity setting $G'_{11} = G'^0_{11} = G'_{ff}$.

2. Then one may calculate G'_{i1}, $i \in [2, ..., L]$ by eq. (E.1):

$$\begin{aligned} G'_{i1} &= G'^0_{i1} - V \left(G'^0_{i1} G'_{21} + G'^0_{i2} G'_{11} \right) \\ &= -V G'^0_{i2} G'_{11} \, . \end{aligned}$$

   Note that the index for i starts at 2, so the element $1,1$ which was set in the before, is not touched! The elements of G of the first row and first column are therefore built up from the impurity Green's function G'_{ff} and the Green's functions of a tight-binding chain with open boundary conditions G'^0_{i2}. Since G' is symmetric $G'_{1i} = G'_{i1}$.

3. Then one may proceed and calculate the diagonal elements G'_{ii}, $i \in [2, ..., L]$ by eq. (E.1):

$$G'_{ii} = G'^0_{ii} - V G'^0_{ii} G'_{1i} \, .$$

4. From here on all missing off diagonal elements are calculated in the same fashion using eq. (E.1). Starting at calculating G'_{i2}, then G'_{i3} up to G'_{iL} always not touching previously calculated elements.

To illustrate the procedure a short outline of the corresponding algorithm is helpful:

```
#Obtain Green's functions of tight binding chain and impurity site
G_ff ← Calculate the local impurity Green's function for a SIAM of length L
G_chain ← Calculate the matrix Green's function for a tight binding model of length L − 1
#Initialize G^0
G^0_11 ← G_ff
G^0_(2:L,2:L) = G_chain
#Obtain G
G_11 ← G^0_11
for j = 1 → L do
  for i = j → L do
    if !((i ==1)&&(j==1)) then
      G_ij ← G^0_ij − V G^0_i1 G_2j − V G^0_i2 G_1j
      G_ji ← G_ij
    end if
  end for
end for
```

F. Mapping a one dimensional chain to effective higher dimensions

Consider a single correlated orbital at the far end of a semi-infinite chain which is one possible realization of the single impurity Anderson model

$$\begin{aligned}\hat{\mathcal{H}} = -\epsilon_f \sum_\sigma f^\dagger_{i\sigma} f_{i\sigma} \quad + U\hat{n^f_\uparrow} n^f_\downarrow - V \sum_\sigma \left(f^\dagger_\sigma c_{i\sigma} + f_{i\sigma} c^\dagger_\sigma\right) \\ - t \sum_{<ij>\sigma} c^\dagger_{i\sigma} c_{j\sigma} \quad - \mu \sum_{i\sigma} c^\dagger_{i\sigma} c_{i\sigma}\end{aligned}$$

The non-interacting semi-infinite one dimensional chain will generate a semi-circular local density of states at the impurity site. For this special setup it is however possible to renormalize the hopping parameters in the chain and obtain a model for an impurity embedded in higher dimensions. Note that after this renormalization the sites of the chain cannot be identified with real orbitals any more but act as an auxiliary bath which produces the desired density of states in the impurity. To obtain the renormalized hoppings we apply a Lanczos procedure where we consider hopping from a central impurity. For the Lanczos procedure we identify the starting vector $|v_0\rangle = |1\rangle$ the impurity site. Normalized vectors will always be denoted as $|v\rangle$ while for unnormalized ones $\widetilde{|v\rangle}$ will be used. The construction procedure now consists of successive single particle hopping out of the impurity

$$\begin{aligned}\widetilde{|v_{n+1}\rangle} &= \hat{\mathcal{H}}\,|v_n\rangle - \epsilon_n\,|v_n\rangle - \beta_n\,|v_{n-1}\rangle \\ \epsilon_n &= \langle v_n|\,\hat{\mathcal{H}}\,|v_n\rangle \\ \beta_n &= \sqrt{\widetilde{\langle v_n|}\widetilde{|v_n\rangle}} = \widetilde{\langle v_n|}\,v_n\rangle \\ |v_{n+1}\rangle &= \frac{\widetilde{|v_{n+1}\rangle}}{\sqrt{\widetilde{\langle v_{n+1}|}}}\,,\end{aligned}$$

which leads to a tridiagonal form of the Hamiltonian

$$\begin{pmatrix} \epsilon_0 & \beta_1 & 0 & 0 & ... \\ \beta_1 & \epsilon_1 & \beta_2 & 0 & ... \\ 0 & \beta_2 & \epsilon_2 & \beta_3 & ... \\ 0 & 0 & \beta_3 & \epsilon_3 & ... \\ ... & ... & ... & ... & ... \end{pmatrix}.$$

F.0.1. Mapping a semi-infinite one dimensional chain to a two dimensional model

Here we build up the renormalized hopping parameters considering one Manhattan distance after the other. Each site is labeled by its Manhattan distance and an arbitrary index (see fig. F.1).

1. **Manhattan distance 0**

$$\begin{aligned}\widetilde{|v_0\rangle} &= |0,1\rangle \\ |v_0\rangle &= |0,1\rangle\end{aligned}$$

2. **Manhattan distance 1**
   We would like to find the first iteration Krylov vectors

$$\widetilde{|v_1\rangle} = \hat{\mathcal{H}}\,|v_0\rangle - \epsilon_0\,|v_0\rangle - \beta_0\,|v_{-1}\rangle\,.$$

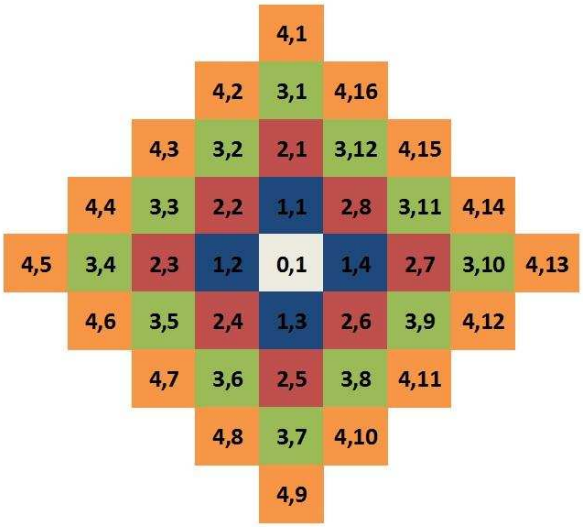

Figure F.1.: Hopping to a two dimensional bath. The impurity is located in the center. Each site is labeled by its Manhattan distance and an arbitrary index.

Therefore we evaluate the action of the Hamiltonian onto the impurity

$$\begin{aligned}\hat{\mathcal{H}}\,|v_0\rangle &= -\epsilon\,|1\rangle - V\left(|1,1\rangle + |1,2\rangle + |1,3\rangle + |1,4\rangle\right)\\ &= -\epsilon\,|1\rangle - V\left\{|1,\mathbf{X}\rangle\right\}\ ,\end{aligned}$$

$\{|1,\mathbf{X}\rangle\}$ is short for a weighed sum over all orbitals within Manhattan distance one. Furthermore we evaluate

$$\begin{aligned}\epsilon_0 &= \langle v_0|\,\hat{\mathcal{H}}\,|v_0\rangle = -\epsilon\\ \beta_0 &= \sqrt{\widetilde{\langle v_0|}\widetilde{|v_0\rangle}} = 1\ .\end{aligned}$$

Plugging this back into the equation for $\widetilde{|v_1\rangle}$ we get

$$\begin{aligned}\tilde{|v_1\rangle} &= -\epsilon\,|1\rangle - V\left\{|0,\mathbf{X}\rangle\right\} - (-\epsilon)\,|v_0\rangle - 1 * 0\\ &= -V\left\{|1,\mathbf{X}\rangle\right\}\ .\end{aligned}$$

The norm of $\widetilde{|v_1\rangle}$ is given by

$$\widetilde{\langle v_1|}\widetilde{|v_1\rangle} = (-V)(1+1+1+1)(-V) = 4V\ .$$

So we end up with the normalized vector

$$|v_1\rangle = -\frac{1}{\sqrt{4}}\left\{|1,\mathbf{X}\rangle\right\}\ .$$

3. **Manhattan distance 2**
   We proceed by calculating the second iteration vector

$$\tilde{|v_2\rangle} = \hat{\mathcal{H}}\,|v_1\rangle - \epsilon_1\,|v_1\rangle - \beta_1\,|v_0\rangle\ .$$

The action of the Hamiltonian onto $|v_1\rangle$ is given by

$$\begin{aligned}\hat{\mathcal{H}}|v_1\rangle &= -\frac{1}{\sqrt{4}}\Big(-\mu|1,\mathbf{X}\rangle - 4V|0,1\rangle \\ &\quad - t\left(|2,1\rangle + |2,2\rangle + |2,8\rangle + |2,2\rangle + |2,3\rangle + |2,4\rangle + |2,4\rangle + |2,5\rangle + |2,6\rangle + |2,6\rangle + |2,7\rangle + |2,8\rangle\right)\Big) \\ &= \frac{1}{\sqrt{4}}\Big(\mu|1,\mathbf{X}\rangle + 4V|0,1\rangle + t|2,\mathbf{X}\rangle\Big),\end{aligned}$$

where

$$|2,\mathbf{X}\rangle = \left(|2,1\rangle + 2|2,2\rangle + |2,3\rangle + 2|2,4\rangle + |2,5\rangle + 2|2,6\rangle + |2,7\rangle + 2|2,8\rangle\right) .$$

Furthermore we evaluate

$$\begin{aligned}\epsilon_1 &= \langle v_1|\hat{\mathcal{H}}|v_1\rangle = -\frac{1}{\sqrt{4}}\langle 1,\mathbf{X}|\frac{1}{\sqrt{4}}\mu|1,\mathbf{X}\rangle = \frac{\mu}{4}\left(1^2+1^2+1^2+1^2\right) = -\mu \\ \beta_1 &= \sqrt{\widetilde{\langle v_1|v_1\rangle}} = 2V .\end{aligned}$$

Plugging this into the expression for $\widetilde{|v_2\rangle}$ we get

$$\begin{aligned}|\tilde{v_2}\rangle &= \frac{1}{\sqrt{4}}\Big(\mu|1,\mathbf{X}\rangle + 4V|0,1\rangle + t|2,\mathbf{X}\rangle\Big) - (-\mu) - \frac{1}{\sqrt{4}}\{|1,\mathbf{X}\rangle\} - 2V|0,1\rangle \\ &= \frac{t}{\sqrt{4}}|2,\mathbf{X}\rangle .\end{aligned}$$

The norm of $\widetilde{|v_2\rangle}$ is given by

$$\widetilde{\langle v_2|v_2\rangle} = \frac{t}{\sqrt{4}}(1+2^2+1+2^2+1+2^2+1+2^2)\frac{t}{\sqrt{4}} = 5t^2 .$$

So we end up with the normalized vector

$$|v_2\rangle = \frac{1}{\sqrt{20}}|2,\mathbf{X}\rangle ,$$

4. **Manhattan distance 3**
The third Lanczos vector is given by

$$|\tilde{v_3}\rangle = \hat{\mathcal{H}}|v_2\rangle - \epsilon_2|v_2\rangle - \beta_2|v_1\rangle .$$

The action of the Hamiltonian onto $|v_2\rangle$ is given by

$$\begin{aligned}
\hat{\mathcal{H}}|v_2\rangle &= \frac{1}{\sqrt{20}}\left(-\mu|2,\mathbf{X}\rangle - t\sum_{<ij>} c_i^\dagger c_j |2,\mathbf{X}\rangle\right) \\
&= \frac{1}{\sqrt{20}}\Bigg(-\mu|2,\mathbf{X}\rangle - t\Bigg(|1,1\rangle + 2|1,1\rangle + 2|1,2\rangle + |1,2\rangle + 2|1,2\rangle + 2|1,3\rangle + |1,3\rangle + 2|1,3\rangle \\
&\quad + 2|1,4\rangle + |1,4\rangle + 2|1,4\rangle + 2|1,1\rangle\Bigg) \\
&\quad - t\Bigg(|3,1\rangle + |3,2\rangle + |3,12\rangle + 2|3,2\rangle + 2|3,3\rangle + |3,3\rangle + |3,4\rangle + |3,5\rangle + 2|3,5\rangle + 2|3,6\rangle + |3,6\rangle \\
&\quad + |3,7\rangle + |3,8\rangle + 2|3,8\rangle + 2|3,9\rangle + |3,9\rangle + |3,10\rangle + |3,11\rangle + 2|3,11\rangle + 2|3,12\rangle\Bigg)\Bigg) \\
&= \frac{1}{\sqrt{20}}\Bigg(-\mu|2,\mathbf{X}\rangle - 5t|1,\mathbf{X}\rangle - t|3,\mathbf{X}\rangle\Bigg),
\end{aligned}$$

with

$$|3,\mathbf{X}\rangle = (|3,1\rangle + 3|3,2\rangle + 3|3,3\rangle + |3,4\rangle + 3|3,5\rangle + 3|3,6\rangle + |3,7\rangle + 3|3,8\rangle + 3|3,9\rangle + |3,10\rangle + 3|3,11\rangle + 3|3,12\rangle) \ .$$

Furthermore we evaluate

$$\begin{aligned}
\epsilon_2 &= \langle v_2|\hat{\mathcal{H}}|v_2\rangle = \frac{1}{\sqrt{20}}\langle 2,\mathbf{X}|\frac{1}{\sqrt{20}} - \mu|2,\mathbf{X}\rangle = \frac{-\mu}{20}(20) = -\mu \\
\beta_2 &= \sqrt{\widetilde{\langle v_2|}\widetilde{|v_2\rangle}} = \sqrt{5}t \ .
\end{aligned}$$

Plugging this into the expression for $\widetilde{|v_3\rangle}$ we get

$$\tilde{|v_3\rangle} = -\frac{t}{\sqrt{20}}|3,\mathbf{X}\rangle \ .$$

The norm of $\widetilde{|v_3\rangle}$ is given by

$$\widetilde{\langle v_3|}\widetilde{|v_3\rangle} = \frac{-t}{\sqrt{20}}(4+72)\frac{-t}{\sqrt{20}} = \sqrt{\frac{76}{20}}t^2 \ .$$

So we end up with the normalized vector

$$|v_2\rangle = -\frac{1}{\sqrt{76}}|3,\mathbf{X}\rangle \ .$$

5. **Manhattan distance 4**
The fourth Lanczos iteration vector is given by

$$\tilde{|v_4\rangle} = \hat{\mathcal{H}}|v_3\rangle - \epsilon_3|v_3\rangle - \beta_3|v_2\rangle \ .$$

The action of the Hamiltonian onto $|v_3\rangle$ is given by

$$\begin{aligned}
\hat{\mathcal{H}}|v_3\rangle &= -\frac{1}{\sqrt{76}}\left(-\mu|3,\mathbf{X}\rangle - t\sum_{<ij>} c_i^\dagger c_j |3,\mathbf{X}\rangle\right) \\
&= \frac{1}{\sqrt{76}}\Bigg(\mu|3,\mathbf{X}\rangle - t\Bigg(\text{terms involving } |2,i\rangle \text{ and terms involving } |4,i\rangle\Bigg),
\end{aligned}$$

where the hopping terms $|2,i\rangle$ and $|4,i\rangle$ can not be written as $\alpha|2,\mathbf{X}\rangle + \beta|4,\mathbf{X}\rangle$. Therefore these terms will not cancel with the expressions coming from $\epsilon_3|v_3\rangle$ and $\beta_3|v_2\rangle$ like in the previous cases. This makes it hardly possible to continue analytically (see fig. 5).

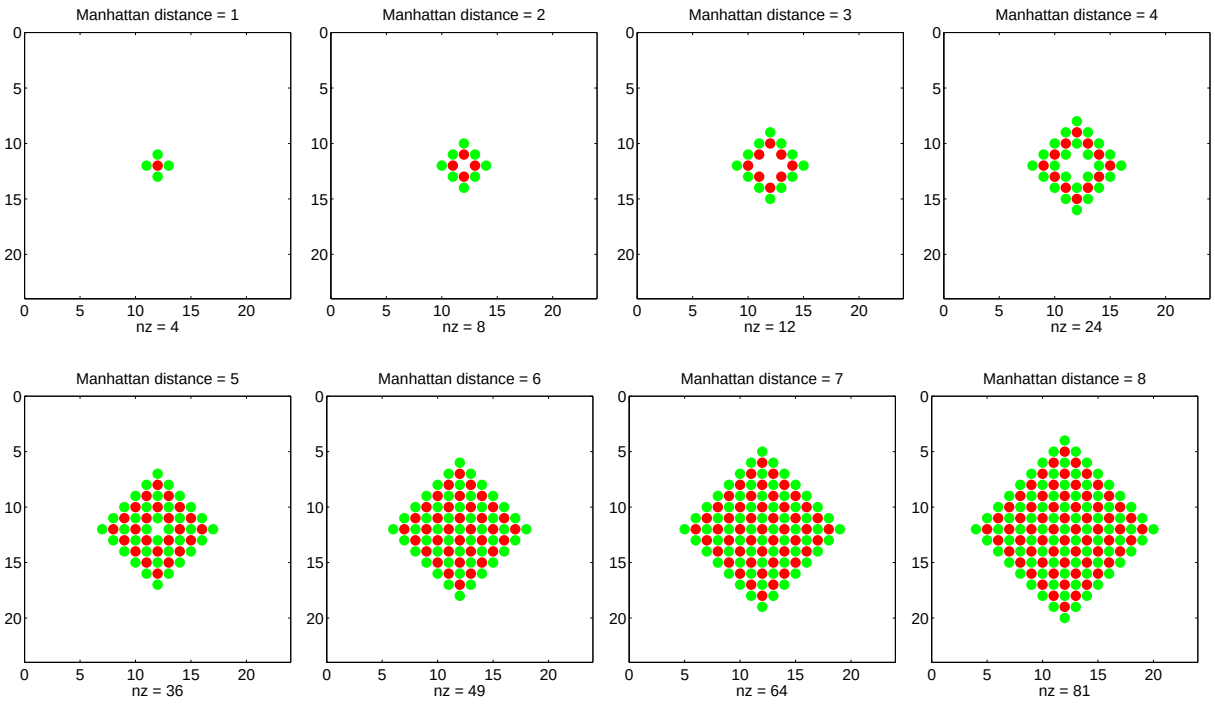

Figure F.2.: Evolution of the sites affected in a certain Manhattan distance in the Lanczos procedure for the mapping of a one dimensional chain to an effective two dimensional model. The red dots indicate the current starting vector superposition. The green dots denote the states contributing at the application of the Hamiltonian. Note that for a Manhattan distance <= 3, a nice 'hopping' outwards takes place, while for distances >= 4 hopping inside and outside takes place making the analytic evaluation of the coefficients not feasible.

F.0.2. Mapping a semi-infinite one dimensional chain to a three dimensional model

The procedure for the mapping to a three-dimensional model is completely analogous to the two-dimensional case and will not be outlined in detail at this point.

F.0.3. Numerical results for two and three dimensions

A numerical evaluation of the iteration however is easily feasible. The rescaled hopping coefficients

$$t(i) = c_i\, t\ ,$$

are displayed in fig. F.0.3 for the mapping to a two-dimensional model (left) and a three-dimensional model (right) and are listed in tab. F.1. The calculation of the rescaled hopping parameters becomes more and more demanding and time consuming with increasing distance from the impurity. For the two-dimensional mapping the coefficients alternate in sign and the two branches may be extrapolated separately with very high accuracy

$$\begin{aligned} c_1 &= 2 \\ c_{2l} &= \frac{1.999999087638(2l)^2 + 3.666362617826(2l) - 1.616035541467}{(2l)^2 + 1.799469717153(2l) - 0.988115961204} \quad \ldots\ l = [1,2,3,\ldots] \\ c_{2l+1} &= \frac{2.000306397205(2l)^2 + 4.968914151507(2l) + 4.012272194344}{(2l)^2 + 2.521186264485(2l) + 2.112147532948} \quad \ldots\ l = [1,2,3,\ldots]\ . \end{aligned}$$

For the three-dimensional case an extrapolation is more difficult because of the erratic behavior of the coefficients. It is however sufficient to use the first twenty or so coefficients and set the rest to the asymptotic value $c_\infty = 3$.
The resulting local density of states at the correlated site $\rho_f(\omega)$ may be evaluated using a continued

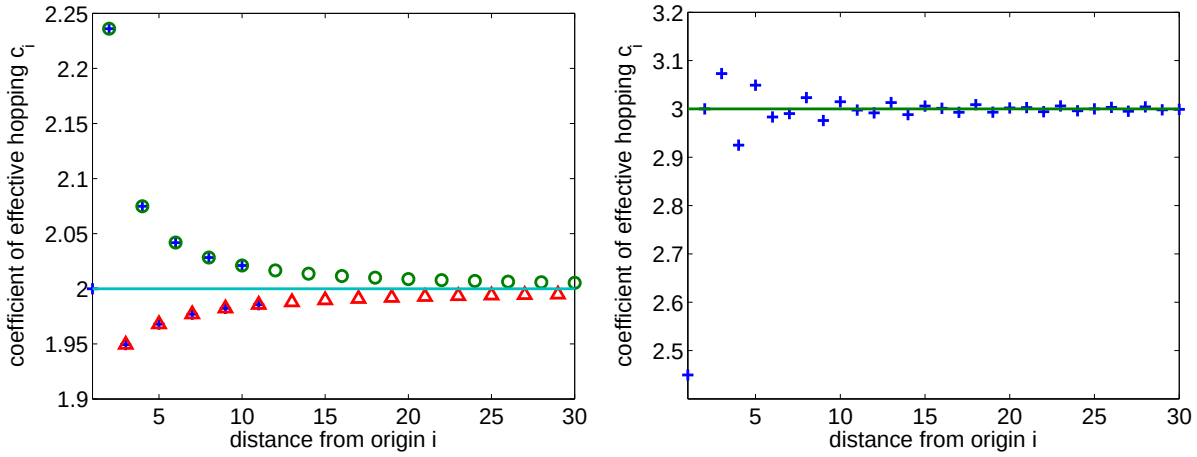

Figure F.3.: Effective hopping coefficients c_i for mapping a chain to two dimensions (left) and to three dimensions (right).

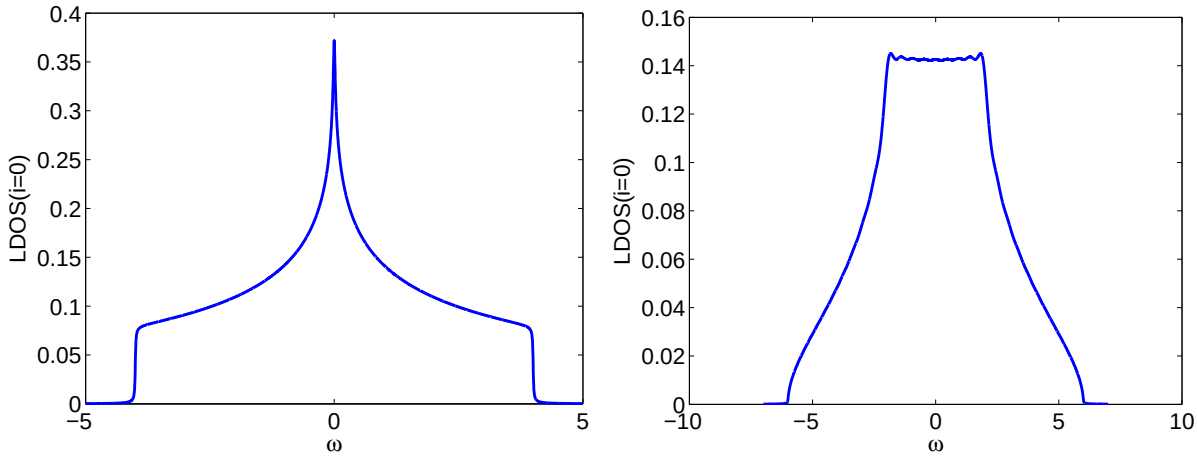

Figure F.4.: Effective local density of states at the interacting site using the coefficients c_i for mapping a chain to two dimensions (left) and to three dimensions (right). The model parameters used were $U = 0$, $t = 1$, $V = 1$.

fraction representation of the Green's function

$$\rho_f\omega = -\frac{1}{\pi}\left(\frac{1}{\omega^+ - \epsilon_f - \frac{(c_1V)^2}{\omega^+-\epsilon_- - \frac{(c_2t)^2}{\omega^+-\epsilon_- - \frac{(c_3t)^2}{\omega^+-\epsilon_-\ldots}}}}\right).$$

The local density of states are displayed in fig. F.0.3 for the mapping to a two-dimensional model (left) and a three-dimensional model (right).

Table F.1.: Hopping coefficients c_i for the mapping of a one dimensional chain to a two- and a three-dimensional effective model.
distance i ... coefficient at bond i away from correlated site
2D c_i ... coefficient for the mapping to two-dimensions
3D c_i ...coefficient for the mapping to three-dimensions

distance i	2D c_i	3D c_i	distance i	2D c_i	3D c_i
c_1	2.000000	2.449490	c_{15}	1.989657	3.005940
c_2	2.236077	3.000000	c_{16}	2.011621	3.001386
c_3	1.949377	3.073182	c_{17}	1.990959	2.993073

continued on next page

Table F.1 – continuation

distance i	2D c_i	3D c_i	distance i	2D c_i	3D c_i
c_4	2.074883	2.924988	c_{18}	2.010051	3.008736
c_5	1.967931	3.049102	c_{19}	1.991982	2.993337
c_6	2.041942	2.983285	c_{20}	2.008840	3.002119
c_7	1.976995	2.990363	c_{21}	1.992806	3.002684
c_8	2.028360	3.023338	c_{22}	2.007881	2.994256
c_9	1.982234	2.976134	c_{23}	1.993483	3.006018
c_{10}	2.021124	3.014898	c_{24}	2.007103	2.996264
c_{11}	1.985607	2.997686	c_{25}	1.994050	3.000146
c_{12}	2.016693	2.991709	c_{26}	2.006460	3.003107
c_{13}	1.987946	3.013275	c_{27}	1.994530	2.995299
c_{14}	2.013729	2.988102	...		